Treatment planning for manifold multi-ion particle therapy

Roumani Alabd

A dissertation submitted for the degree of
Doctorate of Philosophy

School of Electrical and Data Engineering

University of Technology Sydney

March 2023

Certificate of Original Authorship

I, Roumani Alabd, declare that this thesis is submitted in fulfilment of the requirements for the award of Doctor of Philosophy, in the School of Electrical and Data Engineering at the University of Technology Sydney. This thesis is wholly my own work unless otherwise referenced or acknowledged. In addition, I certify that all information sources and literature used are indicated in the thesis. This document has not been submitted for qualifications at any other academic institution. This research is supported by the Australian Government Research Training Program.

Production Note:
Signature removed prior to publication.

March 2023
Roumani Alabd

Acknowledgements

Daniel Franklin, without you this work would have not happened. I shall never forget. I also want to thank Prof Gyorgy Hutvagner for all of his support throughout my time at UTS.

Dedication

For Edith and Marina

Abstract

Conventional charged particle radiation therapy systems utilise a single charged particle species to deliver a therapeutic radiation dose to the target - most commonly protons or carbon ions. While such radiation therapy is highly effective for the treatment of many cancers, there is growing interest in using combinations of two or three ion species for cancer therapy, due to the ability to control both the dose distribution and the linear energy transfer of the radiation throughout the target. However, to date, there has been little research into the potential for going beyond a very limited number of ion species in a single treatment plan due to the limitations of current medical accelerators, and there are presently no treatment planning systems capable of producing a treatment plan integrating a diversity of ion species.

This work presents a new open source treatment planning system for manifold multi-ion particle therapy based on a hybrid Monte Carlo and linear optimisation approach. The developed TPS utilises a library of Monte Carlo simulation data for up to eight individual ion species (^{1}H, ^{4}He, ^{7}Li, ^{12}C, ^{16}O, ^{20}Ne, ^{28}Si and ^{56}Fe) of many different energies in a single target material (polymethyl methacrylate). The library is then adapted for the pencil beam geometry and energy spread of a specific accelerator beamline; next, a raster grid of beam positions is constructed to cover the target volume, and the weighting of individual energy components of each ion beam required at each position is determined by linear optimisation such that the desired spatial distribution of physical dose is achieved in a heterogeneous target. The TPS will optimise the parameters of the ion source (which could be a conventional synchrotron

source or a laser-driven ion source) to produce the desired dose distributions in the target, while accounting for tumour hypoxia/necrosis and organs at risk.

Abbreviations

AAPM	American Association of Physicists in Medicine
ABS	American Brachytheapy Society
AJCC	American Joint Committee on Cancer
ACIM	Australian Cancer Incidence and Mortality workbooks
AIHW	Australian Institute of health and Welfare
BSDF	backscatter dose fraction
BP	Bragg peak
BEAD	broad energy assorted depth
CIRS	Computerized Imaging Reference Systems
CMRP	Centre for Medical Radiation Physics
CRT	conformal radiation therapy
CTV	clinical target volume
CT	Computed Tomography
DVH	dose volume histogram
D90	the minimum dose threshold for the top 90% target volume receiving dose
D50	the minimum dose threshold for the top 50% target volume receiving dose
DNA	deoxyribonucleic acid
DSBs	double-strand breaks
DPBN	dose painting by numbers
EBRT	external beam radiotherapy
ESTRO	The European Society for Radiotherapy and Oncology
FI	functional imaging

FWHM	full width at half maximum
HDR	high dose rate
HB	hole-boring
HSG	human submandibular gland
HIT	heavy ion therapy
ICRU	International Commission on Radiation Units and Measurement
IMPACT	intensity modulated composite particle therapy
IAEA	International Atomic Energy Agency
IEEE	Institute of Electrical and Electronics Engineers
IGRT	Image-guided radiation therapy
IMRT	intensity modulated radiation therapy
ISUP	International Society of Urological Pathology
ISESS	integrated shot-to-shot energy selection system
LAP	laser-accelerated proton
LDR	low dose rate
LET	linear energy transfer
linac	linear accelerator
LS	light sail
MKM	microdosimetric kinetic model
MRI	Magnetic Resonane Image
NIRS	National Institute of Radiological Sciences
NTCP	normal tumour control probability
OER	oxygen enhancement ratio
PTV	planning target volume
pO2	oxygen partial pressure
PET	Positron Emission Tomography
PMMA	polymethyl methacrylate
PT	proton therapy
OARs	Organs at Risks
QA	quality assurance
RBE	relative biological effectiveness
RPA	radiation pressure acceleration
RMSE	root mean square error
Rf	radio frequency
SD	standard deviation

SBR	signal to background ratio
SNR	signal to noise ratio
SSBs	single-strand breaks
SOBP	spread-out Bragg peak
TPS	treatment planning system
SPGC	small portable graphite calorimeter
TCP	tumour control probability
TNSA	Target Normal Sheath Acceleration
V_5	percentage of non-tumour volumes receiving at least%5 of the prescribed Dose
V_{10}	percentage of non-tumour volumes receiving at least%10 of the prescribed Dose
V_{50}	percentage of non-tumour volumes receiving at least%50 of the prescribed Dose
VHEE	very high energy electron
WED	Water-equivalent depth

Table of contents

List of figures

List of tables

CHAPTER 1

Introduction

1.1 Background

Cancer is the second most common cause of human death worldwide, surpassed only by heart disease [1]. One of the most significant developments in medicine over the past century has been progress in developing new and more effective therapies for cancer. Radiation therapy, in which ionising radiation is used to selectively destroy cancerous tissues, is a key element of most cancer treatment plans. The basis of its therapeutic effect is that ionising radiation damages DNA in all cells, especially those which are in the S phase (i.e. the DNA duplication phase). Thus, radiation impacts both cancerous and normal cells; however, cancer cells are malignant because they are undergoing rapid, uncontrolled mitosis, and hence they are more likely to be in the S phase compared to most normal tissue cells. Cancer cells are therefore disproportionately impacted by the radiation, which impedes their rate of mitotic division and hence can slow or reverse tumour progression. Furthermore, the disordered behaviour of cancer cells reduces their ability to repair damage due to ionising radiation compared to normal tissue. Therefore, provided that the radiation dose is carefully controlled, damage to normal tissues can be limited to that which is largely repairable, while still achieving effective tumour ablation.

Charged particle therapy (often simply referred to as particle therapy) is a radiotherapy modality in which a relativistic beam of protons or heavier ions (for example,

helium or carbon ions) is used to deliver a therapeutic radiation dose to a planned treatment volume inside the patient. Charged particles such as protons or heavy ions exhibit a very well-defined, energy-dependent Bragg peak - the depth at which the majority of a particle's energy is deposited as it slows down through matter via electronic interactions. This enables highly conformal dose delivery via control of both the beam spectrum and the transaxial spatial distribution of the beam. These beam attributes can be controlled either by collimating and passively scattering a broad, monoenergetic proton or ion beam with a ridge filter and patient-specific bolus, or by raster-scanning and energy-modulating a narrow pencil beam across the treatment volume. The precise depth-selectivity of proton and heavy ion therapy enables the effective treatment of deep tissues with a much smaller number of treatment fields and fractions than is possible in conventional radiotherapy modalities such as external-beam photon therapy.

At present, the choice of charged particle used for current cancer therapies is largely determined by the availability of a suitable treatment facility nearby and the preferences of the physician. In much of the world (especially in the United States), proton therapy is the dominant form of particle therapy. Elsewhere, especially in Japan and Europe, some treatment facilities offer also charged particle therapy with heavier ions such as helium, carbon or oxygen. Each ion has its own set of unique characteristics due to the specific charge, mass, interaction cross sections and nuclear fragmentation processes; however, in all cases, heavier ions deposit a greater fraction of their kinetic energy at the Bragg peak and are less susceptible to lateral scattering and range straggling compared to lighter ions. This reduces the loss of beam intensity (lateral and axial spreading-out) at the distal end of the particle track, and enables the treatment of deeper tissues with fewer fields compared to proton therapy, since the entrance dose is lower for treatment at a given depth. Due to projectile fragmentation, as ion mass increases, the particles also deliver a progressively greater *tail dose*, which extends some way beyond the Bragg peak - a phenomenon which is absent in proton therapy. This phenomenon limits the usefulness of very heavy nuclei in particle therapy, and the majority of active research in particle therapy concentrated on ions no heavier than silicon (with some interest iron).

The biological impact of particle therapy on tumours and healthy tissue is dependent on several factors, including the total dose, the radiosensitivity of the specific tumour or tissue, and the linear energy transfer (LET) of the radiation (the average rate of energy deposition in the medium per unit length of particle track). In particular, for

hypoxic (poorly vascularised) tumour regions, a high LET is preferable as it results in a higher rate of creation of reactive oxygen species (ROS) which cause damage to the tumour. The relative biological effectiveness (RBE) continues to increase up to a maximum LET of approximately 100 keV/μm, beyond which it begins to decrease again [2, 3]. The LET of charged particles increases with increased particle mass and charge, which is especially important in hypoxic tumour regions which are radioresistant compared to oxic tumours [4]. Due to this complex relationship, the optimal choice of ion depends on several factors such as depth of the tumour, required dose level, the relative radiosensitivity of the tumour and surrounding healthy tissues and the relative position and geometry of the tumour and nearby organs at risk (OARs) to which the dose must be carefully limited [5].

Conventional treatment planning for charged particle therapy is performed with the objective of achieving a uniform dose (either physical or biological) throughout the planning target volume (PTV), while limiting the dose delivered to radiosensitive organs at risk. The target dose is selected to be sufficient to achieve effective tumour ablation within the target volume while not exceeding safe normal-tissue dose limits in OARs. It has been postulated that a higher tumour control probability (TCP) can be achieved by irradiating a tumour with a non-uniform distribution of dose and LET, to account for the spatially variable radiosensitivity of inhomogeneous, hypoxic or necrotic tumours [5–8]. This can be achieved using a composite treatment plan comprising multiple ion species, which can leverage the specific characteristics of each ion to maximise both the conformity of the dose distribution to the objective and to achieve secondary objectives such as hypoxia-based LET adaptation and protection of organs at risk. Several studies indicate that improved therapeutic results may be achieved using a combined irradiation scheme of two or more different ion species per treatment field compared with conventional single-ion particle therapy [5, 9–11].

Simultaneous control of the dose and LET distributions requires irradiation of the target with a range of ion species. However, in practice, this is difficult to achieve in a single treatment fraction using conventional synchrotron-based particle sources. One of the major limitations of particle therapy is the dependence on large particle accelerator facilities which are required to generate the particle beam. While a relatively low-cost cyclotron is sufficient to generate proton beams, to date, generation of beams of heavier ion species has required the use of a synchrotron - a device with a substantial physical footprint and large energy demands, typically requiring a dedicated building and complex power supply and shielding arrangements.

More recently, an alternative accelerator technology has emerged, which promises to greatly reduce the costs of generating a high energy beam of ionised atoms - laser-driven particle acceleration. The basic principle is that a neutral gas is ionised by a high-energy laser pulse. The resulting hot plasma contains both a mixture of both electrons and ions (atomic nuclei with the electrons stripped away). The substantial difference in charge-to-mass ratio between electrons and the ions means that a strong electromagnetic field applied to the plasma can separate the positively-charged ions from the negatively-charged electrons, creating a very large electric field in a small space. By appropriately controlling a wavefront propagating through this plasma, it is possible to accelerate charged particles (ions or electrons) to extremely high energies in the space of a few metres. The achievable energies are of the order required for heavy ion therapy. However, the energy spectrum and particle mix is very different to that offered by a synchrotron ion source.

Using a laser-driven particle accelerator ion source for particle therapy applications is an interesting and relatively unexplored field of research. Due to the wide variety of ion species and energies which can potentially be generated using a laser-based accelerator, treatment planning with such an ion source is a completely different problem to treatment planning using a conventional synchrotron particle source. Charged particle radiotherapy delivered using a laser-driven particle accelerator has the potential to simultaneously achieve dose and LET painting in a single fraction, which may offer substantial enhancements to treatment efficacy and patient well-being. However, to date, no treatment planning system exists which is capable of fully exploiting this type of radiation source.

In this work, a new open source treatment planning system for manifold multi-ion particle therapy is presented, which is ideal for future laser-based therapeutic particle accelerator radiation sources. The developed TPS utilises a library of Monte Carlo simulation data for 8 individual ion species (^{1}H, ^{4}He, ^{7}Li, ^{12}C, ^{16}O, ^{20}Ne, ^{28}Si, ^{56}Fe) of different energies in a single target material. The library is first adapted for the pencil beam geometry and energy spread of a specific beamline; a raster grid of beam positions is then constructed to cover the target volume, and the weighting of individual energy components of each ion beam required at each position is determined by linear optimisation such that the desired spatial distribution of physical

dose is achieved in a heterogeneous target[1]. Low-LET ions can be excluded from known hypoxic sub-volumes within the target volume, and the TPS supports a configurable degree of avoidance of dose to organs at risk.

1.2 Research objectives and overview

The overall aim of this thesis is to develop a treatment planning system for optimal irradiation of a heterogeneous target with arbitrary spatial dose distributions using arbitrary combinations of ions, featuring controllable avoidance of dose in organs at risk and optional linear energy transfer enhancement in hypoxic target sub-volumes, which would be suitable for use with future laser-driven particle accelerator radiation sources. The central hypothesis of this thesis is:

> That a diverse, manifold multi-ion treatment plan will consistently outperform a conventional single-ion or low multi-ion treatment plan by a number of key metrics, including dose uniformity, dose conformance and radiation exposure to healthy tissues, while allowing optimised treatment of hypoxic sub-volumes and minimising the radiation dose to organs at risk.

This hypothesis will be explored through the following specific research objectives:

1. To develop a high-resolution simulation-based dose deposition distribution library via Geant4 Monte Carlo simulations of idealised, perfectly monoenergetic, infinitesimally thin particle beams impinging on a single target material (polymethyl-methacrylate or PMMA) for ions ranging from hydrogen (protons) to iron. These simulations will be performed across a therapeutic range of different energies, progressively incremented such that the Bragg peak depth increases in steps of 1 mm from a minimum of 5 mm to a maximum depth of 217 mm (corresponding to a water-equivalent depths of up to 250 mm);

2. To adapt this library to the beam parameters (energy spread and beam shape) of an arbitrary particle accelerator, such that the one set of simulation data can be applied to any treatment facility;

[1] Physical dose is used here rather than biological dose due to the highly degree of variability of relative biological effectiveness (RBE) for a given ion species between different tissue types.

3. To develop methods based on combined Monte Carlo and linear optimisation approaches which can select an appropriate combinations of ions and energies (subject to configurable restrictions which may apply to that particular accelerator) to achieve a desired spatial distribution of dose subject to linear energy transfer (LET) constraints in an arbitrarily defined heterogeneous target volume. The assumption is that we have anatomical information (based on CT imaging or similar) plus the library of physics data.

4. To extend these methods in three key ways:

   (a) To support the exclusion of dose from organs at risk;

   (b) To support a non-uniform LET distribution such that hypoxic areas are treated exclusively with high-LET radiation; and

   (c) To support multi-field irradiation of a target.

5. And finally, to evaluate the performance of a manifold multi-ion radiation therapy treatment plan and compare it with equivalent single-ion, dual-ion and triple-ion treatment plans subject to equivalent constraints.

Each chapter of this thesis contributes to an important aspects/characteristic of the developed treatment planning system.

Chapter 2 provides an extensive review of the critical literature related to the overall thesis objectives. This includes an overview of particle therapy, including the physics and radiobiological aspects of this treatment modality, the ion species which have been widely utilised or been investigated for their relative biological and physical characteristics. The potential advantages of multi-ion therapy and the best developed treatment planing systems for this modality are discussed. A comprehensive overview of laser-driven particle accelerators and their potential applications in medicine for cancer radiation therapy is presented, including a discussion of the principles of laser-driven ion acceleration and the most common laser plasma acceleration techniques (Target Normal Sheath Acceleration and Radiation Pressure Acceleration), the characteristics of laser-driven ion beams, and in-vitro and in-vivo experiments which investigate the radiobiological impacts of laser-driven particle irradiation. This literature review is an essential precursor in identifying the challenges which multi-ion particle therapy poses and the limitations of existing TPSs, and justifies the need for a new TPS to support future manifold multi-ion particle therapy radiation sources.

This chapter has resulted in the following paper submission:

- **R. Alabd**, A. Bishop and D. Franklin. "Laser-Driven Particle Accelerators for Cancer Therapy: A Review of State-of-The-Art Techniques, Challenges and Opportunities" Submitted to *IEEE REVIEWS IN BIOMEDICAL ENGINEERING*, Jun. 2022.

In **Chapter 3**, we present the design of a new open source treatment planning system for manifold multi-ion particle therapy for optimal irradiation of a heterogeneous target with arbitrary spatial dose distributions using arbitrary combinations of ions. An exhaustive set of plans for different ion combinations for different tumour positions have confirmed the properties of the proposed treatment planning system design and methodology; the performance of the treatment planning system is evaluated under a variety of conditions in a heterogeneous target to demonstrate the dose conformance benefits of treatment with a wide range of ions. Several critical performance metrics are evaluated to compare the resulting plans, including RMS error between the objective and the achieved dose distributions (which measures dose uniformity), D_{50} and D_{90} dose volume percentages (which measure the dose conformance to the objective), and the volumes of non-target tissue which are subject to doses exceeding 5%, 10% and 50% of the objective dose. A sample treatment plan is also implemented as an integrated Geant4 simulation and the resulting dose distribution is compared to that predicted by the corresponding treatment plan.

In **Chapter 4**, we extend the developed treatment planning system introduced in Chapter 3 to include support for protection of radiation-sensitive organs i.e. organs at risk, and to implement linear energy transfer enhancement in hypoxic target subvolumes within the tumour volume. The performance of different treatment plans using a variety of single, dual, triple and manifold ion combinations for different tumour positions, with OARs and/or hypoxic subvolumes, are evaluated and compared using the same metrics introduced in the Chapter 3, confirming the capabilities of the developed TPS.

We have incorporated the design, methodology, algorithm, and results of Chapter 3 and 4 into a paper which has been submitted to *Scientific Reports*:

- **R. Alabd**, A. Bishop, A. Chacon, M. Safavi-Naeini and D. Franklin. "Treatment planning system for manifold multi-ion particle therapy," Submitted to *Scientific Reports*, Nov. 2022.

Chapter 5 further extends the capabilities of the TPS in Chapters 3 and 4 to support sequential multi-field treatment plans; performance is again compared across

a variety of ion combinations, target positions and OAR/hypoxia constraints. We have submitted a Letter based on these results to *Physics in Medicine and Biology*;

- **R. Alabd**, A. Bishop, A. Chacon, M. Safavi-Naeini and D. Franklin. "A computationally efficient algorithm for multi-field manifold multi-ion particle therapy," Submitted to *Physics in Medicine and Biology*, Nov. 2022.

Finally, Chapter 6 provides a summary of the main findings of this the work and discusses the next steps and future work.

1.2.1 Additional research contributions

The author has additionally made a number of relevant contributions to other research outputs during his PhD, including:

- K. J. Wilson, **R. Alabd**, M. Abolhasan, M. Safavi-Naeini, and D. R. Franklin, "Optimisation of monolithic nanocomposite and transparent ceramic scintillation detectors for positron emission tomography," Scientific Reports, vol. 10, no. 1, Jan. 2020.

- K. J. Wilson, **R. Alabd**, M. Abolhasan, D. R. Franklin, and M. Safavi-Naeini, "Localisation of the lines of response in a continuous cylindrical shell PET scanner," in 2019 41st Annual International Conference of the IEEE Engineering in Medicine and Biology Society (EMBC). IEEE, Jul. 2019.

CHAPTER 2

Literature review

2.1 Introduction

While around 90% of current radiation therapy treatments utilise X-ray photons, particle therapy is considered to be a superior treatment modality for certain cancers [12, 13]. This is due to the mechanism by which an energetic charged particle loses kinetic energy as it traverses matter. A beam of protons or heavy ions exhibits a very well-localised maximum in the depth wise energy deposition profile (known as the *Bragg peak*) - with the depth at which this maximum occurs being dependent on the initial kinetic energy of the particle prior to entering the target. This results in the deposition of the majority of the dose near the stopping point of the particle, allowing highly conformal dose delivery by control of the beam spectrum and transaxial spatial distribution of the beam. The depth-selectivity of particle therapies allows for treatment of deep tissues while reducing the dose to healthy tissues proximal or distal to the tumour compared to other radiotherapy modalities such as photon therapy. Yet despite these advantages, the proportion of cancer patients who have been treated using particle therapy remains relatively small. Indeed, since the concept of using high-energy charged particles for cancer therapy was first introduced in 1946 [14], only about 260,000 patients have received charged particle radiation therapy as part of their cancer therapy treatment, compared to the many millions who receive photon-based radiation therapy every year [15, 16].

This chapter provides a review of the critical literature related to particle therapy, including the physics, radiobiological aspects of this treatment modality as well as it outlines the current state of the art in laser plasma accelerators for charged particle radiation therapy, and identify the key challenges and opportunities offered by this radiation source and their potential use in particle radiation therapy.

2.2 Physics of Particle Therapy

In this section, we provide a concise overview of the underlying physics of particle therapy including the different interaction processes that a charged particle or a photon may undergo when they interact with matter. In addition, the section explains some of the fundamental quantities used to describe the behaviour of a charged particle when it passes through an object such as linear energy transfer (LET), Bragg peak (BP), and range.

2.2.1 Interaction of charged particles with matter

When a charged particle travels through matter, its surrounded electric force field interacts with the orbital electrons (collision loss) and nucleus (radiative loss). In each individual atomic interaction, the charged particle transfers a small amount of its energy into the matter, so that the particle undergoes a large number of interactions before it stops and its kinetic energy reaches zero. The gradual decrease in the charged particle energy can be explained by the term *stopping power*. Stopping power as well as other parameters such as range,(BP), and LET are considered critical factors in the selection process of ion species to deliver a desired dose rate to a tumour in particle therapy. These parameters depend on the properties of the charged particle such as charged particle energy, velocity and mass as well as the properties of the absorbing target such as its mass and its density and atomic number [17–19]. In this section we discuss these terms that are relevant to this thesis.

2.2.1.1 Stopping power

It is well known that as a charged particle penetrates matter, it experiences multiple Coulomb interactions with the nuclei and the orbital electrons of the medium atoms before its kinetic energy is vanished. These multiple interactions may alter the charged particle's path through the target depositing some of its energy into the absorber

medium. The rate of energy loss per length unit travelled by a charged particle into an observer object is called *linear stopping power* (-$\frac{dE}{dx}$). By dividing the linear stopping power by the density ρ of the absorbing medium, the new term then is referred to as the mass stopping power S and is typically given in units MeV.cm^2/g. Stopping power is a property of the absorber medium so that, for a beam of charged particles for instance, proton or heavy ion loses more energy as it traverses 1 cm of bone than it passes through 1 cm of water and dramatically less when it travels through 1 cm of air [20]. A charged particle may undergoes multiple Coulomb interactions with the nuclei of the absorber that leads to *radiative stopping power*, only light charged particle may suffer a considerable loss in their kinetic energy as they undergo these interactions which are referred to as *bremsstrahlung interactions*. It also can interact with the orbital electrons of the absorber target leading to *collision(ionisation) stopping power*. These interactions can lead to depositing energy from the charged particle into the medium causing the absorber atoms excitation or ionisation [17–19].

For therapeutic energy and within the scope of this thesis, the collision stopping power that results from inelastic interactions with the absorber electrons atoms is of importance while the radiative stopping power has a negligible impact for charged particle heavier than electrons and positrons. So that the total stopping power for a charged particle of energy E_K traverses a medium with an atomic number Z is given by the collision stopping power and its radiative is neglected.

Several models have been proposed to calculate the ionisation stopping power such as Bethe-Bloch equations that is being the most commonly used [21]

$$S(E) = -\frac{dE}{dx} = \left(\frac{4\pi n z^2}{m_e c^2 \beta^2}\right)\left(\frac{e^2}{4\pi\varepsilon_0}\right)^2\left[\ln\left(\frac{2m_e c^2\beta^2}{I(1-\beta^2)}\right) - \beta^2\right] \tag{2.1}$$

where e the electron charge, ε_0 is the vacuum permittivity, z the multiple of electron charge, m_e the electron mass, n is the electron density of the material, and I the mean excitation potential, and $\beta = v/c$, where v is the speed of particle and c is the speed of light in vacuum.

Although the formula is not trivial, a few characteristics are of particular importance:

1. The amount of deposited energy and consequently, deposited dose depend on the density of the absorber target ρ as well as its chemical compositions;

2. Deposited energy is inversely proportional to the square of the velocity of the particle; for example, at the beginning of the interaction between a charged

particle and a medium, the charged particle has a high velocity, therefore, less dose is deposited into the medium, where as the particle decreases its velocity, it loses more energy to the medium [20]

Therefore, a proton or a charged particle entering the medium will have its maximum energy and with highest velocity. As they travel through an absorber, they experience multiple coulomb interactions with the electrons orbiting the medium atoms losing more energy and depositing increasingly more dose.

2.2.1.2 Range

A charge particle travelling through a medium has a finite range before it stops at the medium. The range of a charged particle in a specific material is an experimental concept that depends on the particle's kinetic energy, charge and as well as its mass, [17, 19, 22]and on the composition of the absorbing object. In therapeutic particle, range (R) is referred to as R_{CSDA}, continuous slowing down approximation that can be calculated as follows[19]:

$$R_{CSDA} = \int_0^{E_{K_i}} \frac{dE}{S_{tot}(E)}, \tag{2.2}$$

where R_{CSDA} is the CSDA range (mean path-length) of the charged particle in the absorber medium, S_{tot} is the total stopping power of the charged particle as a function of its kinetic energy E_k, E_{k_i} is the initial kinetic energy of the charged particle.

2.2.1.3 Elastic nuclear scattering

A charged particle traversing an absorber may experience deflections in its path through the medium. This is due to multiple Coulomb interactions that the particle undergoes with the nuclei of the atoms of the absorber; this is called elastic scattering that leads to a changing the trajectory of the particle [17, 19, 20, 22]. The deflection angle mainly depends on the mass of the incident charged particle and the atomic density as well as the atomic number of the absorbing medium [17, 20]. As such a heavy charged particle, for instance, carbon suffers smaller scattering angle than a proton that experiences a larger scattering angle if both travel the same medium, this will result in a beam of heavy ions being laterally scattered less than a beam of protons [22]

2.2.1.4 Inelastic collision interactions

A charged particle undergoes multiple Coulomb interactions with the electrons orbiting the atoms of an absorber. In each interaction the charged particle transfers a small amount of its energy to the orbiting electrons causing ionisation to the atoms of the medium.

2.2.1.5 Bragg peak (BP)

Bragg peak (BP) is a physical characteristic of the depth-dose profile observed in matter irradiated with charged particles (particularly heavier particles such as protons or ions). For a monoenergetic beam of particles impinging on a homogeneous block of matter, the majority of the dose is deposited in a narrow depth range at a specific depth (Bragg peak) which depends on the energy of the beam. Some energy is deposited prior to this point (which contributes to the so-called *entrance dose*, and very little energy will be deposited beyond it (the *tail dose* - which is almost zero for protons and increases as the particle mass increases due to increased projectile fragmentation causing a more pronounced *fragmentation tail*).

Energy loss in charged particle beams traversing matter is a result of electromagnetic interactions with atoms in the target, and is inversely proportional to the velocity of the charged particle. As a charged particle slows down, it loses progressively more energy per unit path length. The majority of energy deposition occurs within the final few millimetres of the particle's track.

The concept of the Bragg peak is illustrated in Figure 2.1.

2.2.1.6 Spread out Bragg peak (SOBP)

To deliver a dose to a range of depths in a target via charged particle radiation (i.e. to treat the full physical extent of the tumour in the z dimension i.e the depth of the tumour), it is necessary to use a beam consisting of particles with a range of different energies. This can be achieved either using an energy continuum (e.g. by using a ridge filter to spread out the spectrum of a monoenergetic radiation source) or with a combination of discrete energy beams produced sequentially in the particle source. The spectrum should be designed such that it achieves a flat biological effective dose across the entire depth of the target volume; in practice, due to the entrance dose generated from each component monoenergetic beam, which is added to each

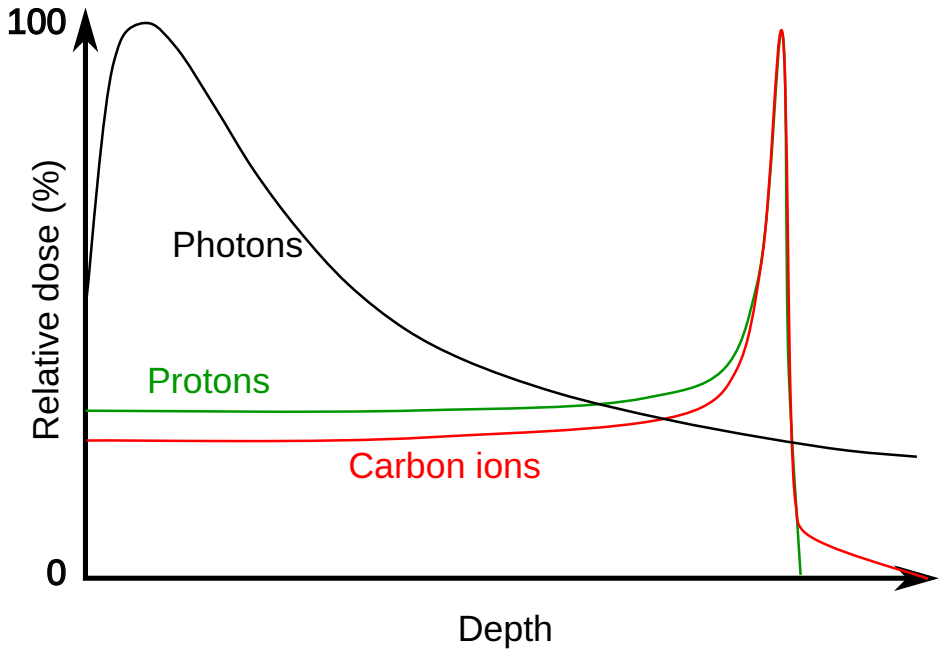

Figure 2.1: Typical peak-normalised dose vs. depth curves for photons, protons and carbon ions, illustrating the Bragg peak. The depth scale is arbitrary.

subsequent lower-energy component, this means that the weighting of the higher-energy beam is much higher than the lowest energy components of the spectrum.

The resulting depth-dose profile features a flat plateau (in terms of biological dose) in the target depth range, with a substantial (but slightly lower) cumulative entrance dose at shallower depths. This profile is known as a spread-out Bragg peak (SOBP) and is shown in Figure 2.2.

2.2.1.7 Linear energy transfer (LET)

The rate of energy lost by charged particles per unit distance travelled in matter is known as linear energy transfer (LET). It is an intrinsic parameter of a given type of radiation traversing a particular material, and describes the average amount of energy loss per unit of track length. It is normally measured in units of keV/μm. Mathematically, LET is proportional to Z^2/v^2, (Z being the ion charge, and v being ion velocity). It is well known that the higher LET of densely-ionising radiation leads to a significantly increased efficacy in tumour-cell-killing ability [24]. An ionising radiation with high LET induces clusters of DNA damage. In relation to radiotherapy, however, it is important to note that it is not necessarily desirable to apply high LET radiation to the entire tumour, since this also introduces a high risk of adverse effects in healthy

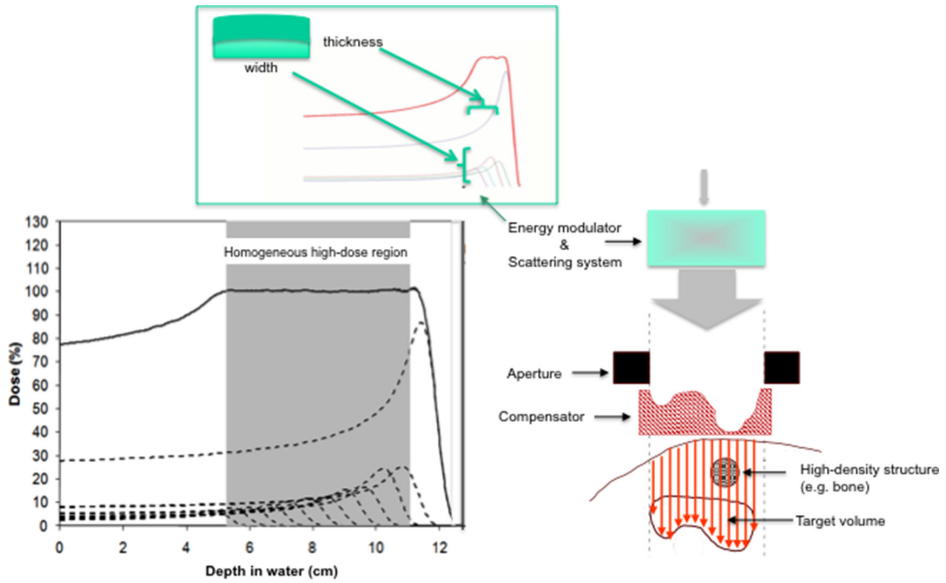

Figure 2.2: Spread-out Bragg peak as a combination of multiple Bragg curves to homogeneously cover and extended region with the same dose as a function of depth [23]

tissues. Amongst the highest-LET forms of radiation are charged particles such as heavy ions and fast neutrons; the lowest-LET radiation is photon radiation. The LET of protons and heavy ions is at a maximum value at the BP, where it can be of the order of 100 keV/μm.

2.3 Radiation biology and the impact of ionising radiation on living matter

The biological properties of any type of radiation derive from the manner in which energy is deposited in cells. Following the discovery of the structure of DNA, it has become clear that radiation's ability to disturb the structure of DNA, is the key cause of its biological effects[25, 26]. Accordingly, the high ionisation density generated along the track of charged particles such as protons and heavy ions lead to clustered DNA damage. Since cancer cells are disordered, their ability to repair DNA damage is reduced. Therefore, a dose of radiation which can induce DNA damage has a differential impact in healthy and cancerous cells. Effective radiation therapy is based on the principle that as long as the radiation dose is low enough that normally-functioning cells can repair themselves, but cancer cells cannot, the net effect is tumour ablation

without severe harm to healthy tissues. This is also the principal behind fractionated dosing of radiation therapy - each fraction kills more cancer cells while being insufficient to irreparably damage most normal cells. Radiation can induce damage to the DNA structure either *directly* by ionising or breaking bonds within the DNA molecule itself or *indirectly* by ionising other molecules such as water inside the cell that in turn, interact with the DNA molecule and disturb it. A range of different mechanisms in which ionising radiation can cause damage to living cells have been studied but the most widely accepted mechanism that is considered as the key driver of the radiobiological impacts on the cells is the DNA double-strand breaks (DSBs) [25]. Radiation can cause damage to the sugar-phosphate backbone which disturbs the structure of DNA double helix. This can result in the damage of one single strand of the DNA double helix structure known as single-strand breaks (SSBs) or the damage of both strands of the DNA double helix (DSBs). Damage caused to to the single-strand breaks has minimal biological impact since the cell can quickly and accurately rebuild the damage strand making use of the opposite undamaged strand as a template. However, in the case of double strand breaks, both strands are severely damaged with multiple base pairs lost, accordingly no strand can serve as a template, and more complex processes are required to repair the damage. This is most probably to introduce at least new genetic alterations or large-scale genomic arrangements[25].

2.3.1 Relative biological effectiveness (RBE)

RBE is an empirical quantity that is know as the ratio between two different doses to achieve the same degree of effect when two modalities are compared e.g. a reference dose and proton radiation.

$$RBE = D_x/D_R \tag{2.3}$$

where D_x is a reference absorbed dose radiation of a standard type x, and D_R is the absorbed dose radiation exposure.

Despite the simple definition, RBE is a complex quantity since it depends on LET, dose rate, particle type and energy involved, and the biological properties of the tissue in question, such as the type of tissue, its oxic/hypoxic status, cell proliferation rate and cell density. These factors result in considerable variations in the tumour response to radiation. For example, two different particles with the same dose may undergo different electromagnetic interactions with the tumour tissue they traverse, resulting

in different RBEs with different surviving fractions for the same physical dose [24]. In addition, research and experimental results have shown that a homogeneous dose may not be effective to all compartments of a heterogeneous tissue [27]. Therefore, for treatment applications, it is generally not appropriate to model all these dependencies explicitly, and approximations have to be made.

RBE remains a controvertial subject in both research and clinical contexts. It is clear that a single value is not meaningful in all contexts; due to the variable LET along the path of the beam, it varies as a function of depth (for a single energy). Different values have been reported in the literature for the same ion, energy and target tissue. The value of RBE is also highly dependent on the type of tissue. An interesting example of this is that although there is broad consensus between medical physicists that the RBE for protons is about 1.1 (relative to X-ray photon radiation), proton RBE is reported to vary slightly between actively-scanned proton beams and passively-scattering systems [28].

Since high RBE is an intrinsic advantage that heavy ions have over the conventional treatment therapy, a precise evaluation of the RBE along with the absorbed dose is needed in order to deliver an accurate calculated biological dose. At the present time, there are several semi-analytic models that can provide a good estimate of the RBE for different ions species [29].

2.3.2 Hypoxia

Tumour hypoxia is a deprived oxygenated subregion structure within solid tumour entity which contributes to radiation resistance. It is considered a limiting factor for radiation therapy that may lead to treatment failure [24]. Hypoxic areas and the degree of hypoxia correlate with the treatment outcome of radiotherapy. In reality, the physiological hypoxia size is on average only 5 % in nonmalignant tissues and < 2 % in most tumours [30] In vitro experimental research shows that in case of hypoxic subvolumes, it needs radiation dose that is up to three times higher than the radiations dose required to achieve the same response for normal oxygen level cells [30, 31]. The concept hypofractionation with heavy ions may, therefore, considered as a potential candidate in the use for clinical trials of radiotherapy with hypoxic tumours. In-vitro experiments have demonstrated that carbon-12 ions solely may not be the best option to overcome tumours with hypoxic volumes that are $> 0.5cm^3$. However, heavier ions such as ^{16}O with a slight dose boost have shown the potential capability to overcome larger hypoxic entities with size range of 1-4 cm^3 [24].

2.3.3 Oxygen enhancement ratio (OER)

Oxygen Enhancement Ratio (OER) is a measure of the effectiveness of radiation in producing biological damage in the absence or presence of oxygen. It is defined as the ratio of the radiation dose required to produce a certain biological effect under hypoxic (low oxygen) conditions to the dose required to produce the same effect under aerobic (normal oxygen) conditions. In other words, the OER represents the relative sensitivity of cells or tissues to radiation damage when exposed to different oxygen levels. Hypoxic cells are generally more resistant to radiation damage compared to aerobic cells, and this is reflected in the OER value. The OER is an important parameter in radiation therapy, as it helps to determine the appropriate radiation dose to deliver to a tumor to achieve the desired therapeutic effect while minimizing damage to healthy tissue. [7, 31].

Several model studies have shown that increasing LET may lead to the decrease of OER values [31–34]. Scifoni E. et al, develop a simple semi-empirical model for mapping the OER as a function of oxygen concentration and dose averaged linear energy transfer (LET) providing tables of OER that can be loaded into the program. In order to test their model, the authors verified model with independent experiments [33].

Moreover, in their study Wenzl et.al, applied the standard linear-quadratic model and the Alper-Howard-Flanders model to derive a phenomenological model for the estimation of the required enhancement factors for dose escalation that depends on oxygen partial pressure (pO_2) levels [31]. The authors collected and analysed data from literature for different ions species where both aerobic and hypoxic tumour were exposed to irradiation. It has been shown that the calculated OER for the in-vitro experiments is in a good agreement with developed model. As it is reported that for the mean OER value for carbon ion was 1.76 and 1.02 and for protons were 2.08 and 1.03 when the oxygen levels were between 0.5 mm and 20 mm.

2.4 Particle therapy and heavy ion therapy

Since Robert R. Wilson originally proposed the therapeutic use of high energy charged particles produced by accelerators in 1946, the exploitation of particle beams for the treatment of cancer has been widely investigated, developed and clinically applied.

The physical properties of charged particle radiation such as protons and heavy ions - in particular, BP - are highly attractive for therapeutic applications.

The typical depth-dose characteristics of monoenergetic beams of photons, electrons, protons and carbon ions are shown in Figure 2.1. Photons deliver the majority of their dose near the surface, necessitating the use of many separate treatment fractions and/or fields to deliver the therapeutic dose to the tumour while limiting the dose received by healthy tissues. In contrast, charged particles deliver most of their dose at a well-defined depth in the target (BP), which is governed by the particle's initial kinetic energy. Due to their low mass, electrons are subject to a much higher degree of scattering in the target, which distributes the dose over a wider range compared to protons and heavier charged particles. All of these forms of radiation can be used therapeutically, and the most appropriate choice for a given cancer will depend on many factors (the depth of the tumour and the tissue type being two of the most important considerations).

It is also well known as the mass of ions increases, the impact of lateral scattering is reduced enabling them to maintain their direction while they traverse the body to the tumour. This results in a very well-defined lateral margin to the dose distribution in the target.

Although ion beams have been applied therapeutically since the 1950s using passively-scattered beam delivery techniques (i.e. where the depth range is produced from a collimated broad beam using ridge filters and a patient-specific depth-compensating bolus), since the mid-1990s particle irradiation systems have been designed around the principle of actively-scanned (or raster-scanned) energy-modulated pencil beams. This transition occurred first for protons [35, 36] and later for carbon ions [37, 38]. By the end of 2018, more than 220,000 patients have been irradiated worldwide using particle therapy. Of these patients, approximately 190,000 have been treated with protons, 28,000 with carbon ions, and a further 3,500 of them with He, pions and other ions [39].

2.4.1 Proton therapy

Since the construction of the first particle accelerators, proton therapy has transitioned an experimental therapy (with the first patient treated in 1954) to a widely used standard clinical technique. Since that time, the number of the proton therapy facilities around the world has exponentially increased [23]. This is principally due to the physical advantages of the proton beam; protons do not undergo fragmentation, so that

essentially zero dose is delivered beyond the maximum depth of the spread-out Bragg peak. This lack of exit dose allows for excellent dose distribution control; however, the entrance dose is still substantial (although much lower than for photon therapy).

The process of generating a proton beam starts with ionising a small quantity of hydrogen gas (typically via a microwave beam) which strips off its electron leaving only the nucleus (a single proton). The protons are electrostatically accelerated and focused into a narrow beam, after which they travel into either a cyclotron or a synchrotron, where they are accelerated to about 60% of the speed of light. For modern actively-scanned treatment systems, the cyclotron or synchrotron is tuned so that the energy of the proton beam will reach the specific depth within the target that is required for the current stage of the treatment plan; passively-scattered beams will be generated at a fixed higher energy and then the energy will be spread using a combination of filters and patient-specific boluses to achieve the desired spectra.

For a single proton traversing through tissue, the peak of energy deposition is extremely sharp. However, a proton *beam* is a statistical combination of many protons, which exhibit a distribution of ranges in the target material due to the differences between the specific interactions that each particle undergoes as it slows down; some may travel further and undergo fewer collisions than others. This results in a broadening of the BP to up to several millimetres in width. This phenomenon is known as *range straggling*.

Proton therapy has achieved impressive clinical results, demonstrating increased local tumour control with reduced late effects compared to photon therapy [28]. Despite this, there remain many challenges in the field of proton therapy. The current technology used to generate proton beams is very high, and treatment facilities are large. This has implications for the widespread clinical adoption of proton therapy, in particular in the developing world [23, 28]. Moreover, there remain physical uncertainties in the treatment process due to imperfect knowledge of the proton stopping power in the patient - this is because the CT imaging normally used to measure the composition and structure of the patient is based on X-ray photon attenuation, and X-rays do not have the same stopping power as protons. Many research efforts are underway around the world which aim to overcome these challenges, by reducing costs, improving the accuracy of the dose distribution and reducing the dose to organs at risk.

2.4.2 Heavy ion therapy

In many respects, heavy ion therapy is very similar to proton therapy. However, since heavy ions include multiple nucleons, a wider range of physical processes occur during irradiation. These result in some significant differences between the characteristics of each mode of therapy.

One of the basic features of heavy ions is their increased linear energy transfer compared to protons. This is responsible for their higher relative biological effectiveness (the RBE of protons is about 1.1 whereas heavy ions may have an RBE of 2-3). The kinetic energy required to treat deep seated tumours is much higher than for protons (even when normalised by the number of nucleons, as is conventionally done). For example, a proton beam of 150 MeV/u can penetrate to a depth of approximately 16 cm in water. However, the same depth is achieved with carbon ions of 300 MeV/u or 250 Mev/u [7, 40, 41].

The ratio of the dose delivered at the BP to the entrance dose is higher for heavy ions than it is for protons. This means that for a given treatment plan, the same target dose distribution can be achieved with a lower entrance dose than for protons; this comes at the cost of the development of a small fragmentation tail beyond the BP [4, 42], resulting in non-zero distal dose. This problem becomes more significant with heavier ions; it is not a significant problem for ions up to oxygen.

Many authors have characterised the potential therapeutic properties of individual ion species. Krämer et al. and Burigo et al. investigated the relevant physical and radiobiological characteristics of ^{4}He ions interacting with biological matter, which are shown to be comparable to protons but with significantly lower lateral scattering [5, 43]. Sokol et al. and Tommasino et al. considered oxygen ions to be of clinical interest due to their high LET (which exceeds that of carbon) which can be utilised in the treatment of the hypoxic regions within the tumours leading to a remarkable reduction in OER [44, 45]. Inaniwa and Kanematsu investigated the utilisation of neon ions in particle therapy [46].

2.4.2.1 Carbon ion therapy

Carbon ions offer a significant improvement in relative biological effectiveness compared to protons that can be useful for radiation-resistant tumours [40, 47]. Moreover, carbon ions are found to have a reduced penumbra of the beam as opposed to proton. While a 150 MeV/u proton beam can traverse water depth of 16 cm, a beam of carbon ions

with energies of 250 MeV/u can achieve the same biological depth resulting in more dose rate to the tumour cells [7, 40, 41].

On the other hand since the LET values for ^{12}C ion beams vary with the associated RBE values, planning the dose distribution for carbon ion is a complex process [41]. Carbon ions also have a fragmentations tail. The tail is developed due to nuclear interactions of the fragmentation of the ^{12}C ions in the primary beam with the atoms in the irradiated medium [41]. Some of these fragmentation traverse the medium beyond their range depositing their energy in the fragmentation tails. Thus, it is critical to calculate include the fragmentation tails in the treatment planning systems to prevent damaging the healthy tissues beyond the beam range [41]. In 1994, the first use of ^{12}C ion beam in the treatment of tumour was conducted in Japan at the National Institute of Radiological Sciences (NIRS) followed by successfully clinical treatments for localised tumour in 1997 in Germany at (GSI) [5]. Several studies have investigated the radibiological properties of protons and carbon ions [41, 48]. Carbon ions are preferred over protons in case of irradiation deep seated tumour close to organs at risks, due to the reduced lateral scattering which results in better dose conformation to the tumour [5]. Carbon ion also is better to apply in case of the tumour is resistant to radiation and surrounded by radiosensitive tissues. Worldwide, 11 carbon ion centres and additional facilities are under construction that have been used to irradiate about 28'000 patients by 2018 [39].

2.4.2.2 Oxygen ion therapy

Oxygen ions are considered of clinical interest since they have higher linear energy transfer that can used for the treatment of hypoxic tumours [44, 45]. Investigating the physical and biological properties and the benefits of applying oxygen ions in particle therapy is an ongoing process, since several studies have investigated the radiobiological properties including RBE and the oxygenation effects [49, 50]. Also, since due to their high LET, Oxygen ions can lead to increased cell killing at both the target volume and the surrounding healthy tissues [44]. Yet, it is not clear whether ^{16}O has considerable advantages compared to ^{12}C in terms of impact on healthy tissues. Thus, future research is required to investigate conditions such as tissue radiosensitivity, the radiation effects on organs at risks and to narrow or broaden the range of cases where oxygen ion is considered a valid treatment in radiotherapy [44].

2.4.2.3 Helium ion therapy

The fact that helium ions have a lower lateral scattering makes them holding the greatest potential as suitable candidates in radiation therapy[30, 47]. Pioneering treatment with ^{4}He with passive beam delivery was performed at LBNL (Berkely, USA)for 2000 patients [51]. However, several ongoing preclinical studies [5, 52] investigated the relevant physical and radiobiological characteristics of ^{4}He ions interacting with biological matters. In their study,[5] Burgio et al., reported that in case of healthy and tumour tissues are both have radiosensitivity similar to HSG cells, ^{4}He is considered to be the best option compared to ^{1}H and, ^{12}C and ^{16}O. In particular, helium can be considered as an attractive option for the use in paediatric patients [30, 53]. In other study [52], the authors created a pragmatic beam model treatment planning system using TRiP98 for therapeutic ^{4}He ions. In order to verify their newly developed model, dosimetric results for absorbed dose as well as measured cell survival distributions as a function of depth are presented [52]. They have used several cell lines such as V79 or Human salivary Gland (HSG) proving that the validity of their model is not for one certain cell line. In order to enable a realistic treatment planning including the biological effects, the authors have provided energy loss tables for all involved primary and secondary particles, nuclear reactions cross sections that describe the loss of primary beam particles, and fragmentation cross sections to calculate the build up of secondary ions as the beam interacts with the traverses matter. A comparison with literature data has been performed which is in a good agreement with the authors' findings. However, the authors reported that yet there is no unique optimal ion species but the treatment option mainly depends on patient specific parameters [52].

2.4.3 Dose painting

Radiobiological and clinical experimental research has shown that using a homogeneous radiation dose to treat individual heterogeneous radiation resistant tumour is incapable of achieving an optimum control since the response of each sub-volume of the tumour to the radiation varies depending on spatial biological factors such as hypoxia, cell proliferating rate and cell density [27]. However, applying heterogeneous dose distributions on a tumour (presumably that a tumour is a heterogeneous entity with variable radiosensitivity sub-regions) can achieve optimum control as a dose escalation will not be applied to the entire tumour prohibiting the risk of post-complications that is known as dose painting. Dose painting has shown to be a promising candidate in

the treatment of radioresistant tumours such as head and neck cancer where higher survival rate might reached [54, 55]. The concept of dose painting was introduced by numerous studies[27, 54, 56, 57]. By using recent imaging functional techniques such as Positron Emission Tomography (PET) together with highly conformal and geometrical accurate radiation technique IMRT and IGRT, a treatment with heterogeneous dose distributions (different energies with different LET) can be applied to abnormal subregion within the tumour target volume. This leads to boosting the dose radiation only to these spotted radioresistant compartments within the tumour volume. Based on the use of functional imaging (FI) together with PET for the application of dose painting, two approaches have been proposed. Ling et al. propose that uniform dose escalation can be given to the biological target volume after the tumour delineating process has been performed [57]. The second approach is dose painting by numbers (DPBN) proposed by Bentzen, S.[58]

2.4.4 LET painting

The concept of LET painting was introduced by Bassler et al.[7].By using FI, individual patient- specific hypoxia and distinct compartments maps can be generated; and since LET changes along the particle beam depth path until it loses its energy and stops in the medium it traverses. Thus, by confining the high LET radiation part to the hypoxic entities in the tumour volume and applying the low LET part to the normoxic regions, and by deliberate sparing of normal tissues from high LET parts or from escalating the dose, higher tumour control can be accomplished by a treatment planning based on LET optimisation. Simulation results have shown that applying carbon ion beam dose which has a high LET to the heterogeneous tumours with hypoxic compartments is not enough to eliminate these radioresistance hypoxic entities [7, 58]. Boosting LET using particles heavier than ^{12}C, would be a solution to eliminate the hypoxic compartments as the whole tumour receives an escalation dose. However, in vitro, experiments have demonstrated that high-LET radiation increases RBE for late damage in normal tissue and severe post complications can result. Restricting high-LET radiation to these hypoxic entities while applying low-LET radiation to elsewhere within the planning target tumour volume results in redistributing LET to match hypoxic structure. This technique is known as LET painting which provides a therapeutic advantage by achieving a tumour control probability (TCP) and reducing normal tumour control probability (NTCP)[24, 30]. In their study, Blaster et al. find that LET-painting with ^{12}C can achieve tumour control for hypoxic entities smaller

than 0.5 cm^3, while LET painting with ^{16}O ions combined with a slight dose boost of (5-20 %) can achieve tumour control probability for larger hypoxic compartments of up to 1 or 2 cm^3 [24].

2.5 Multi ion therapy

Since the optimal ion choice depends on several factors such as depth of the tumour, dose level and the contrast of radiosensitivities of tumour and surrounding healthy tissues [5] and because there is no definite therapeutic method or modality to provide solely the best treatment, several studies suggest that better therapeutic results, robust biological and more conformal dose distribution may be achieved by using a combined irradiation scheme of two or more different ion species in a single field arrangement compared with conventional particle therapy [5, 9–11].

A number of researchers have investigated the potential advantages of multi-ion therapy. In a 2020 study, Kopp et al. proposed a combination of one light and one heavy ion in a single treatment field to achieve uniform effective dose and a constant RBE across the target [10]. The authors compared single field uniform dose for carbon ion $SFUD_c$ treatments with their proposed combined ion beams with constant RBE (CIRC) for $^{12}C/^{1}H$ $CIRC_{C-P}$ and $^{12}C/^{4}He$ $CIRC_{C-He}$. It was found that CIRC with both combinations offered a decreased tail dose relative to single-ion treatment plans. The authors analysed their results and concluded that with $CICR_{C-P}$, a more consistent LET_d was obtained of between $\sim$ 21 keV μm^{-1} and $\sim$ 45 keV μm^{-1}, compared to $\sim$ 45 keV μm^{-1} to $\sim$ 122 keV μm^{-1} for $SFUD_C$. Median target RBE was $\sim$1.50 for $CICR_{C-P}$, providing a $>$ 30% increase and $\sim$ 44% decrease compared with $SFUD_P$ (RBE $\simeq$ 1.15) and $SFUD_C$ (RBE $\simeq$ 2.16) plans, respectively. The combination of carbon/proton $CIRC_{C-P}$ achieved a highly homogeneous RBE distribution compared with single ion treatments. However, minor RBE enhancement is present outside the lateral periphery of the target volume. A sharper lateral penumbra is delivered to the target by $CIRC_{C-P}$ and $CIRC_{C-He}$ fields compared with proton-only treatment plans, resulting in a lower dose to surrounding tissues.

A new therapeutic technique known as intensity modulated composite particle therapy (IMPACT) was introduced by Inaniwa et al. [9]. By using two or more particle species in a single treatment session, both the physical dose and the dose-averaged LET distributions can be optimised across the target volume. IMPACT has demonstrated the ability to control the LET distribution irrespective of the field configurations in

clinical applications - in particular, for the treatment of hypoxic tumours. However, a biophysical model including the oxygen enhancement ratio (OER) and particle spectrum parameters are not provided in this model [9]. Moreover, in-vitro and in-vivo data of radiation responses in various conditions such as oxygen pressure and dose rate are required for IMPACT to be considered an option in clinical applications.

Unkelbach et al. combined proton and photon therapy to optimally deliver a fractionation-based therapeutic dose to a target volume where a healthy organ is located near to the target [59]. While a beam of protons is desirable for irradiation of target regions where hypofractionation was allowed to minimise the dose delivered by X-rays, photon beams delivered most fractions of the prescribed dose. Moreover, this developed method is not suitable for cases where hypoxic regions are present within the target.

In summary, while much work has been done demonstrating the validity of multi-ion therapy in principle, the majority of studies published to date have concentrated on dual-ion therapy only. Therefore, the opportunity exists for multi-ion therapy to be generalised to exploit a wider diversity of ions with the aim of achieving further improvements in dose conformity and additional options for enhanced LET in hypoxic regions and avoidance of dose to OARs.

2.6 Laser plasma accelerators

Charged particle radiation therapy (such as electron, proton and heavy ion therapies) is presently delivered via linear or circular electromagnetic particle accelerators - large, expensive and highly specialised facilities which, in general, can only deliver a single particle species at a time. Recently, laser-driven accelerators have been proposed as an alternative source for therapeutic particle radiation. Laser plasma accelerators can potentially produce a mixture of different ion species with a range of energies or rapidly switch between ion species using multiple targets.

Particle accelerator designs have continued to evolve since the early 20th century [12, 60]. The radiofrequency-driven linear accelerator (linac) was initially proposed by Ising [61], and first implemented by Wideröe [62] for the acceleration of sodium and potassium ions. The key advantage of the linac over purely electrostatic particle accelerators (for example, those based on Van de Graaf generators [63]) is that it does not require the use of enormous DC voltages to achieve acceleration, which limits the achievable particle energies in such accelerators. Improved radiofrequency and

microwave oscillators (magnetrons and kylystrons) developed for radar during World War II enabled the development of linacs for lighter particles, including electron and protons [64, 65]. Linacs can be used both as an X-ray photon sources (if a dense metal target is used), or directly for electron therapy (if a beryllium window is used at the exit port of the linac); linacs are are now the most common variety of clinical particle accelerator [66].

An alternative approach, based on a spiral particle trajectory through a transverse magnetic field was proposed by Wideröe [62] and first demonstrated by Lawrence et al. [67]. This approach is physically compact relative to the linac, and enables the production of stable, high-flux electron and proton beams. Acceleration of heavier particles with a cyclotron is impractical, however, due to the enormous radius that would be required to achieve clinically relevant particle energies. This shortcoming was eliminated by the development of synchrotron accelerators in the 1940s, which allowed the generation of high-intensity particle beams with unprecedented kinetic energies [68, 69]. Therapeutic proton beams are now most commonly produced using cyclotrons (although next-generation linacs are increasingly becoming a viable option, and synchtrotrons may also be used), while heavier ion beams are mostly produced with synchrotrons.

The substantial capital expenditure and physical space required by linacs, cyclotrons and synchrotrons which are currently utilised for the acceleration of charged particles to therapeutically-useful energies have driven research into alternative accelerator technologies which can provide the required beam characteristics in a more compact and cost-effective manner. In 1979, Tajima et al. [70] first proposed a new type of accelerator driven by brief, intense pulses of laser light.

2.6.1 Conventional accelerators vs. *laser-driven* accelerators

Very high energy electron therapy (VHEE), proton therapy (PT) and heavy ion therapy (HIT) represent advanced radiotherapy modalities in which a beam of relativistic electrons, protons or heavy ions is used to irradiate a target at some depth inside the patient. The accelerators used for charged particle therapy must be able to generate particle beams with a range of kinetic energies, with high precision, reproducibility, reliability and stability [60].

The kinetic energies required in very high energy electron therapy extend from between 50 MeV to 250 MeV; for proton therapy of non-superficial tumours the therapeutic energy range extends from 60 MeV to 250 MeV, whereas for carbon ion

therapy, the required energy per nucleon ranges between approximately 120 MeV/u and 430 MeV/u [13, 71]. Presently, generating and delivering charged particle beams with these energies requires the use of either a large linear accelerator, a cyclotron or a synchrotron - expensive, bulky and highly-specialised facilities with a substantial physical footprint and large energy demands, typically requiring a dedicated building and sophisticated power supply and shielding, Such accelerators offer limited capability to quickly switch between different ion species [12].

Laser plasma accelerators offer a striking contrast with traditional accelerator designs due to their potential for achieving high particle kinetic energy over a very short distance [72–78]. Laser-driven electron, proton and ion beams exhibit a number of unique characteristics compared to those produced using conventional accelerators [79–84]. These include pulsed delivery of the dose at very high peak dose rates over short time periods (typically femtoseconds for electrons and picoseconds protons and heavier ions) and a large energy spread (typically greater than 0.1%). Unlike synchrotron-based charged particle sources, laser driven accelerators produce a mix of different ion species in each pulse, each with a relatively broad spectrum of energies (which can then be selectively delivered using appropriate beam optics). Such unique features offer the potential for rapid switching between ion species and energies during a single treatment session [60].

2.6.2 Principles of laser-driven ion acceleration

Laser-driven ion acceleration involves numerous distinct physical mechanisms that operate over different stages of the evolution of the acceleration process. In summary, these are: ionisation and pre-plasma formation; transfer of energy from the main laser pulse to free electrons in the plasma; subsequent evolution of the plasma bubble and the formation of a high-intensity electric field; and the acceleration of charged particles due to this field[77].

Laser plasma acceleration is driven by a pulsed laser beam, structured as a sequence of intense ultra-short pulses (with a power density exceeding 10^{18} W/cm^2 and a pulse duration ranging from tens of femtoseconds to picoseconds) separated by longer periods of lower intensity emission in which the power density is lower by a factor of around 10^6 [85]. The most common lasing medium for this laser type is titanium:sapphire (Ti:Al_2O_3), which is tunable across a wide range of wavelengths, and is thus able to generate extremely short optical pulses with very high peak power.

Depending on the laser pulse intensity, electrons or ions to be accelerated can either be injected into the plasma from an external source or trapped and pulled out of the generated plasma itself. At low laser pulse intensities, the electron density wave, known as the *plasma wakefield* has a low amplitude; consequently, the plasma electrons must be injected externally with sufficient momentum to ensure they are trapped in the plasma wave. In contrast, at high laser intensities, free electrons in the plasma gain sufficiently high energies to ensure that a variable proportion of them are trapped in the plasma wakefield and accelerated.

If the fraction of trapped electrons is small, then protons that are produced due to impurities or hydrocarbon contaminant layers at the target surface can be accelerated first. In the absence of such hydrogen ions (i.e. where contaminant layers are first removed by heating the targets prior to the laser shot), or where the number of protons is not sufficient to balance the charge of the free plasma electrons, a portion of positively-charged heavier ions in the surface material (such as carbon ions) can be accelerated [86].

Several distinct mechanisms have been proposed for laser plasma particle acceleration. The most studied scheme, Target Normal Sheath Acceleration (TNSA), was first proposed by Wilks et al. [87], and has since become the reference framework to describe the laser-plasma particle acceleration process - especially for protons. A comprehensive description of the essential features of this scheme can be found in [77, 87–90]. More recently, an alternative acceleration scheme based on direct radiation pressure from the laser beam has been proposed, which shows great potential for the acceleration of heavier ions [85, 91–93].

2.6.2.1 Target Normal Sheath Acceleration (TNSA)

Target normal sheath acceleration (TNSA) is an extremely efficient acceleration mechanism for light ions such as protons. The principle of TSNA is illustrated in Figure 2.3.

When the pre-pulse phase (an emission which precedes the main pulse peak, at a substantially lower-intensity than the main pulse) of a pulsed laser beam arrives at a very thin solid target foil (with a thickness of the order of a few microns), it ionises the target surface, creating a hot pre-plasma - a mixture of free hot electrons and atomic nuclei. The energy of the main pulse will then be mostly absorbed by free electrons in the plasma, which form a hot gas and are pushed through the target foil by the Lorentz force.

Due to the high inertia of positively charged ions in the plasma (relative to the hot electrons), the ions remain relatively stationary while electrons exit a short distance from the far side of the foil before being pulled back towards their initial positions. This forms a sheath of electrons in the space immediately distal to the far side of the target, with an electric field strength of the order of tens to hundreds of GV/m, which exceeds the ionisation threshold of matter [94–96]. This quasi-static field strips the ionised atoms from the surface of the foil and rapidly accelerates them in the direction of the laser beam in the normal direction to the target at the vacuum located at the rear side of the target. By choosing appropriate surface coatings, a variety of ions (such as protons, carbon or oxygen ions) can be produced.

The TNSA mechanism has been demonstrated to efficiently produce beams of protons with low transverse emittance and up to 6×10^{13} particles per pulse with energies of up to 100 MeV [97]. However, TSNA has a number of disadvantages including poor conversion efficiency from the laser pulse to hot electrons, large beam divergence and low particle density for ions heavier than protons [85, 98].

2.6.2.2 Radiation Pressure Acceleration (RPA)

An alternative acceleration technique, known as radiation pressure acceleration (RPA), offers the potential for more efficient acceleration of heavy ions, and has been the focus of considerable recent research [91–93, 99, 100]. In contrast to the TNSA mechanism, where protons are accelerated in the free space at the rear side of the target due to the quasi-static electric field created by charge separation between plasma ions and the accumulation of electrons at the rear side of the target, in RPA the radiation pressure of the laser pulse itself directly transfers the momentum of the pulse photons to ions generated within a thin target [93].

As described in Section 2.6.2.1, a pre-pulse with a lower intensity compared to the subsequent main peak first interacts with a thin target producing a hot, thin and dense pre-plasma at the front surface of the target. The radiation pressure of the main pulse (with an intensity of 10^{21} W/cm^2 - 10^{23} W/cm^2 [92]) then acts on the pre-plasma, inducing pondermotive forces by which the electrons of the pre-plasma are pushed in the direction of these forces, penetrating the target and becoming separated from the plasma ions. This charge separation creates an enormous electric field, causing the plasma ions to form bunches which are then accelerated towards the interior of the target. This effectively acts as a "piston", pushing forward additional ions in the non-excited regions of the target in a process known as *hole-boring* (HB). Hole boring

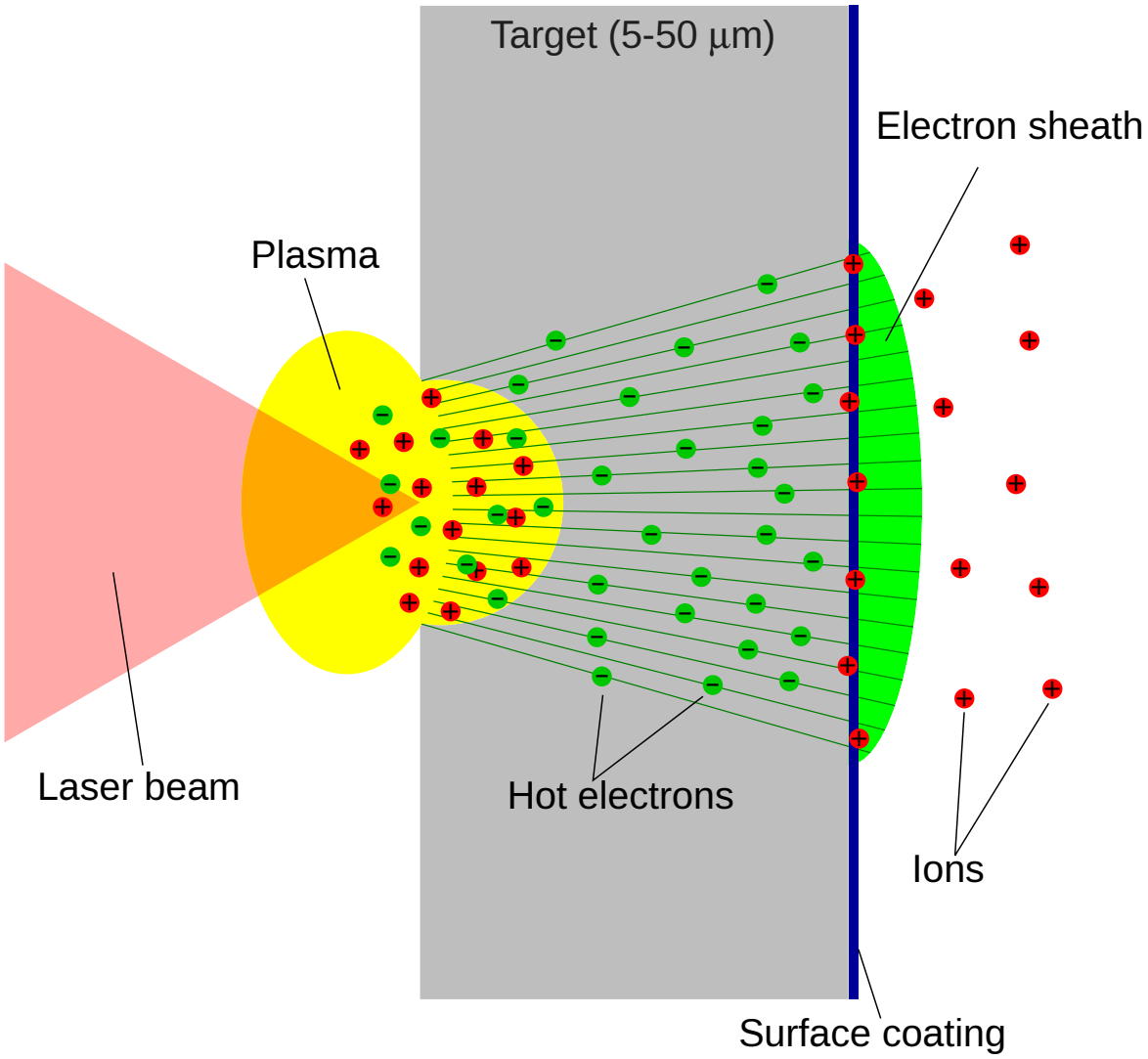

Figure 2.3: Target normal sheath acceleration (TSNA). The acceleration is due to the expulsion of the hot electron gas from the target, which forms a negatively charged sheath above the distal surface of the target. This creates an intense electric field, accelerating ions on the target surface away from it. The efficiency of this process decreases significantly as ion mass increases.

terminates when all ions in both the perturbed and non-perturbed regions of the target have been pushed to the rear side of the target. Hole boring is followed by a second stage known as *light sail* (LS), in which the over-dense plasma bunch containing both accelerated ions and electrons is directly accelerated by the radiation pressure in free space at the rear side of the target. The process is illustrated in Figure 2.4.

RPA has been shown to be a very efficient mechanism for the acceleration of light ions such as protons to high energies compared with TNSA, but perhaps more interestingly, it is also capable of accelerating heavier ions (e.g. carbon) to higher kinetic energies than is possible with TSNA [92]. For example, for a thin compound target (consisting of both hydrogen and heavier elements), protons will be accelerated to high energies more rapidly than the heavier constituents; once they have been pushed out in front of the target, they are shielded from additional radiation pressure by the remaining more slow-moving heavy ions. These heavier ions continue to accelerate, and eventually match the velocity of the protons, at which point the protons can accelerate further. Ultimately, all ion species in the beam reach the same final velocity [92]. Therefore (neglecting relativistic effects), by the end of the acceleration process, the heavier the ion, the greater its kinentic energy; hence, all ions species will reach approximately the same energy per nucleon. As such, a monoenergetic per-nucleon multi-ion spectrum can be achieved with a single pulse applied to a thin compound target.

It is worth-noting that both the laser pulse properties (pulse duration and fluence), together with the target thickness, determine whether the HB or LS stage dominates the acceleration process. In cases where there is either a relatively thick target or low beam fluence, the laser pulse will be fully utilised in the ion acceleration process inside the target, and HB dominates. Conversely, if the target is sufficiently thin, only a portion of the laser pulse will be utilised in the acceleration of ions in the target, resulting in acceleration of all ions in the beam path through the target before the laser pulse terminates. Thus, the remainder of the laser pulse will further accelerate the ions to higher energies via the LS mechanism [85, 90].

Although RPA is clearly a very promising mechanism for the acceleration of ions heavier than protons, petawatt-scale laser pulses with ultra-high intensity ($10^{21} - 10^{23}$ W/cm^2) are required to accelerate ions to very high energies [92]. This requirement is currently at the cutting edge of available laser technology, making practical RPA expensive and only available for study at a limited number of facilities around the world (for example, the EU's ELI-NP facility [101]). Much of the current research exploring

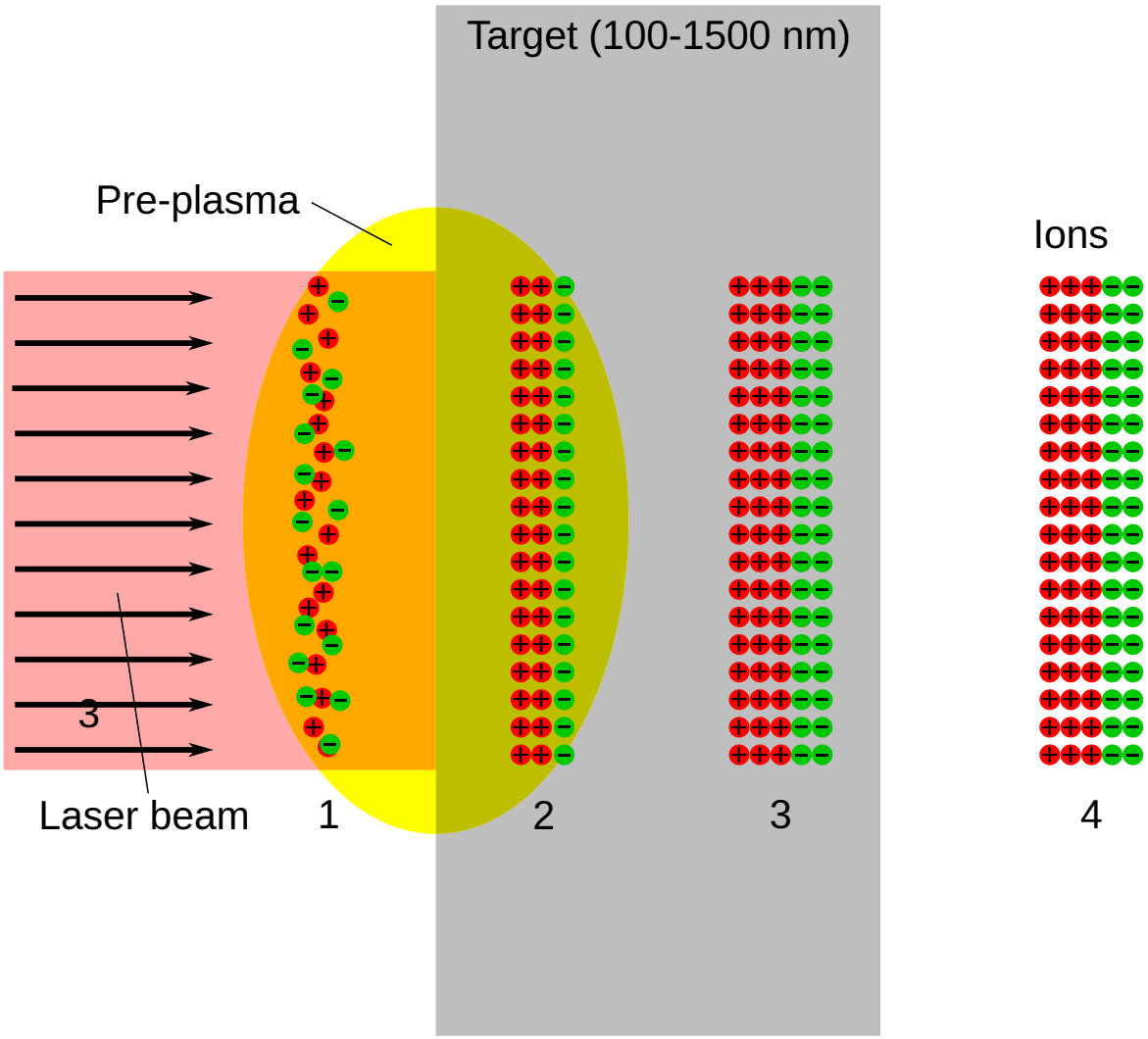

Figure 2.4: Radiation pressure acceleration (RPA). In region 1, lighter ions in the pre-plasma are accelerated by the ponderomotive force due to the laser radiation pressure. As these ions progressively penetrate the surface of the foil (regions 2 and 3), they push additional ions forward like a piston (*hole boring*), with heavier ions shielding lighter ions from the radiation pressure such that they all end up moving at the same velocity. Finally, the ions continue to accelerate forward in free space beyond the end distal surface of the foil (*light sail*). Acceleration is a direct result of the radiation pressure of the laser beam.

the RPA scheme for particle acceleration is theoretical and simulation-based, e.g. utilising 1D and 2D particle-in-cell simulations to investigate the potential of coupling the ultra intense laser pulse over the entire thickness of the target [91]. However, a growing body of experimental research is now dedicated to investigating the properties of the RPA scheme and fully developing its potential

2.6.3 Characteristics of laser-driven ion beams

The characteristics of laser-driven ion beams differ significantly from those generated using conventional synchrotron-based accelerators. The first key difference is the pulse duration; for a laser plasma accelerator, the pulse duration is typically tens of femtoseconds to picoseconds, whereas synchrotron pulses are orders of magnitude longer (of the order of hundreds of picoseconds to nanoseconds, with a pulse period of 5 - 30 MHz) [102–104]. The short pulse duration in laser plasma accelerated particle beams is due to the pulse structure of the driving laser, whereas the pulse structure in a synchrotron source corresponds to the spacing of ion bunches in the circulating beam (a function of the geometry and energy of the beam). The short duration of the laser pulse necessarily implies a broad energy spectrum (due to the time-frequency uncertainty principle); the resulting ion pulses are also similarly short in duration, implying a large spread in projectile momentum and kinetic energy for ion beams generated by laser plasma accelerators compared to a synchrotron-based ion source. The ultra-short pulse duration, combined with the large number of particles generated per pulse, can yield a peak current in the order of several kiloamperes, compared to milliamperes in a cyclotron or synchrotron particle beam.

The wide energy spread of the beam also implies a high beam emittance (the product of source cross section and solid angle of emission) relative to a synchrotron-based source. In addition, beam divergence is much higher than for a synchrotron-based source [75, 86, 102, 105]. Other notable properties of laser-driven ion accelerator beams include high efficiency of laser-to-proton energy conversion, particularly with the RPA-based acceleration techniques [85, 106], the focusability of the particle beam via control of the laser beam geometry and the very large number of ions per shot (up to 10^{13} protons per shot has been reported; although acceleration of heavier ions will produce a lower number of particles) [80, 107, 108].

The first direct measurements of the generation of high energy protons during intense laser-target interaction were reported by Clark et al. [109] and Snavely et al. [106] in 2000, reaching energies of up to 18 MeV and 58 MeV, respectively. These

discoveries led to rapid growth in research on laser-driven ion accelerators with the aim of developing a compact particle accelerator that can produce accelerated charged particles with high energies for a range of applications, including particle physics research and radiotherapy [60].

Since the first laser-driven accelerators emerged in the early 2000s, particle kinetic energies have been steadily increasing. In a recent study, Higginson et al. [97] have successfully accelerated protons up to 90 MeV by using a petawatt-class laser system; Sharma et al. [110] reported laser-based acceleration of protons with peak energy of 350 MeV. Electrons beams with energies of 7.8 GeV have been achieved [111]. Carbon ions with energies of up to 48 MeV/u have been reported by W. Ma et al. [112]; while this is still too low for most therapeutic applications, reported energies and beam quality continue to increase.

2.6.4 Laser-driven accelerators in particle therapy

Particle therapy is an obvious application for laser-driven particle accelerators [72, 73, 86, 113, 114]. Compared to RF-based accelerators, a laser plasma accelerator offers numerous advantages - acceleration is performed with high energy efficiency across a distance of millimetres rather than tens of metres, and very high dose rates are potentially achievable. However, due to the unique properties of the laser-driven particle beam, new solutions for beam capture, shaping and delivery are required [115].

Early theoretical and simulation works [116–118] have shown that proton beams with therapeutically-relevant energies and particle fluence can be generated by a compact laser-driven accelerator. Ma et al. [118] conducted Monte Carlo simulation studies to investigate the characteristics of accelerated beams and evaluated the feasibility of their use in particle therapy. They also proposed the first design for a compact gantry for laser-driven medical accelerators. Masood et al. [119] introduced the *broad energy assorted depth* (BEAD) dose deposition model for laser-accelerated proton (LAP) beams, which provides a large acceptance particle capturing lens and an integrated shot-to-shot energy selection system (ISESS). These novel beam optics and control systems are used together with a proposed isocentric gantry design which is capable of efficiently capturing divergent particle bunches and features an integrated energy filtering system. This design for the laser-driven beam reduces the physical dimensions of the treatment gantry by a factor of 2-3 compared to a conventional proton therapy gantry system.

Laser-driven accelerators promise peak radiation dose rates many orders of magnitude beyond that achievable via RF-based particle accelerators. Recently, the impact of dose rate on the efficacy of radiation therapy has attracted a great deal of interest, due to its apparent enhanced tissue-sparing capability relative to conventional radiotherapy dose rates [120, 121]. This ultra-high-dose-rate regime, referred to as *FLASH* radiotherapy when dose rates exceed 40 Gy/s, is now actively being explored in both photon and charged particle therapy contexts - from electron therapy to proton and heavy ion therapy [121–124]. Due to their high peak dose rates, laser-driven accelerators are an ideal vehicle for the delivery of FLASH particle therapy.

In vitro dose response investigations on different tumour and normal tissue cell lines as well as in-vivo studies on animals irradiated with laser-driven ion beams have now been reported by several authors. Yogo et al. [125] reported that the relative biological effectiveness at a 10% survival fraction (RBE_{10}) for laser-driven proton irradiation of V79 Chinese Hamster cell line was 1.20 ± 0.11. The proton beam used in this study had a mean energy of 2.25 MeV with a spread of 0.66 MeV, with peak dose rate of 10^7 Gy/s and an average dose rate of 0.2 Gy/s; cells were irradiated directly (i.e. not at a simulated depth in tissue). Similarly, Doria et al. [126] estimated the laser-driven proton RBE_{10} of MeV-range TNSA-accelerated protons to be 1.4 ± 0.2 on cultured human salivary gland (HSG) cells; in this case, the peak dose rate was even higher at 10^9 Gy/s. Zeil et al. [127] performed a direct in vitro comparison between the radiobiological effectiveness of a laser-driven proton beam (TNSA with proton energies in the range 8-15 MeV, directly irradiating SKX human squamous-cell carcinoma cultures) and conventionally (tandem Van de Graaf) accelerated protons. This direct comparison revealed no significant difference in RBE between the two proton sources. In addition, Bin et al. [128] obtained RBE values for protons which agreed well with RBE values generated by conventional accelerators.

More recently, Bayart et al. [129] investigated the impact of laser-driven proton radiation on the well-studied and highly radiation-resistant SF763 and U87-MG human glioblastoma multiforme cells lines. The authors evaluated the impact on cell survival fraction, comparing the results to those obtained by conventionally accelerated proton beams. As in other previous studies, their findings show that the impact of laser-driven proton beams and conventional proton beam on cell survival rate is very similar, with no significant difference in the rate of DNA double strand breaks or cell survival measurements observed between laser-driven and conventionally-accelerated proton sources.

Hanton et al. [130] investigated the radiobiological implications of laser-driven proton irradiation at a dose rate of 10^9 Gy/s on human skin fibroblasts, using the AG01522B cell line. Cell cultures were directly irradiated by a 10 MeV laser-driven proton beam, and the rate of double-strand break repair inductions in cellular DNA was evaluated (per cell per Gy) and compared to the results obtained the cells irradiated by 225 kVp X-rays and cyclotron-accelerated protons. The authors showed that under the conditions of their experiments, the widely-accepted RBE of 1.1 for cyclotron-based proton radiation also applies to laser-driven proton source.

Rösch et al. [131] utilised the well-known zebrafish embryo model to evaluate the radiobiological impact of laser-accelerated proton radiation. Embroys with dimensions of 0.5-1 mm were irradiated by between one and 60 shots of 7 MeV TNSA laser-accelerated protons at a pulse rate of 0.5 Hz. Morphological damage was observed in the embryos, with asymmetry present in the malformations, demonstrating the feasibility of the model for the evaluation of laser-accelerated proton radiation. Interestingly, dosimetric imaging results performed using gafchromic film indicated significant inhomogeneity in the beam across the irradiated field, demonstrating the critical need for further improvements in beam optics for this emerging radiation source. The peak per-bunch proton fluence varied between 10^4 and 10^6 protons/mm^2.

Kroll et al. [132] report the first successful in-vivo experiment to utilise a laser-driven proton accelerator. The authors conducted a study on a NMRI Foxn1$^{(nu/nu)}$ xenograft mouse model in which superficial spherical tumours with diameters of approximately 3 mm were induced on the ears of mice via the introduction of human head and neck squamous cell carcinoma tumour cells. A proton beam of about 10^8 particles were emitted from a 220 nm polymer target at the Draco PW laser; peak energy of the proton spread-out Bragg peak was 25 MeV and the mean energy was around 20 MeV. The generated beam yields sufficient particles to deliver a prescribed single shot point dose of 4.0 $\pm$ 0.4 Gy to the target volume. The authors compared the growth of tumours irradiated using the laser plasma acclerated protons to tumours which were irradiated by an equivalent dose using a clinical isochronous cyclotron. Both facilities have produced a comparable mean dose rates of 1.2-2.2 Gy min^{-1} and 3.9 Gy min^{-1} for dose delivered by the laser plasma accelerator and the cyclotron, respectively. Although this study only evaluated a single dose point, the authors demonstrated the feasibility of their system for the study of laser plasma accelerated proton therapy, and showed that the relative depth inhomogeneity observed with the laser-based proton source is comparable to that obtained with the cyclotron proton source. This important

demonstration paves the way for further in vivo studies of laser plasma accelerators for proton therapy, and is a critical step towards clinical translation.

A particularly challenging problem in laser plasma accelerated particle therapy is accurate dosimetry, which is challenging due to the extreme peak dose rates involved. Romano et al. [133] proposed a novel dosimetry technique for laser-driven proton accelerators in which a small portable graphite calorimeter (SPGC) is used to measure the absorbed dose. This approach is based on a previous prototype developed by Palmans et al. [134] for dosimetry in low-energy clinical proton beams. A 15 μm gold target was irradiated by ultra-intense laser pulses ($>10^{20}$ W/cm^2, $\sim$500 fs pulse duration). Proton beams with energies range of 15 MeV to 40 MeV deposited doses in the calorimeter ranging from 1 Gy to 3 Gy per pulse. The signal to noise ratio which was achieved was sufficient to demonstrate the feasibility of dosimetry measurements for future clinical laser-driven proton accelerators.

2.6.4.1 Laser Plasma Accelerated Electron Therapy

In addition to proton and heavy ion acceleration, ongoing research into the use of laser plasma accelerators for electron acceleration has made outstanding progress over the past decade, such that laser-based accelerators can produce electron beams with energies of up to 250 MeV. These energies are suitable for the delivery of therapeutic doses to deep-seated tumours up to a range that can exceed 40 cm [135]. This regime is known as *very high energy electron* (VHEE) therapy, and appears to be an excellent candidate for laser plasma acceleration [71].

The characteristics of laser-accelerated electron beams are different from those that are produced by conventional RF accelerators. For example, extremely short duration bunches can be produced, with durations of the order of a few femtoseconds, which (as for the proton and heavy ion cases) can achieve peak dose rates of the order of 10^9 Gy/s [136, 137]. This dose rate is well within the FLASH regime, potentially eliciting different biological responses compared to those resulting from conventional (non-FLASH) electron radiation. Therefore, several experimental studies have investigated different aspects of the biological response to laser-driven very high dose rate electron therapy over the past decade.

Oppelt et al. [138] conducted the first successful in-vivo study with laser-driven electron radiation on mouse's ears using the human squamous cell carcinoma model FaDu. Prescribed doses of 3 and 6 Gy were delivered to the tumour cells which resulted in tumour growth delay. To validate the biological response of the delivered dose

rate by laser-driven electrons beams to the tumour, the authors employed a reference irradiation with electrons from conventional clinical linac. They found no significant difference between the two modalities; more importantly, their in vivo results were consistent with previous in-vitro investigations with a laser-driven electron accelerator performed by Laschinsky et al. [139].

Recently, Cavallone et al. [140] reported results on dosimetric characterisation of a (relatively) low-energy, kHz pulse-rate laser-driven electron beam accelerator that was used to perform irradiation of cultured HCT116 colorectal cancer cells in vitro. The authors used an IBA Razor Nano Chamber small-field ionisation chamber placed immediately distal to the cell culture to measure dose uncertainty and provide real-time per-shot dosimetry, while gafchromic film (calibrated against a linac) was used to measure the cumulative dose proximal to the cell culture. A nitrogen gas jet target was illuminated by a focused 3.5 fs pulses at a pulse rate of 1 kHz; 3 mJ of energy is imparted to the gas target per shot. This produces an electron beam with a negative-exponential energy spectrum extending up to 2 MeV. The electron beam average dose rate to the target was of 1.1 Gy/s; this compares favourably to typical dose rates obtained with higher peak power but lower pulse rate J-class lasers. Interestingly, the dose ratio of the dose measured using the ionisation chamber to that measured using the gafchromic film did not remain constant as the total dose was escalated; this is most likely due to thermal effects on the beam optics. From their observed dose response curves, the authors concluded that the kHz-rate laser-driven electron beam and a conventional linac-based electron beam will produce radiation with very similar radiobiological effectiveness.

Babayan et al. [141] compared the effects of ultra-high dose rate pulsed electron beams (3.5 MeV, 450 fs pulse duration with a repitition rate of between 2 and 20 Hz and peak dose rate of 1.6×10^{10} Gy/s) to quasi-continuous electron beam radiation (4 MeV linac source) on cultured HeLa (human cervical cancer) and A549 (human epithelial lung cancer) cells. The number of DNA double-strand breaks and subsequent repairs was quantified by evaluating the formation and elimination of γH2Ax and 53BP1 foci as a function of dose at different time points following irradiation. The study concluded that the number of residual foci remaining 24h hours after the ultra-high dose rate pulsed electrons beam was 1.7-2.9 times the number resulting from irradiation by the quasi-continuous electron beam, indicating a slower rate of DNA repair following exposure to the ultra high dose-rate radiation.

Recent dosimetric experiments have demonstrated the feasibility of achieving therapeutic doses for deep seated tumours using current laser-driven electrons accelerators [108]. A mixed helium-nitrogen gas target was irradiated by laser pulses of 6×10^{18} W/cm^2. This operating regime provides electron bunches with energies ranging from 50 MeV to 250 MeV. These energies are suitable for irradiating millimetre-sized targets at depths up to 10 cm. For each laser shot, a dose rate in the order of cGy was obtained. Moreover, for the first time, the authors were able to obtain a cumulative dose of a few Gy using $\sim$ 100 bunches with multi-field irradiation.

These studies have demonstrated the remarkable potential of laser plasma acceleration to produce high-energy electron beams for delivery of highly effective therapeutic doses, fully exploiting the characteristics of FLASH radiotherapy due to the extremely high peak dose rates which are achievable.

2.6.5 Challenges of laser plasma acceleration in radiotherapy

Although laser plasma acceleration of charged particles clearly has great potential for application in radiotherapy, several challenges needed to be addressed before translation towards clinical practice is achieved.

Firstly, the development of a compact laser particle accelerator is itself a major challenge, demanding an extremely powerful laser capable of producing ultra-intense pulses at petawatt-scale peak power levels, such as the ELI facility in Europe [101, 142]. Presently, there are very few suitable lasers, although rapid progress in this field is continuing. Additionally, the optimisation of both target and beam parameters to achieve consistently high ion beam properties remains very challenging and remains under active investigation [143].

Secondly, the use of laser plasma accelerators for ion beam radiotherapy poses a new set of research challenges, such as the need for full characterisation of the radiobiological effects of laser plasma accelerated ion radiation, particularly the impact of the very high peak dose rate, both on cancer and on normal tissue. Development of new techniques for real-time dosimetry, quality assurance and beam monitoring which are capable of quantifying the extremely high peak dose rates in laser plasma accelerators is needed; although much work has been done to advance knowledge in this area, the technology is in its infancy in comparison to that used in RF-based medical particle accelerators [135, 144].

Development of laser plasma accelerator beam lines suitable for clinical use and design of the associated treatment planning systems are also essential precursors to

clinical translation. Clinical beamlines require very high repeatability and uniform beam shapes; however, the shot-to-shot stability of laser-driven ion beams remains a significant problem, both in terms of particle fluence, beam shape and energy spectrum, which are currently beyond acceptable limits for human therapeutic applications [77, 140, 145].

Since electron beam energies produced by laser-driven acceleration can reach up 250 MeV, the established calibration detectors for electrons beams produced by LINAC (typically in the range of 4 - 22 MeV) are not suitable for laser-driven electron beams with very high energy. Dosimetry measurements for laser-driven electron beams have been carried out using gafchromic films [146]. Moreover, The applicability of ionising chambers for dosimetry measurements for electron beams with energies of 165 MeV was explored by [135]. However, additional research and further experimental evidence is needed to extend existing dosimetric techniques to ultra-short pulsed electron beams.

In summary, laser plasma acceleration of charged particles beams has progressively developed over the past two decades, marked by significant increases in the maximum energy that a charged particle can gain, the ability to accelerate an ever-growing range of particles, and improvements in efficiency, particle fluence and beam quality. These developments have been enabled by a deeper understanding of the underlying physics of particle injection and the specific acceleration mechanisms, such as TNSA and RPA. Such recent advances have led to impressive improvements in the beam emittance, divergence, bunch charge, and energy spread. More importantly, this increased knowledge has resulted in dramatic improvements in reproducibility and stability of the charged beam parameters.

Due to the high acceleration gradient of laser plasma accelerators, they can accelerate charged particles to relativistic velocities over a very short distance, leading to extremely compact acceleration devices. Ultimately, these devices will broaden the horizon of the use of accelerated charged particles for many applications and disciplines. In particular, widespread adoption of laser plasma accelerators as a radiation source for charged particle therapy has the potential to significantly reduce the costs and broaden the availability of such therapies to many more patients compared to RF acceleration.

Experimental investigations have reported radiobiological responses due to irradiation using laser plasma acceleration comparable to those effects caused by charged particles beams produced by RF accelerators. However, a critical difference with laser plasma acceleration is that while conventional accelerators can produce charged particles with a therapeutic dose rate of a few Gy/s, the charged particle beam produced

by laser-driven accelerators can deliver a peak dose rate of the order of 10^9 Gy/s. This extraordinarily high peak dose rate makes laser plasma accelerators uniquely suited for the delivery of FLASH radiotherapy, which is seen as one of the most promising developments in radiation therapy in recent years. Much recent research indicates that ultra-high dose rates delivered by ultra-short pulses may induce advantageous differential biological responses on cancer cells compared with normal cells and tissues. Therefore, further in-vitro as well and in-vivo research to investigate the biological effects of laser plasma accelerator based charged particle radiation on DNA double-strand breaks, cell mortality rates, etc., are of paramount importance in making progress towards clinical translation of laser plasma accelerators for cancer therapy. Moreover, further improvements in average dose rate and quality of the accelerated charged particle beam (particularly in terms of energy spread, pulse repeatability and beam divergence) must be realised. Despite these challenges, the enormous therapeutic potential of laser plasma acceleration is clear, and given the recent progress in both the capabilities of laser plasma acceleration, it appears destined to play a major role in future clinical radiation therapy practice.

2.7 Treatment planning

Treatment planning is an essential part of the process of employing radiation therapy for the treatment of cancer. The primary objective is to determine the optimal values for all treatment parameters such that the tumour is destroyed as completely as possible, while limiting the radiation dose to healthy tissue to levels which will not result in an unacceptably high normal tissue complication probability.

The most critical factor in treatment planning is the dose which is to be delivered to the target, and how it is to be divided between multiple treatment fractions and/or fields. The dose must be sufficiently high so as to have a high probability of achieving cancer cell mortality. Depending on the location and degree of radioresistance of the tumour, this may be a total physical dose of the order of 40-60 Gy. Treatment planning is largely a constrained optimisation problem - achieving the prescribed dose throughout the tumour is the objective, while the constraints are the limits to the dose delivered to healthy tissues, both in a single fraction and cumulatively, which may vary according to the tissue types involved.

Fundamentally, treatment planning for external-beam radiation therapy involves several key steps:

- Fully characterising the radiation source, including quantification of its physical, spectral, temporal and spatial properties and how these are affected by tunable parameters (e.g. beam current or accelerator voltage).
- Structural imaging of the patient, to provide a model of the thicknesses and compositions of the tissues through which radiation must pass to reach the patient. This process may be performed with one of a number of alternative imaging modalities, including CT, MRI and ultrasound imaging. The ideal choice of structural imaging technique depends on the location of the tumour and other constraints (e.g. the presence of MRI-incompatible implants) which may apply.
- Functional imaging of the patient, to provide a map of the distribution of the tumour. This would typically be performed using either PET or SPECT, both of which are able to elucidate metabolic activity which is normally heightened in a tumour.
- Identification of organs at risk, which may be especially sensitive to radiation (such as parts of the brain, eyes, mucous membranes etc.).
- Phenotyping of the tumour (typically by tissue biopsy) to determine its genetic characteristics and likely susceptibility to radiation.
- Prescribing an appropriate physical or biological radiation dose to the target
- Determining the limits of radiation dose for various healthy tissues, especially the organs at risk
- Performing an optimisation subject to the calculated constraints which achieves the objective dose distribution by the summation of multiple fields and fractions, according to the known characteristics of the radiation source used.
- And finally, simulating the resulting treatment plan to validate its performance in detail.

The precise optimisation algorithm depends on many factors - linear solutions, such as the classical non-negative least squares algorithms, work well but may be practically limited due to scalability constraints, while non-linear methods based on neural networks are increasingly popular, since they can scale better than a classical linear optimiser - especially when topologies such as convolutional neural networks are employed [147, 148].

A given treatment plan may need to be revised between fractions due to anatomical changes which occur, for example due to oedema (swelling) due to treatment or morphological changes in the tumour.

2.7.1 Monte Carlo methods for treatment planning

Due to the complexity of treatment planning for radiation therapy, it is often difficult to develop an accurate analytical model anything but the simplest of cases. A variety of approaches have been developed to utilise the power of Monte Carlo simulation methods for radiation therapy treatment planning. Monte Carlo based methods are widely regarded as the most accurate approach to treatment planning [149]. However, until relatively recently, the practicality of such methods has been limited by their computational complexity; high-resolution Monte Carlo methods require a large amount resident set size (dimensions of simultaneously-in-memory data structures) and processing capacity [150]. This has led to a number of different approaches - for example, one may perform a low-resolution simulation of an initial proposed treatment plan (which may be generated using some approximate analytical method), and then apply corrections to the plan at successively higher resolutions until the solution converges on the objective. This approach builds on analytic techniques, while enabling precise and accurate correction for discrepancies between the (necessarily) simplified analytical models and the more complete physical description of the interactions between beam and target which can be provided using a Monte Carlo model.

Early progress in Monte Carlo treatment planning for radiation therapy is reviewed by Spezi et al. (2008) and Jabbari (2011) [150, 151]; a common theme discussed in these reviews is that as computational capacity increases and memory and CPU/GPU computational power improves, Monte Carlo based methods will become the preferred approach to treatment planning due to the high accuracy. Recently, this prediction has begun to translate to reality, with many researchers and indeed commercial TPS developers introducing new Monte Carlo treatment planning systems for radiation therapy in general and particle therapy in particular. For example, in 2021 Lysakovski et al. introduced *MonteRay*, a Monte Carlo based TPS for proton therapy which utilises the FLUKA toolkit and relies on MRI for structural image data [152–154]. The spatial resolution of the TPS was 2 mm $\times$ 2 mm $\times$ 2 mm, and TPS was shown to be linearly scalable in execution time, able to process an average of 33000 primary particles per second per core for typical proton therapy treatment plans with more than 8000 individual pencil beam position/energy combinations. This demonstrates

the practicality of a contemporary Monte Carlo based approach; however, the study only considers a single ion species (protons) in which interactions with the target are considerably simpler compared to heavy ions; the simulation of target irradiation using multi-hadron ions such as carbon may be at least an order of magnitude slower. Several GPU-accelerated computational libraries have been developed to speed up execution of Monte Carlo code for proton and heavy ion therapy, such as the Fast Recalculation on GPU (FRoG) system [155]. This library enables orders-of-magnitude speedup of Monte Carlo simulations of a treatment plan.

Massachusetts General Hospital (MGH) is one of the leading global centres for proton therapy, and has a long history of developing Monte Carlo methods for proton therapy, viewing it as the future for treatment planning [156]. MGH researchers are responsible for developing a number of innovative applications for Monte Carlo modelling in proton therapy, including a detailed study of the integration of CT/MC-based treatment planning into the clinical proton therapy workflow [157]. Another major centre for particle therapy, the Heidelburg Ion Therapy centre (HIT), has proposed the use of GPU-accelerated Monte Carlo methods for optimisation of intensity-modulated carbon ion therapy, reporting that plans with several thousand spots could be computed in less than one hour using an array of four GPUs (ca. 2018) [158].

Simulating the behaviour of charged particles in matter is essential for designing and optimising particle therapy treatments. To simulate a particle therapy treatment, the user first needs to obtain a model of the patient's anatomy based on medical imaging data, such as CT or MRI scans. Depending on the imaging modality, the image data would need to be mapped to tissue material definitions, either based on material databases such as those provided by NIST or constructed based on known elemental composition. This structural and compositional image data would then be loaded into the simulation framework, and the planned irradiations can then be simulated by generating a sequence of beams of the chosen particle type, with the desired number of primary particles generated with specified spatial and spectral characteristics at various positions and/or orientations external to the simulated target. The chosen Monte Carlo framework would then simulate the passage of these particles through the patient's anatomy, taking into account the various materials and tissues they encounter along the way. Regions within the target are divided into a scoring volume array, and in each voxel within this region the simulation records information on the energy deposition or dose distribution in the target area and surrounding healthy tissue, as well as any other desired information such as secondary particle generation.

A wide variety of general-purpose Monte Carlo toolkits are available for simulation of radiation transport through matter. The two most popular amongst these are reviewed in the following sections.

s

2.7.1.1 Geant4

Geant4 (Geometry and Tracking version 4) simulation toolkit is a C++ toolkit developed at CERN for the simulation of the passage of particles through matter, and is used in a wide range of applications, from high-energy physics experiments to medical physics and space science [159]. Geant4 is developed by an international collaboration of scientists and is distributed freely under the GNU General Public License; in addition to its C++ API, it features an extensible macro-based scripting language and Python bindings. It includes a comprehensive set of physics models for simulating the interactions of charged particles with matter, including their energy loss, scattering, and secondary particle production. It includes a comprehensive set of physics models, from electromagnetic interactions to hadronic interactions, and provides a flexible framework for users to customise their simulations. At present, Geant4 itself cannot take advantage of GPU-based acceleration, although several projects have attempted to implement this capability in different ways. Geant4 is distributed with an extensive set of examples, including many which relate directly to particle therapy simulations.

In addition to the core Geant4 framework, several other script-based front-ends based on Geant4 have been developed, including GATE and TOPAS, which aim to make Geant4 Monte Carlo simulations easier to set up and use by non-experts for applications such as medical imaging and radiation therapy simulations [160–163].

2.7.1.2 FLUKA

FLUKA is a restricted-open-source Monte Carlo simulation toolkit developed at the United States Department of Energy for simulation of radiation transport [153]. It has been widely used for the simulation of particle therapy, especially by researchers at GSI and MGH [164, 165]. Like Geant4, simulations are written in C++, and can employ a variety of physics models, many of which have been experimentally validated [165]. Although the source code of FLUKA is available, it is not distributed under a license which is considered open source. In general, both its accuracy and computational efficiency are comparable to Geant4.

2.7.2 Treatment planning for particle therapy

Treatment planning is highly dependent on the specific source of radiation; the most common radiation used for cancer therapy, X-ray photons, is relatively simple to plan for since the CT imaging process used to obtain pre-irradiation structural image data is based on the same physics (photon transport) as the therapy itself; attenuation and scattering will be very similar. On the other hand, the physics of charged particle therapy, including proton and heavy ion therapy, is very different to that of photons, due to the Coulombic and, to a lesser extent, nuclear mechanisms of energy deposition which result in the Bragg peak (as discussed in Section 2.2.1.5). In the case of particle therapy, the dose deposition profile for a pencil beam of a specific energy depends on the particle in the beam, its energy and the target composition (as well as any magnetic field which is present, although this is usually not the case). While the dose distribution due to Coulomb interactions is relatively straightforward to predict, nuclear fragmentation is much more complex, with its impact becoming greater as the ion's Z increases. Higher-Z ions offer the advantage of lower entrance dose compared to lighter ions, however due to projectile fragmentation, a progressively larger dose is delivered by those fragments beyond the Bragg peak. Additionally, lateral scattering and range straggling is more severe for lighter ions compared to heavier. The range of nuclear fragments also varies, both with the choice of ion and with target composition.

Although particle and heavy ion therapies are emerging as amongst the best radiotherapy modalities for the treatment of cancer, continuous research is required to develop and improve a robust treatment planning system (TPS) that can precisely deliver the prescribed dose treatment to the tumour while sparing healthy tissues. Developing such treatment planning systems is a complex problem since, since the impact of radiation on the patient and tumour not only depends on the physical parameters of the beam - such as dose rate, total dose, radiation type and energy - but also the interactions between each component of the entire radiation field in the target volume and the tissues to which this field is applied. There are many diverse types of interactions between radiation and living cells and tissues, and accurate prediction of the response to radiation therapy requires that a wide range of physical, biological and biophysicl factors must be properly modelled e.g. RBE, LET, tissue type, cell density, tumour and surrounding tissue radiosensitivity, track structure, oxygen concentration and desired endpoint. Ideally, all of these factors should be incorporated into TPS model [30, 166]. However, compared to treatment planning for photon therapy, treatment planning for particle therapy is a much more mathematically and

computationally complicated process due to the biological and physical mechanisms involved [29].

A number of researchers have developed TPSs for a single ion species or for a pair of ion species for particle therapy. Sokol et al. introduced full multi-ion biological optimisation, (MIBO) for a two-ion treatment system by combining ^{4}He and ^{16}O [11]. This work extended previous research by Scifoni et al. who extended the LET painting concept to tumours with hypoxic regions, and Krämer et al. who utilised proton and carbon ions to achieve a simultaneous biological optimisation of multi-ion treatments [167, 168].

Burigo et al. compared the performance of different single-ion and dual-ion treatments of the same target, including ^{4}He, ^{1}H, ^{12}C, and ^{16}O, both individually and in pairs [5]. Combinations of two ion species demonstrated improved therapeutic dose conformity to the target relative to the single-ion cases. Moreover a summary of dual-ion combinations that provide best treatment (in terms of both dose to the tumour and to the surrounding healthy tissues) was provided in the study.

Bohlen et al. [169] developed a Monte Carlo based treatment planning tool (MCTP) for light ions with $Z \leq 8$, which produced a uniform RBE-weighted dose in the target. Since RBE is different for each ion species, a constant RBE within the tumour was achieved using a combination of protons and carbon ions in a single plan. However, the higher dose delivered by proton beams at the entrance region of the target increased the rate of damage to normal cells in that region. The authors also introduced the concept of a 'high-LET boost' by utilising heavier ions e.g. carbon and oxygen to deliver dose to the radioresistant regions within the target volume e.g hypoxic sub-volumes, while applying proton ion beams to normoxic areas to achieve a flat dose distribution over the entire tumour volume.

In summary, many treatment planning systems have been developed demonstrating the potential benefits of multi-ion therapy in principle. However, the majority of studies published to date have utilised only a pair of ions at most. Therefore, the opportunity exists to develop TPS to optimise the parameters of ion source which could be a conventional synchrotron source or laser-driven ion source which can potentially produce a mixture of different ion species with a range of energies, fully exploiting the advantages of each available ion species that can incorporated in a single multi-ion treatment to produce the desired dose distributions in the target, while accounting for tumour hypoxia/necrosis and organs at risk.

2.8 Conclusion

In this Chapter, we provide a comprehensive overview of the critical literature related to the overall objectives of this thesis, in particular multi-ion particle therapy and laser-driven particle accelerators. It is clear that multi-ion therapy can provide an overall better therapeutic result compared to single-ion therapy, with the potential for the optimisation of LET in different regions enabling superior biological outcomes in terms of tumour control probability (TCP). However, due to the limitations of current accelerators, few authors have explored the potential of treatments involving more than two ions.

The practical problem of rapidly delivering a succession of different ion species appears addressable in the medium turn, via the prospect of laser-driven particle accelerator ion sources in particle therapy. This is an interesting and relatively unexplored field of research, which is currently at a very early stage of development. However, a clear path towards future therapeutic laser-based accelerator sources exists, as laser pulse power, target materials and repetition rates continue to improve. What is currently missing is a suitable mechanism for developing a particle therapy treatment plan which is able to fully exploit the potential of such an accelerator - that is, a TPS which can employ a wide diversity of particle species in combination in a single treatment plan, and so fully exploit the diverse physical properties of the available ions. For such a TPS to be clinically relevant, it will also need to support the exclusion of dose from organs at risk, the independent enhancement of linear energy transfer in hypoxic subvolumes, and the ability to deliver a treatment via multiple irradiation fields.

In the following Chapters, we develop a TPS which is suitable for such future particle accelerators, and which supports the stated constraints and features. Based on the preceding discussion concerning the available Monte Carlo simulation frameworks, Geant4 has been selected as the preferred platform for the simulation-based component of this work, due to its more liberal open source license and the wide variety of high-quality examples relevant to this project which are available. The implemented system is described, and its performance is then evaluated under a variety of conditions and compared with single-ion, dual-ion and triple-ion treatment plans.

CHAPTER 3

Treatment planning for multi-ion particle therapy

3.1 Introduction

Compared with light ions such as protons or electrons, heavier ions provide higher linear energy transfer (LET), and also offer a higher peak to entrance dose ratio - particularly at greater depths. However, some proportion of the projectile nuclei also undergo nuclear fragmentation (in addition to the target fragmentation which can occur in proton therapy). This, in turn, results in an extension of the irradiated region beyond the Bragg peak (for a given energy), an effect which does not occur in proton therapy. Due to their greater momentum, heavier ion species are also less susceptible to lateral scattering compared to protons and light ions. This reduces the loss of beam intensity at the distal end of the particle track, and enables the treatment of deeper tissues with fewer fields compared to proton therapy since the entrance dose is lower for treatment at a given depth. This advantage is compounded by the increased relative biological effectiveness of high-LET ion species - especially impactful in hypoxic tumour regions, which tend to be quite radioresistant [4]. There is growing interest in the optimised treatment of such tumours by utilising a mixture of ion species. This approach - achieving both a prescribed biological dose objective with region-specific LET via a multi-ion treatment - is known as *LET painting* [6, 8, 170].

To date, while some work has been done on multi-ion therapy, it has been limited to a small number of ion species delivered serially via standard synchrotron-based

accelerators. Existing treatment planning systems normally focus on a single ion species, with the limited experimental work on multi-ion particle therapy utilising crudely-calculated treatment plans which do not fully exploit the opportunities for joint optimisation of dose and LET available with a laser-driven ion source. This will be the first time that a comprehensive treatment planning system for quasi-simultaneous multi-ion particle therapy has been proposed.

This Chapter presents the design of a new open source treatment planning system for optimal irradiation of a heterogeneous target with arbitrary spatial dose distributions using arbitrary combinations of ions for manifold multi-ion particle therapy. The developed treatment planning system is described in detail in Section 3.2. A series of different treatment plans are developed with different combinations of ions for target volumes at different depths inside a simplified human head phantom model. The resulting plans are evaluated and compared via a number of metrics including dose uniformity (evaluated using RMS error between the objective and the achieved dose distributions), D_{50} and D_{90} dose volume percentages (evaluating coverage of the target), and the volumes of non-target tissue which are subject to doses exceeding 5%, 10% and 50% of the objective dose (evaluating the impact on non-target tissues). A sample treatment plan is also implemented as an integrated Geant4 simulation in a heterogeneous phantom and the resulting dose distribution is compared to that predicted by the corresponding treatment plan (and the original objective dose distribution). The methodology for these evaluations is presented in Section 3.3, while the results and discussion are presented in Section 3.4. A summary of the key findings from this study and the planned next steps for the TPS is presented in Section 3.5.

Comprehensive documentation for the developed treatment planning system, and its extension to include support for hypoxic sub-volumes, organs at risk and multi-field irradiation, is provided in Appendix A.

3.2 Treatment planning system design

The developed treatment planning system begins with the following 3D volumetric data:

1. A model of the structure and composition of the target, which may be obtained through segmentation of 3D CT or MRI image data. This is represented as a 3D volume V_{struct} in which each voxel is tagged with a tissue type;

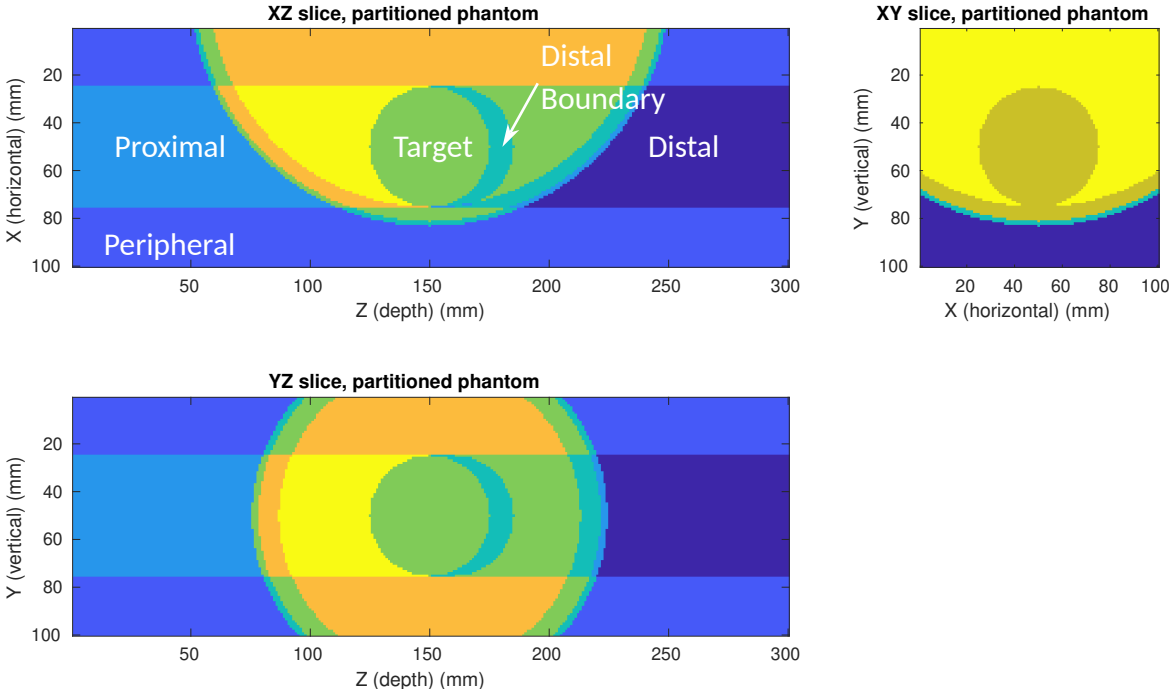

Figure 3.1: Partitioning of the target volume. In this specific example, a 50 mm diameter tumour is offset to the side of a simplified human head phantom 200 mm in diameter, with 2 mm of skin and a 6 mm thick skull.

2. The dose objective volume data V_d, in which the desired dose in each voxel of the target is defined. V_d is segmented into five logical subvolumes; firstly the target proper, where the objective is to deliver the desired physical dose distribution, and four additional subvolumes where the dose should be minimised: the distal boundary, distal, peripheral and proximal, as shown in Figure 3.1. This logical partitioning enables different weights and downsampling factors to be applied to different subvolumes.

Additional user-specified parameters include the relative weighting of dose to each of the different subvolumes, the fraction of points within each subvolume which are sampled for optimisation (which can be 100% if desired), and the beam spot granularity in each dimension.

3.2.1 Dose deposition data library construction

A library of monoenergetic single-ion dose distributions is prepared via Geant4 Monte Carlo simulations (see Table 3.1) in a single homogeneous polymethyl methacrylate (PMMA) target phantom with dimensions of $100 \times 100 \times 300$ mm^3. PMMA is selected as

Table 3.1: Simulation parameters used for the generation of the ion data library used in this study, adapted from Chacon et al. [171].

Parameter	**Value**
Geant4 version	10.02.p03
Physics list	QGSP_BIC_HP
Cut value	0.1 mm
Particles/simulation	20,000
Target material	Polymethyl methacrylate (PMMA)
Target depth range	5 mm-217 mm (250 mm water equivalent depth), in steps of 1 mm
Ions simulated	^{1}H, ^{4}He, ^{7}Li, ^{12}C, ^{16}O, ^{20}Ne, ^{28}Si, ^{56}Fe

the template material as its composition and electron density is somewhat representative of human tissues (the formula of the constituent monomer is $C_5O_2H_8$) [172]. Sample dose distribution profiles are shown in Figures 3.2 and 3.3. For each of the ion species available in the TPS (currently the most common isotope of hydrogen (i.e. protons), helium, lithium, carbon, oxygen, neon, silicon and iron), a set of simulations is performed in which an infinitesimally thin and perfectly monoenergetic pencil beam is applied to a block of PMMA, with the beam energy progressively incremented such that the Bragg peak depth increases in steps of 1 mm from a minimum of 5 mm to a maximum depth of 217 mm (corresponding to a water-equivalent depth of 250 mm). Each simulation scores the 3D dose distribution resulting from the beam with a spatial resolution of 1 mm[31]. This generic library is then adapted for the specific pencil beam geometry of the accelerator to be used for beam delivery by convolving each dose distribution by a 3D kernel representing the 2D transverse beam profile and depthwise energy spread of the physical beam. The resulting dose distributions are saved as a library for use in the treatment planning process. Additionally, for each of the tissue types defined, conversion factors relating the Bragg peak depth for a charged particle in each tissue type to that reached by the same particle with the same kinetic energy in PMMA are determined via offline Monte Carlo simulations and stored in a look-up table.

[1]The spatial resolution can be increased if desired, although this will increase the computational workload of the TPS.

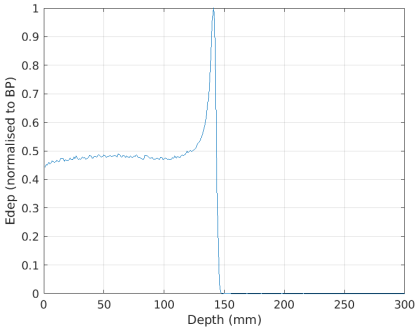

(a) ^{1}H, 153.7 MeV/u

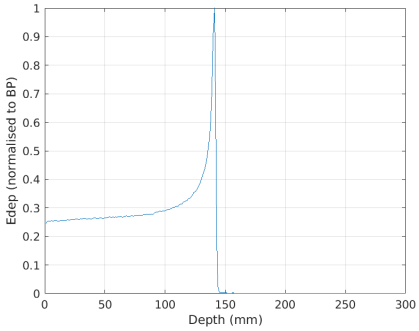

(b) ^{4}He, 152.5 MeV/u

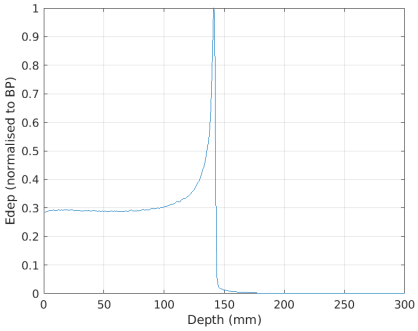

(c) ^{7}Li, 176.2 MeV/u

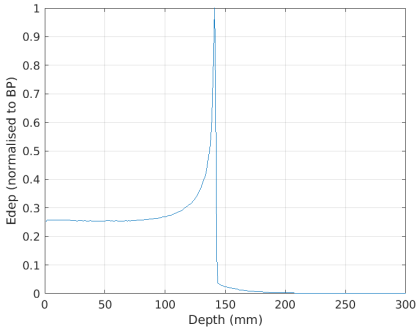

(d) ^{12}C, 290.2 MeV/u

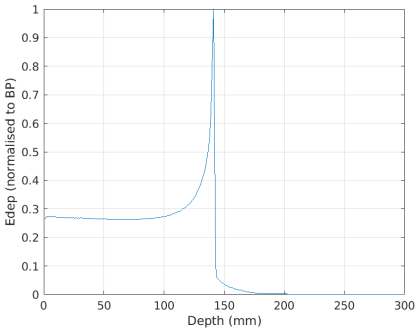

(e) ^{16}O, 345.6 MeV/u

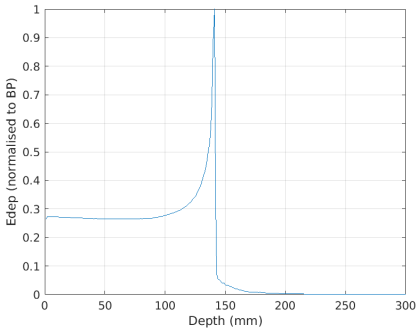

(f) ^{20}Ne, 396.6 MeV/u

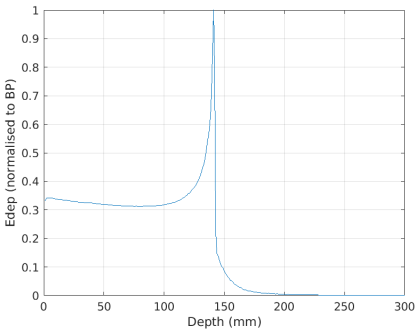

(g) ^{28}Si, 492.9 MeV/u

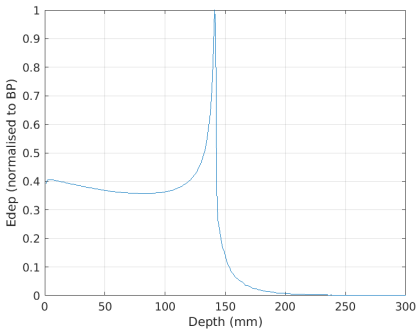

(h) ^{56}Fe, 712 MeV/u

Figure 3.2: Dose distribution profiles for equivalent energies of each of the eight ions available in the constructed library in an PMMA target phantom, where the BP is located at depth of 141 mm.

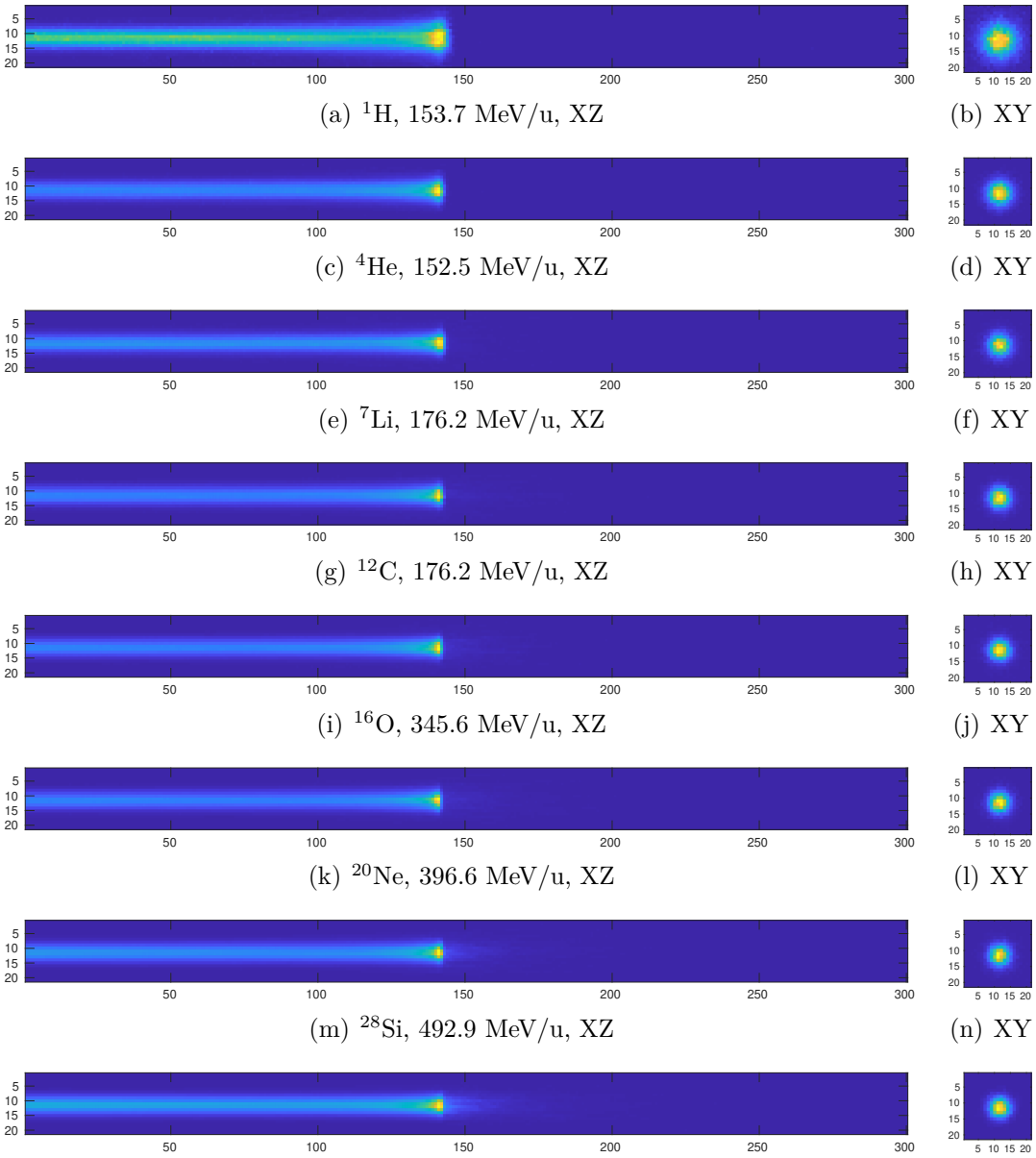

(a) ^{1}H, 153.7 MeV/u, XZ (b) XY

(c) ^{4}He, 152.5 MeV/u, XZ (d) XY

(e) ^{7}Li, 176.2 MeV/u, XZ (f) XY

(g) ^{12}C, 176.2 MeV/u, XZ (h) XY

(i) ^{16}O, 345.6 MeV/u, XZ (j) XY

(k) ^{20}Ne, 396.6 MeV/u, XZ (l) XY

(m) ^{28}Si, 492.9 MeV/u, XZ (n) XY

(o) ^{56}Fe, 712.0 MeV/u, XZ (p) XY

Figure 3.3: 2D transverse beam profiles (XZ and XY; beam is rotationally symmetric, so XZ and YZ profiles are the same) for each of the 8 ion species at energies placing the Bragg peak at a depth of 141 mm.

3.2.2 Beam position, ion and energy selection

A grid of potential transverse (x, y) beam positions is constructed for transverse raster-scanning of the pencil beam. Several alternative grids have been implemented; rigid rectangular or equilateral-triangular beam position grids can be constructed based on a user-specified beam spot granularity, or alternatively an optimal beam separation can be calculated based on the average full width at half-maximum of the dose distributions at their depths of maximum energy deposition.

Each potential beam position is then checked to determine whether it intersects with the target. For each beam position which does intersect the with target, the minimum and maximum depth (along the beam path, i.e. in the z dimension) of the intersection is recorded. These positions are compiled into a list of *active* beam positions for further analysis.

At each of these active beam positions, a vector of tissue types and thicknesses along the beam path is constructed. For voxels at depths $\mathbf{D}$ along the beam path which are a part of the tumour, the *PMMA-equivalent depth* $\mathbf{D}'$ is calculated based on the thickness of each layer of different tissues traversed by the beam to reach this voxel and the tissue-to-PMMA depth conversion ratios previously calculated. These depths are also recorded for each beam position.

Next, a list of potential Bragg peak depths is constructed, based on the desired granularity in the z dimension and the depthwise extent of the tumour (for example, one may choose to place individual Bragg peaks at every 3 mm along the beam path). For each active beam position, the TPS iterates through the list of potential Bragg peak depths and selects the energies for each ion which, when converted to the expected beam depths in the target, will be closest to those which will achieve the selected depths. The dose distributions for each of the selected ion/energy combinations are then stretched or squeezed by spatially interpolating using the previously-calculated $\mathbf{D}'$ vector to give the spatial dose distributions expected in the heterogeneous target. This mini-dose-distribution library - which is specific to each beam position - is stored as part of the treatment plan data structure for later use in the optimisation process together with the actual energies used for this ion at this position.

3.2.3 Dose optimisation

At this point, the matrices describing the task of the optimiser can be constructed. A periodic spatial sampling of the voxels in each subvolume is performed, with an

integer downsampling factor that can be tuned on a per-subvolume basis; a rate of 1 corresponds to sampling 100% of the voxels in that subvolume. The segmented volumetric structural descriptor V_{struct} is linearised and the indices corresponding to the N sampled voxels are concatenated. Next, a matrix $\mathbf{C}$ is constructed as follows:

$$\mathbf{C} = \begin{bmatrix} d_{pos_1,ion_1,e_1,vox_1}, & \cdots, & d_{pos_{N_{pos}},ion_{N_I},e_{N_en},vox_1} \\ d_{pos_1,ion_1,e_1,vox_2}, & \cdots, & d_{pos_{N_{pos}},ion_{N_I},e_{N_en},vox_2} \\ d_{pos_1,ion_1,e_1,vox_3}, & \cdots, & d_{pos_{N_{pos}},ion_{N_I},e_{N_en},vox_3} \\ \cdots & \cdots & \cdots \\ d_{pos_1,ion_1,e_1,vox_N}, & \cdots, & d_{pos_{N_{pos}},ion_{N_I},e_{N_en},vox_N} \end{bmatrix}$$

where the individual columns correspond to the contribution to each of the N sampled voxels of this particular ion beam at this specific position and energy. Dose deposited in regions where dose should be as close to zero as practically possible - the distal boundary, distal and peripheral subvolumes - are multiplied by per-subvolume scaling factors which effectively exaggerate the dose delivered if the weight is greater than one. This is used to heavily penalise any dose deposition into these volumes. Due to the physics of charged particle dose deposition, dose in the proximal region cannot be reduced to zero (entrance dose), and in fact care must be taken to ensure that the weight and sampling rate are not too high, otherwise the optimiser will attempt to minimise the total error by minimising dose in the entrance subvolume at the cost of significantly degrading the conformality of the dose distribution in the target volume.

The desired dose vector $\mathbf{d}$ is constructed by sampling the same N voxels from the linearised dose volume V_d as are used to construct the columns of $\mathbf{C}$. Now, the objective is simply to solve

$$\arg\min_{\mathbf{x}} ||\mathbf{Cx} - \mathbf{d}||^2, \quad x_k \geq 0 \tag{3.1}$$

This is solved using a non-negative least-squares optimisation algorithm[147]. The number of rows in $\mathbf{C}$ corresponds to the number of spatially sampled voxels to be used in the optimisation, while the number of columns is the total number of ion/energy/-position combinations. For the all-ion treatment plans presented in this thesis, the dimensions of C are around 40000-50000 rows and 12000-15000 columns; the vector $\mathbf{d}$ has the same number of rows as $\mathbf{C}$ (and a single column).

The solution is the vector of weights for each of the contributory ion species/energies/positions, $\mathbf{x}$. It will have the same number of rows as the number of columns in $\mathbf{C}$, and provides the linear combination of all of the available individual depth-

adjusted dose distributions which is the best fit to the objective dose distribution at the sampled spatial locations described by the **d**-vector. The solution is globally optimal, but weighted region-by-region by the per-region spatial downsampling factor and weight factor; this factor enables a relatively low importance to be given to the dose distribution in the proximal region (where achieving the ideal dose of zero is physically impossible, which would otherwise massively skew the optimisation process in favour of reducing the error in the proximal region at the expense of significantly underdosing the target region). The non-negative least squares optimiser is a gradient descent algorithm subject to the constraint that each of the resultant weights must be positive, since a negative radiation dose is physically impossible. This is implemented in MATLAB by transforming the problem into a convex quadratic programming problem.

3.3 Materials and methods

The treatment planning system is evaluated in several different single-field scenarios to demonstrate the potential advantages of manifold multi-ion therapy over single-ion and dual-ion therapy. A simulation model is first constructed to represent a simplified human head. Tumours are positioned at three different depths.

Treatment plans are then constructed for each scenario with (1) each of the individual ions included in the library; (2) combinations of light-heavy ion pairs; (3) combinations of ion triplets and (4) all ions available in the library. The physical ion beam geometry is modeled as a circular Gaussian intensity profile with a diameter of 4.47 mm full width at half maximum (FWHM) and energy spread of $\sigma = 0.2\%$ for all ion species and energies.

The treatment plans are evaluated with several metrics, including RMS error in the target volume, D_{50} and D_{90} target volume fractions, and non-target volumes receiving 5%, 10% and 50% of target dose. Additionally, a composite Geant4 simulation of one multi-ion treatment plan is performed and the results are compared to the expected dose distribution predicted by the TPS.

3.3.0.1 Phantom construction

The phantom is modelled on a simplified spherical human head in air. Each of the tissue types in the phantom are based on the material definitions used in Geant4, which are in turn based on the International Commission on Radiation Units and Measurements (ICRU) material definitions [159, 173, 174]. The radius of the head

is 100 mm; the outer 2 mm is skin (G4_SKIN_ICRP), the next 6 mm is cortical bone (G4_BONE_CORTICAL_ICRP)[2], and the remaining volume is brain tissue (G4_BRAIN_ICRP). A 30 mm diameter subvolume of the brain is denoted as a poorly-differentiated tumour, which is assumed to have a similar composition and density to normal brain tissue. The tumour subvolume is located at one of three possible positions T relative to the centre of the phantom:

- Shallow: $T = (-40, 0, 67)$ mm
- Central: $T = (0, 0, 67)$ mm
- Deep: $T = (40, 0, 67)$ mm

The tumour is laterally offset in each case to ensure that the scattering volume proximal to the tumour is significantly asymmetric, and thus demonstrate that the TPS still works correctly even in a relatively extreme case. Note that in practice, a single-field irradiation would be unlikely to be performed as in the deep case; however, this is a possible approach in a multi-field irradiation and so is a valid test case for the TPS.

3.3.0.2 Evaluation of treatment plans

Treatment plans are developed for each of the tumour positions shown in Figure 3.4. The TPS is configured to generate plans using

- Each of the supported single ion species;
- A number of light/heavy ion pairs (proton-carbon, helium-oxygen, lithium-neon);
- A number of triple-ion combinations (proton-helium-oxygen, lithium-carbon-iron, carbon-oxygen-neon); and
- All 8 ions.

[2]This is a simplification of the actual cross-section of the skull, which is itself heterogeneous, but sufficient to demonstrate the TPS.

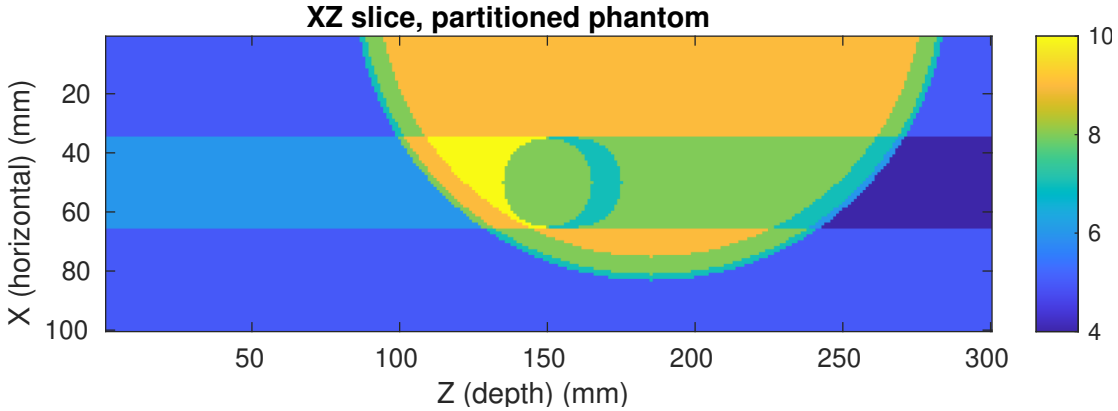

(a) Shallow

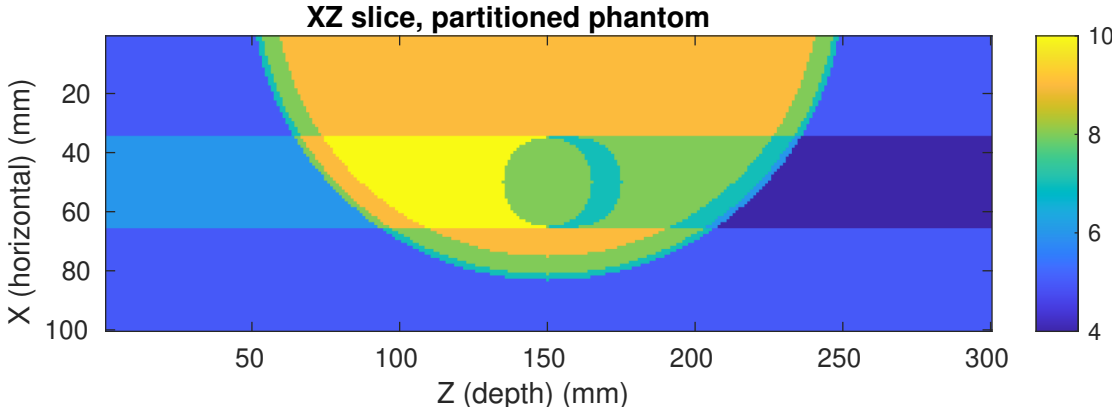

(b) Central

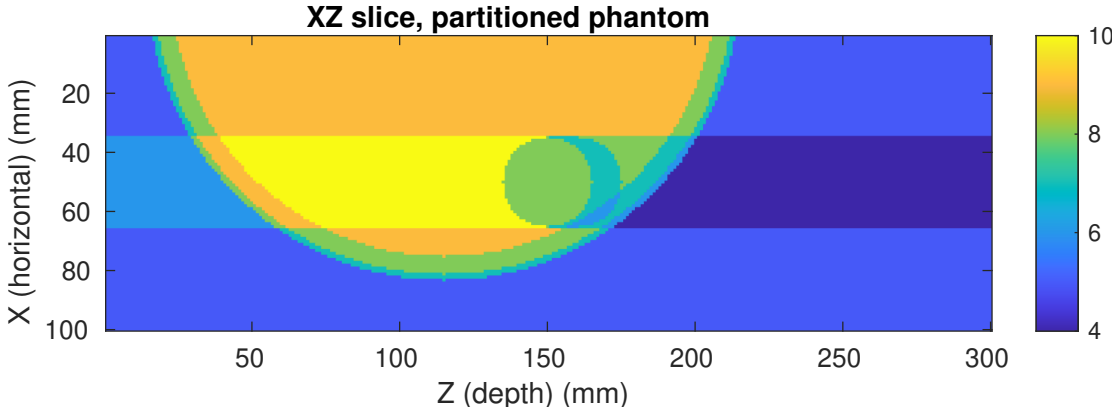

(c) Deep

Figure 3.4: Tumour positions (shown in the xz plane through the centre of the tumour) used for the generation of the evaluation treatment plans.

3.3.0.3 Performance metrics

The obtained treatment plans were evaluated using a number of different performance metrics. First, the percentage dose-volume contribution from each ion species in the multi-ion treatment plans is calculated across the target volume, next,The uniformity of the dose distribution in the target volume was evaluated using the RMS error between the objective and obtained dose distributions in each of the defined subvolumes (target, distal boundary, distal, peripheral and proximal. The percentage of the planning target volume which received at least 50% and 90% of the objective dose (D_{50} and D_{90}) provides a clinically-relevant measure of dose conformity. Volumes of non-target tissue receiving 5%, 10% and 50% (V_5, V_{10} and V_{50}) of the target objective dose are also evaluated. Finally, a selection of images illustrating the achieved 3D volumetric dose distributions, both in total and decomposed into individual contributions from each component ion species, are presented, together with D_{50} and D_{90} isosurfaces.

3.3.1 Integrated simulation of treatment plan

An additional treatment plan for a tumour positioned in the centre of the phantom was constructed and used to generate beam spectra for an integrated Geant4 simulation of the entire treatment plan. The simulation was conducted with the objective of delivering a 1 Gy dose to the target volume and compared with the predicted dose distribution obtained from the TPS; the performance metrics described in Section 3.3.0.3 are also applied in this case.

3.4 Results and discussion

3.4.1 Per-ion dose-volume contributions

The breakdown of the percentage contribution of each individual ion species to the overall dose-volume in the target region for three different target depths is shown in Table 3.2

For the no-hypoxia, no-OAR case, the 8-ion treatment plan for the shallow tumour is dominated by the contribution from helium, with moderate contributions from protons, lithium and carbon and small (but non-zero) contributions from the other ions. At progressively deeper tumour positions, the dominance of helium increases and the use of carbon decreases; several of the other ions are not used at all (for example,

Table 3.2: The percentage contribution of individual ions in each multi-ion treatment plan (no hypoxia, no OAR).

Tumour position	Ion combination	H%	He%	Li%	C%	O%	Ne%	Si%	Fe%
Shallow	^{1}H, ^{12}C	68.17	-	-	31.83	-	-	-	
	^{4}He, ^{16}O	-	74.64	-	-	25.36	-	-	-
	^{7}Li,^{20}Ne	-	-	58.09	-	-	41.91	-	-
	^{1}H, ^{4}He, ^{16}O	23.76	56.67	-	-	19.57	-	-	-
	^{7}Li, ^{12}C, ^{56}Fe	-	-	50.00	23.40	-	-	-	26.60
	^{12}C, ^{16}O, ^{20}Ne	-	-	-	31.72	23.86	44.42	-	-
	All ions	17.31	49.29	15.31	7.57	2.94	2.02	3.90	1.67
Central	^{1}H, ^{12}C	56.20	-	-	43.80	-	-	-	
	^{4}He, ^{16}O	-	99.31	-	-	.69	-	-	-
	^{7}Li,^{20}Ne	-	-	87.02	-	-	12.98	-	-
	^{1}H, ^{4}He, ^{16}O	24.38	74.24	-	-	1.39	-	-	-
	^{7}Li, ^{12}C, ^{56}Fe	-	-	78.41	21.01	-	-	-	0.58
	^{12}C, ^{16}O, ^{20}Ne	-	-	-	63.30	21.55	15.15	-	-
	All ions	23.54	54.33	15.71	3.20	0.00	1.43	1.54	0.26
Deep	^{1}H, ^{12}C	46.06	-	-	53.94	-	-	-	-
	^{4}He, ^{16}O	-	98.42	-	-	1.58	-	-	-
	^{7}Li,^{20}Ne	-	-	93.96	-	-	6.04	-	-
	^{1}H, ^{4}He, ^{16}O	11.95	86.23	-	-	1.82	-	-	-
	^{7}Li, ^{12}C, ^{56}Fe	-	-	83.17	16.83	-	-	-	0.00
	^{12}C, ^{16}O, ^{20}Ne	-	-	-	86.66	11.11	2.23	-	-
	All ions	12.86	64.05	19.57	2.06	0.06	1.40	0.00	0.00

the iron and oxygen are not used in either the central or deepest tumour location). In the proton/carbon plan, the relative proportion of dose-volume contribution from protons steadily decreases with increasing depth. In contrast, for the helium/oxygen plans, the proportion of helium increases to almost completely dominate in the central and deep tumour locations. Across all plans, there is a strong preference for the use of helium when this is available, reflecting its favourable combination of minimal tail dose and moderate lateral scatter.

Figures 3.5 - 3.7 show both the total dose distributions and the dose contributions from each individual ion species for 8-ion treatment plans constructed for three tumour positions.

For the deepest tumour location (Figure 3.7), the dose is dominated by helium ions, with a minor contribution from protons, lithium and carbon. The total dose to the target (background) is relatively uniform, with the higher density of the skull bone through which the beam must pass to reach the tumour resulting in a high local dose deposition in this region. The remaining central and shallow cases (Figures 3.6 and 3.5) show a similar division of dose distribution between ion species in the different cases, however the shallowest cases do demonstrate a greater contribution of the heavier ions - including silicon (and a very small amount of iron) in the shallowest case.

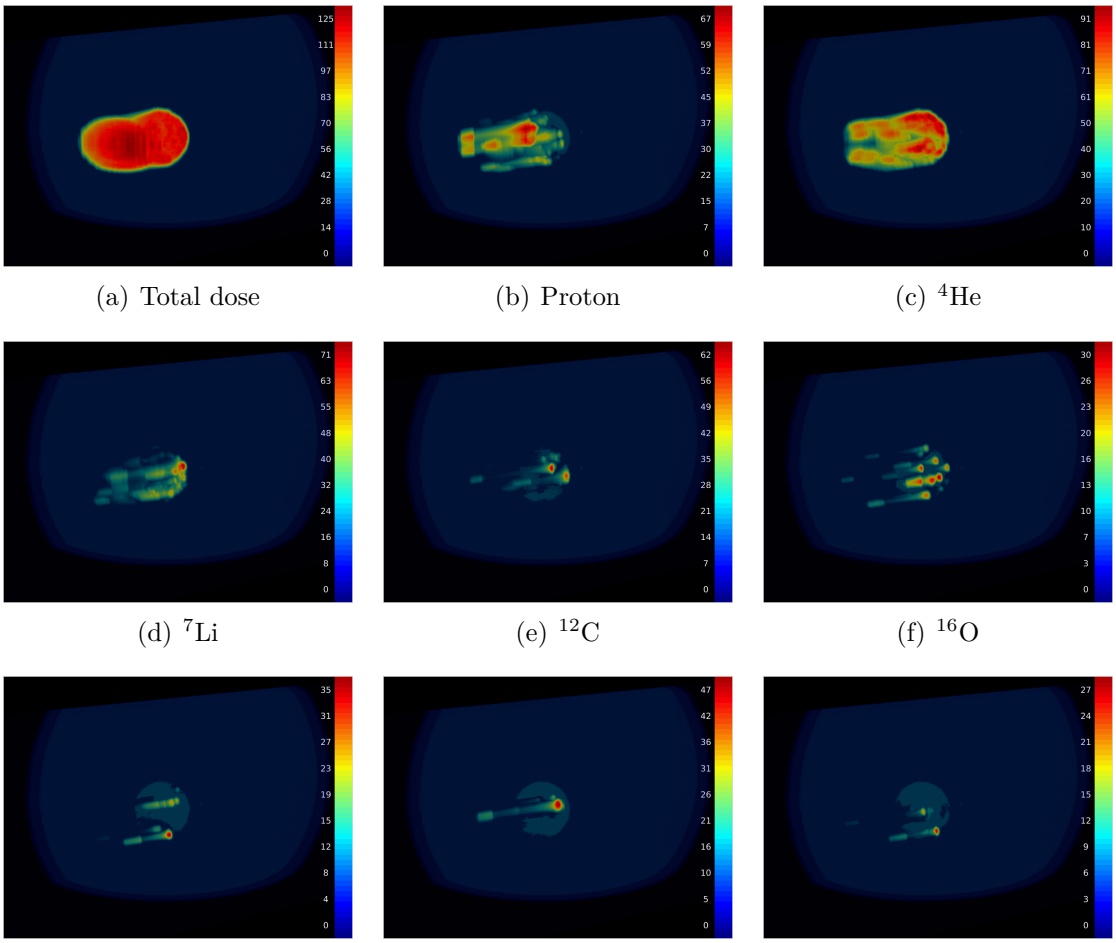

(a) Total dose (b) Proton (c) ^{4}He

(d) ^{7}Li (e) ^{12}C (f) ^{16}O

(g) ^{20}Ne (h) ^{28}Si (i) ^{56}Fe

Figure 3.5: 3D volumetric visualisations of total dose and contributions from each individual ion species, for an 8-ion treatment plan. The tumour is located at the 'shallow' position.

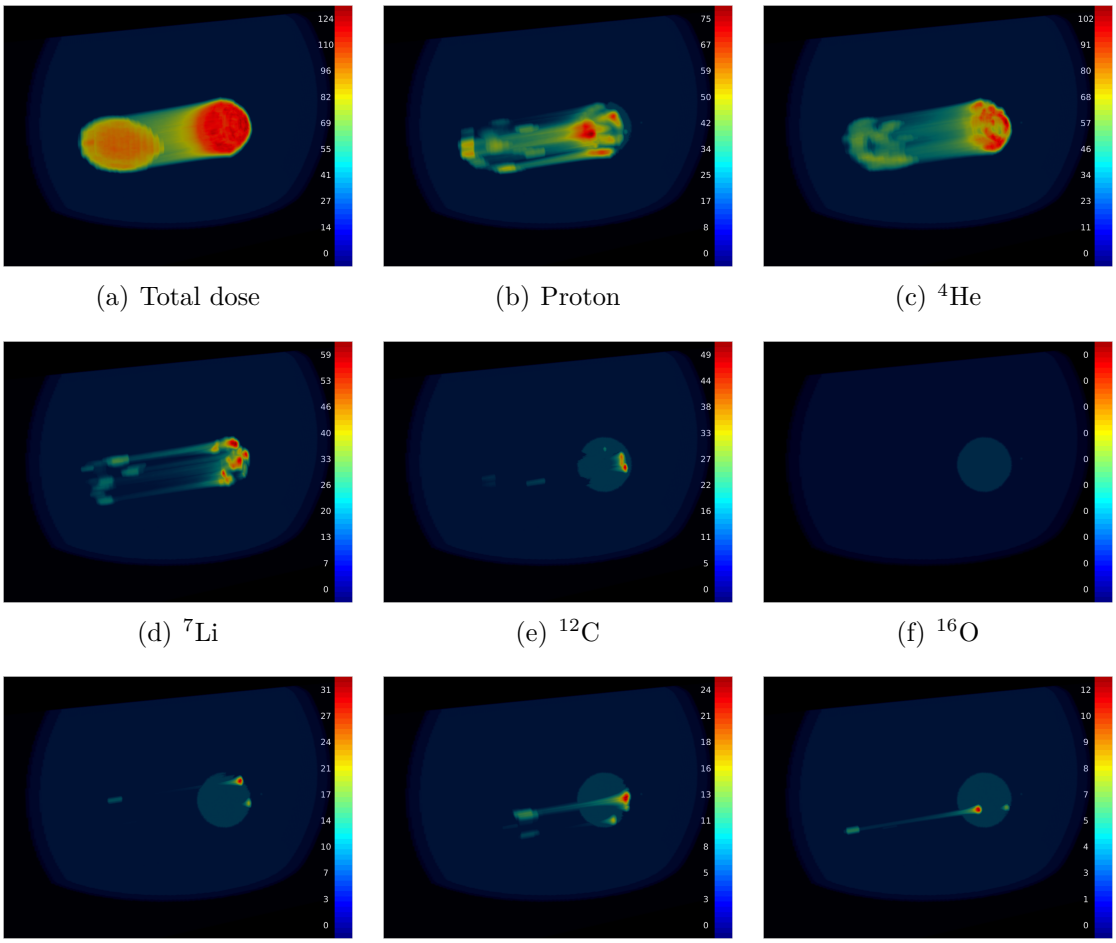

(a) Total dose (b) Proton (c) ^{4}He

(d) ^{7}Li (e) ^{12}C (f) ^{16}O

(g) ^{20}Ne (h) ^{28}Si (i) ^{56}Fe

Figure 3.6: 3D volumetric visualisations of total dose and contributions from each individual ion species, for an 8-ion treatment plan. The tumour is located at the 'central' position.

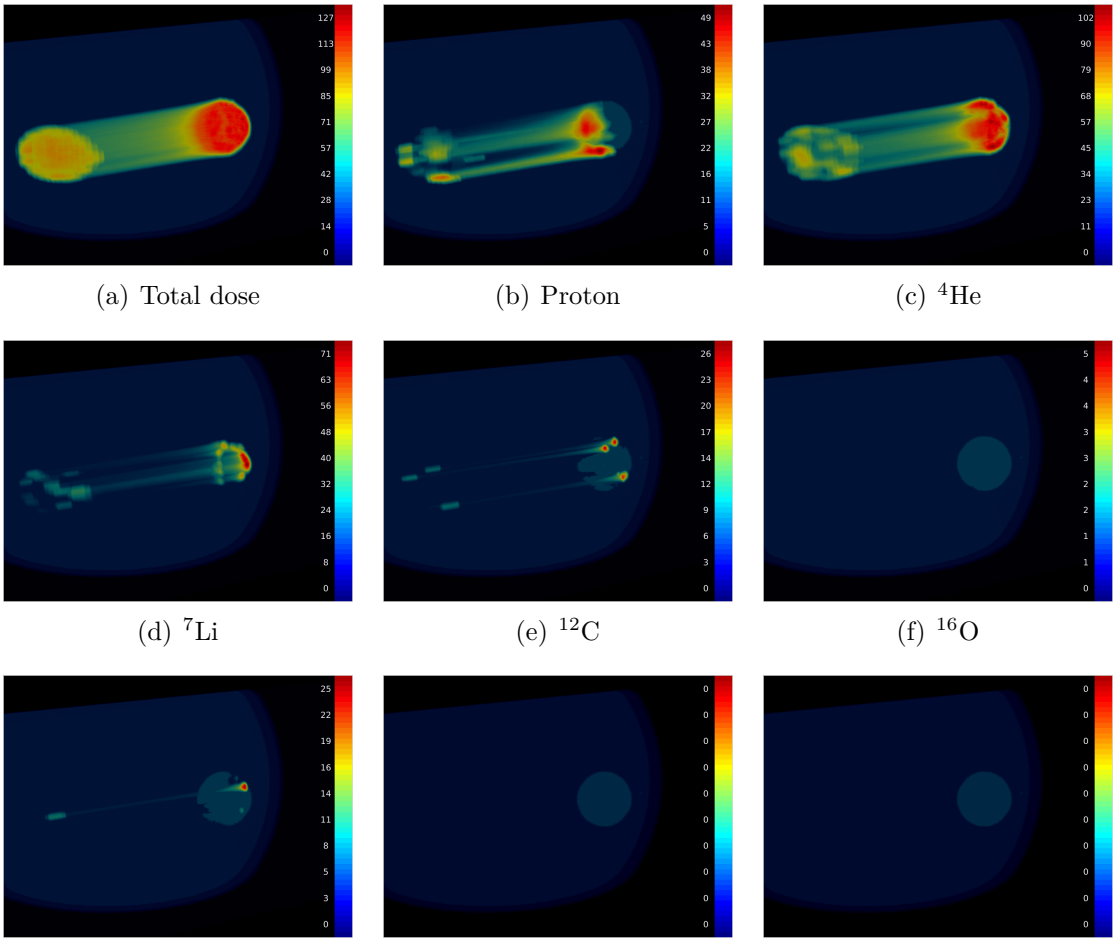

(a) Total dose (b) Proton (c) ^{4}He

(d) ^{7}Li (e) ^{12}C (f) ^{16}O

(g) ^{20}Ne (h) ^{28}Si (i) ^{56}Fe

Figure 3.7: 3D volumetric visualisations of total dose and contributions from each individual ion species, for an 8-ion treatment plan. The tumour is located at the 'deep' position.

Table 3.3: RMS error (Gy) for dose distributions within the target and the surrounding regions.

Tumour position	Ion combination	Target	Distal boundary	Distal	Peripheral	Proximal
Shallow	^{1}H	11.42	16.23	0.01	1.95	39.87
	^{4}He	11.79	15.61	0.15	1.87	40.18
	^{7}Li	11.79	15.61	0.15	1.87	40.18
	^{12}C	12.17	16.15	0.81	1.85	40.56
	^{16}O	12.10	16.13	0.57	1.88	40.43
	^{20}Ne	12.03	16.15	0.61	1.86	40.43
	^{28}Si	11.28	17.20	0.60	1.87	41.10
	^{56}Fe	12.13	16.64	0.49	1.86	41.79
	^{1}H, ^{12}C	11.30	15.77	0.28	1.93	40.14
	^{4}He, ^{16}O	11.26	15.43	0.27	1.87	40.29
	^{7}Li, ^{20}Ne	11.54	15.84	0.46	1.88	40.66
	^{1}H, ^{4}He, ^{16}O	10.98	15.52	0.20	1.90	40.23
	^{7}Li, ^{12}C, ^{56}Fe	11.87	15.87	0.49	1.87	41.06
	^{12}C, ^{16}O, ^{20}Ne	11.61	15.96	0.67	1.88	40.56
	All ions	10.86	15.47	0.27	1.90	40.40
Central	^{1}H	11.89	17.52	0.03	2.46	43.73
	^{4}He	11.53	16.09	0.32	2.20	44.74
	^{7}Li	11.45	17.30	0.87	2.23	45.82
	^{12}C	11.79	18.02	1.91	2.15	45.21
	^{16}O	11.90	18.69	1.62	2.16	45.18
	^{20}Ne	11.93	18.63	1.83	2.15	45.17
	^{28}Si	11.76	20.71	2.02	2.15	46.32
	^{56}Fe	12.08	20.82	1.94	2.16	47.91
	^{1}H, ^{12}C	11.37	16.71	0.90	2.42	44.61
	^{4}He, ^{16}O	11.52	16.09	0.33	2.20	44.75
	^{7}Li, ^{20}Ne	11.36	17.21	1.01	2.22	45.81
	^{1}H, ^{4}He, ^{16}O	11.36	16.06	0.27	2.32	44.54
	^{7}Li, ^{12}C, ^{56}Fe	11.35	17.16	1.09	2.22	45.83
	^{12}C, ^{16}O, ^{20}Ne	11.65	17.96	1.79	2.15	45.31
	All ions	11.13	16.18	0.46	2.32	44.81

3.4.2 Dose uniformity

Table 3.3 shows the RMSE achieved using each individual ion and all evaluated ion combinations at each of the the three tumour depths, where no hypoxic sub-volume and no OAR are present. The lowest RMSE is achieved in the target volume with the 8-ion treatment plan for all tumour positions (Table 3.3). Immediately distal to the target volume (the 'distal boundary'), the 8-ion plan achieves the lowest RMSE for both the shallow and deep tumour position, however, it is very slightly outperformed by the helium/oxygen combination for the central position. The relative performance of the different plans in the other regions is mixed, with no one ion combination standing out amongst others.

Table 3.4: Percentages of the target volume that received at least 50% and 90% of the dose volume.

Tumour position	Ion combination	D_{50}	D_{90}
Shallow	^{1}**H**	99.51	87.23
	^{4}**He**	99.17	87.47
	^{7}**Li**	99.17	87.47
	^{12}**C**	98.98	87.38
	^{16}**O**	99.02	87.37
	^{20}**Ne**	99.12	87.40
	^{28}**Si**	99.41	87.39
	^{56}**Fe**	99.08	86.97
	^{1}**H**, ^{12}**C**	99.47	87.78
	^{4}**He**, ^{16}**O**	99.58	87.80
	^{7}**Li**, ^{20}**Ne**	99.39	87.75
	^{1}**H**, ^{4}**He**, ^{16}**O**	99.61	87.95
	^{7}**Li**, ^{12}**C**, ^{56}**Fe**	99.07	87.62
	^{12}**C**, ^{16}**O**, ^{20}**Ne**	99.34	87.70
	All ions	99.70	88.17
Central	^{1}**H**	99.46	85.72
	^{4}**He**	99.46	87.33
	^{7}**Li**	99.53	86.99
	^{12}**C**	99.35	86.91
	^{16}**O**	99.25	86.63
	^{20}**Ne**	99.24	86.75
	^{28}**Si**	99.41	86.22
	^{56}**Fe**	99.34	85.93
	^{1}**H**, ^{12}**C**	99.46	86.72
	^{4}**He**, ^{16}**O**	99.46	87.33
	^{7}**Li**, ^{20}**Ne**	99.65	87.18
	^{1}**H**, ^{4}**He**, ^{16}**O**	99.51	87.21
	^{7}**Li**, ^{12}**C**, ^{56}**Fe**	99.60	87.16
	^{12}**C**, ^{16}**O**, ^{20}**Ne**	99.39	87.16
	All ions	99.63	87.41
Deep	^{1}**H**	99.27	83.86
	^{4}**He**	99.48	86.75
	^{7}**Li**	99.45	86.64
	^{12}**C**	99.47	86.39
	^{16}**O**	99.36	85.85
	^{20}**Ne**	99.04	86.03
	^{28}**Si**	99.49	84.54
	^{56}**Fe**	99.47	83.81
	^{1}**H**, ^{12}**C**	99.45	85.94
	^{4}**He**, ^{16}**O**	99.48	86.73
	^{7}**Li**, ^{20}**Ne**	99.53	86.62
	^{1}**H**, ^{4}**He**, ^{16}**O**	99.51	86.70
	^{7}**Li**, ^{12}**C**, ^{56}**Fe**	99.58	86.71
	^{12}**C**, ^{16}**O**, ^{20}**Ne**	99.47	86.49
	All ions	99.62	86.86

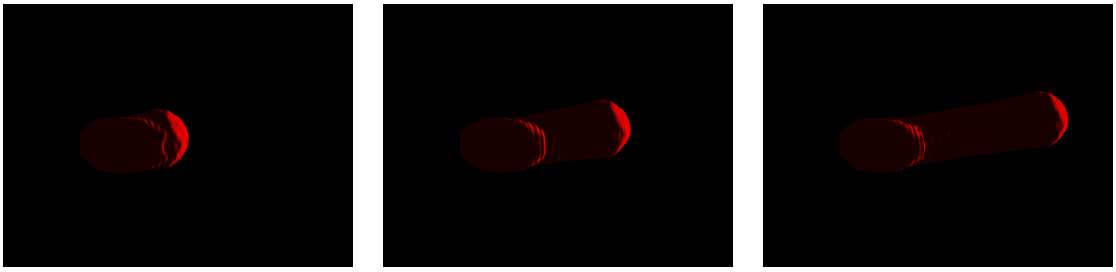

(a) Shallow (b) Centre (c) Deep

Figure 3.8: 50% isodose surfaces for an 8-ion treatment plan for 3 tumour positions.

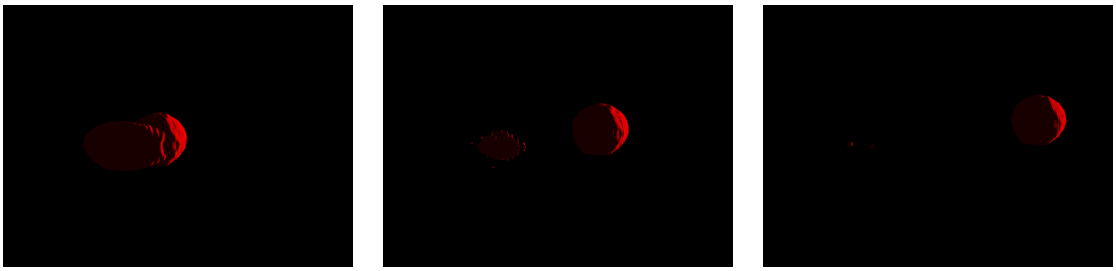

(a) Shallow (b) Centre (c) Deep

Figure 3.9: 90% isodose surfaces for an 8-ion treatment plan for 3 tumour positions.

3.4.3 Dose coverage

All treatment plans achieved excellent coverage of the tumour, with more than 99% of the target receiving at least 50% of the nominal target dose. D_{90} coverage was better than 82.8% for all single-ion and combination treatment plans, with the 8-ion plans achieving the best D_{90} coverage in all cases.

Dose isosurfaces at 50% (Figure 3.8) and 90% (Figure 3.9) of nominal target dose demonstrate excellent dose conformance in the target in all cases. The 50% isodose surface shows the extent of the entrance dose distribution, while the 90% surface shows that peak dose is largely concentrated in the target and some parts of the entrance bone tissue (more so for the shallowest tumour position, where the entrance dose gradient is steeper compared to the other tumour positions).

3.4.4 Normal tissue dose

Table 3.5 presents the volumes of normal tissue (outside of the planning target volume) which receive at least 5%, 10% and 50% of the target dose for each of the three tumour positions (V_5, V_{10} and V_{50}). The PTV is a total of 14000 mm^3.

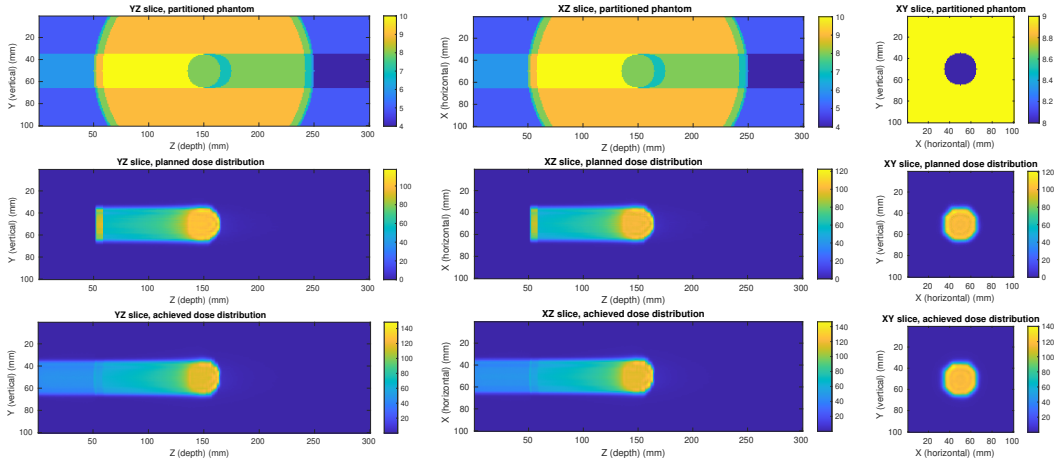

Figure 3.10: Labelled phantom sections and sections through the dose volume generated by the integrated Monte Carlo simulation. The dose to the target region is 100 Gy.

The results for V_5, V_{10} and V_{50} are very similar across all the different ion combinations, neither showing a significant advantage nor disadvantage for the manifold multi-ion treatment plans. One notable observation is that the rarely-used ^{4}He single-ion therapy consistently performs better than the others; this is likely due to its favourable combination of reduced entrance dose compared to protons, minimal fragmentation tail and moderate lateral scattering (relative to protons).

3.4.5 Integrated simulation

The results of the integrated simulation are shown in Figure 3.10. Visual examination of the slices through the centre of the tumour illustrate the high degree of dose uniformity achieved in the tumour volume. Table 3.6 shows the region-by-region RMS errors between:

- The objective dose distribution (a uniform dose of 100 Gy to the tumour, 0‘Gy elsewhere) and the estimated dose distribution in the target and surrounding regions achieved by the TPS;
- The TPS-estimated dose distributions in the target and surrounding volumes and the corresponding dose distributions obtained in the integrated simulation; and
- The objective dose distribution and the corresponding dose distribution obtained in the integrated simulation.

Table 3.5: Total volumes outside the tumour which received at least 5%, 10% and 50% of the target dose volume in mm^3. Planning target volume (PTV) is 14 mm^3.

Tumour position	**Ion combination**	**V_5 mm^3**	**V_{10} mm^3**	**V_{50} mm^3**
	^{1}**H**	30870	27443	15895
	^{4}**He**	29882	26703	15809
	^{7}**Li**	29882	26703	15809
	^{12}**C**	31747	26749	15901
	^{16}**O**	31531	26838	15905
	^{20}**Ne**	31626	26788	15864
	^{28}**Si**	31923	27210	15998
Shallow	^{56}**Fe**	31341	27082	16059
	^{1}**H**,^{12}**C**	30637	27227	15901
	^{4}**He**,^{16}**O**	30028	26726	15814
	^{7}**Li**,^{20}**Ne**	30880	26847	15959
	^{1}**H**,^{4}**He**,^{16}**O**	30325	26963	15861
	^{7}**Li**,^{12}**C**,^{56}**Fe**	30764	26841	16015
	^{12}**C**,^{16}**O**,^{20}**Ne**	31504	26790	15944
	All,ions	30296	26903	15897
	^{1}**H**	73695	65964	39643
	^{4}**He**	70160	63030	39055
	^{7}**Li**	73190	63672	39738
	^{12}**C**	77854	63607	39202
	^{16}**O**	77545	64821	39201
	^{20}**Ne**	78569	64789	39067
	^{28}**Si**	79622	66455	39717
Central	^{56}**Fe**	78646	66091	40448
	^{1}**H**,^{12}**C**	73627	65411	40092
	^{4}**He**,^{16}**O**	70166	63027	39052
	^{7}**Li**,^{20}**Ne**	73913	63661	39693
	^{1}**H**,^{4}**He**,^{16}**O**	71606	64328	39672
	^{7}**Li**,^{12}**C**,^{56}**Fe**	73931	63576	39748
	^{12}**C**,^{16}**O**,^{20}**Ne**	77584	63743	39255
	All ions	71676	64323	39766
	^{1}**H**	113723	101717	55073
	^{4}**He**	105817	95163	57613
	^{7}**Li**	112208	96222	59726
	^{12}**C**	118925	98214	58421
	^{16}**O**	119580	100267	58688
	^{20}**Ne**	120697	100806	58395
	^{28}**Si**	122643	104211	60119
Deep	^{56}**Fe**	121121	104342	61198
	^{1}**H**,^{12}**C**	117130	99853	59323
	^{4}**He**,^{16}**O**	105828	95166	57613
	^{7}**Li**,^{20}**Ne**	112997	96336	59701
	^{1}**H**,^{4}**He**,^{16}**O**	107170	96348	58085
	^{7}**Li**,^{12}**C**,^{56}**Fe**	113584	96227	59685
	^{12}**C**,^{16}**O**,^{20}**Ne**	118911	98120	58539
	All ions	107486	96430	58712

Table 3.6: RMS error (Gy) between the objective dose distribution (100 Gy in tumour) and plan, between plan and simulation, and between objective and simulation.

Comparison	**Target**	**Distal boundary**	**Distal**	**Peripheral**	**Proximal**
Objective-Plan	11.2	16.5	0.578	2.53	49.6
Plan-Simulation	17.7	9.13	0.256	1.17	26.8
Objective-Simulation	18.6	24.8	0.793	3.10	60.0

The main difference between the planned and simulation dose which can be seen in Figure 3.10 is the dose in air; this is neglected by the TPS since it has a negligible impact on the dose deposited in tissue (i.e. the model assumes the patient is in a vacuum); energy deposition is negligible, but the low density of air relative to tissue results in a non-trivial physical dose to the air volume, despite the low level of energy deposition.

RMS errors in between the treatment plan and the objective are comparable to those obtained in the previous simulations; there are several regions in which the RMS error is significantly worse in the simulation compared to the plan - especially the proximal region. This is again a reflection on the fact that dose deposition in air is not modelled by the TPS.

3.5 Conclusion

This Chapter presents a new open source MATLAB-based TPS for manifold multi ion therapy. The TPS has been evaluated with many combinations of ions in a simplified human head phantom, with the target volume being placed at three different depths within the phantom. The TPS demonstrates a consistent advantage in dose uniformity and conformance for manifold multi-ion therapy compared to single or dual-ion therapy; however, there is neither a significant benefit or disadvantage in terms of the total non-target volumes which receive 5%, 10% or 50% of the target dose. A sample treatment plan is also implemented as an integrated Geant4 simulation in a heterogeneous phantom, and the resulting dose distribution is compared to that predicted by the corresponding treatment plan.

The present TPS neither accounts for hypoxic sub-volumes within the tumour nor is able to make any provision for protection of organs at risk. In Chapter 4, the developed TPS is extended to incorporate these two constraints.

CHAPTER 4

Treatment planning for targets with hypoxic regions and organs at risk

4.1 Introduction

In this Chapter, the treatment planning system developed in Chapter 3 is extended to include support for protection of radiation-sensitive organs i.e. organs at risks (OARs) and linear energy transfer enhancement in hypoxic target subvolumes in the treatment plans. Treatment plans analogous to those developed in Chapter 3 are constructed for different single, dual, triple and manifold ion combinations for different tumour positions but with hypoxic sub-volumes and/or and OARs have been constructed and analysed. The developed TPS is shown to be able to meet a specified objective dose distribution subject to linear energy transfer (LET) constraints and dose avoidance in organs at risk (OAR) in a heterogeneous target volume.

Organs at risk are radiation sensitive tissues, damage to which will result in severe harm to the patient. Examples of OARs include the eyes (particularly during treatment of brain cancers), or the bowel (which is often impacted by radiation from prostate cancer therapy). They are outside of the tumour, but may be immediately adjacent to it; it is very important to minimise the dose received by these tissues while still meeting the dose objective in the tumour. In some cases, these objectives are mutually incompatible, so a critically important feature of a TPS is to manage the required

compromise between tumour dose and OAR radiation dose. In the TPS described in this Chapter, this functionality is implemented by defining a new volumetric data object which describes the geometry of the OAR independently of the structural information used to describe the target, and applying a very high cost/penalty factor for dose deposited to this volume (which has an objective dose of zero).

Hypoxic sub-volumes are radiation resistant entities within the target which may need a biological radiation dose that is up to three times higher than that needed to achieve the same response in cells with a normal normal oxygen level. Heavier ions such as ^{12}C and ^{16}O provide higher linear energy transfer, which has shown to be effective in overcoming the radioresistance of deep-seated hypoxic entities within the tumour. It is important to note that it is not necessarily desirable to apply high LET radiation to the entire tumour, since this also introduces a high risk of adverse effects in healthy tissues. In our developed TPS, the optimiser limits the choice of ion in and beyond the hypoxic subvolume to high-LET ions only in order to maximise the LET in this hypoxic region. Therefore, if hypoxia is present, ions whose atomic number Z is below a user-specified threshold will not be used at or beyond the depth of the first hypoxic voxel at this beam location.

4.2 Implementation of support for OAR regions and hypoxic sub-volumes into the TPS design

Adding support for optimised treatment of hypoxic regions and OARs do not fundamentally alter the dose optimisation process in the developed treatment planning system presented in Chapter 3.2; rather, they add additional constraints and weights which enable the objectives of enhancing the relative biological effectiveness (RBE) in the hypoxic region while avoiding dose to the OARs.

4.2.1 Hypoxia

A volumetric data structure - a binary map marking regions of hypoxia (for example, as determined from PET images of the target area obtained with ^{18}F-FMISO or ^{18}F-FRP-170 [175]) - is added as an additional input to the optimiser. The hypoxic region is expected to overlap with the target volume, and a warning will be issued if it does not at least partially overlap.

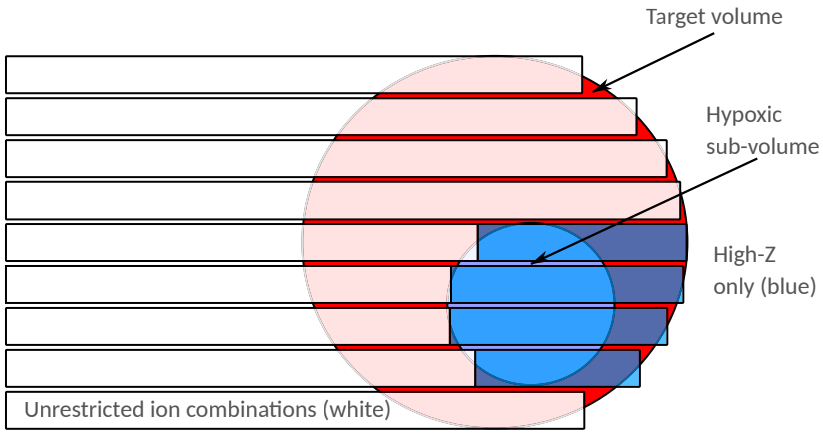

Figure 4.1: Conceptual illustration of beam composition around a hypoxic subvolume within the target volume; unrestricted beams are shown in white, while high-Z-only beams are shown in blue.

As the raster-scanned list of beam positions is being checked for potential intersection with the tumour, the intersection of the beam with any hypoxic regions is also flagged, and the physical depth at which the shallowest hypoxic voxel is detected is recorded for each beam position. At the point at which the potential permitted Bragg peak positions are being evaluated for intersection with the tumour, the hypoxia flag is checked. If at least one of the target voxels along the beam path is flagged as being hypoxic, then the optimiser limits the choice of ion in this position to high-LET ions only along the remainder of the path to maximise the LET in this hypoxic region. Therefore, if hypoxia is present, ions whose atomic number Z is less than or equal to a user-specified threshold will not be used at or beyond the depth of the first hypoxic voxel at this beam location. The concept is illustrated in Figure 4.1.

By excluding low-LET ions, the TPS is forced to use only high-LET ions in order to achieve the objective dose. This will increase the fragmentation tail distal to the hypoxic subvolume and any target region distal to the hypoxic subvolume, and so this feature should only be enabled if no organ at risk is immediately distal to this target volume. This simple method maximises the use of high-LET in hypoxic regions where it will be of most impact, while sparing other areas from needlessly high fragmentation tail dose that would result if only high-LET ion species are used throughout the entire treatment volume.

4.2.2 Organs at Risk

A volumetric data structure - a binary map marking any regions containing organs at risk (i.e. areas where dose should be as close to zero as practically possible) is added as an additional input to the optimiser. The regions tagged as OARs may not overlap with the target volume, and if an overlap is detected, a warning will be issued.

OAR support is simply implemented by using a large, configurable cost/penalty factor for dose deposited in voxels corresponding to OAR regions. The objective (desired) dose in the OAR is always zero; therefore, a high weight factor is applied to exaggerate the residual dose in this volume. This exploits the existing weighting system, and with the result that the dose to this region is aggressively (but controllably) minimised. Where an OAR is immediately adjacent to the tumour, the two objectives (target dose to target volume and zero dose to OAR) are in conflicdt; in this case, the weight can be reduced or otherwise adjusted depending on the specific priorities of the treating clinician. In this case, any form of radiation therapy will clearly be a compromise between tumour ablation efficacy and protection of the OARs.

4.3 Evaluation of proposed hypoxia and OAR support

4.3.1 Phantom construction

The phantoms used for the TPS evaluation performed in Chapter 3 are shown in Figure 4.2 with an OAR region added distal to the tumour and hypoxic subvolume added inside the tumour. The physical composition of the phantom is unchanged; these are logical volumes only and may be mapped to any underlying tissue type via the definition of the target structure in the phantom volumetric data structure.

Exhaustive plans for different ion combinations for the same head phantom (as described in Chapter 3.3.0.1 were generated. Tumours are positioned at three different depths, with and without a radioresistant hypoxic subvolume and a radiosensitive organ at risk (OAR) subvolume.

The tumour subvolume is located at one of three possible positions T relative to the centre of the phantom:

- Shallow: $T = (-40, 0, 67)$ mm

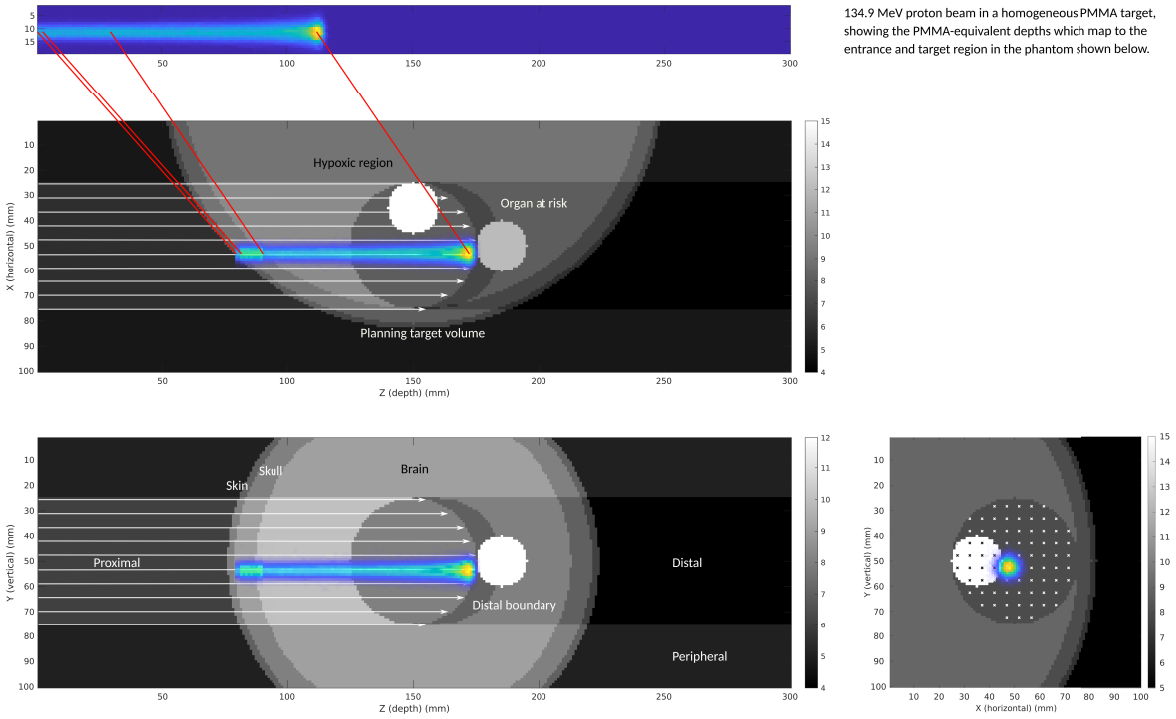

Figure 4.2: XZ, YZ and XY slices through the centre of the tumour, showing how the volume is partitioned into planning target volume (PTV), proximal, distal boundary, distal and peripheral regions. The working volume is a 100 mm×100 mm×100 mm volume centred on the tumour, which in this specific example is 50 mm in diameter, offset to the side of a simplified spherical human head phantom (outer ⌀ = 200 mm, with 2 mm of skin and a 6 mm thick skull). An OAR with a diameter of 20 mm is located distal to the tumour and a 20 mm diameter hypoxic sub-volume is located on the inner edge of the tumour. The beam grid is 5 mm×5 mm, with beam entrance on the left. One beam (protons, 134.9 MeV) is shown at beam grid position (51, 51) mm, reaching the distal margin of the PTV.

- Central: $T = (0, 0, 67)$ mm
- Deep: $T = (35, 0, 67)$ mm

Inside the tumour subvolume, a spherical hypoxic region with a diameter of 10 mm is defined within the left-hand lateral extremity of the spherical tumour volume. Immediately distal to the tumour, a 20 mm diameter spherical region is defined as an organ at risk.

The tumour positions, together with the organs at risk and the hypoxic regions are shown in Figure 4.3.

4.3.1.1 Evaluation of treatment plans

Treatment plans are developed for each of the tumour positions shown in Figure 4.3. The TPS is configured to generate plans using:

- Each of the supported single ion species;
- A number of light/heavy ion pairs (proton-carbon, helium-oxygen, lithium-neon);
- A number of triple-ion combinations (proton-helium-oxygen, lithium-carbon-iron, carbon-oxygen-neon); and
- All 8 ions.

Different sets of constraints are imposed on the TPS:

- OAR, but no hypoxic region;
- Hypoxic region, but no OAR; and
- Both OARs and hypoxic regions.

The plans generated by the TPS were evaluated using the same performance metrics as described in Section 3.3.0.3 of Chapter 3.

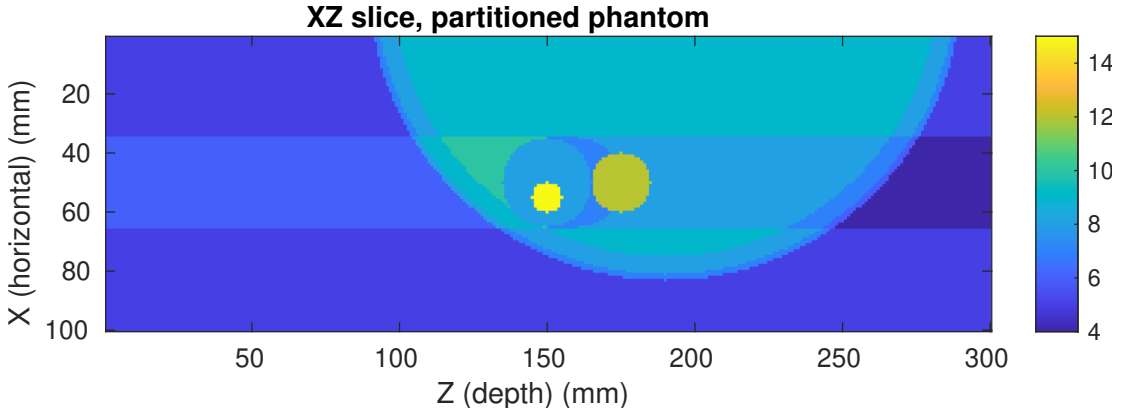

(a) Shallow

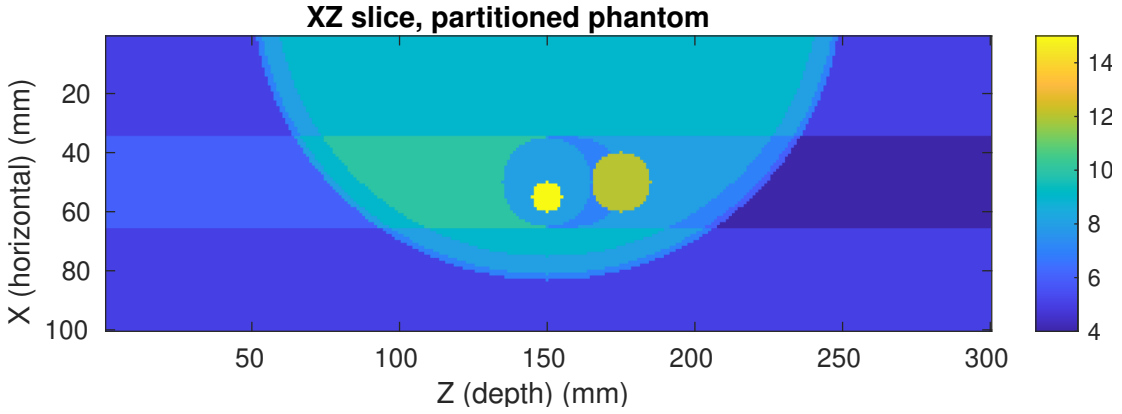

(b) Central

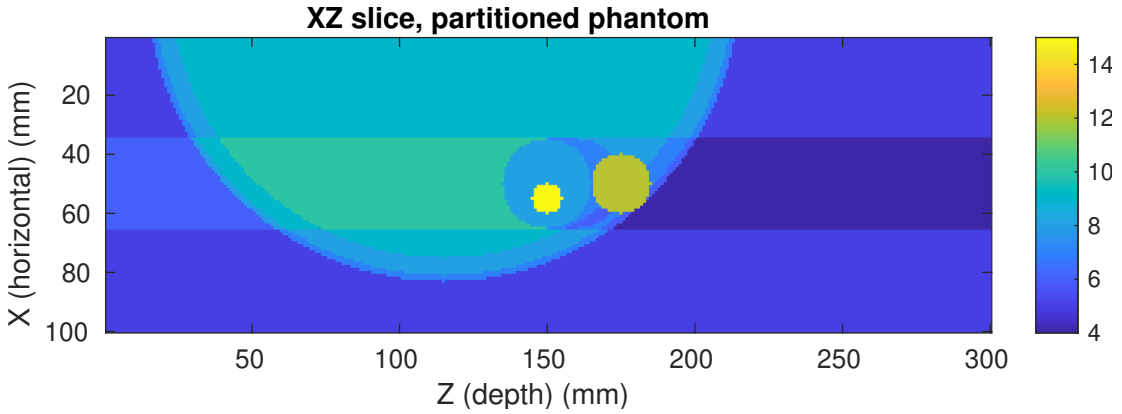

(c) Deep

Figure 4.3: Tumour positions (shown in the xz plane through the centre of the tumour) used for the generation of the evaluation treatment plans.

Table 4.1: The percentage contribution of individual ions in each multi-ion treatment plan. A hypoxic region is located inside the tumour.

Tumour position	Ion combination	H%	He%	Li%	C%	O%	Ne%	Si%	Fe%
Tumour position	**Ion combination**	**H%**	**He%**	**Li%**	**C%**	**O%**	**Ne%**	**Si%**	**Fe%**
	^{1}H, ^{12}C	57.99	-	-	42.01	-	-	-	-
	^{4}He, ^{16}O	-	64.42	-	-	35.58	-	-	-
	^{7}Li,^{20}Ne	-	-	50.41	-	-	49.59	-	-
Shallow	**^{1}H, ^{4}He, ^{16}O**	21.61	48.42	-	-	29.97	-	-	-
	^{7}Li, ^{12}C, ^{56}Fe	-	-	44.98	26.29	-	-	-	28.73
	^{12}C, ^{16}O, ^{20}Ne	-	-	-	32.35	23.39	44.27	-	-
	All ions	15.73	41.79	12.45	9.06	3.01	7.17	6.53	4.27
	^{1}H, ^{12}C	50.28	-	-	49.72	-	-	-	
	^{4}He, ^{16}O	-	85.09	-	-	14.91	-	-	-
	^{7}Li,^{20}Ne	-	-	76.66	-	-	23.34	-	-
Central	**^{1}H, ^{4}He, ^{16}O**	24.41	61.56	-	-	14.03	-	-	-
	^{7}Li, ^{12}C, ^{56}Fe	-	-	68.73	22.33	-	-	-	8.94
	^{12}C, ^{16}O, ^{20}Ne	-	-	-	63.29	21.47	15.24	-	-
	All ions	22.67	46.20	13.02	9.56	0.95	2.75	4.06	0.80
	^{1}H, ^{12}C	43.51	-	-	56.49	-	-	-	-
	^{4}He, ^{16}O	-	86.38	-	-	13.62	-	-	-
	^{7}Li,^{20}Ne	-	-	81.59	-	-	18.41	-	-
Deep	**^{1}H, ^{4}He, ^{16}O**	13.81	73.65	-	-	12.54	-	-	-
	^{7}Li, ^{12}C, ^{56}Fe	-	-	72.11	27.67	-	-	-	0.23
	^{12}C, ^{16}O, ^{20}Ne	-	-	-	86.84	10.99	2.17	-	-
	All ions	13.96	56.79	14.26	12.80	0.88	1.30	0.01	0.00

4.4 Results and discussion

4.4.1 Per-ion dose-volume contributions

The breakdown of the percentage contribution of each individual ion species to the overall dose-volume in the target region for three different target depths is shown in Tables 4.1 and 4.3 for the no hypoxia / OAR case, the hypoxia/no OAR case, and the hypoxia / OAR case respectively.

4.4.1.1 Hypoxic sub-volume within the tumour - no organ at risk present

For the case with a hypoxic tumour sub-volume and no OAR, there tends to be quite a large contribution from heavier ions compared with the other cases. Two or three-ion combinations show a relatively equal split between the different ions in the shallow and central tumour position, while at greater depths, helium or lithium tend to dominate where available. A notably large contribution from iron may be observed for the shallow tumour location for the lithium/carbon/iron plan.

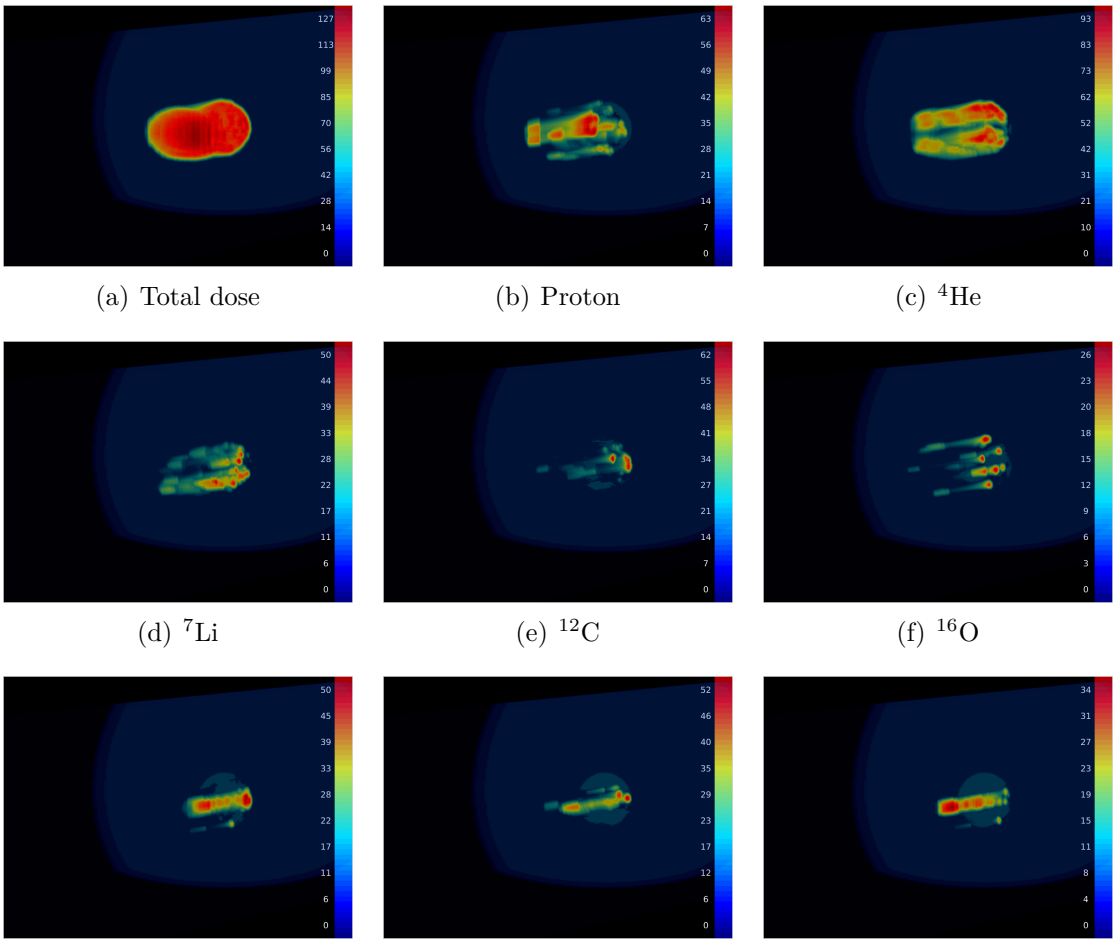

(a) Total dose (b) Proton (c) ^{4}He

(d) ^{7}Li (e) ^{12}C (f) ^{16}O

(g) ^{20}Ne (h) ^{28}Si (i) ^{56}Fe

Figure 4.4: 3D volumetric visualisations of total dose and contributions from each individual ion species, for an 8-ion treatment plan. The tumour is located at the 'shallow' position, a hypoxic region is located inside the tumour, no OAR is defined.

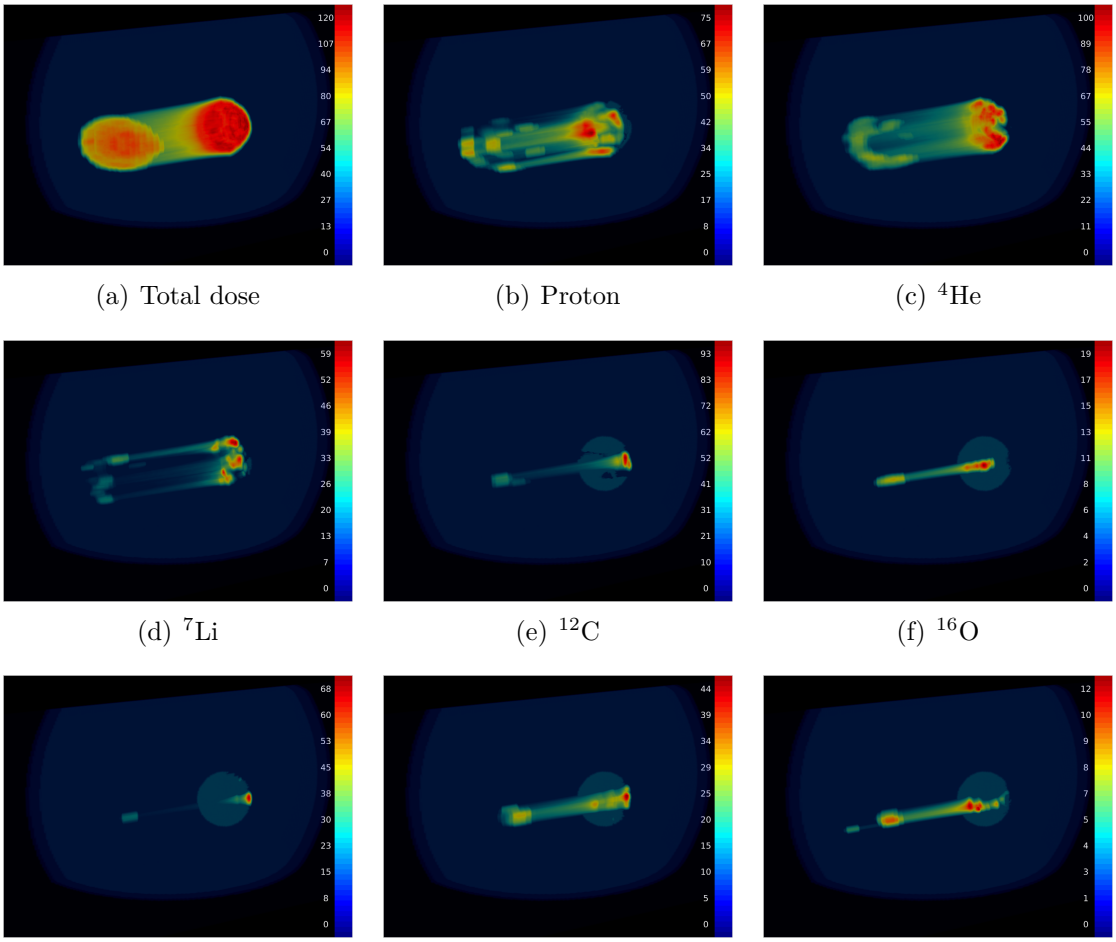

(a) Total dose (b) Proton (c) ^{4}He

(d) ^{7}Li (e) ^{12}C (f) ^{16}O

(g) ^{20}Ne (h) ^{28}Si (i) ^{56}Fe

Figure 4.5: 3D volumetric visualisations of total dose and contributions from each individual ion species, for an 8-ion treatment plan. The tumour is located at the 'central' position, a hypoxic region is located inside the tumour, no OAR is defined.

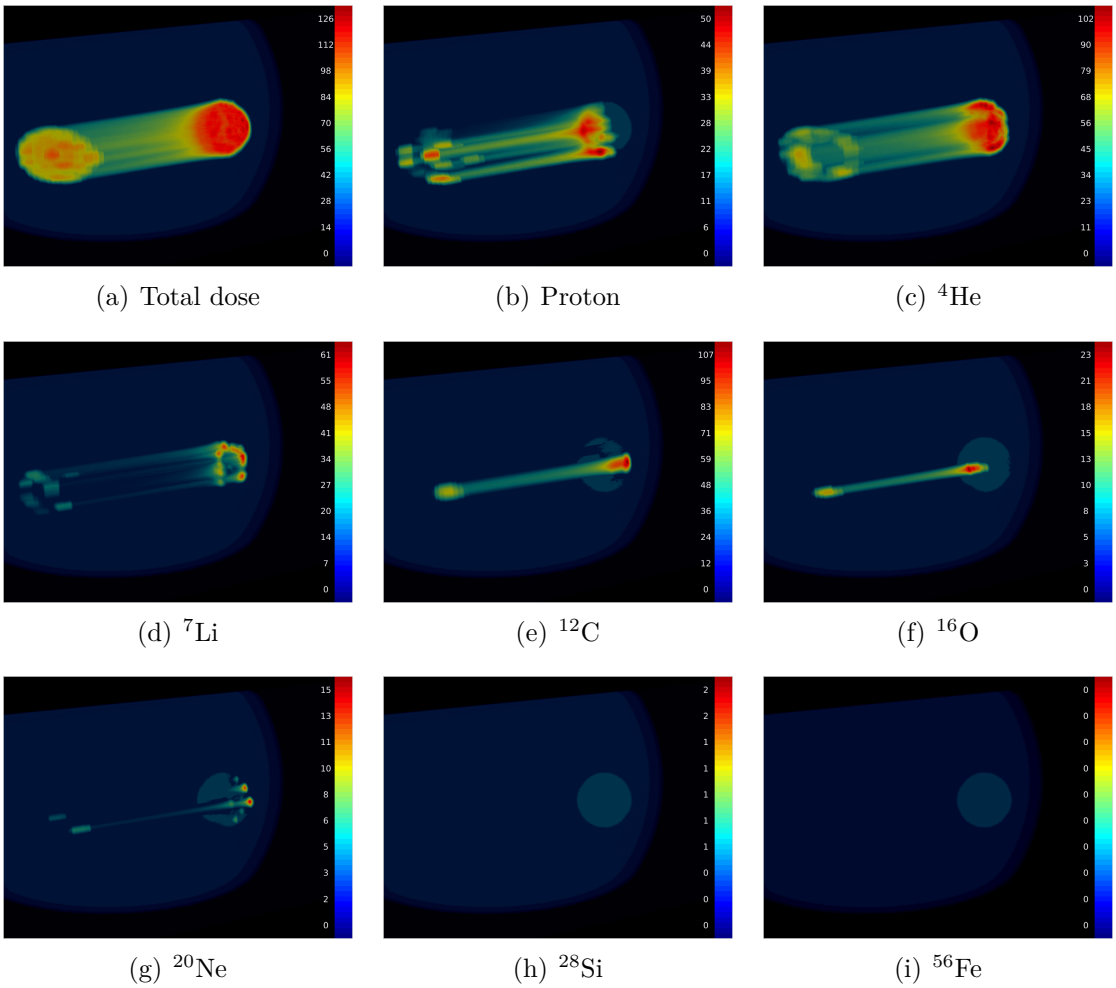

(a) Total dose (b) Proton (c) ^{4}He

(d) ^{7}Li (e) ^{12}C (f) ^{16}O

(g) ^{20}Ne (h) ^{28}Si (i) ^{56}Fe

Figure 4.6: 3D volumetric visualisations of total dose and contributions from each individual ion species, for an 8-ion treatment plan. The tumour is located at the 'deep' position, a hypoxic region is located inside the tumour, no OAR defined.

Table 4.2: The percentage contribution of individual ions in each multi-ion treatment plan. An OAR is located distal (and adjacent) to the tumour.

Tumour position	Ion combination	H%	He%	Li%	C%	O%	Ne%	Si%	Fe%
Shallow	^{1}H, ^{12}C	91.60	-	-	8.40	-	-	-	-
	^{4}He, ^{16}O	-	95.75	-	-	4.25	-	-	-
	^{7}Li,^{20}Ne	-	-	86.05	-	-	13.95	-	-
	^{1}H, ^{4}He, ^{16}O	56.28	39.89	-	-	3.83	-	-	-
	^{7}Li, ^{12}C, ^{56}Fe	-	-	63.76	0.00	-	-	-	36.24
	^{12}C, ^{16}O, ^{20}Ne	-	-	5.77	53.33	40.90	-	-	
	All ions	54.89	36.94	5.25	0.16	0.71	0.93	0.35	0.78
Central	^{1}H, ^{12}C	94.93	-	-	5.07	-	-	-	
	^{4}He, ^{16}O	-	100.00	-	-	0.00	-	-	-
	^{7}Li,^{20}Ne	-	-	99.67	-	-	0.33	-	-
	^{1}H, ^{4}He, ^{16}O	53.70	46.30	-	-	0.00	-	-	-
	^{7}Li, ^{12}C, ^{56}Fe	-	-	87.92	0.00	-	-	-	12.08
	^{12}C, ^{16}O, ^{20}Ne	-	-	-	33.08	58.23	8.70	-	-
	All ions	53.81	45.76	0.27	0.16	0.00	0.00	0.00	0.00
Deep	^{1}H, ^{12}C	95.57	-	-	4.43	-	-	-	-
	^{4}He, ^{16}O	-	100.00	-	-	0.00	-	-	-
	^{7}Li,^{20}Ne	-	-	100.00	-	-	0.00	-	-
	^{1}H, ^{4}He, ^{16}O	44.25	55.75	-	-	0.00	-	-	-
	^{7}Li, ^{12}C, ^{56}Fe	-	-	98.78	0.00	-	-	-	1.22
	^{12}C, ^{16}O, ^{20}Ne	-	-	-	54.36	40.38	5.26	-	-
	All ions	44.25	55.75	0.00	0.00	0.00	0.00	0.00	0.00

For the deepest tumour location with a hypoxic region (Figure 4.6), the dose remains dominated by helium ions; however, now there is a non-trivial contribution from protons, lithium, carbon and neon. As expected, the exclusion of light ions with low LET from the hypoxic region results in an increased contribution from carbon; consequently a 'hole' structure can be seen in the entrance through the skull in the total dose distribution (in front of the hypoxic region), since for a given depth, carbon ions deposit a lower entrance dose relative to the Bragg peak.

4.4.1.2 OAR region present distal (adjacent) to the tumour - no hypoxic sub-volume within the tumour

When an OAR is present, but no hypoxia, the 8-ion plan only uses protons and helium when the tumour is in the central and deep locations, while at the shallow location only minor contributions from ions heavier than helium are used. Again, the lightest available ion tends to dominate in most cases. Notably, the lithium/carbon/iron plan uses a significant proportion of iron in the shallow and central tumour locations, but very little in the deepest location.

The presence of a distal OAR with no hypoxic region (Figure 4.9) is also dominated by helium, with the majority of the remaining dose contributed by protons - especially

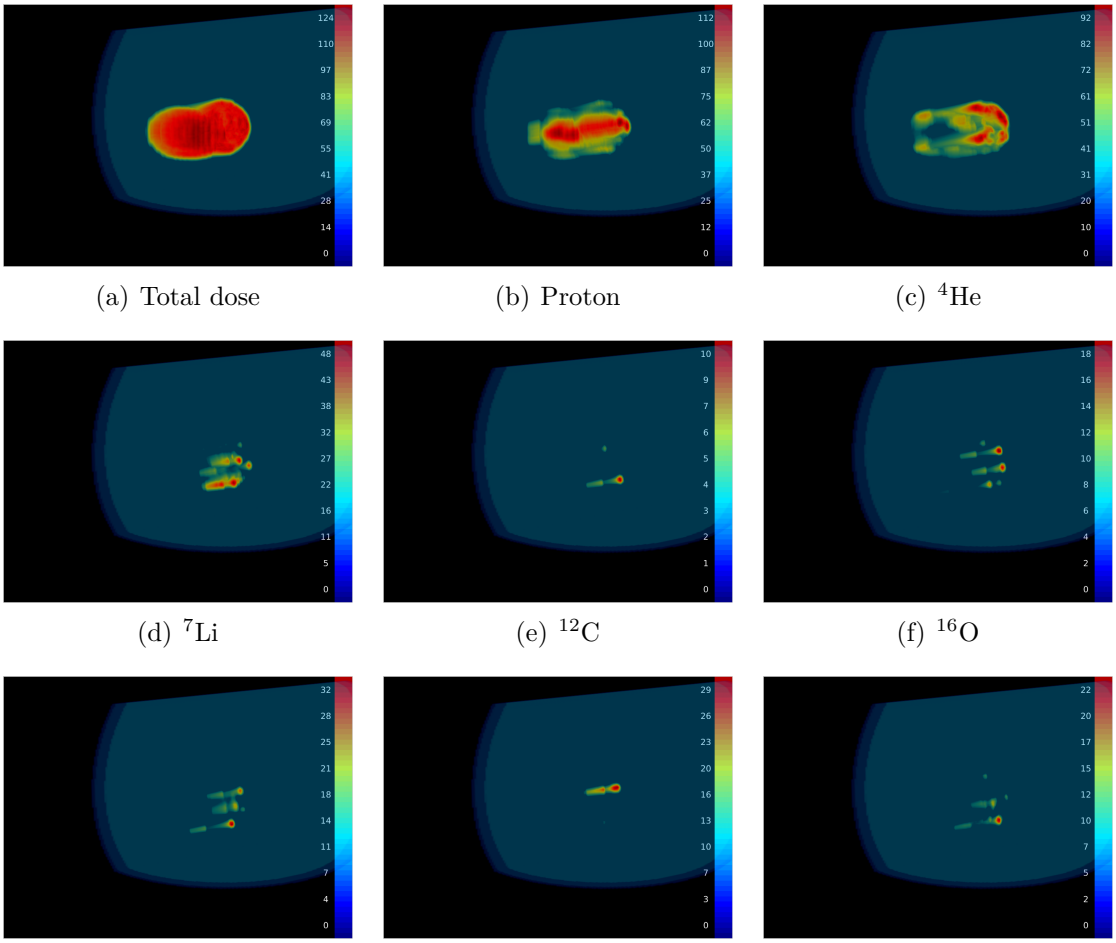

(a) Total dose (b) Proton (c) ^{4}He

(d) ^{7}Li (e) ^{12}C (f) ^{16}O

(g) ^{20}Ne (h) ^{28}Si (i) ^{56}Fe

Figure 4.7: 3D volumetric visualisations of total dose and contributions from each individual ion species, for an 8-ion treatment plan. The tumour is located at the 'shallow' position, no hypoxic regions are present, and an OAR is positioned distal to the tumour.

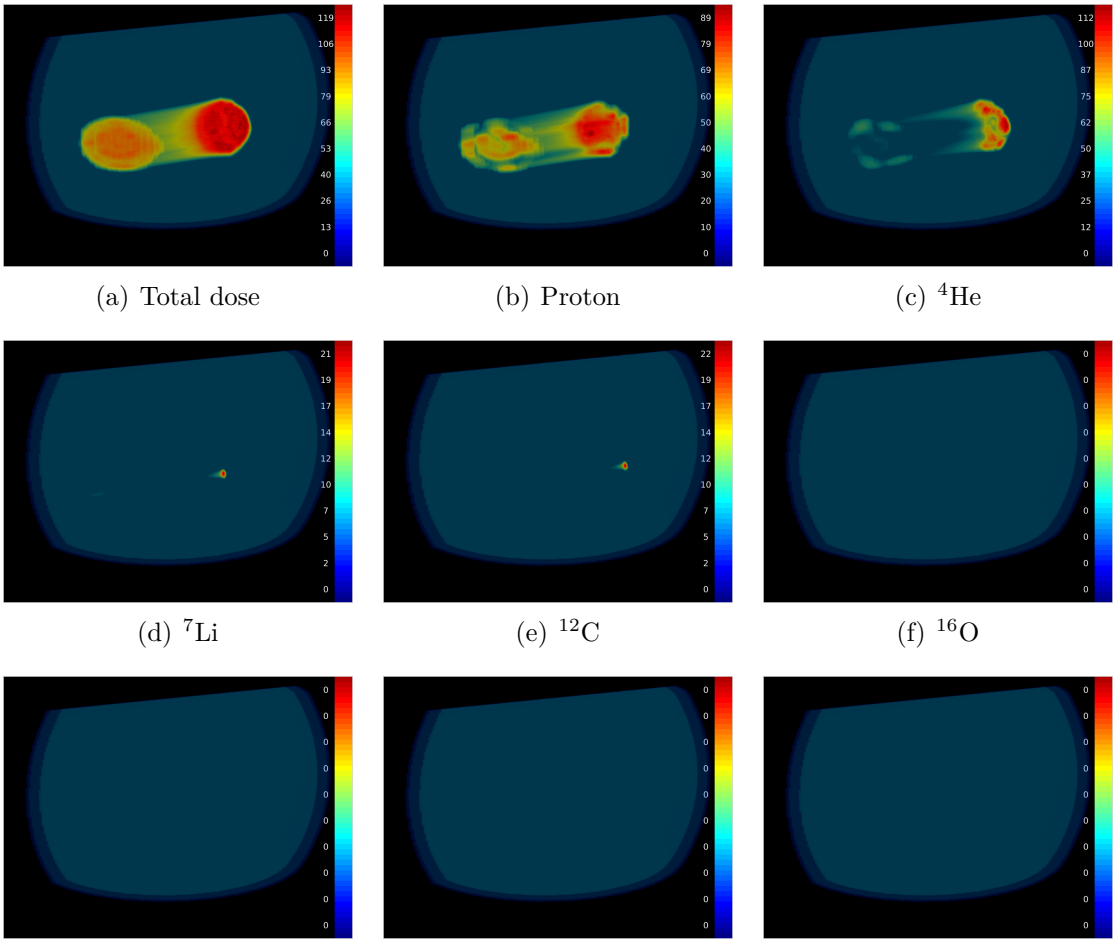

(a) Total dose (b) Proton (c) ^{4}He

(d) ^{7}Li (e) ^{12}C (f) ^{16}O

(g) ^{20}Ne (h) ^{28}Si (i) ^{56}Fe

Figure 4.8: 3D volumetric visualisations of total dose and contributions from each individual ion species, for an 8-ion treatment plan. The tumour is located at the 'central' position, no hypoxic regions are present, and an OAR is positioned distal to the tumour.

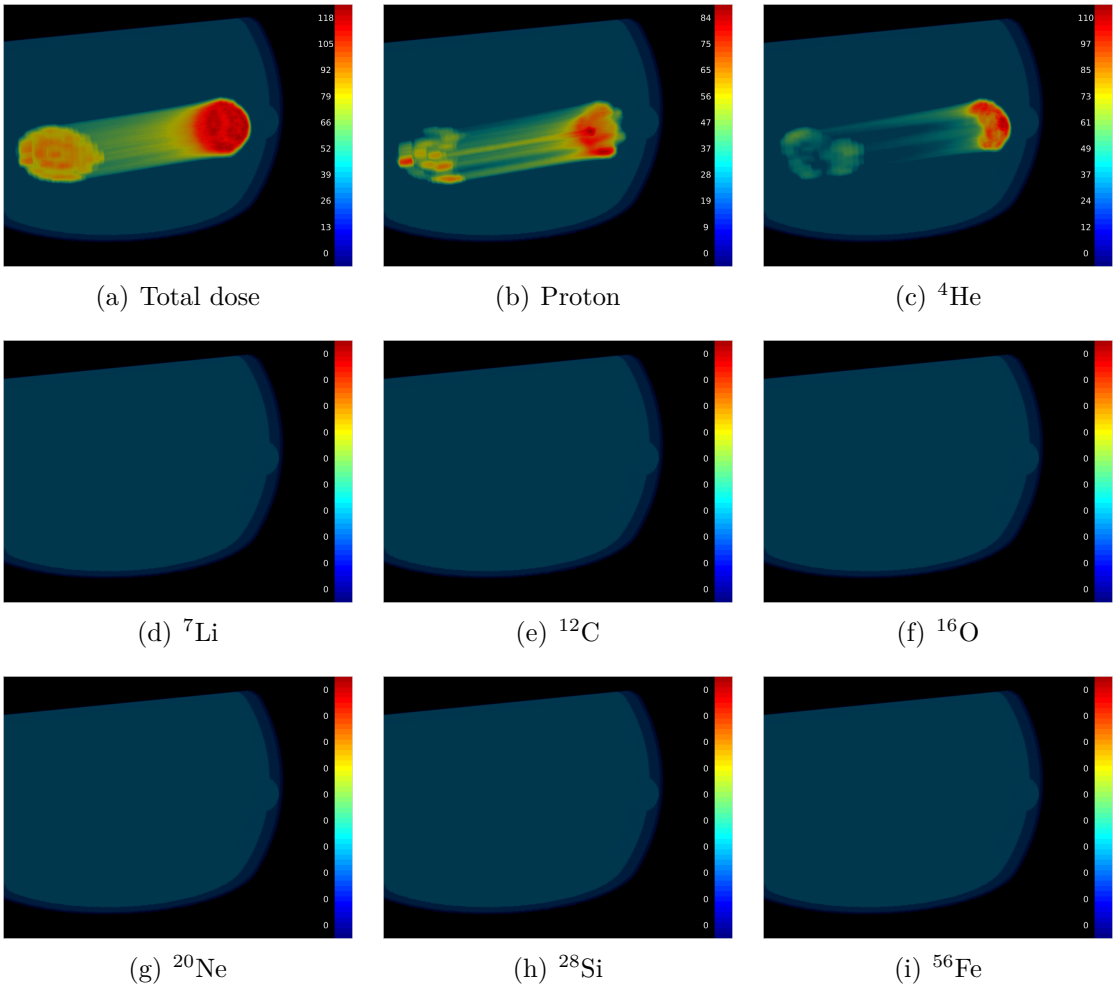

(a) Total dose (b) Proton (c) ^{4}He

(d) ^{7}Li (e) ^{12}C (f) ^{16}O

(g) ^{20}Ne (h) ^{28}Si (i) ^{56}Fe

Figure 4.9: 3D volumetric visualisations of total dose and contributions from each individual ion species, for an 8-ion treatment plan. The tumour is located at the 'deep' position, no hypoxic regions are present, and an OAR is positioned distal to the tumour.

Table 4.3: The percentage contribution of individual ions in each multi-ion treatment plan. A hypoxic region is located inside the tumour and an OAR is positioned distal to the tumour.

Tumour position	Ion combination	H%	He%	Li%	C%	O%	Ne%	Si%	Fe%
	^{1}H, ^{12}C	86.43	-	-	13.57	-	-	-	
	^{4}He, ^{16}O	-	86.34	-	-	13.66	-	-	-
	^{7}Li,^{20}Ne	-	-	76.26	-	-	23.74	-	-
Shallow	**^{1}H, ^{4}He, ^{16}O**	60.83	27.00	-	-	12.18	-	-	-
	^{7}Li, ^{12}C, ^{56}Fe	-	-	52.66	2.88	-	-	-	44.45
	^{12}C, ^{16}O, ^{20}Ne	-	-	-	5.79	53.07	41.15	-	-
	All ions	59.23	24.72	3.16	2.19	2.91	1.86	1.66	4.28
	^{1}H, ^{12}C	91.78	-	-	8.22	-	-	-	
	^{4}He, ^{16}O	-	92.56	-	-	7.44	-	-	-
	^{7}Li,^{20}Ne	-	-	-	-	7.10	-	-	
Central			92.90						
	^{1}H, ^{4}He, ^{16}O	63.69	29.92	-	-	6.39	-	-	-
	^{7}Li, ^{12}C, ^{56}Fe	-	-	80.70	5.62	-	-	-	13.68
	^{12}C, ^{16}O, ^{20}Ne	-	-	-	33.08	58.23	8.70	-	-
	All ions	63.57	29.60 0.26	3.78	2.75	0.00	0.02	0.02	
	^{1}H, ^{12}C	93.94	-	-	6.06	-	-	-	-
	^{4}He, ^{16}O	-	94.84	-	-	5.16	-	-	-
	^{7}Li,^{20}Ne	-	-	95.83	-	-	4.17	-	-
Deep	**^{1}H, ^{4}He, ^{16}O**	58.29	38.28	-	-	3.42	-	-	-
	^{7}Li, ^{12}C, ^{56}Fe	-	-	993.53	5.19	-	-	-	1.28
	^{12}C, ^{16}O, ^{20}Ne	-	-	-	54.36	40.38	5.26	-	-
	All ions	57.86	38.30	0.00	2.66	1.18	0.00	0.00	0.00

for the region of the tumour in front of the OAR. This is due to the need to avoid dose deposition by the fragmentation tail at the distal edge of the tumour, since proton irradiation dose not produce a fragmentation tail.

4.4.1.3 Hypoxic sub-volume within the tumour and OAR region present distal (adjacent) to the tumour

For the case with both a hypoxic subvolume and OAR, the 8-ion treatment plan for the shallow tumour is now dominated by the contribution from protons, with a major secondary contribution from helium, and small (but non-zero) contributions from the other ions. At progressively deeper tumour locations, the relative share of protons and helium changes slightly, and the contribution from other ions tends to decrease. In the proton/carbon plan, the relative proportion of dose-volume contribution from protons now increases with increasing depth (with protons strongly dominating). For the helium/oxygen plans, the proportion of helium also increases with tumour depth (very similarly to the increase in proton in the proton/carbon case). In the majority of ion combinations, there is a strong preference for the lightest available ion, regardless

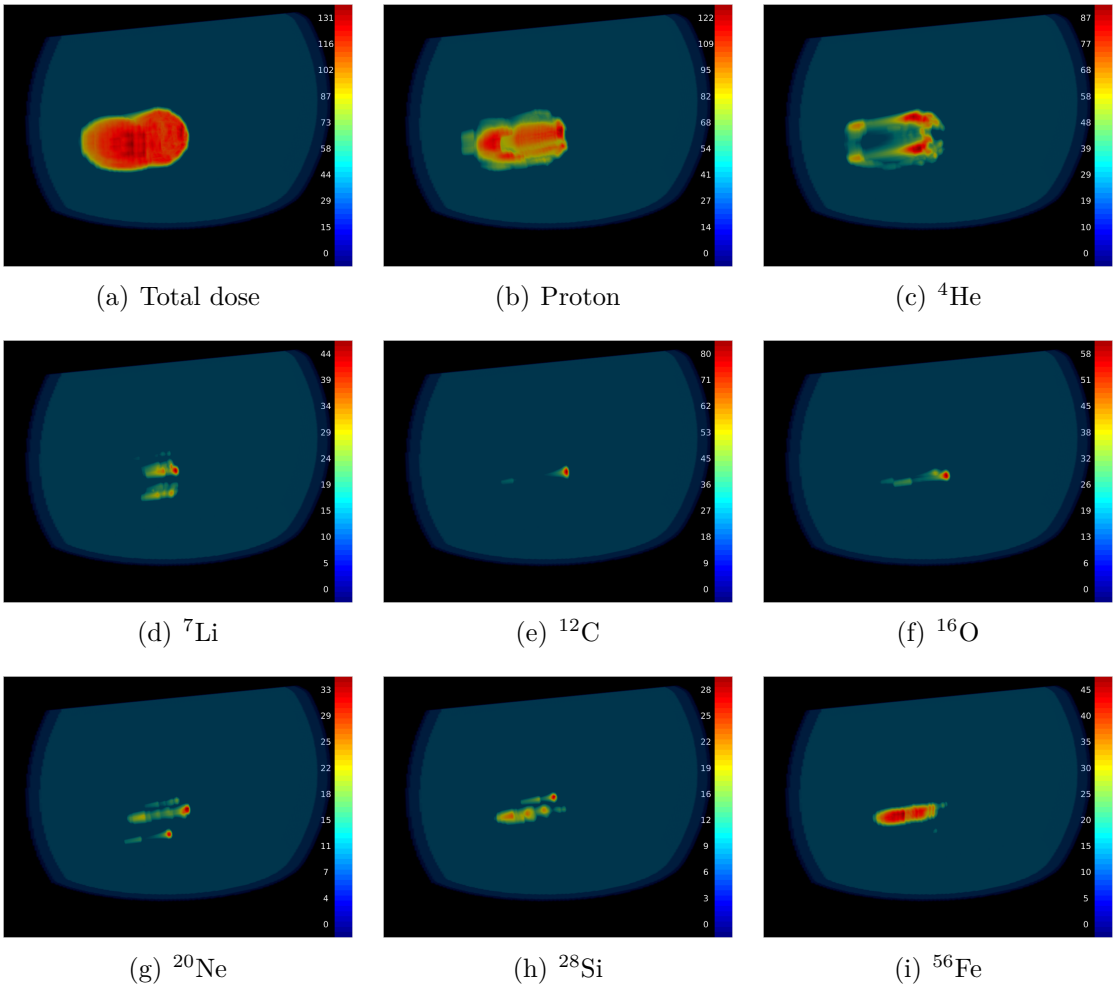

(a) Total dose (b) Proton (c) ^{4}He

(d) ^{7}Li (e) ^{12}C (f) ^{16}O

(g) ^{20}Ne (h) ^{28}Si (i) ^{56}Fe

Figure 4.10: 3D volumetric visualisations of total dose and contributions from each individual ion species, for an 8-ion treatment plan. The tumour is located at the 'shallow' position, a hypoxic region is located inside the tumour and an OAR is positioned distal to the tumour.

of whether that is protons, helium or lithium; the exception is the carbon/oxygen/neon plan, which is dominated by oxygen at the shallow and central tumour locations.

Figure 4.10-4.12 show both the total dose distributions and the dose contributions from each individual ion species for 8-ion treatment plans constructed for three tumour positions, with a hypoxic sub-volume defined inside the tumour and an OAR positioned distal and adjacent to the tumour.

When both a hypoxic region inside the tumour and an OAR distal to the tumour are present (Figure 4.10-4.12), similar divisions of dose contributions between ion species in the different cases are observed in the shallow and central cases; however, the

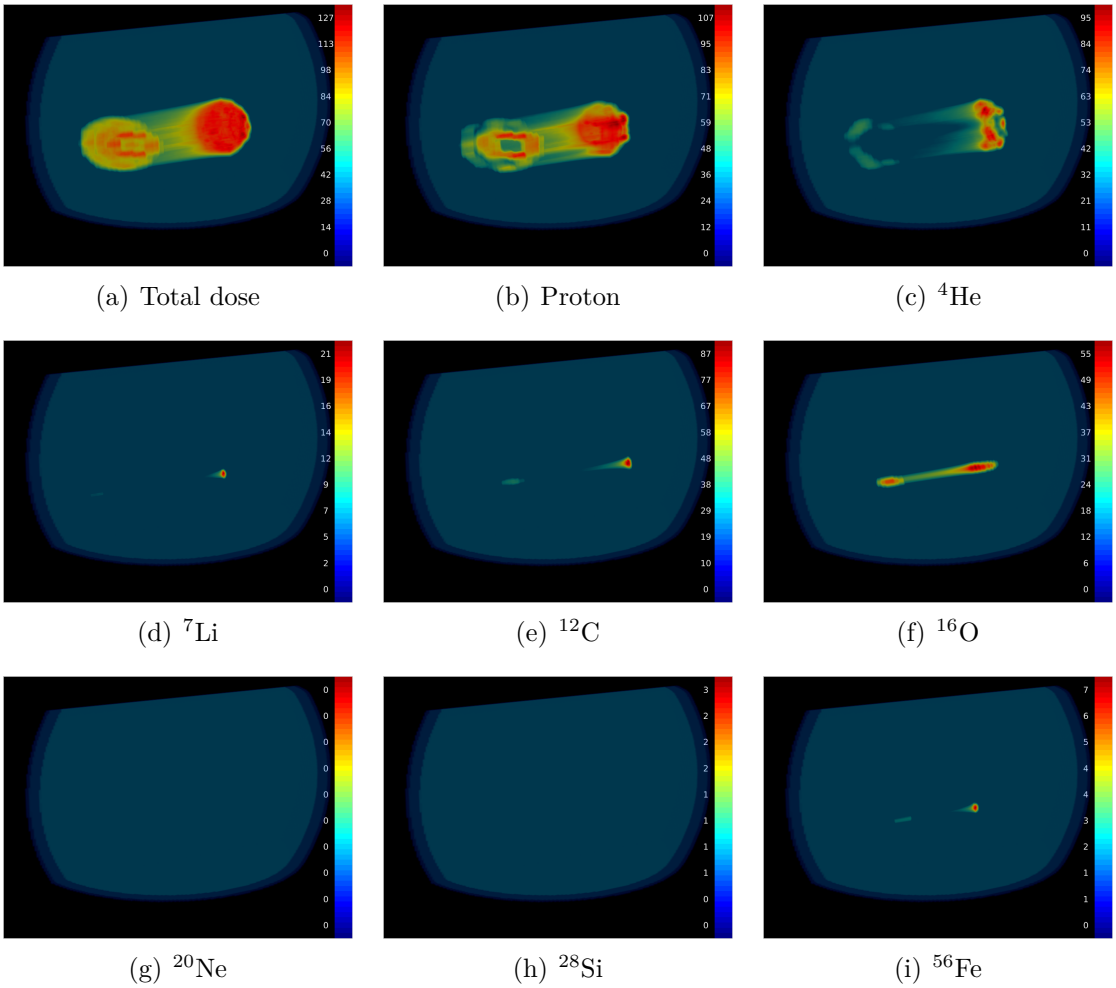

(a) Total dose (b) Proton (c) ^{4}He

(d) ^{7}Li (e) ^{12}C (f) ^{16}O

(g) ^{20}Ne (h) ^{28}Si (i) ^{56}Fe

Figure 4.11: 3D volumetric visualisations of total dose and contributions from each individual ion species, for an 8-ion treatment plan. The tumour is located at the 'central' position, a hypoxic region is located inside the tumour and an OAR is positioned distal to the tumour.

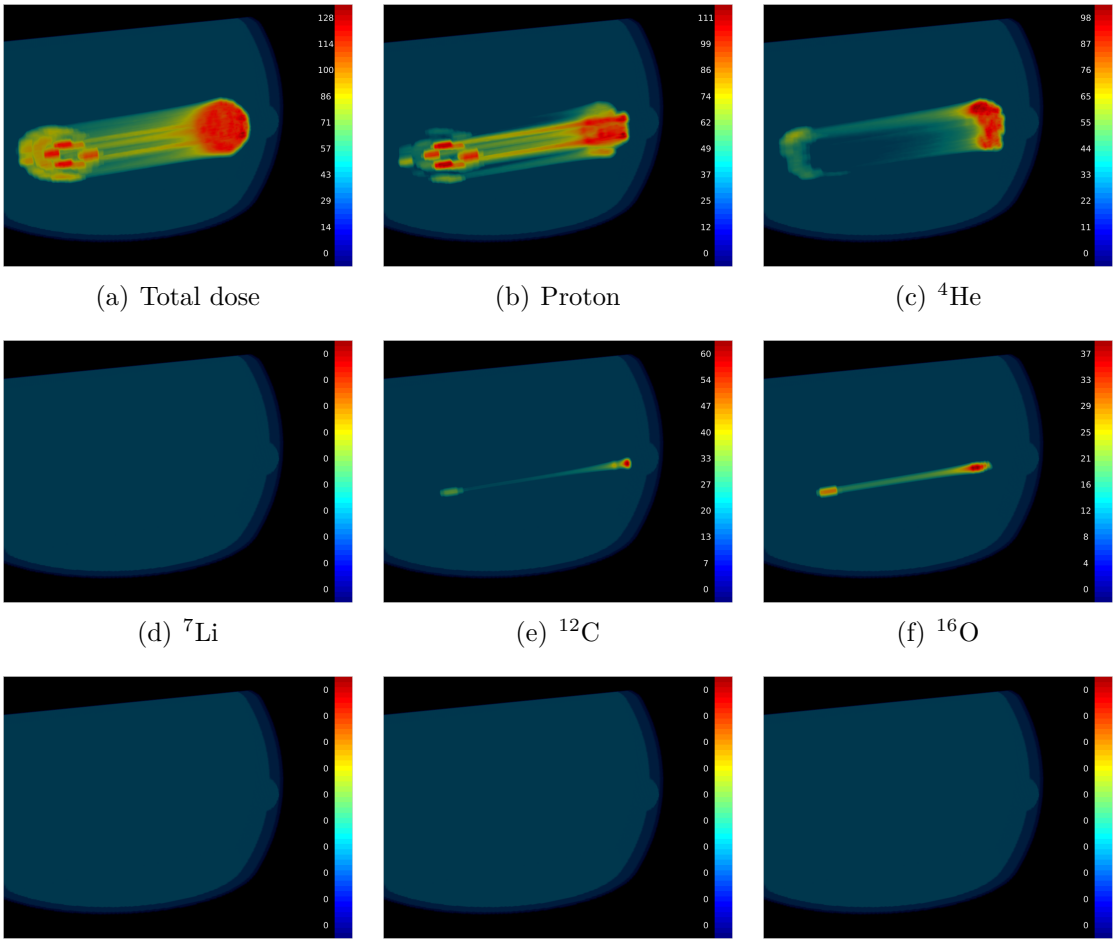

(a) Total dose (b) Proton (c) ^{4}He

(d) ^{7}Li (e) ^{12}C (f) ^{16}O

(g) ^{20}Ne (h) ^{28}Si (i) ^{56}Fe

Figure 4.12: 3D volumetric visualisations of total dose and contributions from each individual ion species, for an 8-ion treatment plan. The tumour is located at the 'deep' position, a hypoxic region is located inside the tumour and an OAR is positioned distal to the tumour.

Table 4.4: RMS error (Gy) for dose distributions within the target and the surrounding regions; hypoxic sub-volume within the tumour, no organs at risk.

Tumour position	Ion combination	Target	Distal boundary	Distal	Peripheral	Proximal
Shallow	^{1}H, ^{12}C	11.46	15.79	0.42	1.90	33.99
	^{4}He, ^{16}O	11.47	15.46	0.35	1.85	34.07
	^{7}Li, ^{20}Ne	11.73	15.87	0.55	1.86	34.37
	^{1}H, ^{4}He, ^{16}O	11.22	15.52	0.28	1.88	34.03
	^{7}Li, ^{12}C, ^{56}Fe	11.88	15.89	0.58	1.85	34.72
	^{12}C, ^{16}O, ^{20}Ne	11.62	15.95	0.77	1.85	34.28
	All ions	10.88	15.54	0.36	1.87	34.20
Central	^{1}H, ^{12}C	11.41	16.81	1.00	2.42	44.69
	^{4}He, ^{16}O	11.55	16.37	0.55	2.21	44.83
	^{7}Li, ^{20}Ne	11.41	17.36	1.09	2.22	45.76
	^{1}H, ^{4}He, ^{16}O	11.37	16.31	0.46	2.32	44.60
	^{7}Li, ^{12}C, ^{56}Fe	11.37	17.24	1.17	2.22	45.75
	^{12}C, ^{16}O, ^{20}Ne	11.65	17.96	1.79	2.15	45.31
	All ions	11.14	16.34	0.65	2.32	44.89
Deep	^{1}H, ^{12}C	11.62	17.61	1.51	2.86	52.03
	^{4}He, ^{16}O	11.72	16.87	0.72	2.48	52.00
	^{7}Li, ^{20}Ne	11.68	18.16	1.54	2.51	53.60
	^{1}H, ^{4}He, ^{16}O	11.65	16.83	0.65	2.58	51.89
	^{7}Li, ^{12}C, ^{56}Fe	11.45	17.96	1.60	2.51	53.57
	^{12}C, ^{16}O, ^{20}Ne	11.70	19.18	2.51	2.37	52.93
	All ions	11.37	16.76	0.82	2.58	52.20

shallowest cases do demonstrate a greater contribution of the heavier ions - including silicon (and a very small amount of iron) in the shallowest case compared to the deepest tumour location.

In the deepest tumour location, the majority of the dose is now delivered by protons, with a slightly smaller contribution from helium and much smaller contributions from other ions, although carbon is again needed to deliver dose to the hypoxic region. When the OAR and hypoxic region are aligned (as they are in our simulation scenario), the exclusion of low-Z ions beyond the first detected hypoxic voxels is performed prior to the optimisation, and so minimisation of dose to the distal OAR necessarily results in some compromise to the dose delivered to the distal edge of the target (since only high-Z ions are available at this point).

4.4.2 Dose uniformity

4.4.2.1 Hypoxic sub-volume within the tumour - no organs at risk present

Since the impact of a hypoxic subvolume on single-ion cases would be to either completely prevent any dose deposition in the hypoxic volume (low-Z ions) or to have

no impact whatsoever (for the high-Z ions), these plans are not evaluated in any results where the hypoxic volume is defined.

For the case with a hypoxic volume and no OAR (Table 4.4), the 8-ion plan again produces the lowest target and distal boundary RMSE for all tumour positions, and no plan produces consistently lower RMSE in the other defined regions.

4.4.2.2 OAR region present distal (adjacent) to the tumour - no hypoxic sub-volume within the tumour

In the absence of hypoxic regions, but with a distal OAR present (Table 4.5), the 8-ion plan again performs well in terms of tumour RMSE - however, in the central and deep tumour locations, it is outperformed by the three-ion combination of proton, helium and oxygen. In the distal boundary region, several single-ion plans perform better than the 8-ion plans (in particular, carbon, oxygen and neon perform well for the shallow and central positions). In the OAR region, proton-only plans perform the best - however, several light-heavy ion combinations also perform well (notably proton/carbon, helium/oxygen and proton/helium/oxygen).

4.4.2.3 Hypoxic sub-volume within the tumour and OAR region present distal (adjacent) to the tumour

Finally, when both hypoxic and OAR regions are defined (Table 4.6), the 8-ion plan also achieves the best target dose conformance in all tumour positions, and is highly competitive with proton-only OAR RMSE.

4.4.3 Dose coverage

All treatment plans achieved excellent coverage of the tumour. For the hypoxia, no-oar case, the 8-ion plan provided the best D_{90} coverage except for the deepest case, where it was outperformed by several 2-ion and 3-ion combinations (in particular lithium/carbon/iron).

With the presence of an OAR (both with and without a hypoxic region), the best D_{50} coverage was again achieved by the 8-ion plans; the 8-ion plans were also able to provide the best D_{90} in most cases (especially for the case where both hypoxic and OAR regions were defined).

Dose isosurfaces at 50% (Figures 4.13-4.17) and 90% (Figures 4.14-4.18) of nominal target dose demonstrate excellent dose conformance in the target in all cases. The

Table 4.5: RMS error (Gy) for dose distributions within the target and the surrounding regions; no hypoxic sub-volume within the tumour, OAR region distal (adjacent) to tumour

Tumour position	Ion combination	Target	Distal boundary	Distal	Peripheral	Proximal	OAR
	^{1}**H**	11.46	18.34	0.01	1.92	33.68	0.19
	^{4}**He**	11.85	17.59	0.14	1.84	33.89	0.73
	^{7}**Li**	12.73	17.39	0.32	1.85	34.05	2.19
	^{12}**C**	14.28	17.20	0.74	1.79	32.94	3.54
	^{16}**O**	13.93	17.32	0.53	1.82	33.29	2.97
	^{20}**Ne**	14.14	17.37	0.55	1.82	33.31	3.09
	^{28}**Si**	15.10	17.72	0.53	1.83	33.88	3.01
Shallow	^{56}**Fe**	14.81	17.82	0.44	1.83	34.70	2.75
	^{1}**H,** ^{12}**C**	11.39	18.12	0.08	1.91	33.73	0.29
	^{4}**He,** ^{16}**O**	11.70	17.53	0.16	1.84	33.90	0.79
	^{7}**Li,** ^{20}**Ne**	12.42	17.40	0.36	1.85	34.04	2.21
	^{1}**H,** ^{4}**He,** ^{16}**O**	11.13	17.68	0.08	1.88	33.81	0.37
	^{7}**Li,** ^{12}**C,** ^{56}**Fe**	12.57	17.76	0.39	1.84	34.41	2.10
	^{12}**C,** ^{16}**O,** ^{20}**Ne**	13.41	17.32	0.55	1.82	33.38	2.93
	All,ions	11.10	17.64	0.09	1.88	33.85	0.39
	^{1}**H**	12.27	19.69	0.04	2.45	43.70	0.47
	^{4}**He**	11.61	18.11	0.28	2.19	44.18	1.18
	^{7}**Li**	14.36	17.94	0.67	2.16	43.79	3.72
	^{12}**C**	20.57	17.56	1.43	1.99	39.72	5.53
	^{16}**O**	22.85	17.50	1.16	2.03	40.72	5.12
	^{20}**Ne**	23.43	17.65	1.32	2.03	40.33	5.50
	^{28}**Si**	27.81	18.45	1.40	2.04	41.18	5.34
Central	^{56}**Fe**	26.81	19.11	1.39	2.12	43.31	5.14
	^{1}**H,** ^{12}**C**	12.09	19.51	0.10	2.44	43.77	0.54
	^{4}**He,** ^{16}**O**	11.61	18.11	0.28	2.19	44.18	1.18
	^{7}**Li,** ^{20}**Ne**	14.36	17.92	0.67	2.15	43.79	3.72
	^{1}**H,** ^{4}**He,** ^{16}**O**	11.45	18.37	0.13	2.37	44.12	0.59
	^{7}**Li,** ^{12}**C,** ^{56}**Fe**	14.26	18.47	0.82	2.16	44.10	3.67
	^{12}**C,** ^{16}**O,** ^{20}**Ne**	19.93	17.76	1.26	2.05	40.88	5.16
	All ions	11.44	18.36	0.14	2.37	44.12	0.60
	^{1}**H**	13.21	20.88	0.06	2.98	50.26	0.53
	^{4}**He**	11.94	18.40	0.28	2.47	50.80	1.48
	^{7}**Li**	17.15	17.77	0.87	2.40	49.50	4.69
	^{12}**C**	27.39	17.25	1.59	2.13	42.75	6.79
	^{16}**O**	31.87	17.71	1.51	2.24	44.04	6.46
	^{20}**Ne**	33.40	17.88	1.71	2.20	42.53	6.73
	^{28}**Si**	39.48	19.72	1.96	2.25	43.66	6.65
Deep	^{56}**Fe**	39.55	21.47	2.23	2.35	45.84	6.51
	^{1}**H,** ^{12}**C**	13.07	20.62	0.13	2.97	50.36	0.63
	^{4}**He,** ^{16}**O**	11.94	18.40	0.28	2.47	50.80	1.48
	^{7}**Li,** ^{20}**Ne**	17.15	17.77	0.87	2.40	49.50	4.69
	^{1}**H,** ^{4}**He,** ^{16}**O**	11.88	18.92	0.16	2.73	51.05	0.88
	^{7}**Li,** ^{12}**C,** ^{56}**Fe**	17.13	17.89	0.92	2.41	49.57	4.68
	^{12}**C,** ^{16}**O,** ^{20}**Ne**	26.77	17.82	1.55	2.20	44.18	6.56
	All ions	11.88	18.92	0.16	2.73	51.05	0.88

Table 4.6: RMS error (Gy) for dose distributions within the target and the surrounding regions; hypoxic sub-volume within the target; OAR region distal (adjacent) to the tumour

Tumour position	Ion combination	Target	Distal boundary	Distal	Peripheral	Proximal	OAR
	^{1}H, ^{12}C	11.81	18.21	0.11	1.91	33.74	0.73
	^{4}He, ^{16}O	12.22	17.53	0.16	1.86	40.08	1.14
	^{7}Li, ^{20}Ne	12.89	17.48	0.32	1.87	40.24	2.35
Shallow	**^{1}H, ^{4}He, ^{16}O**	11.58	17.88	0.09	1.91	40.01	0.72
	^{7}Li, ^{12}C, ^{56}Fe	12.89	17.83	0.35	1.87	40.79	2.19
	^{12}C, ^{16}O, ^{20}Ne	13.40	17.33	0.48	1.84	39.50	2.93
	All ions	11.48	17.82	0.10	1.92	40.10	0.73
	^{1}H, ^{12}C	12.54	19.64	0.16	2.43	43.77	1.02
	^{4}He, ^{16}O	12.93	18.30	0.34	2.17	43.92	1.78
	^{7}Li, ^{20}Ne	15.96	17.97	0.70	2.15	43.61	3.91
Central	**^{1}H, ^{4}He, ^{16}O**	12.35	18.86	0.16	2.38	43.96	1.12
	^{7}Li, ^{12}C, ^{56}Fe	15.31	18.54	0.85	2.15	43.97	3.86
	^{12}C, ^{16}O, ^{20}Ne	19.93	17.76	1.26	2.05	40.88	5.16
	All ions	12.12	18.82	0.18	2.38	44.00	1.08
	^{1}H, ^{12}C	13.52	20.69	0.12	2.95	50.43	0.95
	^{4}He, ^{16}O	13.88	18.81	0.31	2.42	50.58	2.07
	^{7}Li, ^{20}Ne	19.61	17.91	0.88	2.36	49.26	4.83
Deep	**^{1}H, ^{4}He, ^{16}O**	13.04	19.57	0.16	2.73	50.89	1.12
	^{7}Li, ^{12}C, ^{56}Fe	18.66	17.94	0.93	2.39	49.32	4.86
	^{12}C, ^{16}O, ^{20}Ne	26.77	17.82	1.55	2.20	44.18	6.56
	All ions	12.76	19.43	0.16	2.74	50.89	1.14

Table 4.7: Percentages of the target volume that received at least 50%, and 90% of the dose volume; hypoxic sub-volume within the tumour, no organs at risk.

Tumour position	Ion combination	D_{50}	D_{90}
	^{1}H, ^{12}C	99.38	87.68
	^{4}He, ^{16}O	99.45	87.75
	^{7}Li, ^{20}Ne	99.26	87.58
Shallow	**^{1}H, ^{4}He, ^{16}O**	99.52	87.93
	^{7}Li, ^{12}C, ^{56}Fe	99.07	87.55
	^{12}C, ^{16}O, ^{20}Ne	99.34	87.64
	All ions	99.69	88.15
	^{1}H, ^{12}C	99.46	86.84
	^{4}He, ^{16}O	99.44	87.27
	^{7}Li, ^{20}Ne	99.56	87.13
Central	**^{1}H, ^{4}He, ^{16}O**	99.50	87.21
	^{7}Li, ^{12}C, ^{56}Fe	99.53	87.18
	^{12}C, ^{16}O, ^{20}Ne	99.39	87.18
	All ions	99.63	87.40
	^{1}H, ^{12}C	99.44	86.00
	^{4}He, ^{16}O	99.48	86.70
	^{7}Li, ^{20}Ne	99.40	86.60
Deep	**^{1}H, ^{4}He, ^{16}O**	99.50	86.71
	^{7}Li, ^{12}C, ^{56}Fe	99.51	86.68
	^{12}C, ^{16}O, ^{20}Ne	99.48	86.49
	All ions	99.58	86.85

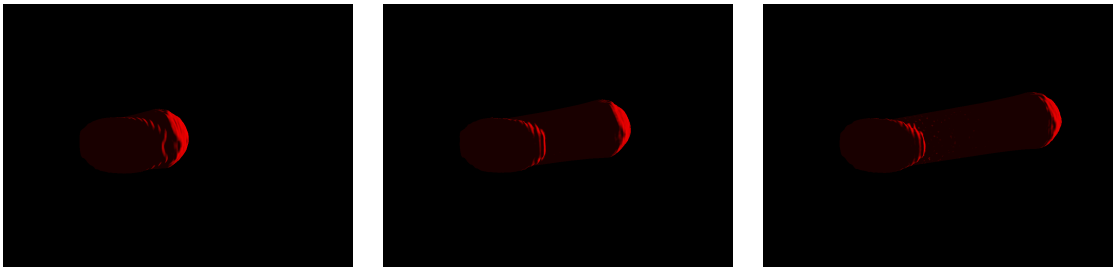

(a) Shallow, hypoxia (b) Centre, hypoxia (c) Deep, hypoxia

Figure 4.13: 50% isodose surfaces for an 8-ion treatment plan for 3 tumour positions; hypoxic region inside the tumour, no OAR defined.

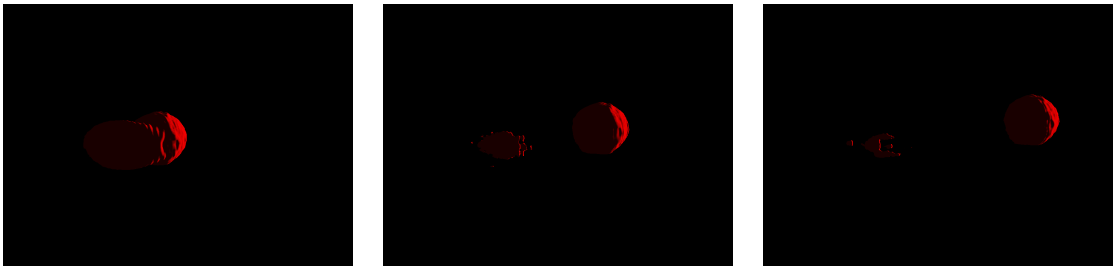

(a) Shallow, hypoxia (b) Centre, hypoxia (c) Deep, hypoxia

Figure 4.14: 90% isodose surfaces for 3 tumour positions, hypoxic region inside the tumour, no OAR defined.

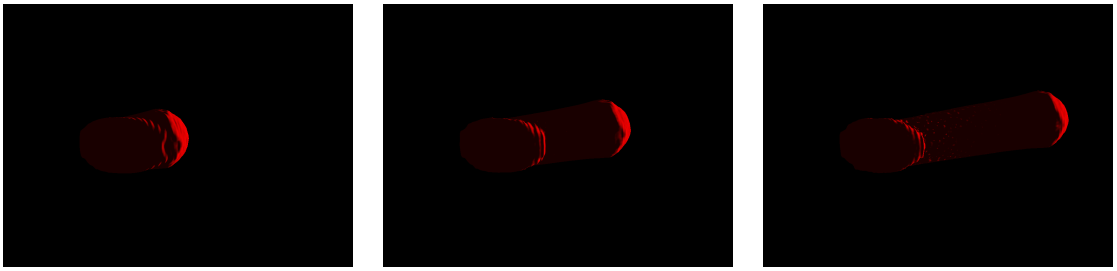

(a) Shallow, OAR (b) Centre, OAR (c) Deep, OAR

Figure 4.15: 50% isodose surfaces for an 8-ion treatment plan for 3 tumour positions; no hypoxic regions are present, OAR is distal to the tumour.

Table 4.8: Percentages of the target volume that received at least 50%, and 90% of the dose volume; no hypoxic sub-volume within the tumour, OAR region distal (adjacent) to tumour.

Tumour position	Ion combination	D_{50}	D_{90}
Shallow	^{1}**H**	99.51	87.13
	^{4}**He**	99.17	87.28
	^{7}**Li**	98.71	84.77
	^{12}**C**	98.16	78.57
	^{16}**O**	98.18	81.64
	^{20}**Ne**	98.28	80.13
	^{28}**Si**	97.50	80.89
	^{56}**Fe**	98.01	81.39
	^{1}**H,** ^{12}**C**	99.55	87.33
	^{4}**He,** ^{16}**O**	99.29	87.29
	^{7}**Li,** ^{20}**Ne**	98.93	84.89
	^{1}**H,** ^{4}**He,** ^{16}**O**	99.62	87.66
	^{7}**Li,** ^{12}**C,** ^{56}**Fe**	98.81	85.13
	^{12}**C,** ^{16}**O,** ^{20}**Ne**	98.52	81.97
	All ions	99.63	87.71
Central	^{1}**H**	99.17	85.34
	^{4}**He**	99.42	87.10
	^{7}**Li**	98.28	76.49
	^{12}**C**	96.62	44.14
	^{16}**O**	93.67	55.42
	^{20}**Ne**	93.87	45.95
	^{28}**Si**	90.29	49.50
	^{56}**Fe**	91.55	50.92
	^{1}**H,** ^{12}**C**	99.39	85.57
	^{4}**He,** ^{16}**O**	99.42	87.10
	^{7}**Li,** ^{20}**Ne**	98.28	76.51
	^{1}**H,** ^{4}**He,** ^{16}**O**	99.51	86.76
	^{7}**Li,** ^{12}**C,** ^{56}**Fe**	98.33	76.91
	^{12}**C,** ^{16}**O,** ^{20}**Ne**	96.70	55.25
	All ions	99.51	86.75
Deep	^{1}**H**	98.79	83.68
	^{4}**He**	99.38	86.31
	^{7}**Li**	97.20	63.95
	^{12}**C**	94.39	21.56
	^{16}**O**	87.38	26.18
	^{20}**Ne**	86.56	21.46
	^{28}**Si**	79.45	19.57
	^{56}**Fe**	80.19	21.49
	^{1}**H,** ^{12}**C**	98.91	83.83
	^{4}**He,** ^{16}**O**	99.38	86.31
	^{7}**Li,** ^{20}**Ne**	97.20	63.95
	^{1}**H,** ^{4}**He,** ^{16}**O**	99.43	85.87
	^{7}**Li,** ^{12}**C,** ^{56}**Fe**	97.20	64.06
	^{12}**C,** ^{16}**O,** ^{20}**Ne**	94.17	25.48
	All ions	99.43	85.87

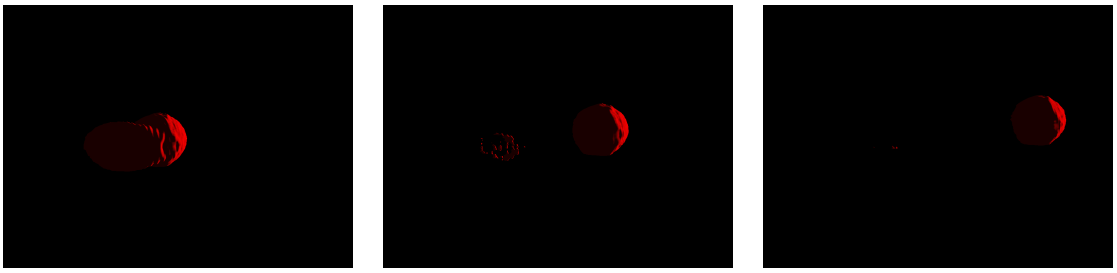

(a) Shallow, OAR (b) Centre, OAR (c) Deep, OAR

Figure 4.16: 90% isodose surfaces for an 8-ion treatment plan for 3 tumour positions; no hypoxic regions are present, OAR is distal to the tumour.

Table 4.9: Percentages of the target volume that received at least 50%, and 90% of the dose volume; hypoxic sub-volume within the target; OAR region distal (adjacent)to the tumour.

Tumour position	**Ion combination**	**D_{50}**	**D_{90}**
Shallow	**^{1}H, ^{12}C**	99.36	87.05
	^{4}He, ^{16}O	99.00	86.74
	^{7}Li, ^{20}Ne	98.64	83.80
	^{1}H, ^{4}He, ^{16}O	99.39	87.26
	^{7}Li, ^{12}C, ^{56}Fe	98.64	84.46
	^{12}C, ^{16}O, ^{20}Ne	98.52	82.02
	All ions	99.49	87.42
Central	**^{1}H, ^{12}C**	99.07	84.27
	^{4}He, ^{16}O	99.10	83.25
	^{7}Li, ^{20}Ne	97.84	71.44
	^{1}H, ^{4}He, ^{16}O	99.25	84.47
	^{7}Li, ^{12}C, ^{56}Fe	98.25	71.59
	^{12}C, ^{16}O, ^{20}Ne	96.70	55.25
	All ions	99.32	84.81
Deep	**^{1}H, ^{4}C**	98.73	82.72
	^{4}He, ^{16}O	98.88	79.97
	^{7}Li, ^{20}Ne	96.17	57.43
	^{1}H, ^{4}He, ^{16}O	99.02	83.06
	^{7}Li, ^{16}C, ^{56}Fe	97.00	57.07
	^{12}C, ^{16}O, ^{20}Ne	94.17	25.48
	Al ions	99.12	83.51

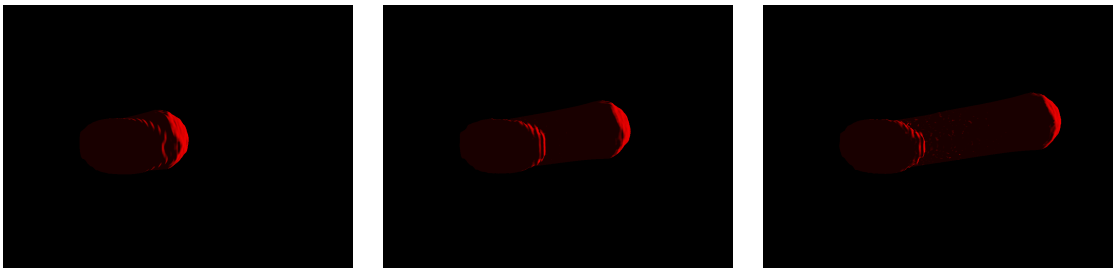

(a) Shallow, hypoxia + OAR (b) Centre, hypoxia + OAR (c) Deep, hypoxia + OAR

Figure 4.17: 50% isodose surfaces for an 8-ion treatment plan for 3 tumour positions; hypoxic region inside the tumour and OAR distal to the tumour.

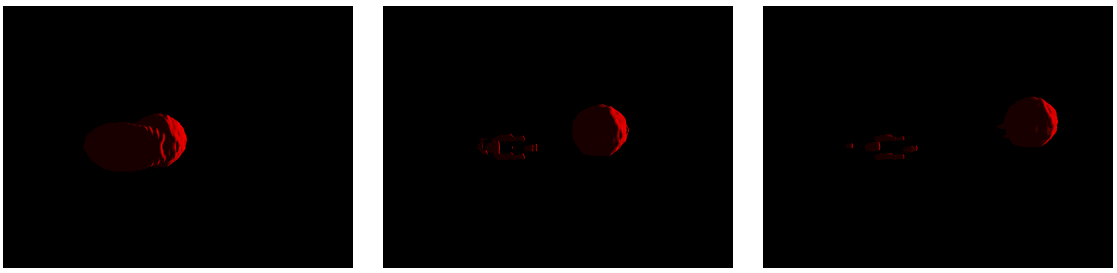

(a) Shallow, hypoxia + OAR (b) Centre, hypoxia + OAR (c) Deep, hypoxia + OAR

Figure 4.18: 90% isodose surfaces for for an 8-ion treatment plan 3 tumour positions; hypoxic region inside the tumour and OAR distal to the tumour.

Table 4.10: Total volumes outside the tumour which received at least 5%, 10% and 50% of the target dose volume in mm^3; hypoxic sub-volume defined within the tumour, no organs at risk. Planning target volume (PTV) is 14000 mm^3.

Tumour position	Ion combination	V_5 mm^3	V_{10} mm^3	V_{50} mm^3
	^{1}H,^{12}C	30589	27140	15905
	^{4}He,^{16}O	30075	26660	15791
	^{7}Li,^{20}Ne	30950	26805	15924
Shallow	^{1}H,^{4}He,^{16}O	30309	26883	15839
	^{7}Li,^{12}C,^{56}Fe	30750	26790	15995
	^{12}C,^{16}O,^{20}Ne	31425	26726	15903
	All ions	30347	26837	15858
	^{1}H,^{12}C	74188	65421	40127
	^{4}He,^{16}O	70767	63094	39049
Shallow	^{7}Li,^{20}Ne	74384	63849	39714
	^{1}H,^{4}He,^{16}O	72065	64383	39694
	^{7}Li,^{12}C,^{56}Fe	74389	63670	39740
	^{12}C,^{16}O,^{20}Ne	77583	63744	39255
	All ions	72310	64367	39799.00
	^{1}H,^{12}C	117478	99899	59235
	^{4}He,^{16}O	107053	95248	57637
Shallow	^{7}Li,^{20}Ne	113884	97061	59708
	^{1}H,^{4}He,^{16}O	108360	96486	57905
	^{7}Li,^{12}C,^{56}Fe	114193.	96605	59680
	^{12}C,^{16}O,^{20}Ne	118919	98125	58536
	All ions	108699	96455	58634

50% isodose surface shows the extent of the entrance dose distribution, while the 90% surface shows that peak dose is largely concentrated in the target and some parts of the entrance bone tissue (moreso for the shallowest tumour position, where the entrance dose gradient is steeper compared to the other tumour positions).

4.4.4 Normal tissue dose

Table 4.10-4.12 present the volumes of normal tissue (outside of the planning target volume) which receive at least 5%, 10% and 50% of the target dose for each of the three tumour positions (V_5, V_{10} and V_{50}) and with the four combinations of with/without a hypoxic region and with/without OAR. The PTV is a total of 14000 mm^3.

The results for V_5, V_{10} and V_{50} are very similar across all the different ion combinations, neither showing a significant advantage nor disadvantage for the manifold multi-ion treatment plans. One notable observation is that the rarely-used ^{4}He single-ion therapy consistently performs better than the others; this is likely due to its favourable combination of reduced entrance dose compared to protons, minimal fragmentation tail and moderate lateral scattering (relative to protons).

Table 4.11: Total volumes outside the tumour which received at least 5%, 10% and 50% of the target dose volume in mm^3; no hypoxic sub-volume within the tumour, OAR region defined distal (adjacent) to the tumour. Planning target volume (PTV) is 14000 mm^3.

Tumour position	Ion combination	V_5 mm^3	V_{10} mm^3	V_{50} mm^3
Shallow	^{1}H	30786	27388	15866
	^{4}He	29803	26653	15758
	^{7}Li	30275	26719	15863
	^{12}C	31070	26493	15550
	^{16}O	31055	26608	15628
	^{20}Ne	31140	26597	15661
	^{28}Si	31330	26799	15773
	^{56}Fe	30927	26825	15947
	^{1}H,^{12}C	30700	27291	15850
	^{4}He,^{16}O	29821	26664	15761
	^{7}Li,^{20}Ne	30322	26698	15871
	^{1}H,^{4}He,^{16}O	30321	26990	15807
	^{7}Li,^{12}C,^{56}Fe	30277	26725	15931
	^{12}C,^{16}O,^{20}Ne	31024	26609	15653
	All ions	30298	26977	15814
Central	^{1}H	73639	65979	39601
	^{4}He	70084	62947	38814
	^{7}Li	72332	63227	39003
	^{12}C	74880	62100	36282
	^{16}O	75054	62702	37378
	^{20}Ne	75612	62561	36744
	^{28}Si	76242	63762	38084
	^{56}Fe	75916	64043	39708
	^{1}H,^{12}C	73464	65843	39577
	^{4}He,^{16}O	70084	62947	38814
	^{7}Li,^{20}Ne	72334	63227	39003
	^{1}H,^{4}He,^{16}O	72255	64909	39618
	^{7}Li,^{12}C,^{56}Fe	72720	63199	39355
	^{12}C,^{16}O,^{20}Ne	75044	62651	37631
	All ions	72267	64917	39628
Deep	^{1}H	113550	101625	54979
	^{4}He	105753	95071	56281
	^{7}Li	109710	95021	56546
	^{12}C	113657	92352	30249
	^{16}O	113974	95011	34891
	^{20}Ne	115534	94531	29672
	^{28}Si	117407	97110	34726
	^{56}Fe	118142	97777	42679
	^{1}H,^{12}C	113458	101513	55212
	^{4}He,^{16}O	105753	95071	56281
	^{7}Li,^{20}Ne	109710	95021	56546
	^{1}H,^{4}He,^{16}O	109408	98275	56450
	^{7}Li,^{12}C,^{56}Fe	110088	95166	56774
	^{12}C,^{16}O,^{20}Ne	114367	93466	35172
	All ions	109408	98275	56450

Table 4.12: Total volumes outside the tumour which received at least 5%, 10% and 50% of the target dose volume in mm^3; hypoxic sub-volume defined within the tumour, OAR region defined distal (adjacent) to the tumour. Planning target volume (PTV) is 14000 mm^3.

Tumour position	Ion combination	V_5	V_{10}	V_{50}
Shallow	^{1}H, ^{12}C	30747	27326	15900
	^{4}He, ^{16}O	29917	26683	15808
	^{7}Li,^{20}Ne	30460	26750	15879
	^{1}H, ^{4}He, ^{16}O	30515	27094	15897
	^{7}Li, ^{12}C, ^{56}Fe	30405	26796	15967
	^{12}C, ^{16}O, ^{20}Ne	31090	26681	15685
	All ions	30492	27092	15920
Central	^{1}H, ^{12}C	73521	65805	39564
	^{4}He, ^{16}O	70179	62904	38668
	^{7}Li,^{20}Ne	72578	63236	38879
	^{1}H, ^{4}He, ^{16}O	72643	65081	39541
	^{7}Li, ^{12}C, ^{56}Fe	72871	63219	39277
	^{12}C, ^{16}O, ^{20}Ne	75044	62651	37631
	All ions	72622	65103	39558
Deep	^{1}H, ^{12}C	113384	101346	52465
	^{4}He, ^{16}O	105710	94793	55047
	^{7}Li,^{20}Ne	109769	94746	53632
	^{1}H, ^{4}He, ^{16}O	110049	98623	52730
	^{7}Li, ^{12}C, ^{56}Fe	110263	94946	54267
	^{12}C, ^{16}O, ^{20}Ne	114367	93466	35172
	All ions	110061	98673	52796

4.5 Conclusion

The manifold multi-ion TPS developed in Chapter 3 has been extended to support exclusion of dose in organs at risk and enhanced LET in hypoxic subvolumes of the tumour. OAR support was implemented by defining a new region with a dose objective of zero and very high optimisation cost/penalty factor, while the LET in hypoxic sub-volumes is enhanced via the exclusion of light low-LET ions at energies beyond that which would penetrate the shallowest hypoxic region, while maintaining the same physical dose objective.

The extended TPS has been evaluated with many combinations of ions in a simplified human head phantom for three different tumour positions (shallow, central, and deep). For each tumour position, we imposed one or both of the added OAR and hypoxic sub-volume constraints, and evaluated a range of treatment plans using single, dual, triple and manifold (8) ion species. The same performance metrics were used as developed for the previous Chapter; the results obtained are similar, with the manifold multi ion treatment plans performing the best, both for dose uniformity and coverage, but without showing any specific advantage in terms of dose to non-target tissues.

The TPS developed in Chapter 3 and extended in this Chapter is designed for single-field irradiation only; in Chapter 5, the TPS is further extended to support multi-field irradiation.

CHAPTER 5

Treatment plan optimisation across multiple fields

5.1 Introduction

During radiation therapy, the total dose is conventionally divided amongst several *fractions* and multiple *fields*. Treatment *fractions* divides the total radiation dose into parts which are delivered at different times to deliver a total therapeutic dose to the target, while allowing the patient's normal tissues to recover between treatment sessions. Treatment *fields*, on the other hand, are the different directions from which an external radiation beam is directed at the target. This is a form of angular spatial fractionation - all dose components pass through the target to deliver the prescribed dose, but as they pass through the target from different angles, normal tissue is only exposed to entrance dose contributions from a fraction of the fields.

Due to the relatively low per-field entrance dose in particle therapy compared to photon therapy, it is usually possible to deliver a prescribed treatment using a much smaller number of high-dose treatment fractions and fields. This approach, known as *hypofractionation*, appears to be well-tolerated by patients, and has been implemented with both proton and carbon ion therapy with as few as one treatment fraction for certain cancers [176, 177]. In general, however, the majority of proton and heavy ion therapy treatments involve both multiple fields and multiple fractions. Therefore, for the developed TPS to be clinically relevant, it is necessary to implement support for dividing the treatment into multiple fields and/or fractions. In this Chapter, we present

a computationally efficient method for distributing a prescribed dose between multiple fields.

5.2 Multi-field treatment planning

There are three basic approaches to extend the developed TPS to support multifield irrdiation; each of these is discussed in detail. All approaches may be applied with rotations performed around either the y (vertical) axis or x and y; there is no substantial benefit to rotating about the z axis (i.e. in the direction of the beam path) other than a possible minor improvement in dose uniformity. For the cases evaluated in this Chapter, we focus on single-axis rotation around the y axis.

5.2.1 Simple fully-independently-optimised angular fractionation

The simplest approach to multi-field irradiation is to treat each field as an independent frontal irradiation of a version of the target and phantom rotated to the desired position with a certain fraction of the prescribed dose - for example, an N Gy dose covering the entire target volume could be delivered from M different angular positions, for each of which a separate treatment plan is independently developed for the delivery of an average N/M Gy dose to the target from that angle. This simple approach can be implemented by applying rotational affine transforms to the target and phantom, and computing the treatment plan for with a target dose of N/M Gy for each angle using the methods described in the previous Chapters. The total dose distribution resulting from this process may then be computed by rotating each irradiated volume back in the opposite direction and summing the resultant dose distribution.

This method works well in the absence of any OAR impinging on one or more of the approach angles. In this case, the total dose to the target will be the desired N Gy. However, while this technique is is very simple to implement, the presence of OARs in the path of one or more of the potential beam positions poses a problem: how can the prescribed fraction of dose be delivered to regions of the target which are *distal* the OAR for some beam angles and positions? The delivery of almost any level of dose to target regions distal to the OAR necessarily introduces a large entrance dose - including in the OAR. However, one of the primary objectives of the TPS is to minimise dose to the OAR, and this is enforced by imposing a very large cost factor to any dose in

the OAR regions, as discussed in Chapter 4. Reducing this cost factor will result in significant dose to the OAR; the alternative of leaving it high will result in underdosing of distal tumour regions. Therefore, while the simple dose-division approach will work well in many cases which avoid dose delivery around OARs, this locally-optimal solution is not a general solution to the problem of multi-field irradiation.

5.2.2 Globally-optimised angular fractionation

A more sophisticated approach can be implemented to achieve a truly global dose optimisation, at the cost of considerably greater computational complexity. The first step is as for the method discussed in Section 5.2.1; the target is rotated to each of the different angles in turn, and for each angle the heterogeneous dose distribution for each tumour-intersecting beam position, ion species and energy are computed. Then, for dose optimisation, instead of rotating the target and sequentially irradiating using fixed ion beams, the original target remains stationary and the heterogeneous dose distributions calculated in the previous step are each rotated about the centre of the target volume (upon which the tumour is centred) to the desired beam angle. This is repeated for all beam angles, until a complete library of dose distributions resulting from each relative angle of beam delivery to the target is constructed. Finally, the weighting between all the rotation angles, individual beam positions, ion species and energies is then optimised in a single step.

This has three notable effects: firstly, optimisation is now performed globally across all fields, rather than locally (field-by-field); secondly, there is a considerable increase in memory requirements required to store the per-beam position libraries of rotated ion beam dose distributions, due to the increased number of positions, and because a long, narrow dose distribution, when rotated about a single axis, may require a considerably larger rectilinear space to store the entire rotated dose distribution (e.g. a 20 mm×20 mm×300 mm = 120000 mm^3 dose distribution rotated to 45° will now require 1024000 mm^3[1]). Thirdly, the matrix C (see (3.1) in Chapter 3.2.3) is now much larger, with a factor of M increase in the number of columns, greatly increasing both the memory required to hold C and the computational burden of solving (3.1). However, if sufficient computational resources exist to implement this method, it should produce a truly globally optimal result.

[1]This may be reduced, at the cost of increased computational complexity, by using a sparse matrix representation in MATLAB, since the majority of these voxels will contain zero dose.

After an initial exploratory evaluation, we concluded that it would be impractical to implement this method on available computing resources at UTS without greatly reducing the tumour size, making it difficult to compare the resulting treatment plans with the single-field results obtained in the previous Chapters.

5.2.3 Semi-independent angular fractionation

The third method is closely related to the first, with a number of improvements which enable it to deal with the vast majority of cases involving OARs. Instead of splitting the dose evenly between each of the angular fractions, the following series of procedures is performed.

1. After rotating the target to each of the angles, the fraction of the target volume which is occluded by OARs is computed and recorded for each field angle.

2. The angles of rotation are then reordered from most-occluded to least occluded.

3. Treatment sub-plans for each angle are then sequentially generated for each field, as before, starting with a nominal target dose of N/M Gy for the most-occluded angle.

4. After the first plan is computed, the achieved dose distribution (which heavily favours avoidance of dose to OARs, and thus which may have underdosed regions of the target volume) is subtracted from the global total dose objective, and the residual dose - which is now non-uniform - is calculated.

5. The next treatment sub-plan is now generated, with the objective dose being a fraction $1/(M-1)$ of the residual dose. This process is repeated until the treatment plans for the final (least-occluded) field angles are computed - which should have the most flexibility to 'top up' or compensate for the low dose in those regions of the target which were occluded in the prior fields.

Assuming that the tumour is not completely surrounded by an OAR region (in which case radiation therapy is not going to be a viable solution in any event), it is reasonable to expect that the plane in which the beam is being rotated has at least one aspect which does not intersect with an OAR. Therefore, this approach should be able to compute a plan which is very close to the globally-optimised solution described in the previous sub-section.

The principal advantage of this approach, then, is in its resident memory requirements, since the sub-plans may be computed sequentially. Computational workload increase linearly with the number of fields, while memory requirements do not increase at all relative to single-field irradiation. Due to these advantages over the globally-optimal solution, this method is the one adopted for the remainder of this Chapter, since it should be able to provide a multi-field treatment plan for the vast majority of realistic scenarios involving tumours with nearby OARs.

5.3 Evaluation of proposed multi-field extension

A reduced subset of ion combinations, including single-ion (^{1}H, ^{4}He, ^{12}C and ^{16}O), dual-ion (^{1}H + ^{12}C, ^{4}He + ^{16}O), triple-ion (^{1}H + ^{4}He + ^{16}O, ^{7}Li + ^{12}C + ^{56}Fe) and all-ions are evaluated in 2, 3, 4 and 5-field treatment plans, for targets at the central tumour position with a distal OAR. The case with a hypoxic region is evaluated using multi-ion (heavy/light) combinations while the no-hypoxia case is evaluated with single-ion plans only.

The same metrics used to evaluate the treatment plans in the previous two Chapters are also adopted here. The specific fraction of different ions used for the multi-ion plans for different numbers of fields is presented in Section 5.4.1, together with images showing the spatial breakdown of different ion dose contributions in each field. Dose uniformity is evaluated in Section 5.4.2 and compared with the single-field results obtained in previous Chapters. Dose coverage is evaluated in Section 5.4.3, while dose to normal tissue is discussed in Section 5.4.4.

5.4 Results and discussion

5.4.1 Per-ion dose-volume contributions

Per-ion dose-volume contributions for all of the multi-ion treatment plans are shown in Table 5.1. The most notable change in per-ion contributions to the total dose as the number of fields is increased with multi-ion treatment plans is a progressive reduction in the contribution from the lightest ion species relative to the second-lightest and third (if any) lightest ions. This is because the use of multiple fields enables more of the tumour to be effectively ‘shallow’; therefore, tail dose from shallow irradiation with

Table 5.1: The percentage contribution of individual ions to the total deposited dose in each multifield multi-ion treatment plan. A hypoxic region is located inside the tumour and an OAR is positioned distal to the tumour.

Number of fields	Ion combination	H%	He%	Li%	C%	O%	Ne%	Si%	Fe%
	^{1}H, ^{12}C	90.79	-	-	9.21	-	-	-	-
	^{4}He, ^{16}O	-	80.98	-	-	19.02	-	-	-
2	^{1}H, ^{4}He, ^{16}O	67.47	23.40	-	-	9.13	-	-	-
	^{7}Li, ^{12}C, ^{56}Fe	-	-	76.86	16.15	-	-	-	6.99
	All ions	67.19	23.60	0.00	4.58	4.46	0.04	0.09	0.05
	^{1}H, ^{12}C	79.94	-	-	20.06	-	-	-	-
	^{4}He, ^{16}O	-	72.27	-	-	27.73	-	-	-
3	^{1}H, ^{4}He, ^{16}O	44.65	37.48	-	-	17.87	-	-	-
	^{7}Li, ^{12}C, ^{56}Fe	-	-	53.96	27.16	-	-	-	18.88
	All ions	43.16	33.82	4.32	6.34	5.11	3.64	2.06	1.55
	^{1}H, ^{12}C	71.28	-	-	28.72	-	-	-	-
	^{4}He, ^{16}O	-	68.37	-	-	31.63	-	-	-
4	^{1}H, ^{4}He, ^{16}O	36.70	41.42	-	-	21.89	-	-	-
	^{7}Li, ^{12}C, ^{56}Fe	-	-	52.85	25.92	-	-	-	21.22
	All ions	33.37	34.95	5.49	5.97	5.00	5.08	6.74	3.39
	^{1}H, ^{12}C	70.88	-	-	29.12	-	-	-	-
	^{4}He, ^{16}O	-	68.74	-	-	31.26	-	-	-
5	^{1}H, ^{4}He, ^{16}O	34.00	44.55	-	-	21.45	-	-	-
	^{7}Li, ^{12}C, ^{56}Fe	-	-	48.28	27.15	-	-	-	24.56
	All ions	29.99	39.39	5.40	7.78	3.55	4.61	5.70	3.57

heavier ions can be incorporated into the total dose to the target without irradiating distal normal tissues.

Total achieved dose, summed across all ions and all fields, is shown in Figure 5.1. The virtual camera viewing angle is offset by 45° from the target around the x-axis and by 30° about the z axis. Field angles are measured anticlockwise around the z axis, relative to an arrow pointing from the centre of the target towards the lower-left of the image (which is the zero degree point in this figure).

As the number of fields increases, the entrance dose for each field relative to the target dose decreases, to the point where it is barely visible at all in the 5-field case. The maximum non-target dose is deposited in the relatively dense skull bone in each case.

The individual dose contributions from each of the field in the 2-field case are broken down for the different ions and are shown in Figure 5.2-5.3. The 180° field avoids the distal OAR, with a very clear ring visible around the OAR in the dose field of dominant ion ^{1}H, and to a lesser extent with several other heavier ions.

The individual dose contributions from each of the field in the 3-field case are broken down for the different ions and are shown in Figure 5.4-5.6. The 90° field shows

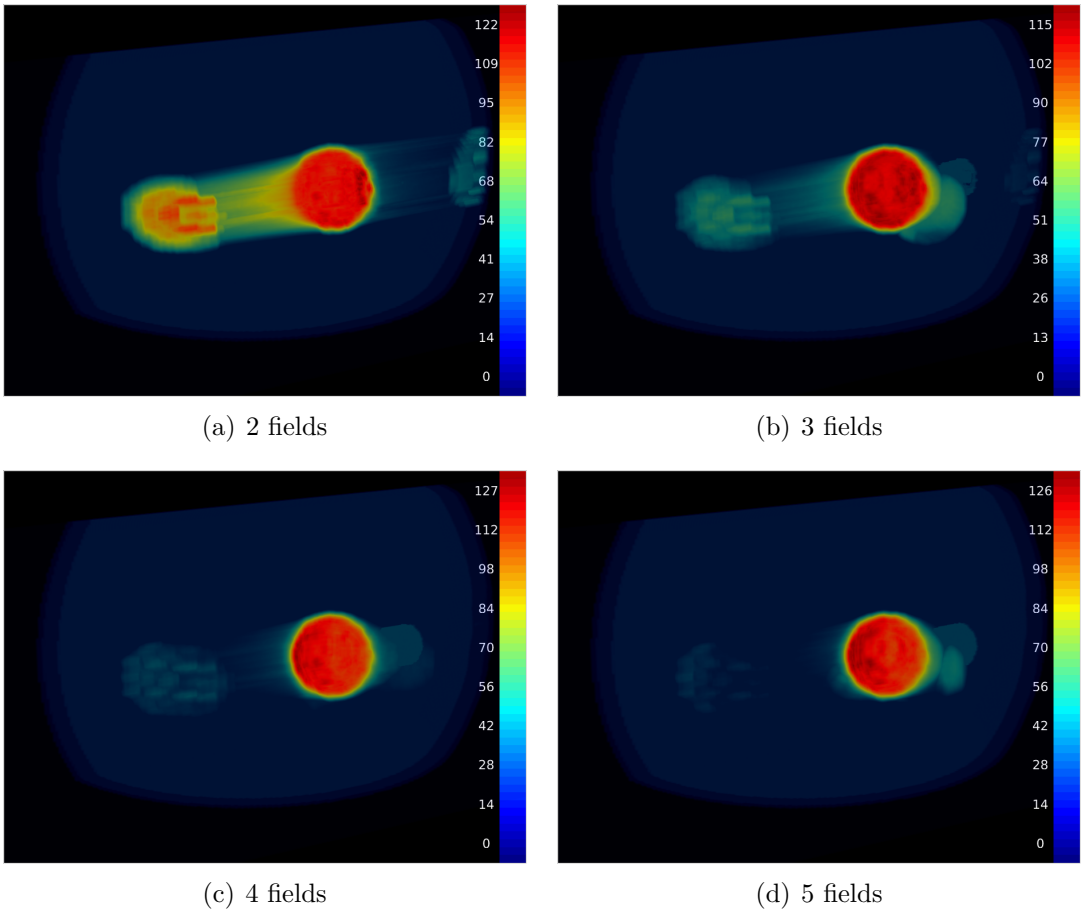

(a) 2 fields (b) 3 fields

(c) 4 fields (d) 5 fields

Figure 5.1: Total deposited dose distributions (sum of all ions and all fields) for 2 (0°/180°, 3 (0°, 90°, 180°), 4 (0°, 60°, 120°, 180°) and 5-field (0°, 45°, 90°, 135°, 180°), 8-ion treatment plans. A hypoxic region is located inside the tumour and an OAR is defined distal to the tumour.

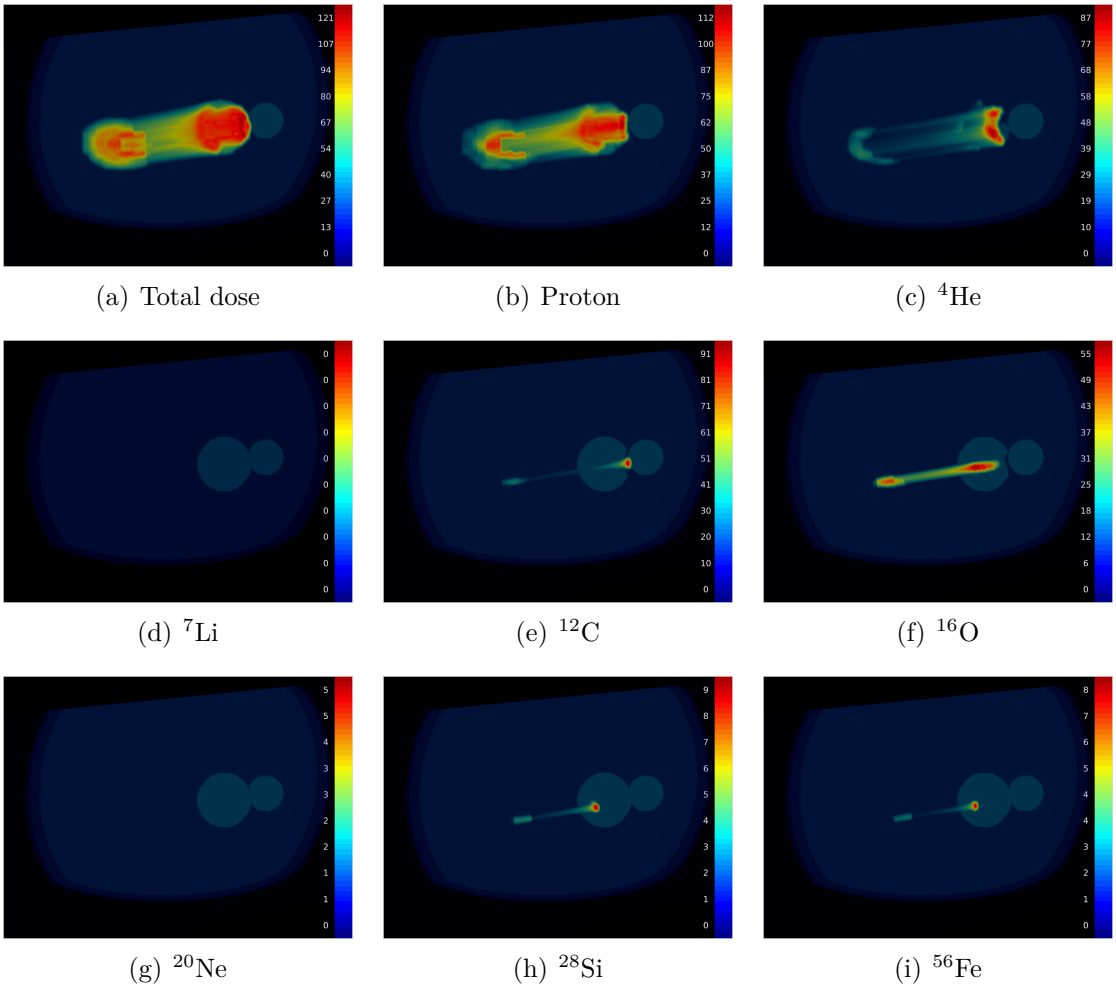

(a) Total dose (b) Proton (c) ^{4}He

(d) ^{7}Li (e) ^{12}C (f) ^{16}O

(g) ^{20}Ne (h) ^{28}Si (i) ^{56}Fe

Figure 5.2: 3D volumetric visualisations of total dose and contributions of the first field by each individual ion species, for a 2-field 8-ion treatment plan. The ion beams are directed at the tumour from an angle of 0°; a hypoxic region is located inside the tumour and an OAR is defined distal to the tumour.

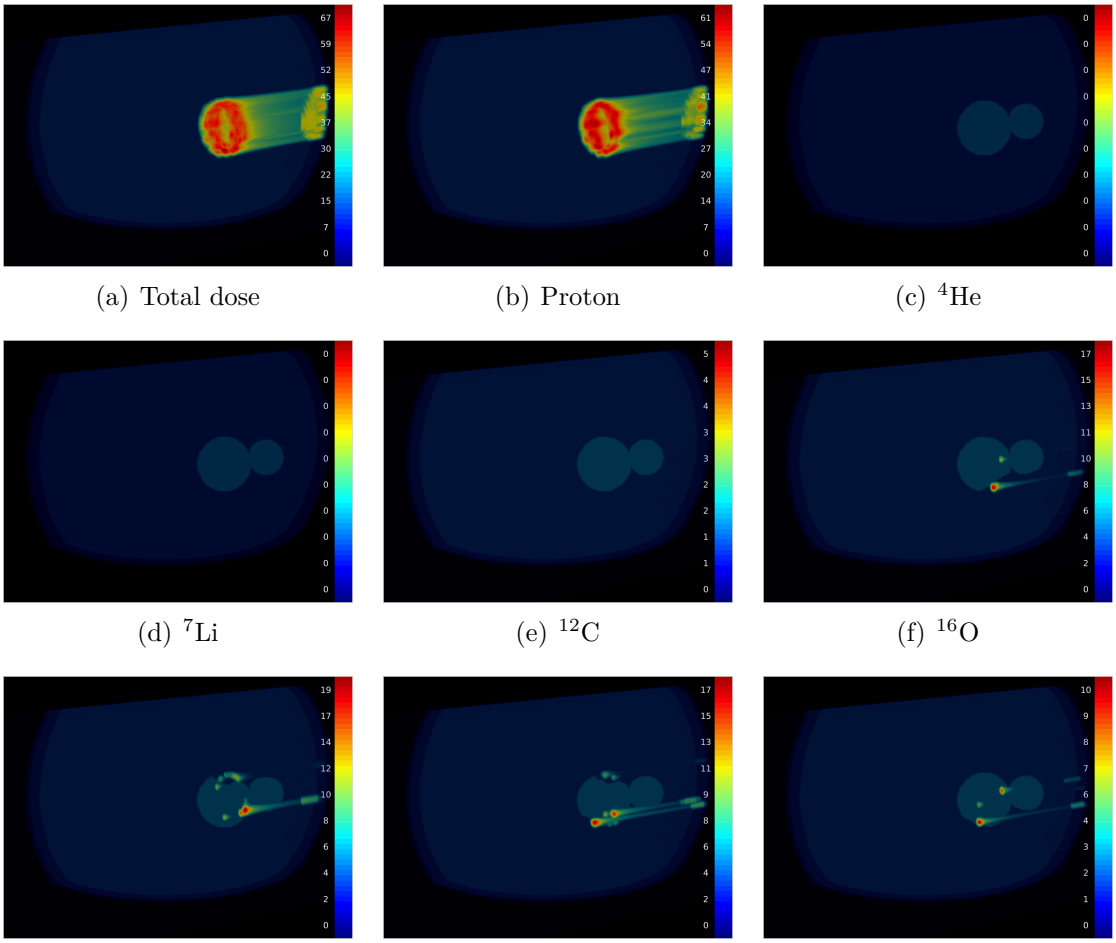

(a) Total dose (b) Proton (c) ^{4}He

(d) ^{7}Li (e) ^{12}C (f) ^{16}O

(g) ^{20}Ne (h) ^{28}Si (i) ^{56}Fe

Figure 5.3: 3D volumetric visualisations of total dose and contributions of the second field by each individual ion species, for a 2-field 8-ion treatment plan. The ion beams are directed at the tumour from an angle of 180°; a hypoxic region is located inside the tumour and an OAR is defined distal to the tumour.

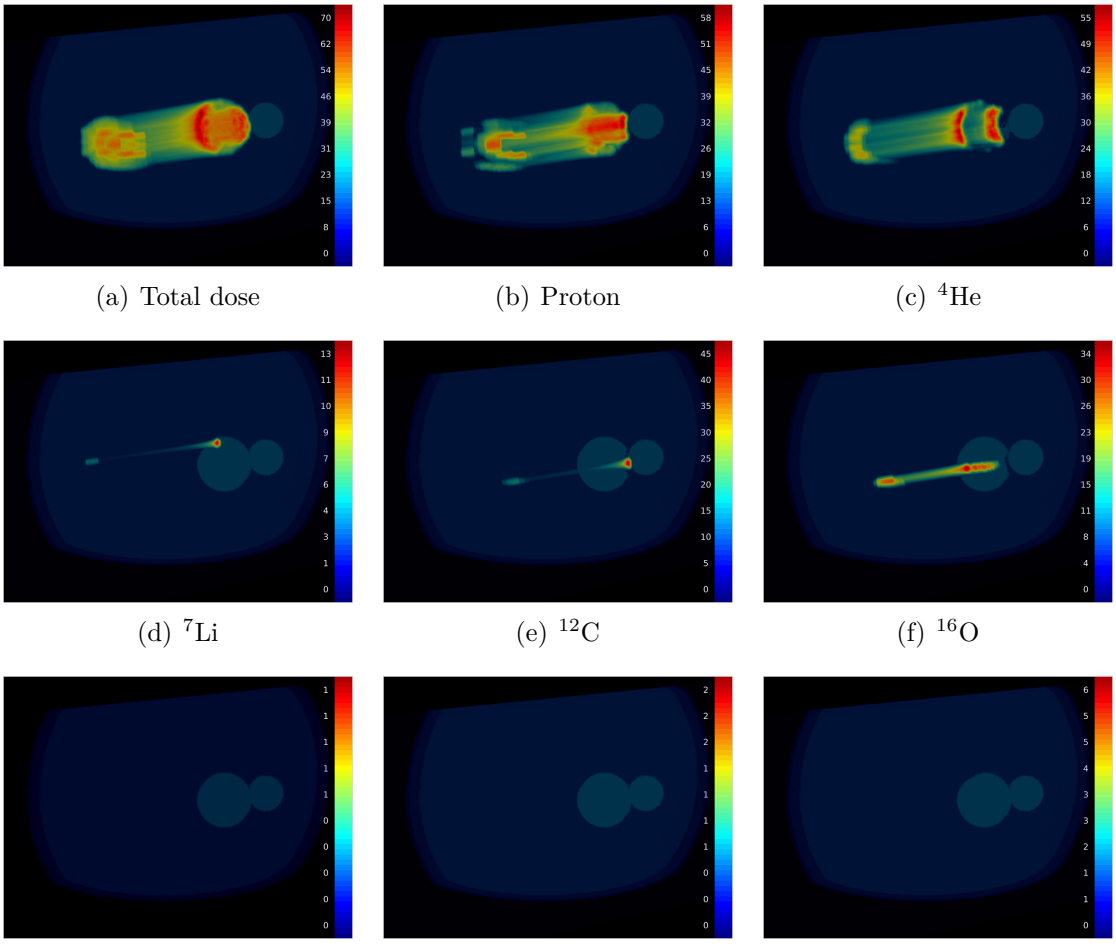

(a) Total dose (b) Proton (c) ^{4}He

(d) ^{7}Li (e) ^{12}C (f) ^{16}O

(g) ^{20}Ne (h) ^{28}Si (i) ^{56}Fe

Figure 5.4: 3D volumetric visualisations of total dose and contributions of the first field by each individual ion species, for a 3-field 8-ion treatment plan. The ion beams are directed at the tumour from an angle of 0°; a hypoxic region is located inside the tumour and an OAR is defined distal to the tumour.

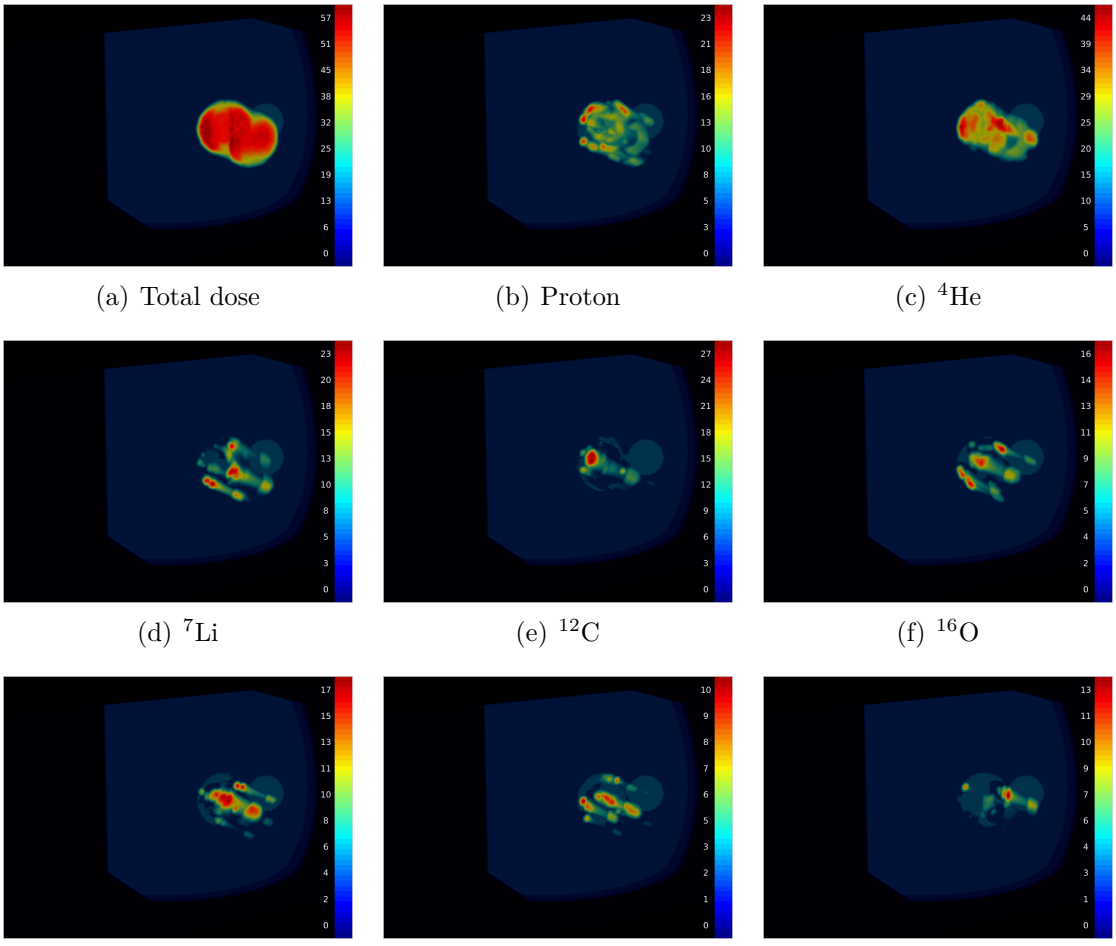

(a) Total dose (b) Proton (c) ^{4}He

(d) ^{7}Li (e) ^{12}C (f) ^{16}O

(g) ^{20}Ne (h) ^{28}Si (i) ^{56}Fe

Figure 5.5: 3D volumetric visualisations of total dose and contributions of the second field by each individual ion species, for a 3-field 8-ion treatment plan. The ion beams are directed at the tumour from an angle of 90°; a hypoxic region is located inside the tumour and an OAR is defined distal to the tumour.

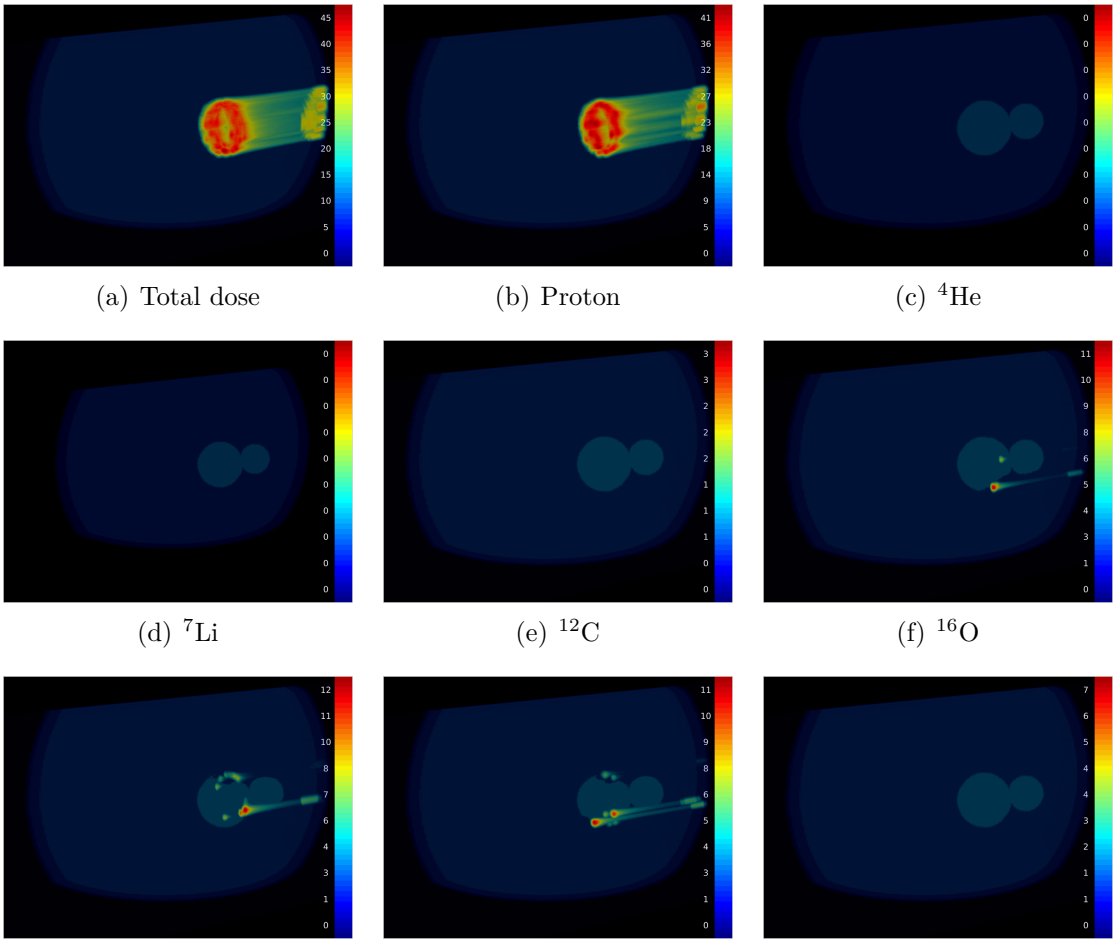

(a) Total dose (b) Proton (c) ^{4}He

(d) ^{7}Li (e) ^{12}C (f) ^{16}O

(g) ^{20}Ne (h) ^{28}Si (i) ^{56}Fe

Figure 5.6: 3D volumetric visualisations of total dose and contributions of the third field by each individual ion species, for a 3-field 8-ion treatment plan. The ion beams are directed at the tumour from an angle of 180°; a hypoxic region is located inside the tumour and an OAR is defined distal to the tumour.

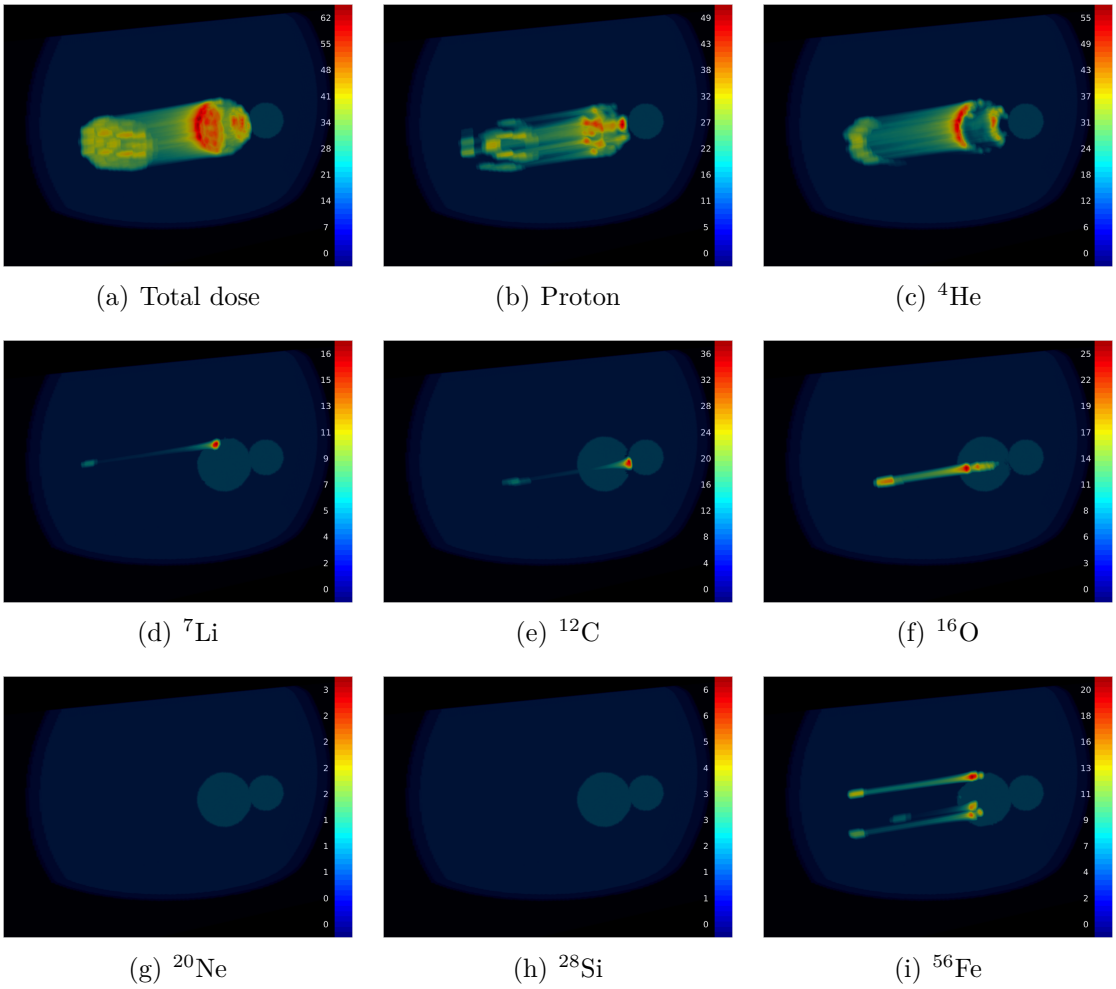

(a) Total dose (b) Proton (c) ^{4}He

(d) ^{7}Li (e) ^{12}C (f) ^{16}O

(g) ^{20}Ne (h) ^{28}Si (i) ^{56}Fe

Figure 5.7: 3D volumetric visualisations of total dose and contributions of the first field by each individual ion species, for a 4-field 8-ion treatment plan. The ion beams are directed at the tumour from an angle of 0°; a hypoxic region is located inside the tumour and an OAR is defined distal to the tumour.

a much more uniform contribution between each of the different ions, with a greater contribution from ^{4}He than ^{1}H compared to the other fields. Again, for the 180° field, there is a prominent ring of ^{1}H dose around the OAR with minor contributions from other ion species.

The individual dose contributions from each of the field in the 4-field case are broken down for the different ions and are shown in Figure 5.7-5.10. Again, for the 180° field, there is a prominent ring of ^{1}H dose around the OAR with minor contributions from other ion species; there is also a partial ring for the third field, since part of this

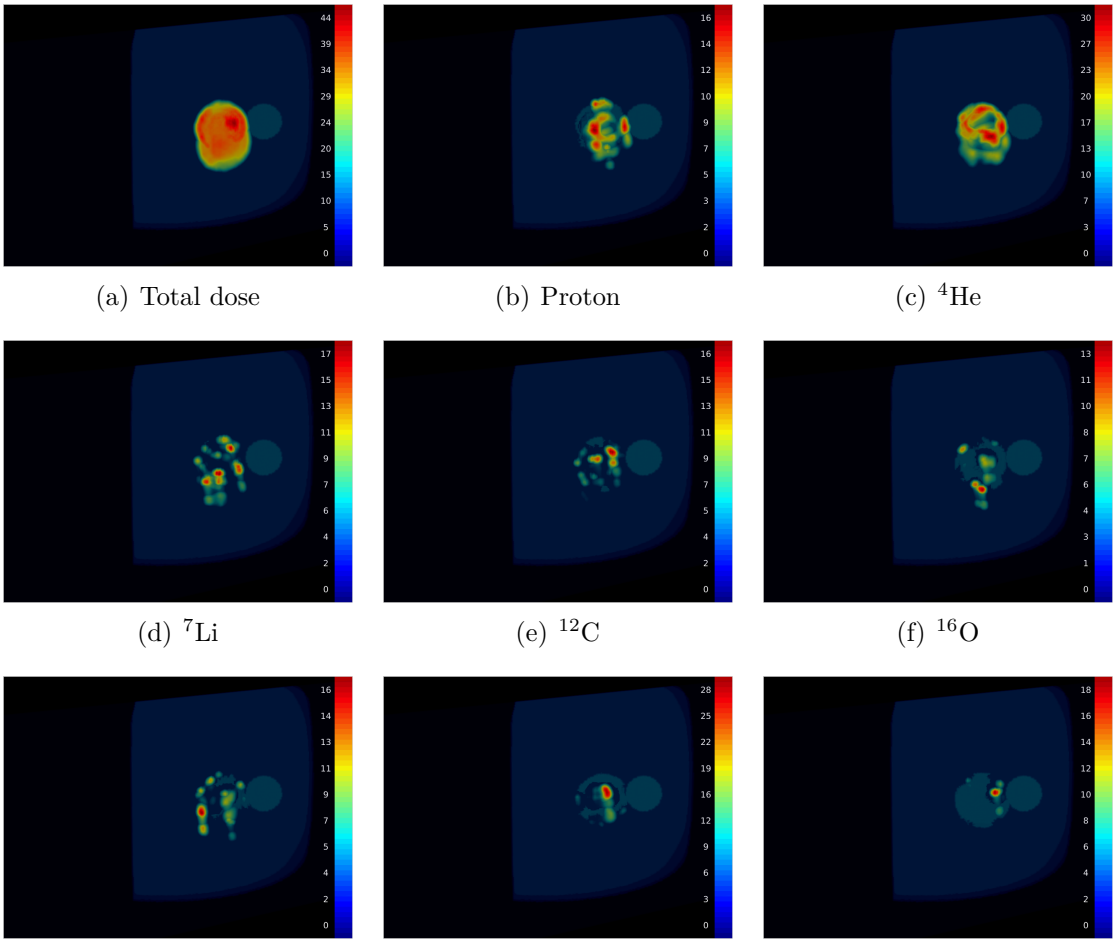

(a) Total dose (b) Proton (c) ^{4}He

(d) ^{7}Li (e) ^{12}C (f) ^{16}O

(g) ^{20}Ne (h) ^{28}Si (i) ^{56}Fe

Figure 5.8: 3D volumetric visualisations of total dose and contributions of the second field by each individual ion species, for a 4-field 8-ion treatment plan. The ion beams are directed at the tumour from an angle of 60°; a hypoxic region is located inside the tumour and an OAR is defined distal to the tumour.

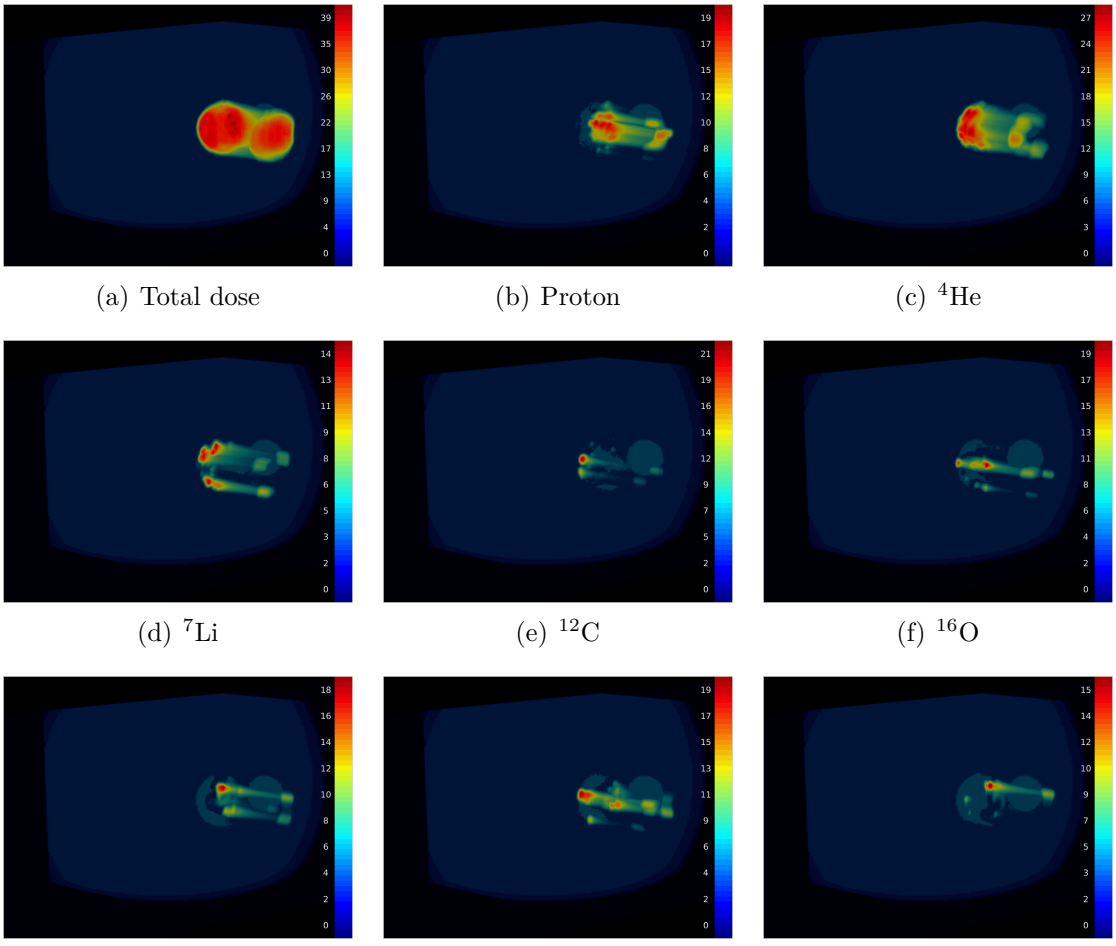

(a) Total dose (b) Proton (c) ^{4}He

(d) ^{7}Li (e) ^{12}C (f) ^{16}O

(g) ^{20}Ne (h) ^{28}Si (i) ^{56}Fe

Figure 5.9: 3D volumetric visualisations of total dose and contributions of the third field by each individual ion species, for a 4-field 8-ion treatment plan. The ion beams are directed at the tumour from an angle of 120°; a hypoxic region is located inside the tumour and an OAR is defined distal to the tumour.

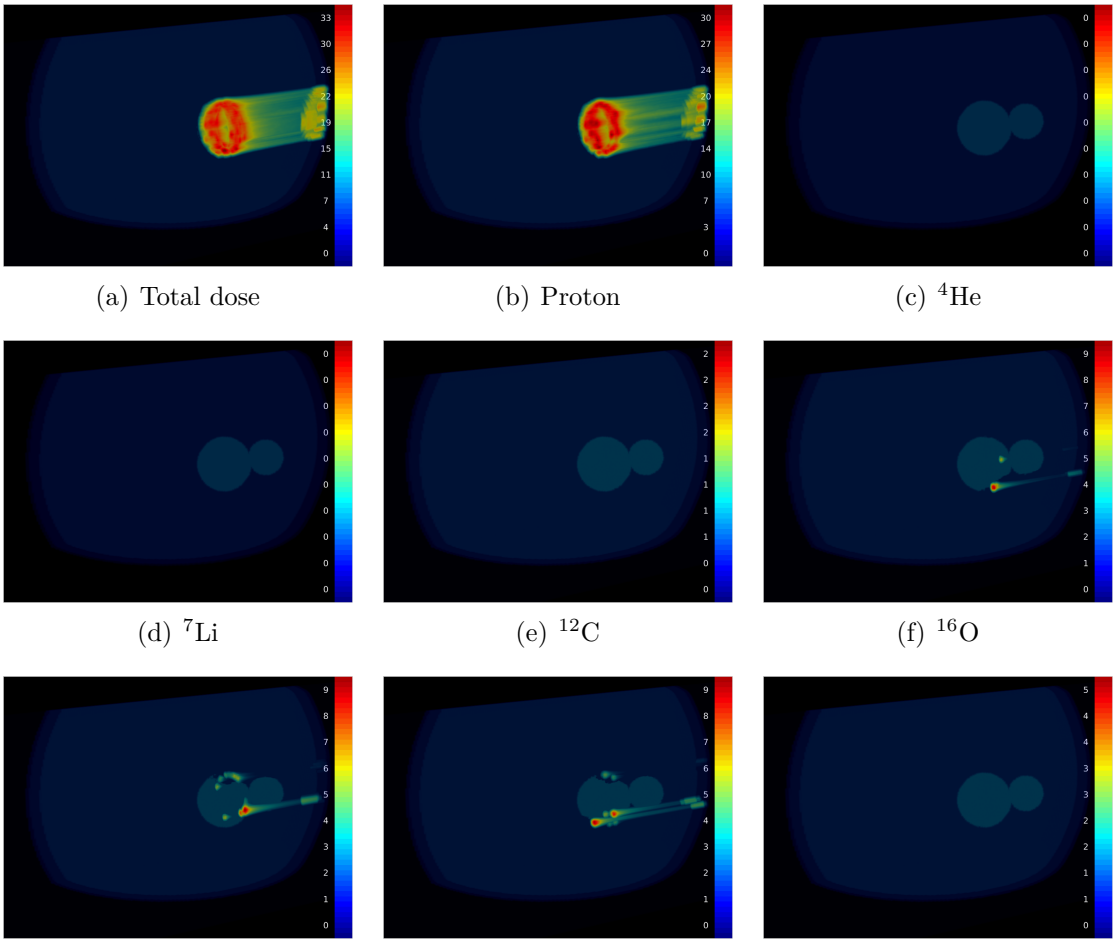

(a) Total dose (b) Proton (c) ^{4}He

(d) ^{7}Li (e) ^{12}C (f) ^{16}O

(g) ^{20}Ne (h) ^{28}Si (i) ^{56}Fe

Figure 5.10: 3D volumetric visualisations of total dose and contributions of the fourth field by each individual ion species, for a 4-field 8-ion treatment plan. The ion beams are directed at the tumour from an angle of 180°; a hypoxic region is located inside the tumour and an OAR is defined distal to the tumour.

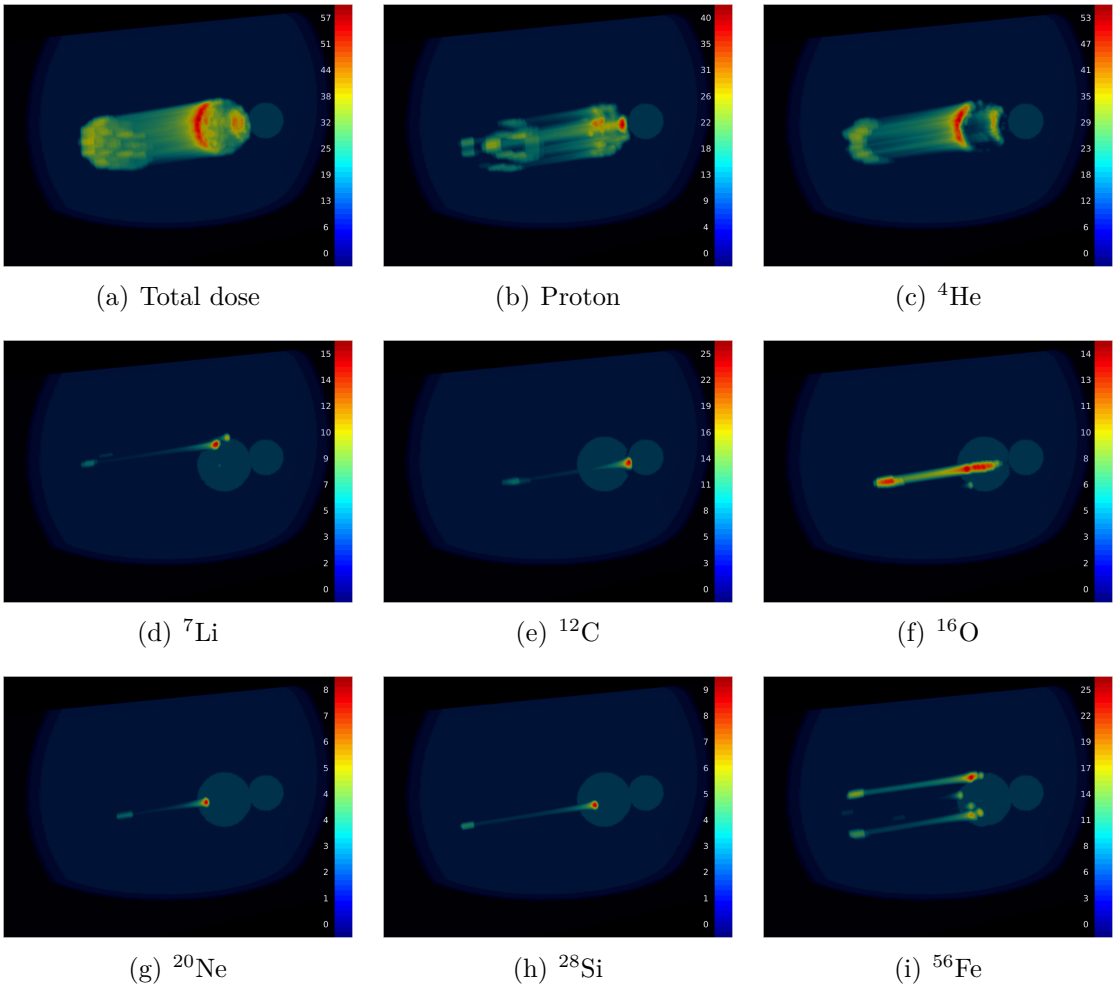

(a) Total dose (b) Proton (c) ^{4}He

(d) ^{7}Li (e) ^{12}C (f) ^{16}O

(g) ^{20}Ne (h) ^{28}Si (i) ^{56}Fe

Figure 5.11: 3D volumetric visualisations of total dose and contributions of the first field by each individual ion species, for a 5-field 8-ion treatment plan. The ion beams are directed at the tumour from an angle of 0°; a hypoxic region is located inside the tumour and an OAR is defined distal to the tumour.

field is occluded by the OAR. Fields 2 and 3 also show greater ion diversity compared to fields 1 and 4, which are both dominated by ^{1}H and ^{4}He.

The individual dose contributions from each of the field in the 5-field case are broken down for the different ions and are shown in Figure 5.11-5.15. Maximum ion species diversity is seen in fields 2 and 3, while field 1 and 4 are dominated by ^{1}H and ^{4}He and almost the entire dose in Field 5 delivered by ^{1}H.

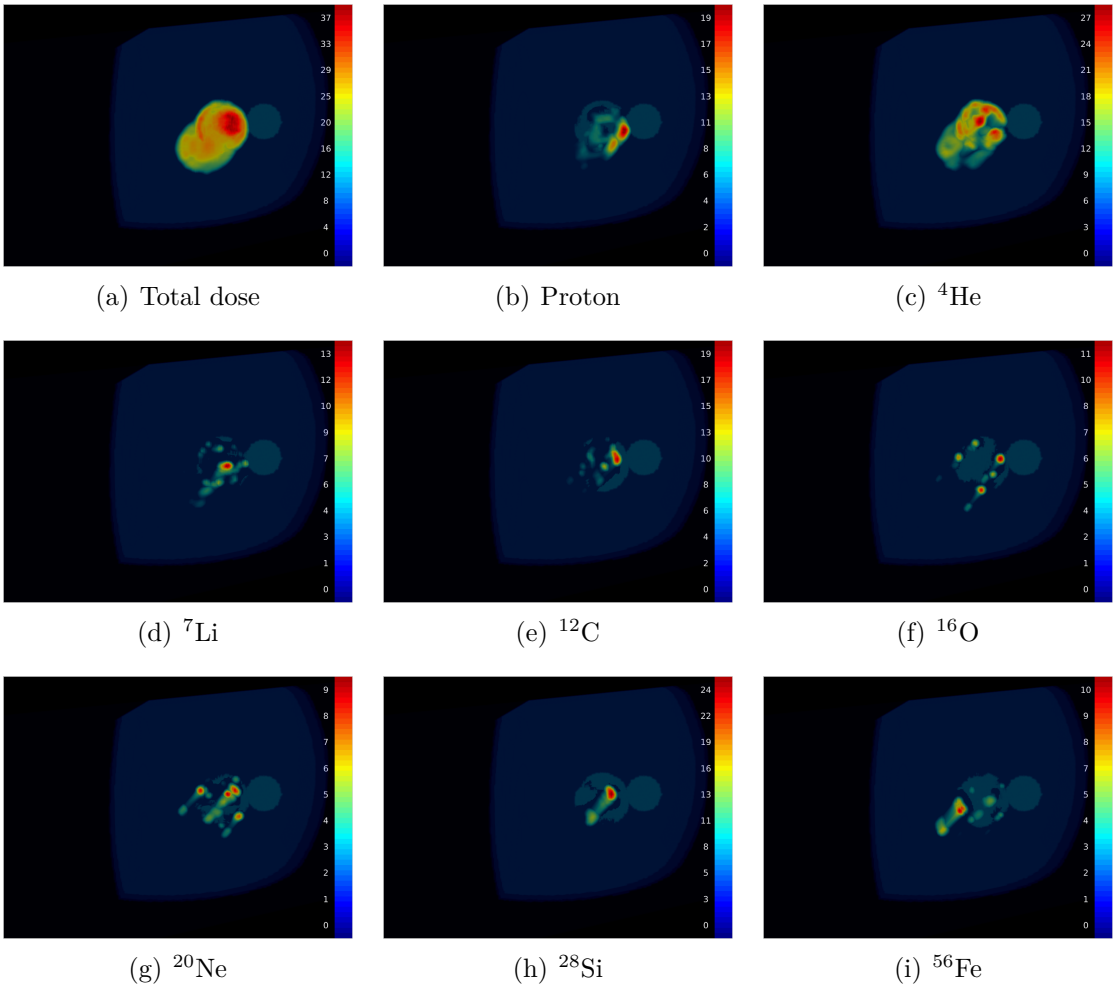

(a) Total dose (b) Proton (c) ^{4}He

(d) ^{7}Li (e) ^{12}C (f) ^{16}O

(g) ^{20}Ne (h) ^{28}Si (i) ^{56}Fe

Figure 5.12: 3D volumetric visualisations of total dose and contributions of the second field by each individual ion species, for a 5-field 8-ion treatment plan. The ion beams are directed at the tumour from an angle of 45°; a hypoxic region is located inside the tumour and an OAR is defined distal to the tumour.

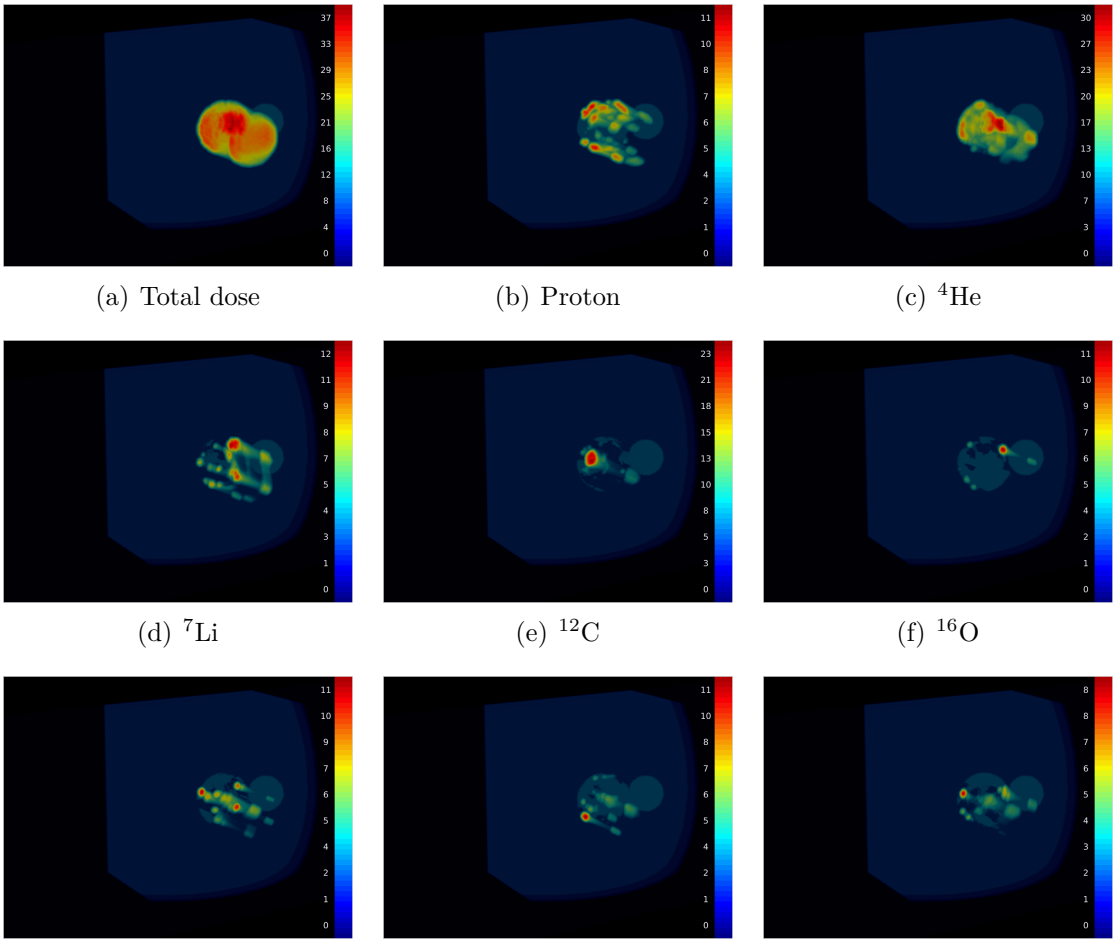

(a) Total dose (b) Proton (c) ^{4}He

(d) ^{7}Li (e) ^{12}C (f) ^{16}O

(g) ^{20}Ne (h) ^{28}Si (i) ^{56}Fe

Figure 5.13: 3D volumetric visualisations of total dose and contributions of the third field by each individual ion species, for a 5-field 8-ion treatment plan. The ion beams are directed at the tumour from an angle of 90°; a hypoxic region is located inside the tumour and an OAR is defined distal to the tumour.

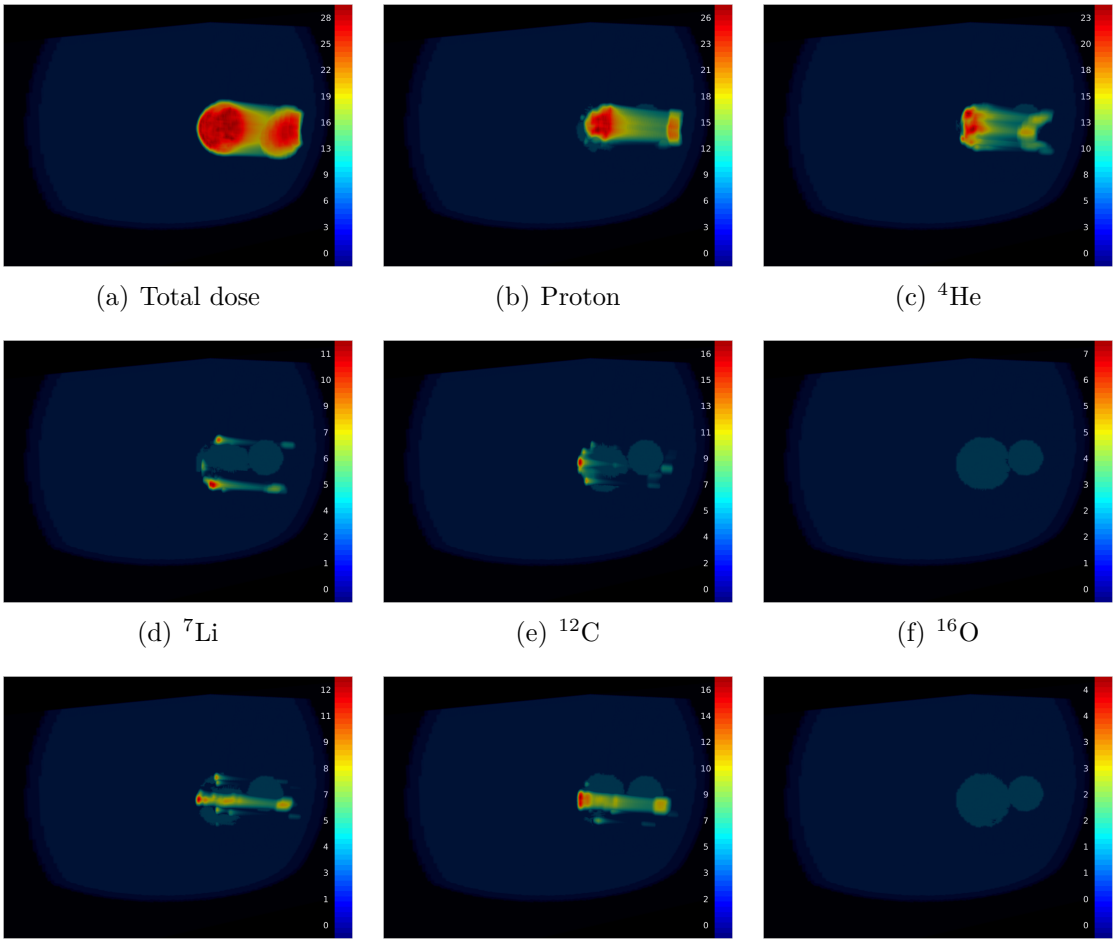

(a) Total dose (b) Proton (c) ^{4}He

(d) ^{7}Li (e) ^{12}C (f) ^{16}O

(g) ^{20}Ne (h) ^{28}Si (i) ^{56}Fe

Figure 5.14: 3D volumetric visualisations of total dose and contributions of the fourth field by each individual ion species, for a 5-field 8-ion treatment plan. The ion beams are directed at the tumour from an angle of 135°; a hypoxic region is located inside the tumour and an OAR is defined distal to the tumour.

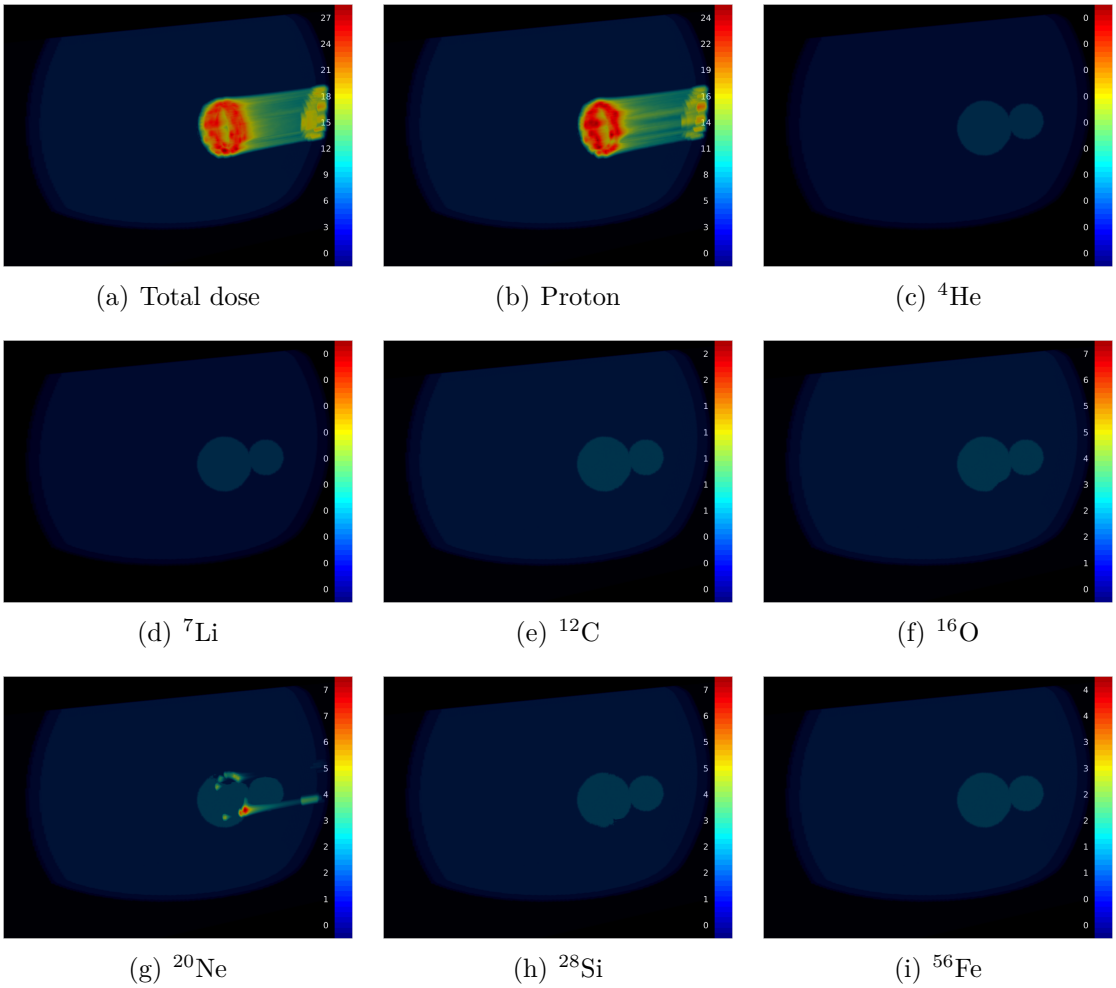

(a) Total dose (b) Proton (c) ^{4}He

(d) ^{7}Li (e) ^{12}C (f) ^{16}O

(g) ^{20}Ne (h) ^{28}Si (i) ^{56}Fe

Figure 5.15: 3D volumetric visualisations of total dose and contributions of the fifth field by each individual ion species, for a 5-field 8-ion treatment plan. The ion beams are directed at the tumour from an angle of 180°; a hypoxic region is located inside the tumour and an OAR is defined distal to the tumour.

Table 5.2: RMS error (Gy) for dose distributions within the target and the surrounding regions; no hypoxic sub-volume within the tumour, OAR region distal to tumour

Number of fields	Ion combination	Target	Non-target	OAR
2	^{1}**H**	8.83	7.71	2.52
	^{4}**He**	8.87	7.72	3.21
	^{12}**C**	15.66	7.08	6.64
	^{16}**O**	16.35	7.27	6.25
3	^{1}**H**	7.46	5.81	1.72
	^{4}**He**	7.63	5.79	2.07
	^{12}**C**	10.40	5.46	3.86
	^{16}**O**	10.62	5.59	3.65
4	^{1}**H**	8.43	5.37	1.37
	^{4}**He**	8.45	5.35	1.66
	^{12}**C**	10.00	5.04	3.02
	^{16}**O**	10.27	5.17	2.87
5	^{1}**H**	8.25	5.14	1.18
	^{4}**He**	8.39	5.11	1.41
	^{12}**C**	9.35	4.91	2.57
	^{16}**O**	9.54	5.01	2.44

5.4.2 Dose uniformity

The RMS error between the objective dose distribution and the achieved treatment plan dose distributions for single-ion multifield treatment plans is shown in Table 5.2. Since there is no meaningful definition of proximal or distal dose in the case of a multifield irradiation, the volume is divided up into three regions - target, non-target (*excluding OAR*) and OAR. These results may best be compared to the no-hypoxia, OAR, central tumour location results presented in Chapter 4 (Table 4.5). The RMS error in the target region is lower in each case (8-15 Gy RMS) than the comparable result for the single-field treatment plans (12-22 Gy RMS), with the error decreasing as the number of fields increases. The RMSE in the OAR is also lower in each case for all ions other than ^{1}H and ^{4}He, both of which achieve very low RMSE in the OAR with a single-field irradiation due to the lack of tail dose.

The RMS error between the objective dose distribution and the achieved treatment plan dose distributions for multi-ion multifield treatment plans is shown in Table 5.3. These results may be compared to the corresponding single-field multi-ion treatment plans in Chapter 4 (Table 4.6). The RMS error in the target region is lower in each case than the comparable result for the single-field treatment plans (7-9 Gy RMS comapred with 12-20 Gy RMS), with the error generally decreasing as the number of fields increases. Doses to the OAR are slightly worse, possibly due to the increased use of heavier ions compared to the single-field case.

Table 5.3: RMS error (Gy) for dose distributions within the target and the surrounding regions; hypoxic sub-volume within the target; OAR region distal to the tumour

Number of fields	Ion combination	Target	Non-target	OAR
2	**^{1}H, ^{12}C**	9.17	7.72	2.99
	^{4}He, ^{16}O	9.83	7.74	3.59
	^{1}H, ^{4}He, ^{16}O	8.96	7.74	3.06
	^{7}Li, ^{12}C, ^{56}Fe	11.32	7.76	5.04
	All ions	8.84	7.76	3.05
3	**^{1}H, ^{12}C**	7.48	5.81	1.96
	^{4}He, ^{16}O	7.68	5.81	2.26
	^{1}H, ^{4}He, ^{16}O	7.21	5.83	2.00
	^{7}Li, ^{12}C, ^{56}Fe	8.41	5.84	3.00
	All ions	7.11	5.84	2.00
4	**^{1}H, ^{12}C**	8.38	5.36	1.60
	^{4}He, ^{16}O	8.53	5.37	1.82
	^{1}H, ^{4}He, ^{16}O	8.18	5.40	1.65
	^{7}Li, ^{12}C, ^{56}Fe	8.78	5.36	2.37
	All ions	8.10	5.42	1.64
5	**^{1}H, ^{12}C**	8.14	5.14	1.37
	^{4}He, ^{16}O	8.27	5.13	1.53
	^{1}H, ^{4}He, ^{16}O	7.93	5.17	1.41
	^{7}Li, ^{12}C, ^{56}Fe	8.41	5.15	2.00
	All ions	7.80	5.19	1.41

5.4.3 Dose coverage

The D_{50} and D_{90} results for single-ion multifield treatment plans are shown in Table 5.4. D_{50} remains extremely high, with the lowest being 97.79% for ^{16}O; however, compared to the single-field cases, D_{90} has modestly increased in most cases, with some exceeding 90%. A notable exception is ^{12}C, which obtained a significantly lower D_{90} score in each case. The reasons for this are unclear, and we are continuing to investigate this unexpected anomaly.

The D_{50} and D_{90} results for multi-ion multifield treatment plans are shown in Table 5.5. As for the single-ion cases, D_{50} remains extremely high, exceeding 99% in all cases and reaching 100% in several instances. Compared to the single-field cases, D_{90} has also modestly increased, with no obvious regressions compared to the single-field cases.

The D_{50} and D_{90} isosurfaces for the all-ion treatment plans are shown in Figure 5.16 and 5.17, respectively.

5.4.4 Normal tissue dose

The volumes of normal tissue outside of the PTV which received doses in excess of 5%, 10% and 50%, respectively are listed in Table 5.6 and 5.7 for the single-ion and multi-ion multifield treatment plans, respectively. Compared to the corresponding

Table 5.4: Percentages of the target volume that received at least 50%, and 90% of the dose volume; no hypoxic sub-volume within the tumour, OAR region distal to tumour.

Number of fields	Ion combination	D_{50}	D_{90}
2	^{1}**H**	99.88	88.49
	^{4}**He**	99.82	88.60
	^{12}**C**	98.53	57.19
	^{16}**O**	97.79	66.61
3	^{1}**H**	100.00	89.78
	^{4}**He**	99.99	90.22
	^{12}**C**	99.89	78.60
	^{16}**O**	99.87	80.55
4	^{1}**H**	99.99	88.61
	^{4}**He**	99.96	89.53
	^{12}**C**	99.89	83.81
	^{16}**O**	99.74	83.66
5	^{1}**H**	100.00	89.11
	^{4}**He**	99.96	90.03
	^{12}**C**	99.90	86.55
	^{16}**O**	99.87	86.24

Table 5.5: Percentages of the target volume that received at least 50%, and 90% of the dose volume; hypoxic sub-volume within the tumour, OAR region distal to the tumour.

Number of fields	Ion combination	D_{50}	D_{90}
2	^{1}**H**, ^{12}**C**	99.79	88.21
	^{4}**He**, ^{16}**O**	99.57	86.68
	^{1}**H**, ^{4}**He**, ^{16}**O**	99.74	88.43
	^{7}**Li**, ^{12}**C**, ^{56}**Fe**	99.30	79.68
	All ions	99.77	88.59
3	^{1}**H**, ^{12}**C**	100.00	89.93
	^{4}**He**, ^{16}**O**	99.99	89.89
	^{1}**H**, ^{4}**He**, ^{16}**O**	100.00	90.59
	^{7}**Li**, ^{12}**C**, ^{56}**Fe**	99.99	87.63
	All ions	100.00	90.72
4	^{1}**H**, ^{12}**C**	99.99	88.79
	^{4}**He**, ^{16}**O**	99.95	89.41
	^{1}**H**, ^{4}**He**, ^{16}**O**	99.96	89.51
	^{7}**Li**, ^{12}**C**, ^{56}**Fe**	99.96	88.36
	All ions	99.96	89.72
5	^{1}**H**, ^{12}**C**	99.99	89.38
	^{4}**He**, ^{16}**O**	99.96	90.05
	^{1}**H**, ^{4}**He**, ^{16}**O**	99.99	90.15
	^{7}**Li**, ^{12}**C**, ^{56}**Fe**	99.96	89.29
	All ions	99.99	90.26

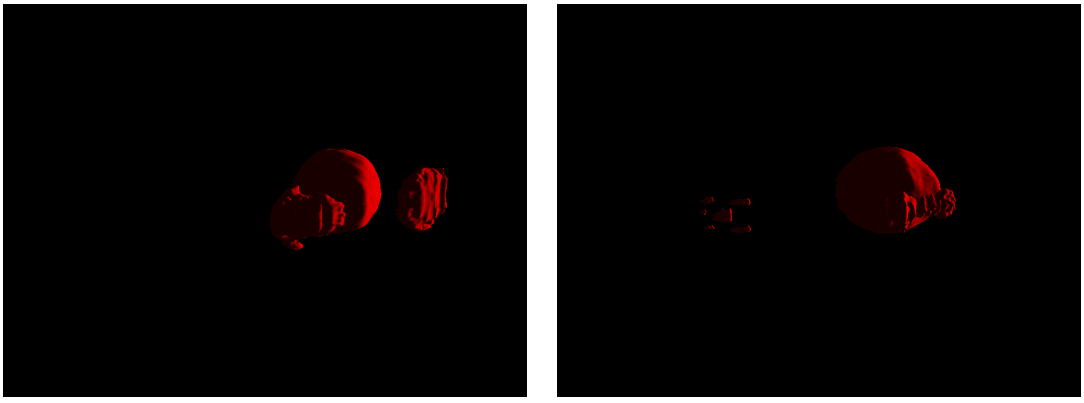

(a) 2 fields

(b) 3 fields

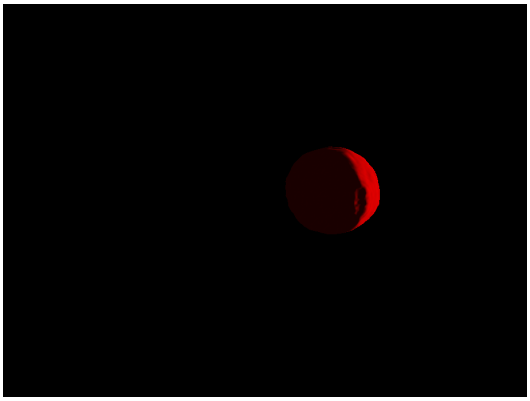

(c) 4 fields

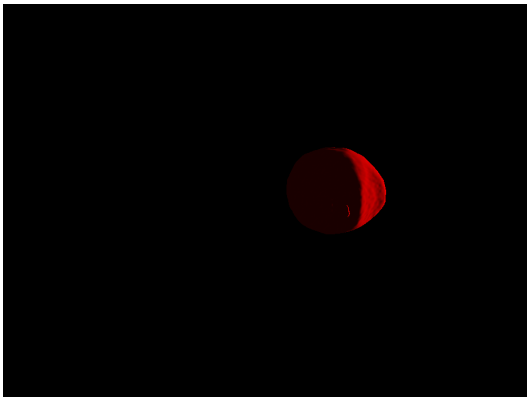

(d) 5 fields

Figure 5.16: 50% isodose surfaces for 8-ion, 2/3/4/5-field treatment plans; a hypoxic sub-volume is defined within the tumour and an OAR region defined distal to the tumour.

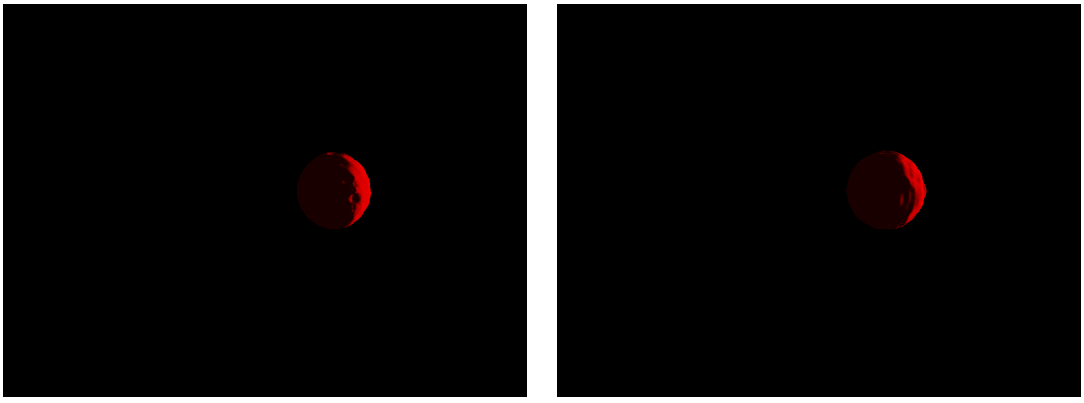

(a) 2 fields

(b) 3 fields

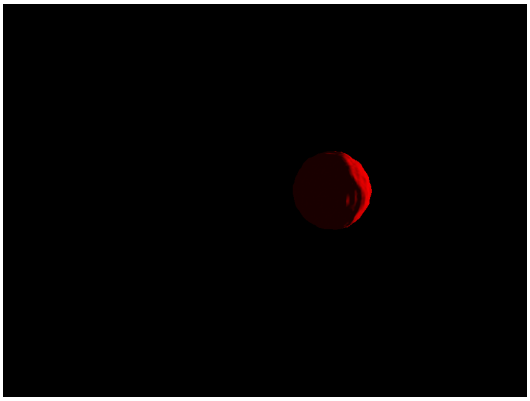

(c) 4 fields

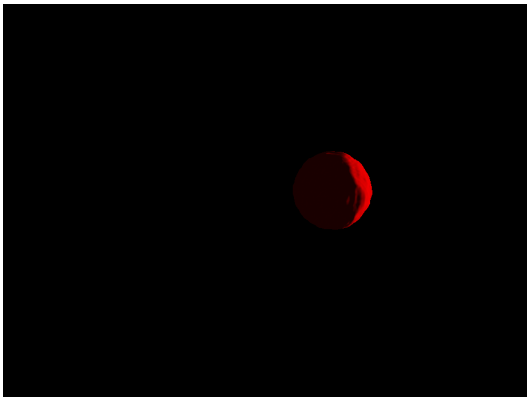

(d) 5 fields

Figure 5.17: 90% isodose surfaces for 8-ion, 2/3/4/5-field treatment plans; a hypoxic sub-volume is defined within the tumour and an OAR region defined distal to the tumour.

Table 5.6: Total volumes outside the tumour which received at least 5%, 10% and 50% of the target dose volume in mm^3; no hypoxic sub-volume within the tumour, OAR region defined distal to the tumour. Planning target volume (PTV) is 14147 mm^3.

Number of fields	Ion combination	V_5 mm^3	V_{10} mm^3	V_{50} mm^3
2	^{1}**H**	113250	95770	27568
	^{4}**He**	109255	92206	27683
	^{12}**C**	114131	93168	24201
	^{16}**O**	113412	93867	25341
3	^{1}**H**	119611	99151	6659
	^{4}**He**	115887	95926	6588
	^{12}**C**	118132	97278	5780
	^{16}**O**	118401	97602	6041
4	^{1}**H**	126931	102740	6296
	^{4}**He**	123414	99659	5755
	^{12}**C**	126014	101833	4899
	^{16}**O**	126241	102002	5293
5	^{1}**H**	129387	101426	6026
	^{4}**He**	126210	97700	5564
	^{12}**C**	128957	101842	4992
	^{16}**O**	129082	101879	5314

Table 5.7: Total volumes outside the tumour which received at least 5%, 10% and 50% of the target dose volume in mm^3; hypoxic sub-volume defined within the tumour, OAR region defined distal to the tumour. Planning target volume (PTV) is 14147 mm^3.

Number of fields	Ion combination	V_5 mm^3	V_{10} mm^3	V_{50} mm^3
2	^{1}**H**,^{12}**C**	113479	95944	27344
	^{4}**He**,^{16}**O**	110552	93388	27638
	^{1}**H**,^{4}**He**,^{16}**O**	113337	95865	27346
	^{7}**Li**,^{12}**C**,^{56}**Fe**	112698	94082	27860
	All ions	113407	96020	27402
3	^{1}**H**,^{12}**C**	119847	99295	6848
	^{4}**He**,^{16}**O**	116945	97024	6788
	^{1}**H**,^{4}**He**,^{16}**O**	119514	99115	6920
	^{7}**Li**,^{12}**C**,^{56}**Fe**	118065	98277	7129
	All ions	119543	99309	6973
4	^{1}**H**,^{12}**C**	127394	103242	6131
	^{4}**He**,^{16}**O**	124855	101260	5832
	^{1}**H**,^{4}**He**,^{16}**O**	126982	102978	6119
	^{7}**Li**,^{12}**C**,^{56}**Fe**	126075	102565	5640
	All ions	127206	103356	6110
5	**H**,^{12}**C**	129936	102350	5924
	^{4}**He**,^{16}**O**	127619	100425	5632
	^{1}**H**,^{4}**He**,^{16}**O**	129350	101974	5894
	^{7}**Li**,^{12}**C**,^{56}**Fe**	129128	102838	5594
	All ions	129697	102676	5908

single-field results in Chapter 4 (Tables 4.11-4.12), it is clear that the normal tissue receiving a high dose is greatly reduced in each case, while the volume of tissue receiving a low dose has increased. The V_{50} results are now smaller than for the single-field cases by a factor of 1/2 to 1/9; on the other hand, volumes V_5 and V_{10} have increased by a factor of 2-5. This demonstrates the ability of multifield treatments to spread the normal tissue dose rather than concentrating it in a single volume of tissue.

5.5 Conclusion

A multifield extension to the treatment planning system introduced in Chapter 3 and extended in Chapter 4 has been implemented, demonstrated and evaluated using similar objectives and metrics as the single-field version of the TPS. The multifield algorithm offers a good trade-off between global near-optimality and computational efficiency. The resulting treatment plans exhibit a range of improved performance metrics compared to single-field treatment plans, including improved uniformity, moderate improvements to dose coverage and reduced dose to normal tissue. A multifield, multi-ion treatment plan also enables more use to be made of the diversity of ion beam characteristics, since the it allows more of the tumour to be treated as 'shallow' and hence the fragmentation tail present in heavy ion therapy can contribute to dose to the target rather than delivering unwanted dose to normal tissues or OARs.

CHAPTER 6

Conclusions and Future Work

This thesis addressed the problem of achieving optimal irradiation of a tumour in a heterogeneous physical structure with an arbitrary objective spatial dose distributions using arbitrary combinations of a wide range of ions. The TPS aimed to minimse the dose to the surrounding normal tissues and organs at risk in particular, while enabling enhanced LET in hypoxic subvolumes within the tumour, which tend to be highly resistant to radiation damage. Our hypothesis - that this objective can be achieved more effectively with a manifold multi-ion treatment plan - was confirmed in all evaluated test scenarios, regardless of tumour depth relative to the target phantom, and with and without hypoxic subvolumes present in the tumour or OARs behind the tumour. Metrics including dose uniformity and dose conformance both strongly supported our hypothesis. There was no significant benefit observed in terms of minimising the dose to healthy tissues; however, the manifold multi-ion treatment plans also did not perform significantly worse than single-ion, dual-ion or triple-ion treatment plans. Therefore, we conclude that provided a suitable multi-ion radiation source (such as future laser-driven multi-ion therapy systems) is available, manifold multi-ion therapy should offer a therapeutic advantage over single-ion or limited multi-ion therapy. This is because treatment plans exploiting a diversity of light and heavy ions can construct their dose distributions by using an optimal combination of the best physical properties of each individual ion. The methods developed in our TPS will be ready for the advent of such manifold multi-ion radiation sources.

6.1 Summary of Contributions

In Chapter 2, the underlying physics of charged particles, their biological impacts on tumours, and their application in radiation therapy for cancer are introduced. The specific characteristics of different ion species used in particle therapy, and the impact of these characteristics on cancer cells and macroscopic tumours are discussed. A comprehensive overview of one of the most promising future technologies for particle therapy delivery - laser-driven particle accelerators - is presented, together with a discussion of the factors which will guide the application of laser-driven accelerators in medicine for cancer radiation therapy. The principles of laser-driven ion acceleration are introduced, and the most common laser plasma acceleration techniques (Target Normal Sheath Acceleration and Radiation Pressure Acceleration), the characteristics of laser-driven ion beams, and in-vitro and in-vivo experiments investigating the radiobiological impacts of laser-driven particle irradiation are discussed.

The design of a new open source multi-ion particle therapy is presented in Chapter 3. The TPS is based on a combined Monte Carlo and linear optimisation based approach, which can select an appropriate combinations of ions and energies (subject to configurable parameters which apply to a specific particular accelerator) to achieve a desired spatial distribution of dose in a heterogeneous target. A range of treatment plans are developed for tumours at different positions in a simple human head phantom, using single ion species, pairs of ions, triplets of ions and the full set of supported ions. Several critical performance metrics are evaluated to compare the resulting plans, including RMS error between the objective and the achieved dose distributions (which evaluates dose uniformity) and the fraction of the target which receives more than 50% and 90% of the target dose (D_{50} and D_{90}). The lowest RMSE is consistently achieved in the target volume with the 8-ion treatment plan for all tumour positions. Additionally, all treatment plans achieved excellent coverage of the tumour, with more than 99% of the target receiving at least 50% of the nominal target dose. The D_{90} coverage was better than 82.8% for all single-ion and combination treatment plans, with the 8-ion plans achieving the best D_{90} coverage in all cases; again, this supports the hypothesis. Finally, The results for V_5, V_{10} and V_{50} are very similar across all the different ion combinations, neither showing a significant advantage nor disadvantage for the manifold multi-ion treatment plans compared to analogous single ion or dual/triple ion treatment plans.

In Chapter 4, the TPS described in Chapter 3 is extended to include protection for radiation-sensitive organs (organs at risk) and linear energy transfer enhancement in hypoxic target subvolumes. For the case with a hypoxic volume and no OAR, the 8-ion plan again produces the lowest target and distal boundary RMSE for all tumour positions, and no plan produces consistently lower RMSE in the other defined regions. Our data also shows that in the absence of hypoxic regions, but with a distal OAR present, the 8-ion plan again performs well in terms of tumour RMSE - however, in the central and deep tumour locations, it is outperformed by the three-ion combination of proton, helium and oxygen. Finally, when both hypoxic and OAR regions are defined, the 8-ion plan also achieves the best target dose conformance in all tumour positions, and is highly competitive with proton-only OAR RMSE. With the presence of an OAR (both with and without a hypoxic region), the best D_{50} coverage was again achieved by the 8-ion plans; the 8-ion plans were also able to provide the best D_{90} in most cases (especially for the case where both hypoxic and OAR regions were defined). The vast majority of these results support the hypothesis that superior dose uniformity and target coverage can be achieved using a multi-ion combination treatment plan.

Chapter 5 extended the developed TPS to support multifield irradiation. An algorithm was developed which required minimal additional resident memory requirements beyond those needed for single-field treatment planning, yet is able to satisfactory deal with cases where part of the target is obscured by an OAR from some field angles. The performance of the multifield TPS was evaluated and the benefits over a single-field plan demonstrated for multifield irradiation with a single axis of rotation. The multifield TPS can be trivially extended to support two-axis rotations as well if desired, although this is rarely necessary in practice.

This thesis has been completed as a joint project between the School of Biomedical Engineering and the School of Electrical and Data Engineering at UTS, and the contributions described above neatly straddle the two fields. From a biomedical engineering perspective, this work has demonstrated the potential advantages of extending single-ion and dual/limited multi-ion therapy to manifold combinations of ions due to the improved dose conformance which can be achieved. It is very likely that improved (or at least more consistent and predictable) clinical outcomes will be achieved as a result of the increased degree of control afforded by such a scheme. From an electrical and data engineering perspective, this work has demonstrated the computational feasibility of a number of novel approaches to treatment planning with

a diverse array of ion species, and developed and applied new algorithms for achieving a complex multi-objective optimised treatment plan.

6.1.1 Recommendations & future work

The key finding from this work is that there are consistent benefits in terms of both dose uniformity and conformance to the target volume which may be achieved using manifold multi-ion therapy compared with single-ion, dual-ion or triple-ion treatment plans. As treatment objectives become more sophisticated with improvements in biophysical modelling and cancer imaging (especially the imaging of hypoxic tumour regions), the advantages of precise control of dose and LET distributions which can be provided by manifold multi-ion therapy will become even more relevant.

Further work is needed to demonstrate the TPS in an anthropomorphic phantom, including the definition of real OARs. As Geant4 already includes support for an ICRU male and female adult anthropomorphic phantom, this will be a straightforward extension of the work presented in Chapters 3 - 5. Beyond this, it would be highly desirable to implement the treatment plans at a pencil-beam particle therapy facility capable of supporting several different ions (e.g. Japan's HIMAC), and perform irradiations of a heterogeneous 3D-printed anthoropomorphic phantom with a 3D gafchromic dosimetric gel insert.

If biological dose is required rather than physical dose optimisation, it is a relatively straightforward process to extend the TPS to implement this, given reliable RBE models for each of the target tissues. This can be estimated for a single cell line by either obtaining LET data from Geant4 simulations and applying a suitable biophysical model with appropriate parameters, or using experimental RBE measurements. Unfortunately, a complete database of such experimental data does not yet exist, and moreover, where it does exist, tends to assume that cancer and normal tissue response to dose is independent of dose rate. With the emergence of FLASH radiotherapy modalities demonstrating that this is not generally the case, it is clear that a general biophysical model which properly considers dose, LET and dose rate should be developed if true biological dose is to be used in treatment planning. This remains an open topic for research.

A number of serious challenges led to this work taking longer than originally planned. The computational workload was chiefly related to optimisation of treatment plans rather than the Geant4 simulations used to construct the dose distribution libraries. There are several ways in which this could be accelerated - firstly, through the use

of improved optimisation algorithms, for example by replacing MATLAB's default `lsqnonlin` optimiser by an implementation of the Fast NNLS algorithm [178]; and secondly, by the use of GPU acceleration for the optimisation algorithm (which may require an implementation in CUDA or OpenCL to be developed). Development of automatic algorithms for determining an optimal number of samples from each subvolume of the target and surrounding tissues would also be a valuable addition, as this will minimise the size of the matrix $\mathbf{C}$ which dominates the order of magnitude of computational complexity of the developed algorithm. Finally, faster and larger memory (possibly exploiting sparsity and in-memory compression) would enable a complete, simultaneous multi-field or spot-scanning hadron arc therapy treatment planning system to be implemented, which may outperform the solution developed for multi-field treatment planning in this work.

6.1.2 Concluding remarks

In summary, this thesis has demonstrated a working treatment planning system which is capable of producing optimised treatment plans using a wide range of ion species. The method is extremely general and can be extended to any number of ions. The proposed TPS is ideally suited to future laser-driven therapeutic particle accelerator systems, while also being applicable to existing synchrotron-based sources. The technique has been used to demonstrate the potential improvements in dose conformance which are achievable using a wider range of ions compared to the dual and triple ion combinations hitherto explored in the literature.

Bibliography

[1] W. Wang, W. Li, J. Liu, Z. Zhang, R. Qi, C. Yu, J. Liu, M. Fang, Z. Qin, C. Wang, Y. Xu, F. Wu, Y. Leng, R. Li, and Z. Xu, "High-brightness high-energy electron beams from a laser wakefield accelerator via energy chirp control," *Physical Review Letters*, vol. 117, Sept. 2016.

[2] E. L. Alpen, *Radiation Biophysics*. Academic Press, 2 ed., Oct. 1997.

[3] H. Murshed, ed., *Fundamentals of radiation oncology*. San Diego, CA: Academic Press, 3 ed., Mar. 2019.

[4] D. Schardt, T. Elsässer, and D. Schulz-Ertner, "Heavy-ion tumor therapy: Physical and radiobiological benefits," *Reviews of Modern Physics*, vol. 82, pp. 383–425, Feb. 2010.

[5] L. Burigo, I. Pshenichnov, I. Mishustin, and M. Bleicher, "Comparative study of dose distributions and cell survival fractions for1h, 4he, 12c and16o beams using geant4 and microdosimetric kinetic model," *Physics in Medicine and Biology*, vol. 60, pp. 3313–3331, Mar. 2015.

[6] E. Malinen and Å. Søvik, "Dose or 'LET' painting – what is optimal in particle therapy of hypoxic tumors?," *Acta Oncologica*, vol. 54, pp. 1614–1622, July 2015.

[7] N. Bassler, O. Jäkel, C. S. Søndergaard, and J. B. Petersen, "Dose- and LET-painting with particle therapy," *Acta Oncologica*, vol. 49, pp. 1170–1176, Sept. 2010.

[8] R. Grün, T. Friedrich, M. Krämer, K. Zink, M. Durante, R. Engenhart-Cabillic, and M. Scholz, "Assessment of potential advantages of relevant ions for particle therapy: A model based study," *Medical Physics*, vol. 42, pp. 1037–1047, Jan. 2015.

[9] T. Inaniwa, N. Kanematsu, K. Noda, and T. Kamada, "Treatment planning of intensity modulated composite particle therapy with dose and linear energy transfer optimization," *Physics in Medicine and Biology*, vol. 62, pp. 5180–5197, May 2017.

[10] B. Kopp, S. Mein, I. Dokic, S. Harrabi, T. T. Böhlen, T. Haberer, J. Debus, A. Abdollahi, and A. Mairani, "Development and validation of single field multi-ion particle therapy treatments," *International Journal of Radiation Oncology∗Biology∗Physics*, vol. 106, pp. 194–205, Jan. 2020.

[11] O. Sokol, M. Krämer, S. Hild, M. Durante, and E. Scifoni, "Kill painting of hypoxic tumors with multiple ion beams," *Physics in Medicine & Biology*, vol. 64, p. 045008, Feb. 2019.

[12] A. Giulietti, *Laser-driven particle acceleration towards radiobiology and medicine*. Springer, 2016.

[13] C. Grau, M. Durante, D. Georg, J. A. Langendijk, and D. C. Weber, "Particle therapy in europe," *Molecular Oncology*, vol. 14, pp. 1492–1499, Apr. 2020.

[14] R. R. Wilson, "Radiological use of fast protons," *Radiology*, vol. 47, pp. 487–491, Nov. 1946.

[15] P. T. C.-O. Group, "Statistics of patients treated in particle therapy facilities worldwide:." https://ptcog.ch/index.php/patient-statistics, 2021.

[16] D. A. Jaffray and M. K. Gospodarowicz, "Radiation therapy for cancer," *Disease Control Priorities, Third Edition (Volume 3): Cancer*, p. 239–247, Nov 2015.

[17] D. S. Chang, F. D. Lasley, I. J. Das, M. S. Mendonca, J. R. Dynlacht, *et al.*, *Basic radiotherapy physics and biology*. Springer, 2014.

[18] G. F. Knoll, *Radiation detection and measurement*. John Wiley & Sons, 2010.

[19] E. B. Podgorsak, *Radiation Physics for Medical Physicists*. Springer International Publishing, 2016.

[20] A. J. Lomax, "Charged particle therapy: The physics of interaction," *The Cancer Journal*, vol. 15, pp. 285–291, July 2009.

[21] F. Bloch, "Zur bremsung rasch bewegter teilchen beim durchgang durch materie," *Annalen der Physik*, vol. 408, no. 3, pp. 285–320, 1933.

[22] B. Gottschalk, "Radiotherapy proton interactions in matter," *arXiv preprint arXiv:1804.00022*, 2018.

[23] H. Paganetti, "Proton beam therapy," in *Proton Beam Therapy*, IOP Publishing, 2016.

[24] N. Bassler, J. Toftegaard, A. Lühr, B. S. Sørensen, E. Scifoni, M. Krämer, O. Jäkel, L. S. Mortensen, J. Overgaard, and J. B. Petersen, "LET-painting increases tumour control probability in hypoxic tumours," *Acta Oncologica*, vol. 53, pp. 25–32, Sept. 2013.

[25] S. J. McMahon, "The linear quadratic model: usage, interpretation and challenges," *Physics in Medicine & Biology*, vol. 64, p. 01TR01, Dec. 2018.

[26] P. Metcalfe, T. Kron, and P. Hoban, *The physics of radiotherapy x-rays and electrons*. Medical Physics Publ., 2012.

[27] K. Tanderup, D. R. Olsen, and C. Grau, "Dose painting: Art or science?," *Radiotherapy and Oncology*, vol. 79, pp. 245–248, June 2006.

[28] A. R. Smith, "Proton therapy," *Physics in Medicine and Biology*, vol. 51, pp. R491–R504, June 2006.

[29] T. Inaniwa, T. Furukawa, Y. Kase, N. Matsufuji, T. Toshito, Y. Matsumoto, Y. Furusawa, and K. Noda, "Treatment planning for a scanned carbon beam with a modified microdosimetric kinetic model," *Physics in Medicine and Biology*, vol. 55, pp. 6721–6737, Oct. 2010.

[30] M. Durante, R. Orecchia, and J. S. Loeffler, "Charged-particle therapy in cancer: clinical uses and future perspectives," *Nature Reviews Clinical Oncology*, vol. 14, pp. 483–495, Mar. 2017.

[31] T. Wenzl and J. J. Wilkens, "Modelling of the oxygen enhancement ratio for ion beam radiation therapy," *Physics in Medicine and Biology*, vol. 56, pp. 3251–3268, May 2011.

[32] L. Antonovic, E. Lindblom, A. Dasu, N. Bassler, Y. Furusawa, and I. Toma-Dasu, "Clinical oxygen enhancement ratio of tumors in carbon ion radiotherapy: the influence of local oxygenation changes," *Journal of Radiation Research*, vol. 55, pp. 902–911, Apr. 2014.

[33] E. Scifoni, W. Tinganelli, W. K. Weyrather, M. Durante, A. Maier, and M. Krämer, "Including oxygen enhancement ratio in ion beam treatment planning: model implementation and experimental verification," *Physics in Medicine and Biology*, vol. 58, pp. 3871–3895, May 2013.

[34] R. D. Stewart, V. K. Yu, A. G. Georgakilas, C. Koumenis, J. H. Park, and D. J. Carlson, "Effects of radiation quality and oxygen on clustered DNA lesions and cell death," *Radiation Research*, vol. 176, pp. 587–602, Nov. 2011.

[35] E. Pedroni, S. Scheib, T. Böhringer, A. Coray, M. Grossmann, S. Lin, and A. Lomax, "Experimental characterization and physical modelling of the dose distribution of scanned proton pencil beams," *Physics in Medicine and Biology*, vol. 50, pp. 541–561, Jan. 2005.

[36] E. Pedroni, T. Böhringer, A. Coray, E. Egger, M. Grossmann, S. Lin, A. Lomax, G. Goitein, W. Roser, and B. Schaffner, "Initial experience of using an active beam delivery technique at PSI," *Strahlentherapie und Onkologie*, vol. 175, pp. 18–20, June 1999.

[37] T. Haberer, W. Becher, D. Schardt, and G. Kraft, "Magnetic scanning system for heavy ion therapy," *Nuclear Instruments and Methods in Physics Research Section A: Accelerators, Spectrometers, Detectors and Associated Equipment*, vol. 330, pp. 296–305, June 1993.

[38] G. KRAFT, "Tumor therapy with heavy charged particles," *Progress in Particle and Nuclear Physics*, vol. 45, pp. S473–S544, 2000.

[39] Particle Therapy Co-Operative , "Statistics about patient treated with particles: 2018." https://www.ptcog.ch/, 2020.

[40] O. Jäkel, "Heavy ion radiotherapy," in *New Technologies in Radiation Oncology*, pp. 365–377, Springer, 2006.

[41] H. Suit, T. DeLaney, S. Goldberg, H. Paganetti, B. Clasie, L. Gerweck, A. Niemierko, E. Hall, J. Flanz, J. Hallman, and A. Trofimov, "Proton vs carbon ion beams in the definitive radiation treatment of cancer patients," *Radiotherapy and Oncology*, vol. 95, pp. 3–22, Apr. 2010.

[42] M. Durante and H. Paganetti, "Nuclear physics in particle therapy: a review," *Reports on Progress in Physics*, vol. 79, p. 096702, aug 2016.

[43] M. Krämer, E. Scifoni, C. Schuy, M. Rovituso, W. Tinganelli, A. Maier, R. Kaderka, W. Kraft-Weyrather, S. Brons, T. Tessonnier, *et al.*, "Helium ions for radiotherapy? physical and biological verifications of a novel treatment modality," *Medical physics*, vol. 43, no. 4, pp. 1995–2004, 2016.

[44] O. Sokol, E. Scifoni, W. Tinganelli, W. Kraft-Weyrather, J. Wiedemann, A. Maier, D. Boscolo, T. Friedrich, S. Brons, M. Durante, and M. Krämer, "Oxygen beams for therapy: advanced biological treatment planning and experimental verification," *Physics in Medicine & Biology*, vol. 62, pp. 7798–7813, Sept. 2017.

[45] F. Tommasino, E. Scifoni, and M. Durante, "New ions for therapy," *International Journal of Particle Therapy*, vol. 2, pp. 428–438, Dec. 2015.

[46] T. Inaniwa and N. Kanematsu, "Adaptation of stochastic microdosimetric kinetic model for charged-particle therapy treatment planning," *Physics in Medicine & Biology*, vol. 63, p. 095011, May 2018.

[47] F. Guan, L. Bronk, U. Titt, S. H. Lin, D. Mirkovic, M. D. Kerr, X. R. Zhu, J. Dinh, M. Sobieski, C. Stephan, C. R. Peeler, R. Taleei, R. Mohan, and D. R. Grosshans, "Spatial mapping of the biologic effectiveness of scanned particle beams: towards biologically optimized particle therapy," *Scientific Reports*, vol. 5, May 2015.

[48] J. J. Wilkens and U. Oelfke, "Direct comparison of biologically optimized spread-out bragg peaks for protons and carbon ions," *International Journal of Radiation Oncology∗Biology∗Physics*, vol. 70, pp. 262–266, Jan. 2008.

[49] I. Dokic, A. Mairani, M. Niklas, F. Zimmermann, N. Chaudhri, D. Krunic, T. Tessonnier, A. Ferrari, K. Parodi, O. Jäkel, J. Debus, T. Haberer, and A. Abdollahi, "Next generation multi-scale biophysical characterization of high precision cancer particle radiotherapy using clinical proton, helium-, carbon- and oxygen ion beams," *Oncotarget*, vol. 7, Aug. 2016.

[50] D. Habermehl, K. Ilicic, S. Dehne, S. Rieken, L. Orschiedt, S. Brons, T. Haberer, K.-J. Weber, J. Debus, and S. E. Combs, "The relative biological effectiveness for carbon and oxygen ion beams using the raster-scanning technique in hepatocellular carcinoma cell lines," *PLoS ONE*, vol. 9, p. e113591, Dec. 2014.

[51] W. Saunders, J. R. Castro, G. T. Y. Chen, J. M. Collier, S. R. Zink, S. Pitluck, T. L. Phillips, D. Char, P. Gutin, G. Gauger, C. A. Tobias, and E. L. Alpen, "Helium-ion radiation therapy at the lawrence berkeley laboratory: Recent results of a northern california oncology group clinical trial," *Radiation Research*, vol. 104, p. S227, Nov. 1985.

[52] M. Krämer, E. Scifoni, C. Schuy, M. Rovituso, W. Tinganelli, A. Maier, R. Kaderka, W. Kraft-Weyrather, S. Brons, T. Tessonnier, K. Parodi, and M. Durante, "Helium ions for radiotherapy? physical and biological verifications of a novel treatment modality," *Medical Physics*, vol. 43, pp. 1995–2004, Mar. 2016.

[53] B. Knäusl, H. Fuchs, K. Dieckmann, and D. Georg, "Can particle beam therapy be improved using helium ions? – a planning study focusing on pediatric patients," *Acta Oncologica*, vol. 55, pp. 751–759, Jan. 2016.

[54] D. Thorwarth, M. Soukup, and M. Alber, "Dose painting with IMPT, helical tomotherapy and IMXT: A dosimetric comparison," *Radiotherapy and Oncology*, vol. 86, pp. 30–34, Jan. 2008.

[55] K. Chao, W. R. Bosch, S. Mutic, J. S. Lewis, F. Dehdashti, M. A. Mintun, J. F. Dempsey, C. A. Perez, J. A. Purdy, and M. J. Welch, "A novel approach to overcome hypoxic tumor resistance: Cu-ATSM-guided intensity-modulated radiation therapy," *International Journal of Radiation Oncology∗Biology∗Physics*, vol. 49, pp. 1171–1182, Mar. 2001.

[56] Y. Kim and W. A. Tomé, "Dose-painting IMRT optimization using biological parameters," *Acta Oncologica*, vol. 49, pp. 1374–1384, Apr. 2010.

[57] C. Ling, J. Humm, S. Larson, H. Amols, Z. Fuks, S. Leibel, and J. A. Koutcher, "Towards multidimensional radiotherapy (MD-CRT): biological imaging and biological conformality," *International Journal of Radiation Oncology∗Biology∗Physics*, vol. 47, pp. 551–560, June 2000.

[58] S. M. Bentzen, "Theragnostic imaging for radiation oncology: dose-painting by numbers," *The Lancet Oncology*, vol. 6, pp. 112–117, Feb. 2005.

[59] J. Unkelbach, M. Bangert, K. De Amorim Bernstein, N. Andratschke, and M. Guckenberger, "Optimization of combined proton-photon treatments," *Radiotherapy and Oncology*, vol. 128, no. 1, pp. 133–138, 2018.

[60] P. Bolton, K. Parodi, and J. Schreiber, *Applications of laser-driven particle acceleration*. CRC Press, 2018.

[61] G. Ising, "Prinzip einer methode zur herstellung von kanalstrahlen hoher voltzahl," *Ark. Mat. Astron. Fys.*, vol. 18, no. 30, pp. 1–4, 1924.

[62] R. Wideröe, "Über ein neues prinzip zur herstellung hoher spannungen," *Archiv für Elektrotechnik*, vol. 21, pp. 387–406, July 1928.

[63] R. J. Van De Graaff, K. Compton, and L. Van Atta, "The electrostatic production of high voltage for nuclear investigations," *Physical Review*, vol. 43, no. 3, p. 149, 1933.

[64] E. L. Ginzton, W. W. Hansen, and W. R. Kennedy, "A linear electron accelerator," *Review of scientific instruments*, vol. 19, no. 2, pp. 89–108, 1948.

[65] L. W. Alvarez, H. Bradner, J. V. Franck, H. Gordon, J. D. Gow, L. C. Marshall, F. Oppenheimer, W. K. Panofsky, C. Richman, and J. R. Woodyard, "Berkeley proton linear accelerator," *Review of Scientific Instruments*, vol. 26, no. 2, pp. 111–133, 1955.

[66] S. Dutta, R. K. Woo, and T. M. Krummel, "Advanced and emerging surgical technologies and the process of innovation," in *Pediatric Surgery*, pp. 37–75, Elsevier, 2012.

[67] E. O. Lawrence and M. S. Livingston, "The production of high speed light ions without the use of high voltages," *Physical Review*, vol. 40, pp. 19–35, Apr. 1932.

[68] V. I. Veksler, "A new method of acceleration of relativistic particles," *J. Phys.*, vol. 9, pp. 153–158, 1945.

[69] E. M. McMillan, "The synchrotron—a proposed high energy particle accelerator," *Physical Review*, vol. 68, no. 5-6, p. 143, 1945.

[70] T. Tajima and J. M. Dawson, "Laser electron accelerator," *Physical Review Letters*, vol. 43, pp. 267–270, July 1979.

[71] L. Whitmore, R. I. Mackay, M. van Herk, J. K. Jones, and R. M. Jones, "Focused vhee (very high energy electron) beams and dose delivery for radiotherapy applications," *Scientific Reports*, vol. 11, July 2021.

[72] S. V. Bulanov and V. S. Khoroshkov, "Feasibility of using laser ion accelerators in proton therapy," *Plasma Physics Reports*, vol. 28, pp. 453–456, May 2002.

[73] V. Malka, S. Fritzler, E. Lefebvre, E. d'Humières, R. Ferrand, G. Grillon, C. Albaret, S. Meyroneinc, J.-P. Chambaret, A. Antonetti, *et al.*, "Practicability of protontherapy using compact laser systems," *Medical physics*, vol. 31, no. 6, pp. 1587–1592, 2004.

[74] A. Caldwell, K. Lotov, A. Pukhov, and F. Simon, "Proton-driven plasma-wakefield acceleration," *Nature Physics*, vol. 5, pp. 363–367, Apr. 2009.

[75] E. Esarey, C. B. Schroeder, and W. P. Leemans, "Physics of laser-driven plasma-based electron accelerators," *Reviews of Modern Physics*, vol. 81, pp. 1229–1285, Aug. 2009.

[76] P. Bolton, T. Hori, H. Kiriyama, M. Mori, H. Sakaki, K. Sutherland, M. Suzuki, J. Wu, and A. Yogo, "Toward integrated laser-driven ion accelerator systems at the photo-medical research center in japan," *Nuclear Instruments and Methods in Physics Research Section A: Accelerators, Spectrometers, Detectors and Associated Equipment*, vol. 620, no. 1, pp. 71–75, 2010.

[77] H. Daido, M. Nishiuchi, and A. S. Pirozhkov, "Review of laser-driven ion sources and their applications," *Reports on Progress in Physics*, vol. 75, p. 056401, Apr. 2012.

[78] R. Pompili, D. Alesini, M. P. Anania, M. Behtouei, M. Bellaveglia, A. Biagioni, F. G. Bisesto, M. Cesarini, E. Chiadroni, A. Cianchi, G. Costa, M. Croia, A. D. Dotto, D. D. Giovenale, M. Diomede, F. Dipace, M. Ferrario, A. Giribono, V. Lollo, L. Magnisi, M. Marongiu, A. Mostacci, L. Piersanti, G. D. Pirro, S. Romeo, A. R. Rossi, J. Scifo, V. Shpakov, C. Vaccarezza, F. Villa, and A. Zigler, "Energy spread minimization in a beam-driven plasma wakefield accelerator," *Nature Physics*, Jan. 2021.

[79] M. Borghesi, A. J. Mackinnon, D. H. Campbell, D. G. Hicks, S. Kar, P. K. Patel, D. Price, L. Romagnani, A. Schiavi, and O. Willi, "Multi-MeV proton source investigations in ultraintense laser-foil interactions," *Physical Review Letters*, vol. 92, Feb. 2004.

[80] T. E. Cowan, J. Fuchs, H. Ruhl, A. Kemp, P. Audebert, M. Roth, R. Stephens, I. Barton, A. Blazevic, E. Brambrink, J. Cobble, J. Fernández, J.-C. Gauthier, M. Geissel, M. Hegelich, J. Kaae, S. Karsch, G. P. L. Sage, S. Letzring, M. Manclossi, S. Meyroneinc, A. Newkirk, H. Pépin, and N. Renard-LeGalloudec, "Ultralow emittance, multi-MeV proton beams from a laser virtual-cathode plasma accelerator," *Physical Review Letters*, vol. 92, May 2004.

[81] H. Ruhl, T. Cowan, and J. Fuchs, "The generation of micro-fiducials in laser-accelerated proton flows, their imaging property of surface structures and application for the characterization of the flow," *Physics of Plasmas*, vol. 11, pp. L17–L20, May 2004.

[82] J. Schreiber, M. Kaluza, F. Grüner, U. Schramm, B. Hegelich, J. Cobble, M. Geissler, E. Brambrink, J. Fuchs, P. Audebert, D. Habs, and K. Witte, "Source-size measurements and charge distributions of ions accelerated from thin foils irradiated by high-intensity laser pulses," *Applied Physics B*, vol. 79, pp. 1041–1045, Dec. 2004.

[83] M. Roth, E. Brambrink, P. Audebert, M. Basko, A. Blazevic, R. Clarke, J. Cobble, T. E. Cowan, J. Fernandez, J. Fuchs, M. Hegelich, K. Ledingham, B. G. Logan, D. Neely, H. Ruhl, and M. Schollmeier, "Laser accelerated ions in ICF research prospects and experiments," *Plasma Physics and Controlled Fusion*, vol. 47, pp. B841–B850, Nov. 2005.

[84] M. Nishiuchi, I. Daito, M. Ikegami, H. Daido, M. Mori, S. Orimo, K. Ogura, A. Sagisaka, A. Yogo, A. S. Pirozhkov, H. Sugiyama, H. Kiriyama, H. Okada, S. Kanazawa, S. Kondo, T. Shimomura, M. Tanoue, Y. Nakai, H. Sasao, D. Wakai,

H. Sakaki, P. Bolton, I. W. Choi, J. H. Sung, J. Lee, Y. Oishi, T. Fujii, K. Nemoto, H. Souda, A. Noda, Y. Iseki, and T. Yoshiyuki, "Focusing and spectral enhancement of a repetition-rated, laser-driven, divergent multi-MeV proton beam using permanent quadrupole magnets," *Applied Physics Letters*, vol. 94, p. 061107, Feb. 2009.

[85] J. Badziak, "Laser-driven ion acceleration: methods, challenges and prospects," *Journal of Physics: Conference Series*, vol. 959, p. 012001, Jan. 2018.

[86] J. Schreiber, P. R. Bolton, and K. Parodi, "Invited review article: "hands-on" laser-driven ion acceleration: A primer for laser-driven source development and potential applications," *Review of Scientific Instruments*, vol. 87, p. 071101, July 2016.

[87] S. C. Wilks, A. B. Langdon, T. E. Cowan, M. Roth, M. Singh, S. Hatchett, M. H. Key, D. Pennington, A. MacKinnon, and R. A. Snavely, "Energetic proton generation in ultra-intense laser–solid interactions," *Physics of Plasmas*, vol. 8, pp. 542–549, Feb. 2001.

[88] S. P. Hatchett, C. G. Brown, T. E. Cowan, E. A. Henry, J. S. Johnson, M. H. Key, J. A. Koch, A. B. Langdon, B. F. Lasinski, R. W. Lee, A. J. Mackinnon, D. M. Pennington, M. D. Perry, T. W. Phillips, M. Roth, T. C. Sangster, M. S. Singh, R. A. Snavely, M. A. Stoyer, S. C. Wilks, and K. Yasuike, "Electron, photon, and ion beams from the relativistic interaction of petawatt laser pulses with solid targets," *Physics of Plasmas*, vol. 7, pp. 2076–2082, May 2000.

[89] J. Badziak, "Laser-driven generation of fast particles," *Opto-Electronics Review*, vol. 15, no. 1, pp. 1–12, 2007.

[90] A. Macchi, M. Borghesi, and M. Passoni, "Ion acceleration by superintense laser-plasma interaction," *Reviews of Modern Physics*, vol. 85, pp. 751–793, May 2013.

[91] A. P. L. Robinson, M. Zepf, S. Kar, R. G. Evans, and C. Bellei, "Radiation pressure acceleration of thin foils with circularly polarized laser pulses," *New Journal of Physics*, vol. 10, p. 013021, Jan. 2008.

[92] T. V. Liseykina, M. Borghesi, A. Macchi, and S. Tuveri, "Radiation pressure acceleration by ultraintense laser pulses," *Plasma Physics and Controlled Fusion*, vol. 50, p. 124033, Nov. 2008.

[93] M. Grech, S. Skupin, A. Diaw, T. Schlegel, and V. T. Tikhonchuk, "Energy dispersion in radiation pressure accelerated ion beams," *New Journal of Physics*, vol. 13, p. 123003, Dec. 2011.

[94] S. M. Hooker, "Developments in laser-driven plasma accelerators," *Nature Photonics*, vol. 7, pp. 775–782, Sept. 2013.

[95] R. Bingham and R. Trines, "Introduction to plasma accelerators: the basics," *CERN Yellow Reports*, pp. Vol 1 (2016): Proceedings of the 2014 CAS–CERN Accelerator School: Plasma Wake Acceleration, 2016.

[96] V. Malka, "Plasma wake accelerators: Introduction and historical overview," *CERN Yellow Reports*, pp. Vol 1 (2016): Proceedings of the 2014 CAS–CERN Accelerator School: Plasma Wake Acceleration, 2016.

[97] A. Higginson, R. Gray, M. King, R. Dance, S. Williamson, N. Butler, R. Wilson, R. Capdessus, C. Armstrong, J. Green, S. Hawkes, P. Martin, W. Wei, S. Mirfayzi, X. Yuan, S. Kar, M. Borghesi, R. Clarke, D. Neely, and P. McKenna, "Near-100 mev protons via a laser-driven transparency-enhanced hybrid acceleration scheme," *Nature communications*, vol. 9, no. 1, pp. 1–9, 2018.

[98] K. F. Kakolee, M. Borghesi, M. Zepf, S. Kar, D. Doria, B. Ramakrishna, K. Quinn, G. Sarri, J. Osterholz, M. Cerchez, O. Willi, X. Yuan, and P. McKenna, "Scaling of ion spectral peaks in the hybrid RPA-TNSA region," *Journal of the Korean Physical Society*, vol. 68, pp. 768–771, Mar. 2016.

[99] O. Klimo, J. Psikal, J. Limpouch, and V. T. Tikhonchuk, "Monoenergetic ion beams from ultrathin foils irradiated by ultrahigh-contrast circularly polarized laser pulses," *Phys. Rev. ST Accel. Beams*, vol. 11, p. 031301, Mar. 2008.

[100] C. A. J. Palmer, J. Schreiber, S. R. Nagel, N. P. Dover, C. Bellei, F. N. Beg, S. Bott, R. J. Clarke, A. E. Dangor, S. M. Hassan, P. Hilz, D. Jung, S. Kneip, S. P. D. Mangles, K. L. Lancaster, A. Rehman, A. P. L. Robinson, C. Spindloe, J. Szerypo, M. Tatarakis, M. Yeung, M. Zepf, and Z. Najmudin, "Rayleigh-taylor instability of an ultrathin foil accelerated by the radiation pressure of an intense laser," *Phys. Rev. Lett.*, vol. 108, p. 225002, May 2012.

[101] ELI-NP, "Extreme Light Infrastructure - Nuclear Physics (ELI-NP)," 2022.

[102] M. J. Easton, K. Zhu, K. Wang, M. Wu, C. Lin, and X. Yan, "Emittance growth due to energy spread in a laser-driven proton beamline," *Results in Physics*, vol. 29, p. 104779, Oct. 2021.

[103] A. Chacon, M. Kielly, H. Rutherford, D. R. Franklin, A. Caracciolo, L. Buonanno, I. D'Adda, A. Rosenfeld, S. Guatelli, M. Carminati, C. Fiorini, and M. Safavi-Naeini, "Detection and discrimination of neutron capture events for ncept dose quantification," *Scientific Reports*, vol. 12, Apr. 2022.

[104] S. Humphries, *Principles of Charged Particle Acceleration*. Dover Publications, 2013.

[105] V. Malka, "Laser plasma accelerators," *Physics of Plasmas*, vol. 19, p. 055501, may 2012.

[106] R. A. Snavely, M. H. Key, S. P. Hatchett, T. E. Cowan, M. Roth, T. W. Phillips, M. A. Stoyer, E. A. Henry, T. C. Sangster, M. S. Singh, S. C. Wilks, A. MacKinnon, A. Offenberger, D. M. Pennington, K. Yasuike, A. B. Langdon, B. F. Lasinski, J. Johnson, M. D. Perry, and E. M. Campbell, "Intense high-energy proton beams from petawatt-laser irradiation of solids," *Physical Review Letters*, vol. 85, pp. 2945–2948, Oct. 2000.

[107] F. Nürnberg, M. Schollmeier, E. Brambrink, A. Blažević, D. C. Carroll, K. Flippo, D. C. Gautier, M. Geißel, K. Harres, B. M. Hegelich, O. Lundh, K. Markey, P. McKenna, D. Neely, J. Schreiber, and M. Roth, "Radiochromic film imaging spectroscopy of laser-accelerated proton beams," *Review of Scientific Instruments*, vol. 80, p. 033301, Mar. 2009.

[108] L. Labate, D. Palla, D. Panetta, F. Avella, F. Baffigi, F. Brandi, F. D. Martino, L. Fulgentini, A. Giulietti, P. Köster, D. Terzani, P. Tomassini, C. Traino, and L. A. Gizzi, "Toward an effective use of laser-driven very high energy electrons for radiotherapy: Feasibility assessment of multi-field and intensity modulation irradiation schemes," *Scientific Reports*, vol. 10, Oct. 2020.

[109] E. L. Clark, K. Krushelnick, J. R. Davies, M. Zepf, M. Tatarakis, F. N. Beg, A. Machacek, P. A. Norreys, M. I. K. Santala, I. Watts, and A. E. Dangor, "Measurements of energetic proton transport through magnetized plasma from intense laser interactions with solids," *Physical Review Letters*, vol. 84, pp. 670–673, Jan. 2000.

[110] A. Sharma and C. Kamperidis, "High energy proton micro-bunches from a laser plasma accelerator," *Scientific Reports*, vol. 9, Sept. 2019.

[111] A. Gonsalves, K. Nakamura, J. Daniels, C. Benedetti, C. Pieronek, T. de Raadt, S. Steinke, J. Bin, S. Bulanov, J. van Tilborg, C. Geddes, C. Schroeder, C. Tóth, E. Esarey, K. Swanson, L. Fan-Chiang, G. Bagdasarov, N. Bobrova, V. Gasilov, G. Korn, P. Sasorov, and W. Leemans, "Petawatt laser guiding and electron beam acceleration to 8 GeV in a laser-heated capillary discharge waveguide," *Physical Review Letters*, vol. 122, Feb. 2019.

[112] W. Ma, I. J. Kim, J. Yu, I. Choi, P. Singh, H. W. Lee, J. H. Sung, S. K. Lee, C. Lin, Q. Liao, J. Zhu, H. Lu, B. Liu, H. Wang, R. Xu, X. He, J. Chen, M. Zepf, J. Schreiber, X. Yan, and C. H. Nam, "Laser acceleration of highly energetic carbon ions using a double-layer target composed of slightly underdense plasma and ultrathin foil," *Physical Review Letters*, vol. 122, Jan. 2019.

[113] E. Fourkal, J. S. Li, W. Xiong, A. Nahum, and C.-M. Ma, "Intensity modulated radiation therapy using laser-accelerated protons: a monte carlo dosimetric study," *Physics in Medicine and Biology*, vol. 48, pp. 3977–4000, Dec. 2003.

[114] K. W. D. Ledingham, W. Galster, and R. Sauerbrey, "Laser-driven proton oncology — a unique new cancer therapy?," *The British Journal of Radiology*, vol. 80, pp. 855–858, Nov. 2007.

[115] U. Masood, T. E. Cowan, W. Enghardt, K. M. Hofmann, L. Karsch, F. Kroll, U. Schramm, J. J. Wilkens, and J. Pawelke, "A light-weight compact proton gantry design with a novel dose delivery system for broad-energetic laser-accelerated beams," *Physics in Medicine & Biology*, vol. 62, pp. 5531–5555, June 2017.

[116] V. Malka, S. Fritzler, E. Lefebvre, E. d'Humières, R. Ferrand, G. Grillon, C. Albaret, S. Meyroneinc, J.-P. Chambaret, A. Antonetti, and D. Hulin, "Practicability of protontherapy using compact laser systems," *Medical Physics*, vol. 31, pp. 1587–1592, May 2004.

[117] W. Luo, E. Fourkal, J. Li, and C.-M. Ma, "Particle selection and beam collimation system for laser-accelerated proton beam therapy," *Medical Physics*, vol. 32, pp. 794–806, Mar. 2005.

[118] C. Ma, I. Veltchev, E. Fourkal, J. S. Li, W. Luo, J. Fan, T. Lin, and A. Pollack, "Development of a laser-driven proton accelerator for cancer therapy," *Laser Physics*, vol. 16, pp. 639–646, Apr. 2006.

[119] U. Masood, M. Bussmann, T. E. Cowan, W. Enghardt, L. Karsch, F. Kroll, U. Schramm, and J. Pawelke, "A compact solution for ion beam therapy with laser accelerated protons," *Applied Physics B*, vol. 117, pp. 41–52, Apr. 2014.

[120] V. Favaudon, L. Caplier, V. Monceau, F. Pouzoulet, M. Sayarath, C. Fouillade, M.-F. Poupon, I. Brito, P. Hupé, J. Bourhis, J. Hall, J.-J. Fontaine, and M.-C. Vozenin, "Ultrahigh dose-rate FLASH irradiation increases the differential response between normal and tumor tissue in mice," *Science Translational Medicine*, vol. 6, pp. 245ra93–245ra93, July 2014.

[121] J. R. Hughes and J. L. Parsons, "FLASH radiotherapy: Current knowledge and future insights using proton-beam therapy," *International Journal of Molecular Sciences*, vol. 21, p. 6492, Sept. 2020.

[122] E. S. Diffenderfer, B. S. Sørensen, A. Mazal, and D. J. Carlson, "The current status of preclinical proton flash radiation and future directions," *Medical Physics*, vol. 49, p. 2039–2054, Oct. 2021.

[123] T. Tessonnier, S. Mein, D. W. Walsh, N. Schuhmacher, H. Liew, R. Cee, M. Galonska, S. Scheloske, C. Schömers, U. Weber, S. Brons, J. Debus, T. Haberer, A. Abdollahi, A. Mairani, and I. Dokic, "Flash dose rate helium ion beams: First in vitro investigations," *International Journal of Radiation Oncology*Biology*Physics*, vol. 111, p. 1011–1022, Nov. 2021.

[124] U. A. Weber, E. Scifoni, and M. Durante, "Flash radiotherapy with carbon ion beams," *Medical Physics*, vol. 49, p. 1974–1992, Aug. 2021.

[125] A. Yogo, T. Maeda, T. Hori, H. Sakaki, K. Ogura, M. Nishiuchi, A. Sagisaka, H. Kiriyama, H. Okada, S. Kanazawa, T. Shimomura, Y. Nakai, M. Tanoue, F. Sasao, P. R. Bolton, M. Murakami, T. Nomura, S. Kawanishi, and K. Kondo, "Measurement of relative biological effectiveness of protons in human cancer cells using a laser-driven quasimonoenergetic proton beamline," *Applied Physics Letters*, vol. 98, p. 053701, Jan. 2011.

[126] D. Doria, K. F. Kakolee, S. Kar, S. K. Litt, F. Fiorini, H. Ahmed, S. Green, J. C. G. Jeynes, J. Kavanagh, D. Kirby, K. J. Kirkby, C. L. Lewis, M. J. Merchant, G. Nersisyan, R. Prasad, K. M. Prise, G. Schettino, M. Zepf, and M. Borghesi, "Biological effectiveness on live cells of laser driven protons at dose rates exceeding 109gy/s," *AIP Advances*, vol. 2, p. 011209, Mar. 2012.

[127] K. Zeil, M. Baumann, E. Beyreuther, T. Burris-Mog, T. E. Cowan, W. Enghardt, L. Karsch, S. D. Kraft, L. Laschinsky, J. Metzkes, D. Naumburger, M. Oppelt,

C. Richter, R. Sauerbrey, M. Schürer, U. Schramm, and J. Pawelke, "Dose-controlled irradiation of cancer cells with laser-accelerated proton pulses," *Applied Physics B*, vol. 110, pp. 437–444, Nov. 2012.

[128] J. Bin, K. Allinger, W. Assmann, G. Dollinger, G. A. Drexler, A. A. Friedl, D. Habs, P. Hilz, R. Hoerlein, N. Humble, S. Karsch, K. Khrennikov, D. Kiefer, F. Krausz, W. Ma, D. Michalski, M. Molls, S. Raith, S. Reinhardt, B. Röper, T. E. Schmid, T. Tajima, J. Wenz, O. Zlobinskaya, J. Schreiber, and J. J. Wilkens, "A laser-driven nanosecond proton source for radiobiological studies," *Applied Physics Letters*, vol. 101, p. 243701, Dec. 2012.

[129] E. Bayart, A. Flacco, O. Delmas, L. Pommarel, D. Levy, M. Cavallone, F. Megnin-Chanet, E. Deutsch, and V. Malka, "Fast dose fractionation using ultra-short laser accelerated proton pulses can increase cancer cell mortality, which relies on functional PARP1 protein," *Scientific Reports*, vol. 9, July 2019.

[130] F. Hanton, P. Chaudhary, D. Doria, D. Gwynne, C. Maiorino, C. Scullion, H. Ahmed, T. Marshall, K. Naughton, L. Romagnani, S. Kar, G. Schettino, P. McKenna, S. Botchway, D. R. Symes, P. P. Rajeev, K. M. Prise, and M. Borghesi, "DNA DSB repair dynamics following irradiation with laser-driven protons at ultra-high dose rates," *Scientific Reports*, vol. 9, Mar. 2019.

[131] T. F. Rösch, Z. Szabó, D. Haffa, J. Bin, S. Brunner, F. S. Englbrecht, A. A. Friedl, Y. Gao, J. Hartmann, P. Hilz, C. Kreuzer, F. H. Lindner, T. M. Ostermayr, R. Polanek, M. Speicher, E. R. Szabó, D. Taray, T. Tőkés, M. Würl, K. Parodi, K. Hideghéty, and J. Schreiber, "A feasibility study of zebrafish embryo irradiation with laser-accelerated protons," *Review of Scientific Instruments*, vol. 91, p. 063303, June 2020.

[132] F. Kroll, F.-E. Brack, C. Bernert, S. Bock, E. Bodenstein, K. Brüchner, T. E. Cowan, L. Gaus, R. Gebhardt, U. Helbig, L. Karsch, T. Kluge, S. Kraft, M. Krause, E. Lessmann, U. Masood, S. Meister, J. Metzkes-Ng, A. Nossula, J. Pawelke, J. Pietzsch, T. Püschel, M. Reimold, M. Rehwald, C. Richter, H.-P. Schlenvoigt, U. Schramm, M. E. P. Umlandt, T. Ziegler, K. Zeil, and E. Beyreuther, "Tumour irradiation in mice with a laser-accelerated proton beam," *Nature Physics*, vol. 18, pp. 316–322, Mar. 2022.

[133] F. Romano, A. Subiel, M. McManus, N. D. Lee, H. Palmans, R. Thomas, S. McCallum, G. Milluzzo, M. Borghesi, A. McIlvenny, H. Ahmed, W. Farabolini, A. Gilardi, and A. Schüller, "Challenges in dosimetry of particle beams with ultra-high pulse dose rates," *Journal of Physics: Conference Series*, vol. 1662, p. 012028, Oct. 2020.

[134] H. Palmans, R. Thomas, M. Simon, S. Duane, A. Kacperek, A. DuSautoy, and F. Verhaegen, "A small-body portable graphite calorimeter for dosimetry in low-energy clinical proton beams," *Physics in Medicine and Biology*, vol. 49, pp. 3737–3749, July 2004.

[135] A. Subiel, V. Moskvin, G. H. Welsh, S. Cipiccia, D. Reboredo, C. DesRosiers, and D. A. Jaroszynski, "Challenges of dosimetry of ultra-short pulsed very high energy electron beams," *Physica Medica*, vol. 42, pp. 327–331, Oct. 2017.

[136] O. Lundh, J. Lim, C. Rechatin, L. Ammoura, A. Ben-Ismaïl, X. Davoine, G. Gallot, J.-P. Goddet, E. Lefebvre, V. Malka, and J. Faure, "Few femtosecond, few kiloampere electron bunch produced by a laser–plasma accelerator," *Nature Physics*, vol. 7, pp. 219–222, Jan. 2011.

[137] H. Kotaki, K. Kawase, Y. Hayashi, M. Mori, M. Kando, J. K. Koga, and S. V. Bulanovt, "Direct observation of the pulse width of an ultrashort electron beam," *Journal of the Physical Society of Japan*, vol. 84, p. 074501, July 2015.

[138] M. Oppelt, M. Baumann, R. Bergmann, E. Beyreuther, K. Brüchner, J. Hartmann, L. Karsch, M. Krause, L. Laschinsky, E. Leßmann, M. Nicolai, M. Reuter, C. Richter, A. Sävert, M. Schnell, M. Schürer, J. Woithe, M. Kaluza, and J. Pawelke, "Comparison study of in vivo dose response to laser-driven versus conventional electron beam," *Radiation and Environmental Biophysics*, vol. 54, pp. 155–166, Jan. 2015.

[139] L. Laschinsky, M. Baumann, E. Beyreuther, W. Enghardt, M. Kaluza, L. Karsch, E. Lessmann, D. Naumburger, M. Nicolai, C. Richter, R. Sauerbrey, H.-P. Schlenvoigt, and J. Pawelke, "Radiobiological Effectiveness of Laser Accelerated Electrons in Comparison to Electron Beams from a Conventional Linear Accelerator," *Journal of Radiation Research*, vol. 53, pp. 395–403, 05 2012.

[140] M. Cavallone, L. Rovige, J. Huijts, É. Bayart, R. Delorme, A. Vernier, P. G. Jorge, R. Moeckli, E. Deutsch, J. Faure, and A. Flacco, "Dosimetric characterisation and application to radiation biology of a kHz laser-driven electron beam," *Applied Physics B*, vol. 127, Mar. 2021.

[141] N. Babayan, N. Vorobyeva, B. Grigoryan, A. Grekhova, M. Pustovalova, S. Rodneva, Y. Fedotov, G. Tsakanova, R. Aroutiounian, and A. Osipov, "Low repair capacity of DNA double-strand breaks induced by laser-driven ultrashort electron beams in cancer cells," *International Journal of Molecular Sciences*, vol. 21, p. 9488, Dec. 2020.

[142] E. L. I. Whitebook, "Science and technology with ultra-intense lasers," 2011.

[143] L. Karsch, E. Beyreuther, W. Enghardt, M. Gotz, U. Masood, U. Schramm, K. Zeil, and J. Pawelke, "Towards ion beam therapy based on laser plasma accelerators," *Acta Oncologica*, vol. 56, pp. 1359–1366, Aug. 2017.

[144] M. McManus, F. Romano, N. D. Lee, W. Farabolini, A. Gilardi, G. Royle, H. Palmans, and A. Subiel, "The challenge of ionisation chamber dosimetry in ultra-short pulsed high dose-rate very high energy electron beams," *Scientific Reports*, vol. 10, June 2020.

[145] U. Linz and J. Alonso, "What will it take for laser driven proton accelerators to be applied to tumor therapy?," *Physical Review Special Topics - Accelerators and Beams*, vol. 10, Sept. 2007.

[146] A. Subiel, V. Moskvin, G. H. Welsh, S. Cipiccia, D. Reboredo, P. Evans, M. Partridge, C. DesRosiers, M. P. Anania, A. Cianchi, A. Mostacci, E. Chiadroni, D. D. Giovenale, F. Villa, R. Pompili, M. Ferrario, M. Belleveglia, G. D. Pirro, G. Gatti,

C. Vaccarezza, B. Seitz, R. C. Isaac, E. Brunetti, S. M. Wiggins, B. Ersfeld, M. R. Islam, M. S. Mendonca, A. Sorensen, M. Boyd, and D. A. Jaroszynski, "Dosimetry of very high energy electrons (VHEE) for radiotherapy applications: using radiochromic film measurements and monte carlo simulations," *Physics in Medicine and Biology*, vol. 59, pp. 5811–5829, Sept. 2014.

[147] C. L. Lawson, R. J. Hanson, and Society for Industrial and Applied Mathematics, *Solving least squares problems*. Society for Industrial and Applied Mathematics, 1995. OCLC: 752259709.

[148] M. Valueva, N. Nagornov, P. Lyakhov, G. Valuev, and N. Chervyakov, "Application of the residue number system to reduce hardware costs of the convolutional neural network implementation," *Mathematics and Computers in Simulation*, vol. 177, p. 232–243, Nov 2020.

[149] I. J. Chetty, B. Curran, J. E. Cygler, J. J. DeMarco, G. Ezzell, B. A. Faddegon, I. Kawrakow, P. J. Keall, H. Liu, C.-M. C. Ma, D. W. O. Rogers, J. Seuntjens, D. Sheikh-Bagheri, and J. V. Siebers, "Report of the aapm task group no. 105: Issues associated with clinical implementation of monte carlo-based photon and electron external beam treatment planning," *Medical Physics*, vol. 34, p. 4818–4853, Nov 2007.

[150] E. Spezi and G. Lewis, "An overview of monte carlo treatment planning for radiotherapy," *Radiation Protection Dosimetry*, vol. 131, p. 123–129, Aug 2008.

[151] K. Jabbari, "Review of Fast Monte Carlo Codes for Dose Calculation in Radiation Therapy Treatment Planning," *Journal of Medical Signals and Sensors*, pp. 73–86, Jan 2011.

[152] P. Lysakovski, A. Ferrari, T. Tessonnier, J. Besuglow, B. Kopp, S. Mein, T. Haberer, J. Debus, and A. Mairani, "Development and benchmarking of a monte carlo dose engine for proton radiation therapy," *Frontiers in Physics*, vol. 9, Nov 2021.

[153] A. Ferrari, P. Sala, A. Fasso, and J. Ranft, "Fluka: A multi-particle transport code," tech. rep., U.S. Department of Energy, Dec 2005.

[154] T. Böhlen, F. Cerutti, M. Chin, A. Fassò, A. Ferrari, P. Ortega, A. Mairani, P. Sala, G. Smirnov, and V. Vlachoudis, "The fluka code: Developments and challenges for high energy and medical applications," *Nuclear Data Sheets*, vol. 120, p. 211–214, Jun 2014.

[155] S. Mein, K. Choi, B. Kopp, T. Tessonnier, J. Bauer, A. Ferrari, T. Haberer, J. Debus, A. Abdollahi, and A. Mairani, "Fast robust dose calculation on gpu for high-precision 1h, 4he, 12c and 16o ion therapy: the frog platform," *Scientific Reports*, vol. 8, Oct 2018.

[156] H. Paganetti, "Monte carlo simulations will change the way we treat patients with proton beams today," *The British Journal of Radiology*, vol. 87, p. 20140293, Aug 2014.

[157] J. M. Verburg, C. Grassberger, S. Dowdell, J. Schuemann, J. Seco, and H. Paganetti, "Automated monte carlo simulation of proton therapy treatment plans," *Technology in Cancer Research & Treatment*, vol. 15, p. NP35–NP46, Jul 2016.

[158] N. Qin, C. Shen, M.-Y. Tsai, M. Pinto, Z. Tian, G. Dedes, A. Pompos, S. B. Jiang, K. Parodi, and X. Jia, "Full monte carlo–based biologic treatment plan optimization system for intensity modulated carbon ion therapy on graphics processing unit," *International Journal of Radiation Oncology*Biology*Physics*, vol. 100, p. 235–243, Jan 2018.

[159] S. Agostinelli, J. Allison, K. Amako, J. Apostolakis, H. Araujo, P. Arce, M. Asai, D. Axen, S. Banerjee, G. Barrand, F. Behner, L. Bellagamba, J. Boudreau, L. Broglia, A. Brunengo, H. Burkhardt, S. Chauvie, J. Chuma, R. Chytracek, G. Cooperman, G. Cosmo, P. Degtyarenko, A. Dell'Acqua, G. Depaola, D. Dietrich, R. Enami, A. Feliciello, C. Ferguson, H. Fesefeldt, G. Folger, F. Foppiano, A. Forti, S. Garelli, S. Giani, R. Giannitrapani, D. Gibin, J. G. Cadenas, I. González, G. G. Abril, G. Greeniaus, W. Greiner, V. Grichine, A. Grossheim, S. Guatelli, P. Gumplinger, R. Hamatsu, K. Hashimoto, H. Hasui, A. Heikkinen, A. Howard, V. Ivanchenko, A. Johnson, F. Jones, J. Kallenbach, N. Kanaya, M. Kawabata, Y. Kawabata, M. Kawaguti, S. Kelner, P. Kent, A. Kimura, T. Kodama, R. Kokoulin, M. Kossov, H. Kurashige, E. Lamanna, T. Lampén, V. Lara, V. Lefebure, F. Lei, M. Liendl, W. Lockman, F. Longo, S. Magni, M. Maire, E. Medernach, K. Minamimoto, P. M. de Freitas, Y. Morita, K. Murakami, M. Nagamatu, R. Nartallo, P. Nieminen, T. Nishimura, K. Ohtsubo, M. Okamura, S. O'Neale, Y. Oohata, K. Paech, J. Perl, A. Pfeiffer, M. Pia, F. Ranjard, A. Rybin, S. Sadilov, E. D. Salvo, G. Santin, T. Sasaki, N. Savvas, Y. Sawada, S. Scherer, S. Sei, V. Sirotenko, D. Smith, N. Starkov, H. Stoecker, J. Sulkimo, M. Takahata, S. Tanaka, E. Tcherniaev, E. S. Tehrani, M. Tropeano, P. Truscott, H. Uno, L. Urban, P. Urban, M. Verderi, A. Walkden, W. Wander, H. Weber, J. Wellisch, T. Wenaus, D. Williams, D. Wright, T. Yamada, H. Yoshida, and D. Zschiesche, "Geant4—a simulation toolkit," *Nuclear Instruments and Methods in Physics Research Section A: Accelerators, Spectrometers, Detectors and Associated Equipment*, vol. 506, pp. 250–303, July 2003.

[160] S. Jan, G. Santin, D. Strul, S. Staelens, K. Assie, D. Autret, S. Avner, R. Barbier, M. Bardies, P. Bloomfield, *et al.*, "Gate: a simulation toolkit for pet and spect," *Physics in Medicine & Biology*, vol. 49, no. 19, pp. 4543–4561, 2004.

[161] S. Jan, D. Benoit, E. Becheva, T. Carlier, F. Cassol, P. Descourt, T. Frisson, L. Grevillot, L. Guigues, L. Maigne, *et al.*, "Gate v6: a major enhancement of the gate simulation platform enabling modelling of ct and radiotherapy," *Physics in Medicine & Biology*, vol. 56, no. 4, pp. 881–901, 2011.

[162] J. Perl, J. Shin, J. Schumann, B. Faddegon, and H. Paganetti, "TOPAS: An innovative proton Monte Carlo platform for research and clinical applications," *Medical Physics*, vol. 39, p. 6818, 2012.

[163] B. Faddegon, J. Ramos-Mendez, J. Schuemann, A. McNamara, J. Shin, J. Perl, and P. H., "The TOPAS Tool for Particle Simulation, a Monte Carlo Simulation Tool for Physics, Biology and Clinical Research," *Physica Medica*, 2020.

[164] K. Parodi, A. Mairani, S. Brons, B. G. Hasch, F. Sommerer, J. Naumann, O. Jäkel, T. Haberer, and J. Debus, "Monte carlo simulations to support start-up and treatment planning of scanned proton and carbon ion therapy at a synchrotron-based facility," *Physics in Medicine and Biology*, vol. 57, p. 3759–3784, May 2012.

[165] G. Battistoni, J. Bauer, T. T. Boehlen, F. Cerutti, M. P. W. Chin, R. Dos Santos Augusto, A. Ferrari, P. G. Ortega, W. Kozłowska, G. Magro, A. Mairani, K. Parodi, P. R. Sala, P. Schoofs, T. Tessonnier, and V. Vlachoudis, "The fluka code: An accurate simulation tool for particle therapy," *Frontiers in Oncology*, vol. 6, May 2016.

[166] M. Scholz and G. Kraft, "Track structure and the calculation of biological effects of heavy charged particles," *Advances in Space Research*, vol. 18, pp. 5–14, Jan. 1996.

[167] E. Scifoni, W. Tinganelli, W. K. Weyrather, M. Durante, A. Maier, and M. Krämer, "Including oxygen enhancement ratio in ion beam treatment planning: model implementation and experimental verification," *Physics in Medicine and Biology*, vol. 58, pp. 3871–3895, May 2013.

[168] M. Krämer, E. Scifoni, F. Schmitz, O. Sokol, and M. Durante, "Overview of recent advances in treatment planning for ion beam radiotherapy," *The European Physical Journal D*, vol. 68, no. 10, pp. 1–6, 2014.

[169] T. T. Bohlen, J. Bauer, M. Dosanjh, A. Ferrari, T. Haberer, K. Parodi, V. Patera, and A. Mairani, "A monte carlo-based treatment-planning tool for ion beam therapy," *Journal of Radiation Research*, vol. 54, pp. i77–i81, July 2013.

[170] L. Burigo, I. Pshenichnov, I. Mishustin, and M. Bleicher, "Comparative study of dose distributions and cell survival fractions for 1h, 4he, 12c and 16o beams using geant4 and microdosimetric kinetic model," *Physics in Medicine & Biology*, vol. 60, no. 8, p. 3313, 2015.

[171] A. Chacon, S. Guatelli, H. Rutherford, D. Bolst, A. Mohammadi, A. Ahmed, M. Nitta, F. Nishikido, Y. Iwao, H. Tashima, E. Yoshida, G. Akamatsu, S. Takyu, A. Kitagawa, T. Hofmann, M. Pinto, D. R. Franklin, K. Parodi, T. Yamaya, A. Rosenfeld, and M. Safavi-Naeini, "Comparative study of alternative geant4 hadronic ion inelastic physics models for prediction of positron-emitting radionuclide production in carbon and oxygen ion therapy," *Physics in Medicine & Biology*, vol. 64, p. 155014, Aug. 2019.

[172] D. R. White, J. Booz, R. V. Griffith, J. J. Spokas, and I. J. Wilson, "Report 44," *Journal of the International Commission on Radiation Units and Measurements*, vol. os23, pp. NP–NP, Jan. 1989.

[173] P. Sigmund, R. Bimbot, H. Geissel, H. Paul, and A. Schinner, "Icru report 73: stopping of ions heavier than helium," *J ICRU*, vol. 5, no. 1, pp. 1–235, 2005.

[174] P. Sigmund, A. Schinner, and H. Paul, "Errata and addenda for icru report 73, stopping of ions heavier than helium," *J ICRU*, vol. 5, no. 1, pp. 1–10, 2009.

[175] I. N. Fleming, R. Manavaki, P. J. Blower, C. West, K. J. Williams, A. L. Harris, J. Domarkas, S. Lord, C. Baldry, and F. J. Gilbert, "Imaging tumour hypoxia with positron emission tomography," *British Journal of Cancer*, vol. 112, p. 238–250, Dec. 2014.

[176] C. E. Vargas, W. F. Hartsell, M. Dunn, S. R. Keole, L. Doh, E. Eisenbeisz, and G. L. Larson, "Hypofractionated versus standard fractionated proton-beam therapy for low-risk prostate cancer," *American Journal of Clinical Oncology*, vol. 41, p. 115–120, Feb 2018.

[177] T. D. Malouff, A. Mahajan, S. Krishnan, C. Beltran, D. S. Seneviratne, and D. M. Trifiletti, "Carbon ion therapy: A modern review of an emerging technology," *Frontiers in Oncology*, vol. 10, Feb 2020.

[178] R. Bro and S. De Jong, "A fast non-negativity-constrained least squares algorithm," *Journal of Chemometrics: A Journal of the Chemometrics Society*, vol. 11, no. 5, pp. 393–401, 1997.

APPENDIX A

Software documentation

All source code for the treatment planning system is available at the following URL:
https://bitbucket.org/Roumani/multi_ion_tps

The Monte Carlo simulation code used in this project is available at the following URL:
https://bitbucket.org/Roumani/hit_uts

A.1 Workflow Overview

Prior to running the TPS, it is necessary to generate the monoenergtic dose distributions for each ion species. These are generated using the Geant4 Monte Carlo simulator `hit_uts`; beam geometry can be either set to an infinitesimally-thick pencil beam (which must then be adapted to each individual accelerator by convolving it by an appropriate beam shape / energy spread kernel) or by directly simulating the specific geometry of the desired scanner beam. Both methods entail a similar level of computational complexity.

Running the TPS itself is a two-step process:

1. Constructing the configuration file, which specifies the main parameters with which the TPS is to be executed; and

2. Running the driver script which constructs the chosen phantom and target, sets up each field, and sequentially executes the TPS proper for each field, and generates the various outputs.

Once the TPS has finished, there are several steps which may then be followed to visualise the result (including an animation of the resulting dose distribution) or construct a simulation in Geant4.

A.2 Configuration file

The configuration file should be called `parameters.m` and saved in the folder where the TPS is to be executed. The sample files distributed in the git repository are not named `parameters.m` deliberately in order to avoid problems if that repository is added to MATLAB's path. The appropriate sample file should be copied to `parameters.m`, moved to the desired location, and edited as appropriate.

```
% Anything with Z less than or equal to this threshold will not be used in hypoxic regions
hypoxic_threshold_Z = 3;
% For multifield
beam_angles = [0 45 90 135 180];
% Dose in Gy
dose = 100;
% target, tail, distal, peripheral, proximal, OAR downsample factors
reg_decimations = [10, 10, 25, 200, 25, 10];
% 3 will be slower but smoother
%reg_decimations = [3, 3, 25, 200, 25, 3, -1];
% Relative weightings given to the respective regions
reg_weights = [1, 1, 1, 1, 0.01, 10];
% Beam grid resolution
grid_x = 5;
grid_y = 5;
grid_z = 5;
% Create target dose distribution - sphere centred on the target volume
% Size of workspace in pixels
xpix = 450;
ypix = 100;
zpix = 450;
% Size of volume for actual optimisation procedure
xrun = 100;
yrun = 100;
zrun = 300;
% Location of centre of target
centrex = xpix / 2;
centrey = ypix / 2;
centrez = zpix / 2;
% Phantom parameters
head_r = 100;
skin_t = 2;
skull_t = 6;
% Tumour parameters
tumour_r = 25;
tumourx = 67;
tumoury = 0;
tumourz = 0;
% OAR - set oar_r to 1 if you don't want an OAR
oar_r = 10;
oarx = 67;
```

```
oary = 0;
oarz = 35;
% Hypoxia - set hypoxic_r to 1 if you don't want hypoxia
hypoxic_r = 10;
hypoxicx = 52;
hypoxicy = 0;
hypoxicz = 0;
% Full set of ion data; you can also select a subset, for example
ion_data_subset = ion_data;
% proton only:
%ion_data_subset = ion_data(1)
```

A.3 Generating the dose distribution library

The individual 3d dose distributions are generated using the Geant4 simulation code `hit_uts`. The target is a PMMA block, 300 mm deep; dose distributions are recorded around the beam in a 100 mm × 100 mm volume. A fully-ionised ion beam of the specified ion type and energy is directed at this target, and the resulting dose distribution is scored throughout the entire volume. The key parameters for the simulation are supplied via a macro file (typically called `run.mac`. An example `run.mac` file, as distributed with `hit_uts`, is shown below:

```
##########################################
#
# define scoring mesh
#
/score/create/boxMesh boxMesh_1
#
/score/mesh/boxSize 50. 50. 150. mm
/score/mesh/nBin 100 100 300
/score/mesh/translate/xyz 0 0 0 mm

#/score/quantity/doseDeposit dDep
/score/quantity/energyDeposit eDep
#
/score/close
/score/list

#/score/quantity/nOfStep nOfStepGamma
#/score/filter/particle gammaFilter gamma
#/score/quantity/nOfStep nOfStepEMinus
#/score/filter/particle eMinusFilter e-
#/score/quantity/nOfStep nOfStepEPlus
#/score/filter/particle ePlusFilter e+

# Homogeneous PMMA phantom 100x100x300 mm block
/phantomparams/newPhantomShape rectangular_prism
/phantomparams/newPhantomMaterial pmma
/phantomparams/newPhantomParent World
/phantomparams/newPhantomName Phantom
/phantomparams/newPhantomDimensions 100. 100. 300. 0. 0. 0. 0. 0. 0. 0. 0. 0. mm
/phantomparams/newPhantomAt 0. 0. 0. mm

# Heterogeneous head phantom
#/phantomparams/newPhantomShape ellipsoid
#/phantomparams/newPhantomMaterial skin
#/phantomparams/newPhantomParent World
#/phantomparams/newPhantomName Skin
#/phantomparams/newPhantomDimensions 200. 200. 200. 0. 0. 0. 0. 0. 0. 0. 0. 0. mm
#/phantomparams/newPhantomAt 0. 0. 0. mm
```

```
39
40 #/phantomparams/newPhantomMaterial bone
41 #/phantomparams/newPhantomParent Skin
42 #/phantomparams/newPhantomName Skull
43 #/phantomparams/newPhantomDimensions 196. 196. 196. 0. 0. 0. 0. 0. 0. 0. 0. 0.  mm
44 #/phantomparams/newPhantomAt 0. 0. 0. mm
45
46 #/phantomparams/newPhantomMaterial brain
47 #/phantomparams/newPhantomParent Skull
48 #/phantomparams/newPhantomName Brain
49 #/phantomparams/newPhantomDimensions 184. 184. 184. 0. 0. 0. 0. 0. 0. 0. 0. 0.  mm
50 #/phantomparams/newPhantomAt 0. 0. 0. mm
51
52 #/phantomparams/newPhantomMaterial tumour
53 #/phantomparams/newPhantomParent Brain
54 #/phantomparams/newPhantomName Tumour
55 #/phantomparams/newPhantomDimensions 50. 50. 50. 0. 0. 0. 0. 0. 0. 0. 0. 0.  mm
56 #/phantomparams/newPhantomAt 0. 0. 0. mm
57 #
58 ########################################
59 #
60 /control/verbose 2
61 /run/verbose 1
62 # Beam parameters
63 /gps/pos/shape Circle
64 /gps/pos/type Beam
65 /gps/pos/radius 0. mm
66 /gps/pos/sigma_r 0.1898 cm
67 ####### Setting Beam position ###
68 /gps/pos/centre 0. 0. -150 mm
69 /gps/direction 0 0 1
70 ####### Setting the ion ###
71 /gps/particle ion
72 /gps/ion 6 12 6
73 ####### Setting beam energy ###
74 /gps/ene/type Gauss
75 /control/alias energyPerNucleon 290  #change the energy per nucleon by changing this value
76 /control/multiply totalEnergy {energyPerNucleon} 12
77 /control/multiply spreadEnergy {totalEnergy} 0.002
78 /gps/ene/mono {totalEnergy} MeV
79 /gps/ene/sigma {spreadEnergy} MeV #energy spread
80 # Number of primaries
81 /run/beamOn 20000
82 #/score/dumpQuantityToFile boxMesh_1 dDep dDep1.txt
83 /score/dumpQuantityToFile boxMesh_1 eDep eDep1.txt
84 #run2
85 /gps/ene/type Gauss
86 /control/alias energyPerNucleon 146  #change the energy per nucleon by changing this value
87 /control/multiply totalEnergy {energyPerNucleon} 12
88 /control/multiply spreadEnergy {totalEnergy} 0.002
89 /gps/ene/mono {totalEnergy} MeV
90 /gps/ene/sigma {spreadEnergy} MeV #energy spread
91 # Number of primaries
92 /run/beamOn 20000
93 # output file for dose distribution
94 /score/dumpQuantityToFile boxMesh_1 dDep dDep1.txt
95 # if energy rather than dose is preferred, use this:
96 #/score/dumpQuantityToFile boxMesh_1 eDep eDep2.txt
```

A.4 TPS

Toplevel execution of the TPS is managed using a driver script. Several of these are included in the git repository, but the most complete/comprehensive is `run_tps_multifield_1c` which implements the multifield TPS method described in Chapter 5. This script

should be run from inside MATLAB; however, note that it is NOT a MATLAB function. The driver script should be run from the folder where you want the output files to be saved.

In summary, this script:

1. Loads the ion data library. It will attempt to do so from a file called `simulated_ion_data_small` from the current working directory if it hasn't already been loaded into a variable called `ion_data`; you can either create a symbolic link to the `.mat` file containing this data or pre-load it in MATLAB beforehand;

2. Reads the key parameters for running the TPS from the configuration file described in the previous section;

3. Constructs the phantom, target, oar and hypoxic volumes, saving each to a .mat file

4. Iterates through each of the field angles - for each field angle θ_k:

   - Rotates the phantom, OAR, hypoxic volume and target by $-\theta_k$ and store the rotated volumes in cell arrays for future use; and
   - Determines the fraction of the target volume which is occluded by the OAR for each position.

5. Sorts the field angles in order of most-occluded to least

6. Divides the total objective dose by the desired number of fractions, yielding a nominal fractional target dose

7. Iterates through each of the sorted field angles - for each field angle θ_k, from most-occluded to least-occluded

   - Runs the TPS (`tps3D_het.m`) on the rotated volume
   - Rotate the achieved fractional dose distribution back to zero
   - Subtracting the achieved fractional dose (which maybe less than the nominal fractional dose) from the total remaining dose to the target
   - Dividing the remaining dose by the remaining number of fractions to produce an updated fractional target dose

- Rotate the achieved fractional dose distribution add it to the cumulative total achieved dose distribution

Note that the final field should be the least-occluded and hence has maximum flexibility for the delivery of that dose. It is nevertheless possible that for a pathological occlusion, the total objective dose may be unachievable, in which case approaching the target from a different set of angles or a different plane is the only solution.

8. Compute real time and CPU time, saving to `times.dat` (plain text)
9. Save the total dose distribution to `Vt.mat`
10. Save all individual-field dose distributions to `V.mat`
11. Save complete treatment plan (all fields) to `plan.mat`
12. Save part of the plan to `plan_consolidated.mat` - this is just used for calculating some of the errors etc. afterwards
13. Visualise some sections through the objective and final result, and then calculate the RMS error and various other performance metrics, saving to appropriately-named files

Several of the key MATLAB functions used by this driver are now described.

A.4.1 `tps3D_het.m`

This is the main function which generates the treatment plan for a single field. Given the various parameters and constraints documented below, it creates an appropriate beam grid, determines the range of position/energy/ion combinations which are needed, performs depth adjustments for each of those to account for the heterogeneity of the phantom, constructs a matrix of the dose distributions resulting from each of these, plus a vector of the desired dose distribution, performs the non-negative least squares optimisation, and finally returns a complete plan (amongst other things).

Usage:

```
function [plan, C, d, x, resnorm, residual] = tps3D_het (phantom_volume, target_volume, library,
    reg_decimations_weights, grid_x, grid_y, grid_z, latticetype,
    oar, hypoxic, hypoxic_threshold_Z)
```

Arguments:

- `phantom_volume`: 3D volumetric array of phantom; materials are labelled according to labels defined in `get_labels ()`
- `target_volume`: 3D volumetric array of desired target dose distribution in Gy
- `library`: ion data library for all ions to be used in the plan
- `reg_decimations_weights`: 2-row matrix; first row is the decimation (spatial downsampling - every Nth voxel) factors, second row is the relative weights for target, distal boundary, distal, peripheral, proximal and OAR
- `grid_x, grid_y, grid_z`: separation between grid points in x, y and z dimension. Interpreted slightly differently depending on `latticetype`
- `latticetype`: either `'rect'` or `'tri'`. This is the grid for the permitted position for the Bragg peaks of individual monoenergetic beam components. If `'tri'` then then `grid_y` is ignored, `grid_x` is the side length of the equilateral triangular mesh.
- `oar, hypoxic`: optional 3D volumetric binary arrays delineating the organ at risk and hypoxic regions, if any
- `hypoxic_threshold_Z`: ions with Z lower than or equal to this threshold will not be used distal to hypoxic regions due to the high entrance dose

Return values:

- `plan`: treatment plan data structure, containing depth-adjusted per-ion/energy dose deposition library (`realdoseprofiles`, list of used energies and ions `energies`, copy of target volume (`target_volume`) and phantom volume (`phantom_volume`) plus OAR (`oar`) and hypoxic (`hypoxic`) volumes, if applicable, x, y and z dimensions of these volumes (`targ_x, targ_y, targ_z`), beam position grid (`beamgrid`) and weights (`weights`).
- `C, d`: dose distribution contribution$\mathbf{C}$-matrix (each column is the unrolled dose distribution corresponding to a particular beam position, ion species and energy) and dose-objective unrolled $\mathbf{d}$-vector
- `x`: resulting set of optimal weights from minimising $||\mathbf{Cx} - \mathbf{d}||^2$

- `resnorm, residual`: resnorm and residual error from optimisation process `lsqnonneg`.

A.4.2 `generate_dose_matrix_het.m`

This function constructs the **C**-matrix and **d**-vector used by the optimiser. Each column of **C** corresponds to the unrolled dose contribution from one energy of one ion in one position irradiating the heterogeneous phantom in that position. Similarly, **d** is the unrolled objective dose distribution; it is scaled by the factors listed in the second row of `reg_decimations_weights`, according to the regions identified by the function `partition_regions`.

Usage:

```
function [C, d] = generate_dose_matrix_het (plan, reg_decimations_weights)
```

Arguments:

- `plan`: the prototypical plan (which has been prepopulated with all of the input plan parameters, such as the various phantom, target, OAR and hypoxic volumes, plus the depth-adjusted ion library.
- `reg_decimations_weights`: see documentation for tps3D_het.m

Return values:

- `C, d`: see documentation for tps3D_het.m

A.4.3 `partition_regions.m`

Usage:

```
function [regions, idx, partitioned_idx] = partition_regions (plan, reg_decimations)
```

Arguments:

- `plan`: the prototypical plan (which has been prepopulated with all of the input plan parameters, such as the various phantom, target, OAR and hypoxic volumes, plus the depth-adjusted ion library.

- `reg_decimations`: the first row of the matrix passed to `tps3D_het`.

Return values:

- `regions`: volumetric representation of relative-positional regions within the target volume, labelled according to whether each voxel is in the target, at the distal boundary of the target, distal further to this, peripheral to the beam, proximal to target or in the OAR
- `idx`: list of indices in the unrolled target volume (i.e. linearised representation of 3D volumetric matrix) where we want to fit the weighted sum of dose distributions.
- `partitioned_idx`: cell array of the indices corresponding to each of the different positional regions.

A.4.4 `get_regions.m`

Generates two structures containing labels and attributes for each tissue type - one by name, one by value.

Usage:

```
function [T_by_name, T_by_value] = get_labels ()
```

Return values:

- `T_by_name` - structure of structures containing elements whose name corresponds to the tissue type. Each of these, in turn, is a structure with elements named `value` (numerical label - currently we have defined `Air, Water, Skin, Bone, Brain, Adipose, Tumour and PMMA` as numerical values 1-8, respectively), `PERR` (PMMA-equivalent range ratio), `PEDR` (PMMA-equivalent dose ratio - unused) and `density` (g/cm^3).
- `T_by_value` - linear array of structures, whose index corresponds to the values defined above. Each structure contains the same information as the elements of `T_by_name`.

A.4.5 `create_spherical_phantom_target_oar.m`

Generates a spherical head phantom with a tumour, and (optionally) an OAR and hypoxic region.

Usage:

```
function [phantom, target, oar, hypoxic] = create_spherical_phantom_target_oar (dimensions_px, ↩
    centre_coords_px,
    head_r, skin_t, skull_t, tumour_coords, tumour_r, tumour_tissue,
    oar_coords, oar_r, oar_tissue, hypoxic_coords, hypoxic_r, dose, debug)
```

Arguments:

- `dimensions_px`: size of phantoms to be generated, in pixels/voxels (assuming 1 mm cubic voxels) (e.g.

  $$100, 100, 300$$

)

- `centre_coords_px`: location of the tumour within the volume - normally in the centre of the volume defined above (e.g.

  $$50, 50, 150$$

)

- `head_r, skin_t, skull_t`: radius of spherical head, thickness of skin, thickness of skull

- `tumour_coords, tumour_r, tumour_tissue`: position, radius and tissue type of a spherical tumour relative to the centre of the head. The tumour always remains at the absolute position `centre_coords_px` inside the target volume, and the head is then positioned relative to the tumour

- `oar_coords, oar_r, oar_tissue`: position, radius and tissue type of a spherical OAR, if desired. As for the tumour, the position of the OAR is defined relative to the centre of the head. To temporarily disable an OAR you can make the radius imaginary.

- `hypoxic_coords, hypoxic_r`: position and radius for a spherical hypoxic region, if desired. No tissue type is defined as this is strictly a region definition.

- `dose`: objective dose to the tumour, in Gy
- `debug`: not used any more, formerly used to enable visualisation of the phantom/target/oar/hypoxic region.

Return values:

- `phantom, target, oar, hypoxic`: 3D phantom, target, OAR and hypoxic volumes. The phantom values are the labels sas defined in `get_labels ()`. The target volume contains dose values, OAR and hypoxic volumes are binary (0 or 1).

A.4.6 `calculate_multi_ion_dose_distribution_het`

Calculate the total dose distribution from a single field treatment plan in a heterogeneous phantom.

Usage:

```
1 function ddist = calculate_multi_ion_dose_distribution_het (plan, debug)
```

Arguments:

- `plan`: one individual field plan
- `debug`: integer, if specified, print out varying levels of debug info depending on the value. Probably no longer needed.

Return values:

- `ddist`: resulting dose distribution

A.5 Visualisation

Several useful functions are provided for visualising output via slices through inputs/outputs and generation of animated GIFs.

A.5.1 plan_and_result.m

Generates XY, XZ and YZ slices through the specified point in the plan, result, and difference volumes, saving as EPS and PDF files.

Usage:

```
function [rms_by_reg, D50, D90, PTV, V5, V10, V50] = plan_and_result (plan, result, cfov)
```

Arguments:

- `plan`: one individual field plan - e.g. one element of the multifield plan as provided by `run_tps_multifield_1c`. This is used to conveniently pass the phantom, target, OAR and hypoxic volumes through for partitioning and visualisation.
- `result`: the total volumetric dose distribution resulting from the plan
- `cfov`: coordinates of the centre of the field of view, through which the slices will be taken

Return values:

- `rms_by_reg`: cell array containing the RMS error in each region (i.e. target, distal boundary, distal, peripheral, proximal and OAR
- `D50, D90`: total volumes (in mm^3) receiving at least 50% and 90% of the dose, respectively
- `PTV`: planning target volume (i.e. total volume in mm^3 that we want to irradiate, according to the target volume in `plan`)
- `V5, V10, V50`: total non-target volumes subject to dose exceeding 5%, 10% and 50% of dose to target

A.5.2 dosevis.m

Generate a set of images of dose contributions from each ion in each field (`dose_FIELD_ION.png`), plus total dose in each field (`totaldose_FIELD.png`), plus total dose (`totaldose.png`).

In addition, there is a driver script (`dosevis_all`) which calls dosevis.m repeatedly on multiple plans in multiple folders - read the script to see an example as to how this works.

Usage:

```
function dosevis (plan, theta, map)
```

Arguments:

- `plan`: multi-field treatment plan (cell array of individual fields)
- `theta`: angle from which to generate images
- `map`: (optional) colour map to use - defaults to `jet`

A.5.3 `anim.m, anim_simple.m, anim_phantom.m, anim_isodose.m`

Generate an animated GIF of the achieved dose distribution + phantom, just dose distribution, just phantom, or isodose surface, showing two full rotations of the volume.

Usage:

```
function anim (plan, V, filename, map)
function anim_simple (V, filename, map)
function anim_phantom (plan, filename, map)
function anim_isodose (plan, V, filename, map, percentage)
```

Arguments:

- `plan`: single-field plan (used to obtain phantom, target, OAR and hypoxic regions; not used for `anim_simple`)
- `V`: 3D array of achieved dose distribution (not used for `anim_phantom`)
- `filename`: (optional) output filename (will write to a GIF file) - defaults to `animation.gif`
- `map`: (optional) colour map to use - defaults to `jet`
- `percentage`: (optional, isodose only) percentage threshold (e.g. 50 for D50 surface, enclosing volume with at least 50% of objective dose)

A.5.4 `split_plan.m`

Separates the dose contribution from each ion for a multi-ion treatment plan (one field only), returning the result as a cell array. This is used for `sanim_split.m`

Usage:

```
function split = split_plan (plan)
```

Arguments:

- `plan`: single-field plan

Return value:

- `split`: cell array containing dose contributions from each ion

A.5.5 `anim_split.m`

Generate multiple animated GIFs for the dose contributions + phantom of each ion in a multi-ion plan. Note; we don't need to explicitly pass the dose volume `V` here as it is generated on the fly from the plan using `split_plan.m`.

Usage:

```
function anim_split (plan, filename_pattern, map)
```

Arguments:

- `plan`: single-field plan (used to obtain phantom, target, OAR and hypoxic regions; not used for `anim_simple`)
- `filename`: (optional) output filename (will write to a GIF file) - defaults to `animation.gif`
- `map`: (optional) colour map to use - defaults to `jet`

A.5.6 Driver scripts for multi-field animations

Several hackish driver scripts are provided for bulk-animating multi-field treatment plans. These are NOT matlab functions and are very context-specific - users are advised to read the scripts and use them as examples if you need to do multiple animations, rather than trying to run them blindly. Here they are only listed and not documented in detail:

- `anim_all.m` - visualise all fields in multi-field treatment plan, for a range of tumour positions
- `anim_split_all.m` - visualise all fields, broken down by individual ion contributions, in multi-field treatment plan, for a range of tumour positions

A.6 Monte Carlo simulations of resulting treatment plans

A.6.1 `plan_to_g4mac_mono_en.m`

Generates a set of Geant4 macros suitable for use with `hit_uts` for generating a Monte Carlo simulation corresponding to the generated treatment plan.

Usage:

```
function plan_to_g4mac_mono_en (plan, library, reduction_factor)
```

Arguments:

- `plan`: single-field plan
- `library`: the ion data library, as used by the TPS
- `reduction_factor`: (optional) factor by which the dose to target is reduced compared to the plan (e.g. for a quick simulation of 1% of the planned dose)

APPENDIX B

Supporting tables for Chapter 4

Table B.1: RMS error for dose distributions within the target and the surrounding regions; no hypoxic sub-volume within the tumour, OAR region 10 mm distal to tumour.

Tumour position	Ion combination	Target	Distal boundary	Distal	Peripheral	Proximal	OAR
Shallow	^{1}**H**	11.45	16.25	0.0141	1.96	39.88	0.0092
	^{4}**He**	11.27	15.86	0.1343	1.866	40.16	0.4320
	^{7}**Li**	12.23	15.73	0.3192	1.891	40.61	0.9108
	^{12}**C**	12.54	15.80	0.6900	1.845	39.88	2.206
	^{16}**O**	12.08	16.17	0.5704	1.863	40.38	1.507
	^{10}**Ne**	12.25	15.95	0.5271	1.8436	40.05	1.597
	^{28}**Si**	11.63	16.92	0.5184	1.871	40.70	1.620
	^{56}**Fe**	12.22	16.58	0.4242	1.864	41.54	1.310
	^{1}**H,** ^{12}**C**	11.32	15.98	0.1135	1.949	39.98	0.2513
	^{4}**He,** ^{16}**O**	11.05	15.66	0.1757	1.869	40.20	0.5134
	^{7}Li,^{20}Ne	12.05	15.74	0.3476	1.874	40.59	0.9373
	^{1}**H,** ^{4}**He,** ^{16}**O**	10.91	15.66	0.1159	1.901	40.10	0.2965
	^{7}**Li,** ^{12}**C,** ^{56}**Fe**	12.08	15.74	0.3437	1.886	40.81	0.9111
	^{12}**C,** ^{16}**O,** ^{20}**Ne**	12.10	15.94	0.5129	1.843	40.08	1.484
	All ions	10.8519	15.5959	0.1321	1.8983	40.2035	0.3205
Central	^{1}**H**	11.85	17.56	0.0297	2.458	43.72	0.0131
	^{4}**He**	11.57	16.08	0.2821	2.188	44.37	0.7750
	^{7}**Li**	12.01	16.89	0.7560	2.18	44.92	1.986
	^{12}**C**	14.75	16.82	1.5776	2.024	41.75	4.078
	^{16}**O**	14.02	17.72	1.359	2.097	42.83	3.429
	^{10}**Ne**	14.94	17.40	1.497	2.068	42.55	3.886
	^{28}**Si**	16.15	18.43	1.634	2.068	43.40	4.043
	^{56}**Fe**	16.16	18.86	1.588	2.137	45.40	3.902
	^{1}**H,** ^{12}**C**	11.6824	17.28	0.1907	2.449	43.87	0.3259
	^{4}**He,** ^{16}**O**	11.68	17.28	0.1907	2.449	43.87	0.3259
	^{7}Li,^{20}Ne	12.01	16.89	0.7560	2.176	44.92	1.986
	^{1}**H,** ^{4}**He,** ^{16}**O**	11.36	16.19	0.1618	2.360	44.19	0.4364
	^{7}**Li,** ^{12}**C,** ^{56}**Fe**	12.01	16.90	0.7591	2.177	44.93	1.986
	^{12}**C,** ^{16}**O,** ^{20}**Ne**	13.99	17.69	1.391	2.083	42.85	3.420
	All ions	11.33	16.19	0.1752	2.363	44.23	0.4501

Table B.2: RMS error for dose distributions within the target and the surrounding regions; hypoxic sub-volume within the target; OAR region 10 mm distal to the tumour.

Tumour position	Ion combination	Target	Distal boundary	Distal	Peripheral	Proximal	OAR
Shallow	^{1}**H,** ^{12}**C**	11.56	16.03	0.1453	1.953	40.01	0.5258
	^{4}**He,** ^{16}**O**	11.27	15.70	0.2027	1.869	40.20	0.6914
	^{7}Li,^{20}Ne	12.09	15.79	0.3593	1.878	40.58	1.070
	^{1}**H,** ^{4}**He,** ^{16}**O**	11.18	15.68	0.1423	1.906	40.12	0.4839
	^{7}**Li,** ^{12}**C,** ^{56}**Fe**	12.03	15.92	0.3455	1.887	40.91	1.011
	^{12}**C,** ^{16}**O,** ^{20}**Ne**	1210	15.94	0.5129	1.843	40.08	1.484
	All ions	10.95	15.68	0.1540	1.902	40.26	0.5026
Central	^{1}**H,** ^{12}**C**	11.87	17.59	0.1938	2.447	43.80	0.6795
	^{4}**He,** ^{16}**O**	11.97	16.30	0.3809	2.187	44.32	1.170
	^{7}Li,^{20}Ne	12.57	16.91	0.7994	2.177	44.83	2.24
	^{1}**H,** ^{4}**He,** ^{16}**O**	11.97	16.30	0.3810	2.187	44.32	1.170
	^{7}**Li,** ^{12}**C,** ^{56}**Fe**	12.51	16.89	0.8036	2.179	44.91	2.233
	^{12}**C,** ^{16}**O,** ^{20}**Ne**	13.99	17.69	1.391	2.083	42.85	3.420
	All ions	11.62	16.52	0.2423	2.370	44.17	0.7250

Table B.3: Percentages of the target volume that received at least 50% and 90% of the dose volume; no hypoxic sub-volume within the tumour, OAR region 10 mm distal to tumour.

Tumour position	Ion combination	D_{50}	D_{90}
Shallow	**^{1}H**	99.49	87.19
	^{4}He	99.43	87.62
	^{7}Li	98.91	86.90
	^{12}C	98.82	85.86
	^{16}O	98.91	86.82
	^{10}Ne	98.98	86.68
	^{28}Si	99.26	86.83
	^{56}Fe	99.05	86.22
	^{1}H, ^{12}C	99.58	87.43
	^{4}He, ^{16}O	99.67	87.83
	^{7}Li,^{20}Ne	99.05	87.11
	^{1}H, ^{4}He, ^{16}O	99.72	87.88
	^{7}Li, ^{12}C, ^{56}Fe	99.00	87.00
	^{12}C, ^{16}O, ^{20}Ne	99.01	87.06
	All ions	99.77	88.00
Central	**^{1}H**	99.51	85.86
	^{4}He	99.47	87.21
	^{7}Li	99.31	86.03
	^{12}C	98.47	71.24
	^{16}O	98.48	78.65
	^{10}Ne	98.13	73.00
	^{28}Si	97.58	70.88
	^{56}Fe	97.53	71.95
	^{1}H, ^{12}C	99.55	86.11
	^{4}He, ^{16}O	99.47	87.21
	^{7}Li,^{20}Ne	99.31	86.03
	^{1}H, ^{4}He, ^{16}O	99.54	86.99
	^{7}Li, ^{12}C, ^{56}Fe	99.31	86.07
	^{12}C, ^{16}O, ^{20}Ne	98.49	78.96
	All ions	99.58	87.00

Table B.4: Percentages of the target volume that received at least 50%, and 90% of the dose volume; hypoxic sub-volume within the target; OAR region distal to the tumour.

Tumour position	Ion combination	D_{50}	D_{90}
Shallow	**^{1}H, ^{12}C**	99.55	85.81
	^{4}He, ^{16}O	99.51	87.74
	^{7}Li,^{20}Ne	99.01	87.03
	^{1}H, ^{4}He, ^{16}O	99.59	87.76
	^{7}Li, ^{12}C, ^{56}Fe	99.074	86.87
	^{12}C, ^{16}O, ^{20}Ne	99.01	87.06
	All ions	99.75	87.96
Central	**^{1}H, ^{12}C**	99.53	85.72
	^{4}He, ^{16}O	99.34	86.61
	^{7}Li,^{20}Ne	99.19	83.68
	^{1}H, ^{4}He, ^{16}O	99.34	86.61
	^{7}Li, ^{12}C, ^{56}Fe	99.25	83.94
	^{12}C, ^{16}O, ^{20}Ne	98.49	78.96
	All ions	99.46	86.66

Table B.5: Planning target volume (PTV) of 14147 mm^3 and volumes outside the tumour which received at least 5%, 10% and 50% of the target dose volume in mm^3; 5%, 10% and 50% of the target dose volume in mm^3; no hypoxic sub-volume within the tumour;OAR region 10 mm distal to the tumour.

Tumour position	Ion combination	V_5 mm^3	V_{10} mm^3	V_{50} mm^3
	^{1}H	30970	27466	15905
	^{4}He	30041	26821	15787
	^{7}Li	30518	26825	15952
	^{12}C	31467	26617	15762
	^{16}O	31375	26767	15807
	^{10}Ne	31362	26729	15789
	^{28}Si	31805	27170	15939
Shallow	**^{56}Fe**	31276	27058	16039
	^{1}H, ^{12}C	30805	27325	15897
	^{4}He, ^{16}O	30039	26836	15773
	^{7}Li,^{20}Ne	30491	26807	15919
	^{1}H, ^{4}He, ^{16}O	30418	27039	15843
	^{7}Li, ^{12}C, ^{56}Fe	30431	26798	15989
	^{12}C, ^{16}O, ^{20}Ne	30431	26798	15989
	All ions	30330	26996	15845
	^{1}H	73601	65933	39726
	^{4}He	70203	63100	38883
	^{7}Li	72781	63446	39370
	^{12}C	76328	62508	37634
	^{16}O	76711	63983	38275
	^{10}Ne	77192	63719	38119
	^{28}Si	78074	65146	38665
Central	**^{56}Fe**	77601	65283	39779
	^{1}H, ^{12}C	73408	65826	39825
	^{4}He, ^{16}O	70203	63100	38883
	^{7}Li,^{20}Ne	72781	63446	39370
	^{1}H, ^{4}He, ^{16}O	71948	64746	39665
	^{7}Li, ^{12}C, ^{56}Fe	72775	63452	39382
	^{12}C, ^{16}O, ^{20}Ne	76748	63885	38206
	All ions	71994	64775	39723

Table B.6: Planning target volume (PTV) of 14147 mm^3 and volumes outside the tumour which received at least 5%, 10% and 50% of the target dose volume in mm^3; 5%, 10% and 50% of the target dose volume in mm^3; hypoxic sub-volume within the target; OAR region distal 10 mm to the tumour.

Tumour position	Ion combination	V_5	V_{10}	V_{50}
	^{1}H, ^{12}C	30873	27357	15950
	^{4}He, ^{16}O	30110	26817	15799
	^{7}Li,^{20}Ne	30681	26820	15910
Shallow	**^{1}H, ^{4}He, ^{16}O**	30486	27050	15877
	^{7}Li, ^{12}C, ^{56}Fe	30486	27050	15877
	^{12}C, ^{16}O, ^{20}Ne	31369	26706	15806
	All ions	30449	27017	15887
	^{1}H, ^{12}C	73446	65817	39714
	^{4}He, ^{16}O	70448	63137	38848
	^{7}Li,^{20}Ne	73173	63524	39398
Central	**^{1}H, ^{4}He, ^{16}O**	70448	63137	38848
	^{7}Li, ^{12}C, ^{56}Fe	73059	63486	39410
	^{12}C, ^{16}O, ^{20}Ne	76748	63885	38206
	All ions	72307	64932	39672